Search for CP Violation in Singly Cabibbo-Suppressed Charm Decays

By

Ryan Mackenzie White

Bachelor of Science
University of Massachusetts, Amherst 2001
Bachelor of Arts
University of Massachusetts, Amherst 2001
Master of Science
University of South Carolina 2005

Submitted in Partial Fulfillment of the Requirements

for the Degree of Doctor of Philosphy in

Physics

College of Arts and Sciences

University of South Carolina

2010

Accepted by:

Milind V. Purohit, Major Professor

Jeff Wilson, Committee Member

Brett Altshcul, Committee Member

David B. Hitchcock, Committee Member

Dr. Tim Mousseau, Interim Dean of the Graduate School

Acknowledgments

I like to thank my dissertation advisor, Dr. Milind V. Purohit, for his support and wealth of knowledge he shared with me over the years. I also like to thank my family for their guidance, caring, and patience throughout my graduate student career. As well, I must thank my close friend and colleage, Nathan Baltzell, who struggled through the Ph.D. program alongside me, for our conversations about physics. And finally, I like to thank my few close and trusted friends, Andy and Lie, Mark, and James, for believing in me and staying in touch with me all these years.

Abstract

CP violation in singly Cabibbo-Suppressed (SCS) weak decays of charged D mesons is predicted in the Standard Model (SM) to have asymmetries on the order of 10^{-3}. CP violation has not yet been observed in the Charm sector; however, the BaBar experiment now has extremely large data samples of charged D mesons which may have the sensitivity to make such a measurement. The CP asymmetry will be measured by studying the asymmetry of the Dalitz plot for D^+ and D^-. A fit of the Dalitz plot will give insight of the underlying physics of the decay by measuring the amplitudes and relative phases of resonant (*i.e.* ϕ and K^{*0}) and the non-resonant states.

Preface

From our observations of the universe, we believe that we live in an almost empty expanse of matter. Our nieve assumption is that indeed the entire universe is dominated by matter and so little anti-matter exists that we must create small amounts of it in a laboratory in order to study its properties. The physicists' quest to understand this asymmetry between matter and anti-matter is an underlying motivation behind today's particle physics experiments. Theory cannot provide a definitive answer as to why we live in such a world but does provide a guide as to what experimentalists should look for.

In 1967, before much of the theoretical work began in Grand-Unification Theory (GUT) and shortly after two very important experimental observations were announced, Andrei Sakharov [**1**] published his seminal paper entitled "Violation of CP Invariance, C Asymmetry, and Baryon Asymmetry of the Universe". This work was most likely inspired by the observation of Cosmic Microwave Background Radiation (CMBR), an observational signature of the Big Bang, and the discovery of Charge-Parity (CP) violation in the decays of neutral kaons, an unexpected violation of the symmetry thought to be obeyed by the weak nuclear force. Sakharov explained how there must be three conditions that were satisfied simulataneously during the early universe which lead to the non-zero baryon density that we observe today:

1) There must be baryon number violating transitions.

2) CP invariance must be broken.

3) The baryon number and CP violating transitions must proceed out of thermal equilibrium.

We have not observed any baryon-number violating process, but CP violating decays in the kaon and B mesons have been established. Our knowledge of the fundamental forces and the constituent particles which make up matter, known as the Standard Model, allows for a tiny amount of CP violation through a single weak phase. All measurements of either direct or indirect CP violating decays agree with the predictions of the Standard Model. This agreement between theory and observations creates an even greater mystery because the amount of anti-matter that could have been generated from such CP violating transitions can only account for a tiny fraction of anti-matter. This suggests that we do not have a theory which can describe the origins of the universe.

As an experimentalist, this is actually encouraging, because theory and experiment give us an indication of where to look for other CP violating transitions. Decays of charm mesons provide a unique laboratory to look for CP violation because charm changing neutral currents are hugely suppressed and the CP violating asymmetries are extremely small. Therefore, charm decays with potential for observing CP violation have almost zero-background with respect to New Physics!

Contents

List of Tables

List of Figures

Chapter 1

Introduction

Charm mesons provide a unique probe for Charge-Parity (CP) symmetry violation and new physics beyond the Standard Model (SM). The Wolfenstein parametrization [**3**] of the Cabibbo-Kobayashi-Maskawa (CKM) quark mixing matrix expresses the elements in terms of four real quantities λ, A, ρ, and η. The unitarity of the matrix leads to six triangles, one of which is related to quantities describing charm decays

$$V_{ud}V_{cd}^* + V_{us}V_{cs}^* + V_{ub}V_{cb}^* = \delta_{uc} = 0 \tag{1.0.1}$$

where the ratio of two sides of the triangle

$$\frac{V_{ub}V_{cb}^*}{V_{us}V_{cs}^*} \propto \frac{\mathcal{O}(\lambda^5)}{\mathcal{O}(\lambda)} \approx 2.3 \cdot 10^{-3} \tag{1.0.2}$$

is the angle corresponding to CP asymmetry shown in powers of λ (the CP-nonconserving term), and suggests that a significant observation of CP asymmetry of order 1% or higher in a charm decay would be an indication of new physics. The weak phases of charm decays within the SM are expected to be small, and background SM processes (with respect to new physics processes) attributed to CP violating effects will be minimal. On theoretical grounds this makes charm decays an ideal laboratory to search for new physics. Experimentally, there are a number of reasons why charm decays are optimal for CP studies. (i) *BABAR* is producing charm states in large numbers. (ii) Their branching ratios to kaon and pion final states are large. (iii) They reside in a resonance region where direct CP asymmetries can be enhanced by final state interactions (FSI); these can be determined by analyzing π-π, $\pi - K$, and $K - K$ rescattering [**4**].

1.1. Theoretical Motivation

CP violation in mesons is possible in two scenarios. (i) Direct CP violation – the partial widths of the decay of $A \to f \neq \bar{A} \to \bar{f}$. (ii) Indirect CP violation – occurs either through mixing or the interference of mixing and direct decays. The focus of this research is the study of direct CP violation of charged singly Cabibbo-supressed (SCS) $D^{\pm}$ meson decays. Since strong and electromagnetic forces conserve CP, there must exist at least two weak amplitudes in order to exhibit direct CP violation. This cannot occur via Cabibbo allowed and doubly Cabibbo-supressed decays (DCSD) since they are fed by a single weak amplitude. In the decays of $D^{\pm} \to K^{\pm}K^{\mp}\pi^{\pm}$, interference between tree-level and penguin-level processes leads to decay-rate asymmetries (Figure 1.1).

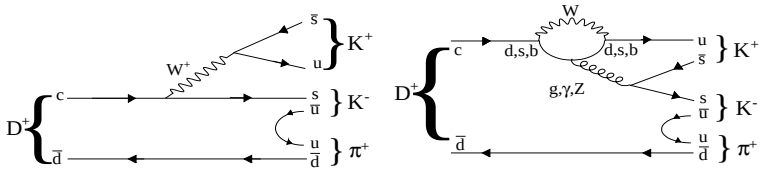

Figure 1.1: Tree-level (left) and penguin-level (right) feynman diagrams

Consider the transition $D \to f$, which decays coherently via the tree-level and penguin-level quark transition amplitudes a_1 and a_2

$$A(D \to f) \equiv A_f = |a_1|e^{i(\delta_1+\phi_1)} + |a_2|e^{i(\delta_2+\phi_2)} \tag{1.1.1}$$

where δ_i are the CP conserving strong phases which may arise from FSI, while ϕ_i are the complex weak phases in the CKM matrix (or may arise from new physics). The CP conjugate decay amplitude is given by

$$\bar{A}(\bar{D} \to \bar{f}) \equiv \bar{A}_{\bar{f}} = |a_1|e^{i(\delta_1-\phi_1)} + |a_2|e^{i(\delta_2-\phi_2)} \tag{1.1.2}$$

The CP asymmetry is defined as

$$A_{CP} = \frac{|A_f|^2 - |\bar{A}_{\bar{f}}|^2}{|A_f|^2 + |\bar{A}_{\bar{f}}|^2} \tag{1.1.3}$$

and using the decay amplitudes A_f and $\bar{A}_{\bar{f}}$, the CP asymmetry in charged meson decays is then given by [**5**]

$$A_{CP} = \frac{2|a_1 a_2| \sin(\delta_2 - \delta_1) \sin(\phi_2 - \phi_1)}{|a_1|^2 + |a_2|^2 + 2|a_1 a_2| \cos(\delta_2 - \delta_1)} \tag{1.1.4}$$

In order for CP violation to occur, two conditions must be met regardless of the underlying dynamics of the decay. (i) There must be a relative phase , $\phi_2 - \phi_1 \neq 0$, between the weak couplings which arises from the fact that such an effect can only occur in SCS decays within the SM. (ii) FSI must induce a phase shift , $\delta_2 - \delta_1 \neq 0$, between the amplitudes which implies that the FSI is nontrivial.

D decays proceed in an environment with many hadronic resonances, and there is no reason to suggest that strong FSI are absent or even small [**6**]. However, the complication arises that these effects are not calculable. The strong phase difference, $\delta_2 - \delta_1$, must be measured along with the amplitude ratio $\frac{a_2}{a_1}$ in order to extract the CP violating weak phase difference.

1.2. Analysis Technique

Previous searches for direct CP violation in SCS decays of charm mesons have not observed a signal [**7**] . These searches measured the partial widths to the resonant and non-resonant decay channels, integrating over phase space. CP violating effects that occur in regions of a Dalitz plot may not be revealed in phase-space integrated measurements.

Weak nonleptonic decays of D mesons proceed dominantly through resonant two-body channels. The amplitudes, A_f and $\bar{A}_{\bar{f}}$, of these decays can be measured using a Dalitz plot analysis technique [**11**], which uses the minimum number of independent observables. For three-body decays of a spin-0 particle to all pseudoscalar final states

$D \to abc$, the decay rate is

$$\Gamma = \frac{1}{(2\pi)^3 32\sqrt{s^3}} |\mathcal{M}|^2 dm_{ab}^2 dm_{bc}^2 \tag{1.2.1}$$

where m_{ij} is the invariant mass of particles i and j. The coefficient of the amplitude contains all the kinematics of the decay, while the $|\mathcal{M}|^2$ contains the dynamics. The scatter plot m_{ab}^2 versus m_{bc}^2 is the Dalitz plot (Figure 1.2). If $|\mathcal{M}|^2$ is constant, the kinematically allowed region of the Dalitz plot will be uniformly populated. Variations in the population over the Dalitz plot will be due to dynamical effects rather than kinematical effects. These dynamical effects are attributed to scattering such as quasi two-body intermediate resonant states.

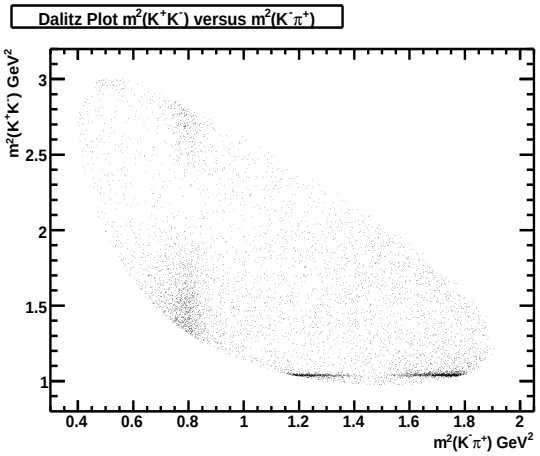

Figure 1.2: Dalitz plot of the decay $D^{\pm} \to K^{\pm}K^{\mp}\pi^{\pm}$ shows dynamical structure around 1 GeV^2 in $m^2(K^{\pm}K^{\mp})$ and 800 MeV^2 in $m^2(K^{\mp}\pi^{\pm})$, indicating the presence of resonant states $\phi(1020)$ and various $\bar{K}^{*0}$ states.

The modeling of the dynamical and kinematical effects in the Dalitz plot is required to extract the CP violating weak phases of the decay as well as the phase shift due to FSI. The amplitude for the decay of the D meson to some intermediate state, $D \to rc$, $r \to ab$, where r is the intermediate resonance, and a,b, and c are pseudoscalar particles, is given by

(1.2.2)

The sum is over the helicity states λ of r, J is the total angular momentum of D (which is zero), L is the orbital angular momentum between the resonance r and the spectator c, l is orbital angular momentum between a and b (the spin of r), $\vec{p}$ and $\vec{q}$ are the momenta of c and a in the rest frame of r, Z describes the angular distribution of the final-state particles, B_L^R and B_L^r are the centrifugal barrier factors for the production of rc and ab, and T_r is the dynamical function describing the intermediate resonance r. The angular distributions, barrier factors, and dynamical functions have various parametrizations.

1.3. Experiment and Data

The analysis uses 460 fb^{-1} integrated luminosity of e^+e^- colliding beam data recorded on or below the Υ(4S) resonance with the *BABAR* detector located at the PEP-II asymmetric storage ring facility at the Stanford Linear Accelerator Center (SLAC). The entire data set from runs 1 through 6, using the latest *BABAR* software release will provide the largest sample of singly Cabibbo-suppressed charm decays in the world. The reconstruction efficiency of the decay is about 10% which results in a sample size on the order of 300,000 signal events above background. The combined D^+ and D^- Dalitz plots will be fit to extract resonant and non-resonant amplitudes in $D^\pm$ decays in this mode assuming no CP violation, while seperate fits of the D^+ and D^- Dalitz plots will be performed to search for CP-violation.

The *BABAR* detector [**21**] is comprised of a Silicon-Vertex Tracker (SVT) at the innermost layer surrounded by a Drift Chamber (DCH) embedded in a 1.5-T solonoid magnetic field which measures charge track momenta and energy loss (dE/dx). A ring-imaging Cherenkov detector (DIRC) is used for particle identification. Photons are detected and electrons identified in the Electromagnetic Calorimeter (EMC). The outermost detector system is the muon detector which is made of Limited-Streamer Tubes (LSTs).

Although muon detection is not important in the Dalitz plot analysis of $D^\pm \to K^\pm K^\mp \pi^\pm$, the outermost part of the *BABAR* detector is crucial to the physics goals of

the experiment. The previous muon chambers were resistive plate chambers (RPCs) which had been failing since the start of *BABAR* . As a service project, I participated in the installation of the new LST muon chambers during the fall of 2006. Additional service work with the Particle Identification Group resulted in a Masters Thesis in the summer of 2005 on the topic of systematic errors in particle ID.

1.4. Conclusion

Previous searches using phase-space integrated measurements of partial widths did not show evidence of CP violation. The search for CP violation in the Dalitz plot of $D^{\pm} \to K^{\pm}K^{\mp}\pi^{\pm}$ may reveal asymmetries in regions of phase space that were previously integrated over. A measurement of A_{CP} greater than 1% would be a clear indication of the presence of the new physics. The study of the Dalitz plot with such high statistics has also never been performed, and comparisons to previous analyses by FOCUS [**29**] may lead to a greater understanding of the underlying dynamics in three-body charm decays.

Chapter 2

Babar Detector

2.1. Introduction

The primary goal of the Babar detector is the systematic study of CP-violating decays of neutral B mesons which provide a sensitive measurement of the CKM matrix element, V_{ub}, and to measure a number of rare B meson decays. Together, the goals of the Babar experiment will enable constraints to be placed on fundamental parameters within the Standard Model. The secondary goals of the experiment include other B physics, the physics of charm mesons, tau leptons, and two-photon physics, which are accessible due to the high luminosity of the PEP-II B Factory. The design of the detector is optimized for CP violation studies but is well suited for these other studies as well.

The PEP-II B Factory is an asymmetric e^+e^- storage ring facility operating at a center of mass (c.m.) energy of 10.58 GeV, which is the $\Upsilon(4S)$ resonance. The $\Upsilon(4S)$ resonance decays exclusively to $B^0\overline{B}^0$ and B^+B^- pairs and serves as an ideal laboratory for the study of B mesons. The PEP-II electron beam operates at 9.0 GeV, while the positron beam operates at 3.1 GeV. The two beams collide head-on, resulting in a Lorentz boost to the $\Upsilon(4S)$ resonance of $\beta\gamma = 0.56$. The boost makes it possible to fully reconstruct the decay vertices of the B mesons; doing so will determine their relative decays and thus provide a means to determine the time dependence of the decay rates.

The comparison of the time-dependent decay rates for the B^0 and $\overline{B}^0$ to self-conjugate states is the crucial test for CP invariance. This requires events in which one of Bs decays to a fully reconstructed CP eigenstate, while the other B is tagged

from its decay products: charged lepton and a charged kaon, as well as the slow pion (π_s) from a D^*.

The particular modes Babar uses to measure CP asymmetries, which correspond to the angles α, β, and γ of the unitary triangle, include the following:

• For $\sin 2\beta$: $B^0 \to J/\psi K^0_S$, $B^0 \to J/\psi K^0_L$, $B^0 \to J/\psi K^{*0}$, $B^0 \to D^+D^-$, $B^0 \to D^{*+}D^{*-}$, *etc.*

• For $\sin 2\alpha$: $B^0 \to \pi^+\pi^-$, $B^0 \to \pi^+\pi^-\pi^0$, $B^0 \to a_1\pi$

• For γ: $B^0 \to D^{0(*)}K^{(*)-}$, $D^{*-}\rho^+$, ...

The small branching fraction of the B mesons, on the order of 10^{-6} to 10^{-4}, as well as the requirement to fully reconstruct one of the final CP eigenstates while tagging the other B from decay products, places stringent requirements on the Babar detector, which include the following:

• The maximum possible acceptance in the center of mass system, resulting in a large uniform acceptance down to small polar angles relative to the boost direction. As a requirement of the boost, the detector is asymmetric.

• Detector components must be very close to the interaction region. The high luminosity provided at PEP-II to achieve the physics goals of Babar involve the use of unusual beam optics.

• Vertex resolution down to 80 μm transverse to the beam direction and 100 μm parallel to the beam direction. The B mesons travel almost parallel to the z-axis, and their decay time difference is measured from the difference in the z-components of their decay positions. Excellent vertex resolution helps in the discrimination of beauty, charm, and light quark vertices. Vertex resolution minimizes multiple scattering.

• High track reconstruction efficiency over a range of 60 MeV/c $< p_T <$ 4 GeV/c for charged particles.

• Momentum resolution better than 7% to separate small signal from background.

• Energy resolution below 5σ and angular resolution between 12 mrad and 3 mrad over a range of 20 MeV to 4 GeV for the detection of photons from π^0 and η^0 decays as well as radiative decays.

• 80% efficient in electron and muon identification while maintaining low misidentification probabilities for hadrons. This is neccesary to properly tag the B flavor, reconstruct the charmonium states, as well as the study of decays involving leptons.

• Identification of hadrons over a wide kinematic range is also neccesary for B tagging. Reconstruction of final states for modes such as $B^0 \to K^{\pm}\pi^{\mp}$ or $B^0 \to \pi^+\pi^-$ also require hadron identification.

• Detection of π^0s over a range of 20 MeV $< E <$ 5 GeV.

• Detection of neutral hadrons.

• Flexible, redundant, and selective trigger system.

• Low noise electronics.

• High bandwidth data-acquisition and control system.

• Detailed monitoring and automated calibration.

• Online computing and network system which controls, processes, and stores the high volume of data.

• The detector components must also tolerate significant radiation doses and operate reliably under high background conditions. The Babar experiment is conducted at a B factory, so shutdown time is minimal to ensure high integrated luminosities.

The Babar detector was designed and built by an international team of scientists and engineers to provide all of the features described above. Figure 2.2 shows a longitudinal section through the detector center and an end view of the detector. The detector surrounds the PEP-II interaction region. The entire detector is offset relative to the beam-beam interaction point by 0.37 m in the direction of the lower energy beam, maximizing the geometric acceptance for the boosted Υ(4S) decays. The major subsystems of the detector include (see Figure 2.1):

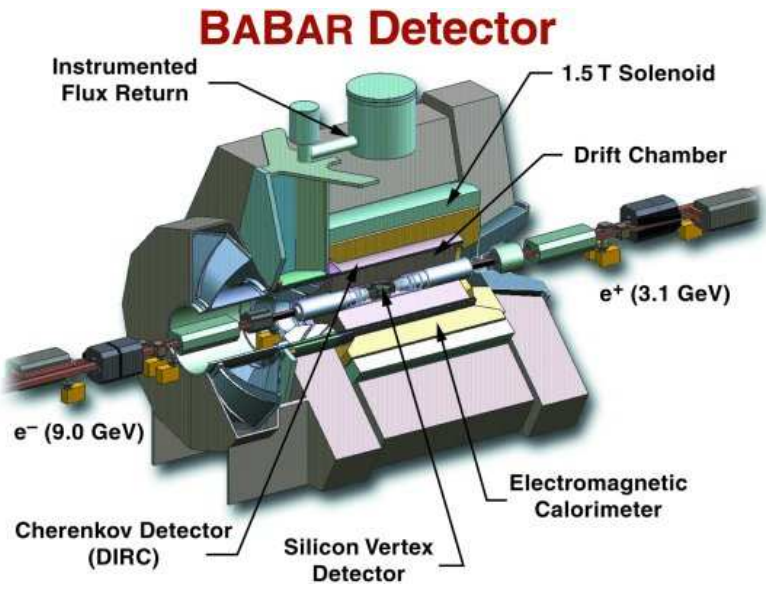

Figure 2.1: Babar Detector Systems

1. Silicon Vertex Tracker (SVT) - The innermost component of the detector provides precise position information in charged tracks, and also is the sole tracking device for very low-energy charged particles.

2. Drift Chamber (DCH) - The DCH provides the main momentum measurements for charged particles as well as providing particle identification through dE/dx measurements for p $>$ 180 MeV/c.

3. Detector of Internally Reflected Cherenkov Light (DIRC) - The primary component for particle identification, designed and optimized for charged hadron.

4. Cesium Iodide Calorimeter (EMC) - Measures electromagnetic showers for neutral hadron identification. The EMC also provides good electron identification down to about 0.5 GeV. The resolution of EMC is on the order of 1% to 2%.

5. Super-conducting coil which surrounds the inner detector systems, producing a 1.5 T solenoidal magnetic field.

6. Instrumented Flux Return (IFR) - Muon identification down to about 0.6 GeV and neutral hadron identification. The latter is of importance in the CP-violating time-dependent asymmetries in $B^0 \to J/\psi K_L^0$ as a cross-check to the result in the $B^0 \to J/\psi K_S^0$ channel.

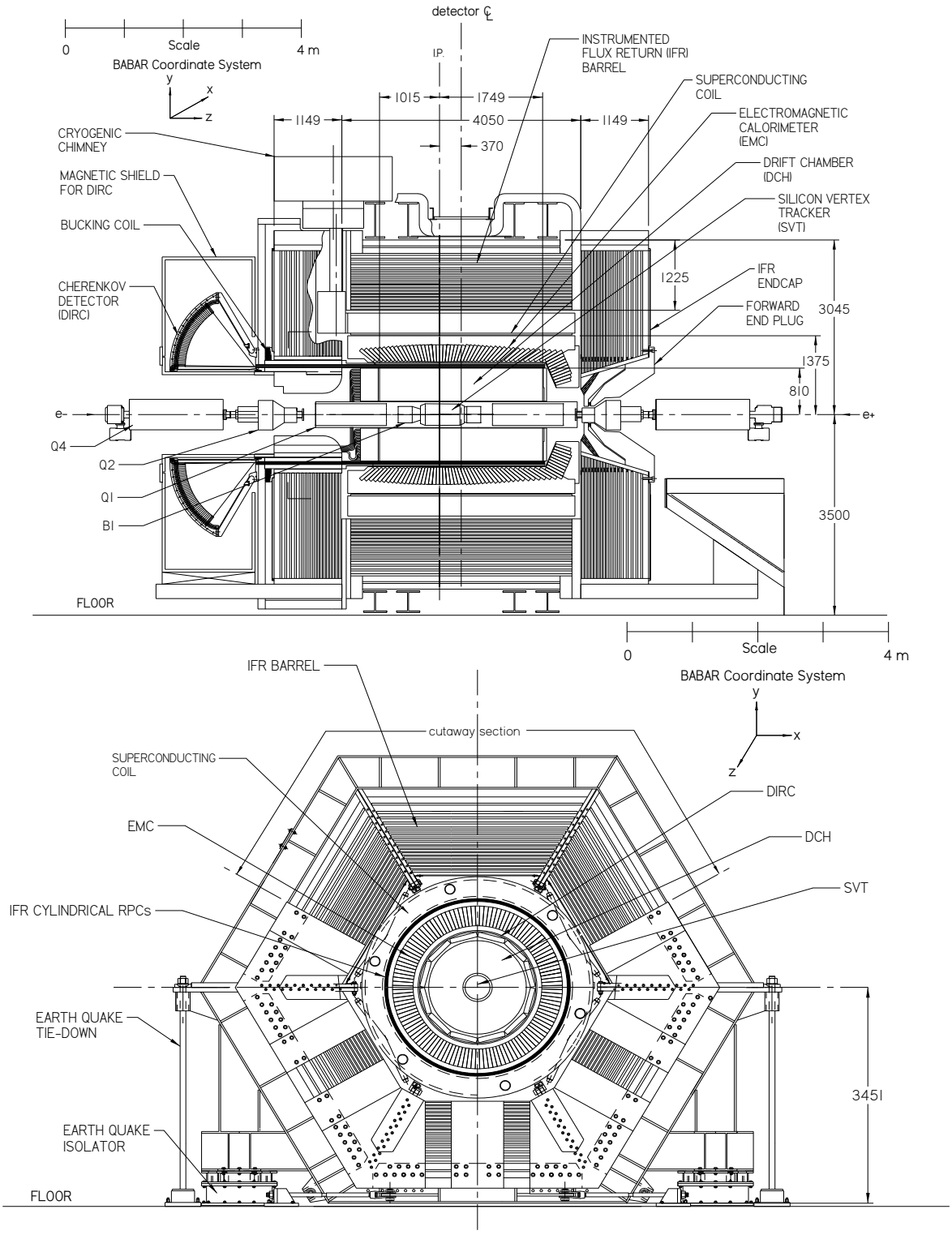

Figure 2.2: Babar Detector longitudinal section (top) and transverse section (bottom)

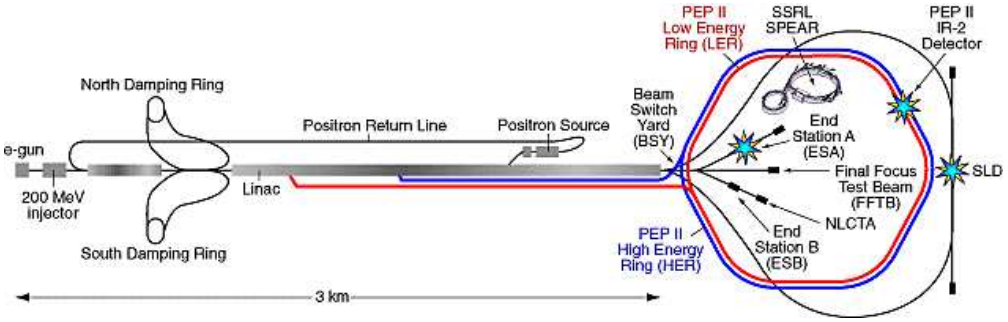

Figure 2.3: Aerial view of the Linac and PEP-II storage ring system

2.1.1. Linac, PEP-II, and the Interaction Region. The Babar experiment rests on the ability to produce $B^0\overline{B}^0$ pairs at the $\Upsilon(4S)$ resonance, fully reconstruct final CP eigenstates of the B mesons, as well as measure the relative decay rates. The first requirement is satisfied by an e^+e^- collider, the second is satisfied from high-luminosity beams, and the third is accomplished by using asymmetric beam energies.

The Linac produces e^+e^- pairs that are injected into the PEP-II storage rings. PEP-II is an asymmetric e^+e^- storage ring facility that collides e^- at 9.0 GeV with e^+ at 3.1 GeV to annihilate at the Interaction Point (IP). The Linac, PEP-II, and the Interaction Region at the Babar detector, shown in Figure 2.3 met the requirements of the experiment and surpassed early expectations of the performance of the machine.

The SLAC Linear Accelerator (Linac) is a two mile-long accelerator, consisting of a cylindrical, disc-loaded, copper waveguide placed on concrete girders in a tunnel about 25 feet underground. The machine consists of an electron gun, the Linac, damping rings, a positron source, klystrons, and bypass tunnels for the injection of particles into the PEP-II storage rings. The electron gun is used to produce the bunches of electrons to inject into the Linac. Some of the electrons produced are accelerated and smashed into a tungsten target, which produces e^+e^- pairs. The positrons are captured and sent back to the portion of the Linac that accelerates the particles to be fed into the damping rings.

The damping rings are used to cool the electrons and refocus the beam to produce the positrons. Once the positrons are produced the damping rings are used by both particles. After the first ten feet of the Linac the bunches are already at energies of 10 MeV, which means the electrons and positrons are already traveling at nearly the speed of light. During the acceleration process, these bunches have a tendency to spread out. The more spread the beams become the less the collisions are likely to occur. The damping rings are used to focus the beams so that more collisions may occur.

Once the beams are focused the particles are fed into the Linac. The Linac accelerates electrons and positrons inside a copper waveguide with an electronmagnetic wave. The particles ride the crest of the wave analogous to a surfer on a water wave, where, in this case, the wave is electromagnetic and travels less than c due to the waveguide. The electromagnetic waves are intense microwaves produced by the klystrons which feed into the accelerator via the copper waveguide. The electrons are accelerated to an energy of 9.0 GeV and the positrons are accelerated to an energy of 3.1 GeV. Once the particles reach these energies, they are sent into the bypass tunnels to be injected into the PEP-II storage rings.

The PEP-II e^+e^- storage ring system is designed to produce a luminosity of at least $3 \times 10^{33} cm^{-2} s^{-1}$ and operate at a c.m. energy of 10.58 GeV, corresponding to to the mass of the $\Upsilon(4S)$ resonance. The electrons feed into the high energy ring (HER) at 9.0 GeV with a current of 0.75 A, and the positrons feed into the low energy ring (LER) with a current of 2.15 A. The PEP-II is designed for 1658 bunches, containing 2.1×10^{10} electrons (HER) and 5.9×10^{10} positrons, spaced 4.2 ns apart. PEP-II typically operates on 40 to 50 minute fill cycles, taking about 3 minutes to replenish the beams.

The high beam currents and the large number of closely spaced bunches neccesary to produce the high luminosity of PEP-II couple detector design and interaction region layout. The two beams must collide only at the interaction point (IP) which is surrounded by the detector. The bunches collide head-on and are magnetically

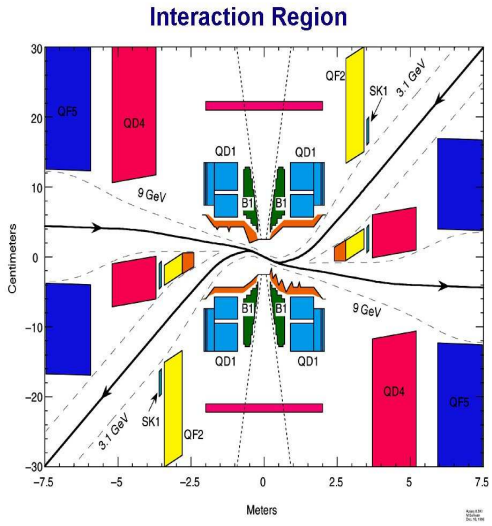

Figure 2.4: Layout of the Interaction Region

held in the horizontal plane by a pair of dipole magnets (B1), followed by offset quadrupole magnets. The layout of the interaction region is shown in Figure 2.4 which illustrates the position of the magnets used to collide the bunches at the IP. The IP spans of distance of less than 300 μm and is located at the center of the interaction region.

The interaction region is enclosed by a water-cooled beam pipe with a 27.9 mm outer radius. The beam pipe is made of two layers of beryllium with a water channel between them. The inner surface is coated with a 4 μm thin layer of gold to attenuate synchrotron radiation. The beam pipe is wrapped with 150 μm tantalum foil on either side of the IP.

2.2. Silicon Vertex Tracker

2.2.1. Introduction. The SVT (Figure 2.5) is the innermost subsystem of the Babar detector, providing precise position and momentum measurements for reconstruction of charged particle trajectory and decay vertices near the IP. Precision measurements on momentum and angles allow for full reconstruction of B and D meson decays, which is an essential design requirement of Babar. The SVT provides

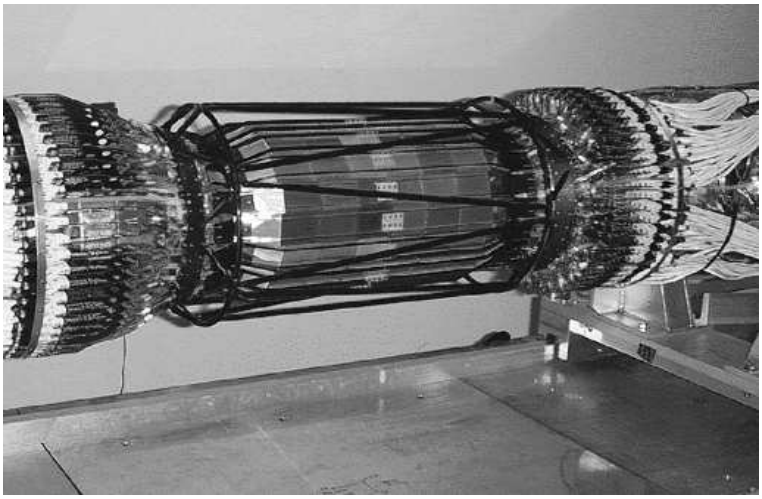

Figure 2.5: Assembled Silicon Vertex Tracker

high resolution tracking measurements at higher momenta, allowing for full reconstruction of charged tracks. The track measurements of the SVT are also important for extrapolation to the DIRC, EMC, and IFR.

2.2.1.1. *Design Requirements and Constraints.* The majority of B decays have low p_T, thus requiring the SVT to have excellent vertex resolution along z, the axis along the beam direction. To fully reconstruct the B, the mean vertex resolution along z is better than 80 μm . Resolution, on the order of 100 μm, in the $x - y$ plane allows for reconstruction of the B, τ, and charm decays.

The SVT has efficient tracking greater than 70% for low p_T. In order to track the slow pion (π_S) from D^* decays, tracking is achieved for particles less than 120 MeV/c. The SVT also provides the best measurement for track angles. Measurements of track angles are essential to achieve the design resolution for the Cherenkov angle of high momentum tracks. The SVT extends 20^0 in polar angle from the beam in the forward direction and 30^0 in the backward direction, maximizing the overall angle coverage of the tracker.

Due to the high luminosity and continual run time of PEP-II, the SVT must withstand 2 MRad of ionizing radiation. The SVT is located completely inside the innermost portion of the detector and is inaccessible during operation, so reliability and robustness are important factors in the design as well.

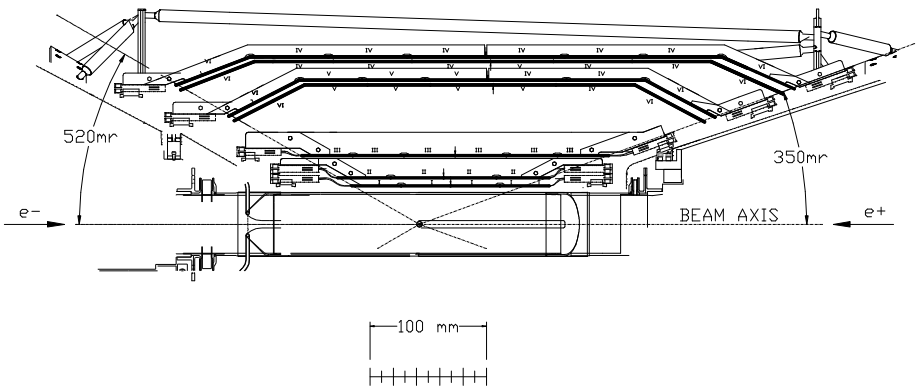

Figure 2.6: Longitudinal schematic view of the SVT. The Roman numerals denote the six different types of sensors.

2.2.2. Layout of the SVT. The design requirements and constraints discussed previously led to a design of five 300-μm-thick double-sided layers of silicon strips. To fulfill the physics requirements for transverse tracks, the spatial resolution is 10-15 μm in three inner layers which perform the impact parameter measurements. The outer layers have a resolution of 40 μm, providing low p_T tracking and pattern recognition. See Figure 2.6 and Figure 2.7.

The double-sided silicon strips are organized in 6 modules for the first three layers, 16 modules for the fourth layer, and 18 modules for the outermost layer. The strips on opposite sides of each sensor are orthogonal to each other. The ϕ measuring strips run parallel to the beam and the z measuring strips are perpendicular to the beam axis. The inner three modules are straight and tilted in ϕ by 5^0, forming an overlap region between adjacent modules which provides full azimuthal coverage and aids with alignment. The two outer modules are arch shaped and cannot be tilted due to this geometry. Thus to avoid gaps and to have overlapping in ϕ, layers 4 and 5 are divided into sublayers and placed at slightly different radii. Five different sensor shapes are required to assemble the planar sections of the layers, satisfying the different geometric requirements of the five SVT layers.

The readout electronics are mounted entirely outside the active detector volume, minimizing the material in the acceptance region. There are approximately 150,000

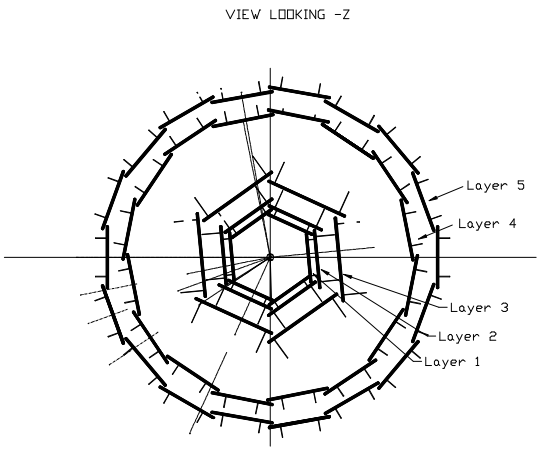

Figure 2.7: Transverse schematic view of the SVT

readout channels. The remaining components are the fanout circuits and the Front End Electronics (FEE). The FEE retain signals from all the strips, improving spatial resolution. The ampliflier for the electronics is sensitive to both positive and negative charge. The overall peaking time is at a minimum of 100 ns for the inner layer and up to 400 ns for the outer layer. The FEEs have small dimensions and can withstand up to 2.5 MRad of ionizing radiation.

The SVT has a rigid support structure composed of two carbon-fiber cones connected to a frame also made of carbon fiber. The SVT is attached to the B1 magnets in such a way to allow for relative motion of the two magnets. The support tube structure is mounted to the PEP-II accelerator supports, allowing for movement between the SVT and Babar.

The five-layer SVT, comprised of double-sided silicon strips, satisfies the design goals and meets the needs of the experiment. The SVT provides high tracking efficiency, excellent hit resolution, and low p_T track reconstruction.

2.3. Drift Chamber

2.3.1. Purpose and Design Requirements. The purpose of the DCH, like the SVT, is the efficient detection of charged particles and precision measurements of their momenta and angles. The DCH complements the SVT measurements for the

impact parameter and particle trajectory near the IP. As well, DCH measurements extrapolate charged tracks to the DIRC, EMC, and IFR.

The reconstruction of decay and interaction vertices outside the SVT volume rely solely on DCH measurements. In order to provide accurate measurements of decays, such as the K_S^0, the chamber measures transverse momenta and direction, as well as longitudinal position of tracks, all with a resolution of about 1 mm.

The DCH provides particle identification for low momentum particles through ionization loss (dE/dx) with a resolution around 7%, allowing for π/K separation up to 700 MeV/c. This ability complements the DIRC, but in the extreme forward and backward region, the DCH is the only detector subsystem providing discrimination between particles of different mass.

The material of the DCH is minimal on the inside and front end of the chamber volume, reducing the amount of mutiple scattering. The DCH is operational under the presence of large backgrounds. The large beam-generated backgrounds have rates about 5 kHz/cell in the innermost region of the chamber.

2.3.2. Drift Chamber Layout. The DCH is small in diameter, with an inner radius of 23.6 cm and an outer radius of 80.9 cm, but extends 2.8 m in length. A schematic drawing is shown in Figure 2.8. The chamber is comprised of 40 layers of small hexagonal cells, providing up to 40 spatial and ionization loss measurements for charged particles with transverse momenta greater than 180 MeV/c. Longitudinal position is accomplished by placing 24 of the 40 innermost layers of wires at small angles with respect to the z-axis.

Reduction of multiple scattering is accomplished inside the chamber by using low-mass aluminum wires and a helium-based gas mixture. The gas is an 80:20 mixture of helium:isobutane with a radiation length of 807 m and dE/dx resolution of 6.9%. The gas system maintains the mixture at constant pressure of 4 mbar. The chamber volume is about 5.3 m^3. During normal operation, the entire gas volume is recirculated in six hours, and one volume of gas is added every 36 hours.

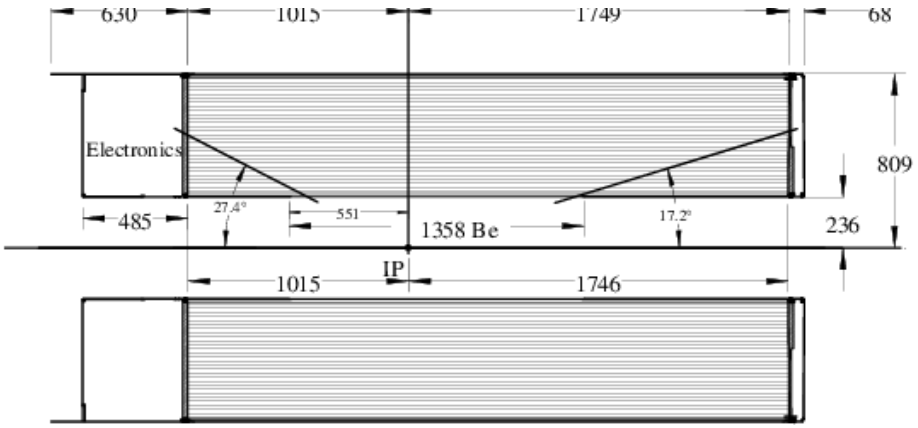

Figure 2.8: Longitudinal section of the DCH with dimensions in mm; the chamber is offset from the IP by 370 mm

The DCH has a thin inner cylindrical wall which facilitates the matching of SVT and DCH tracks, improves track resolution for high momenta tracks, and minimizes background from electromagnetic interactions. The inner wall, carrying 40% of the load, is made of five sections, a central 1 mm-thick beryllium tube with two aluminum extensions and two aluminum end flanges to form a 3 m-long cylindrical part.

The outer wall bears 60% of the axial wire load between the end plates. The material on the outer wall and in the forward direction is minimized to ensure performance of the DIRC and EMC. All of the readout electronics are placed on the backward end plate of the chamber.

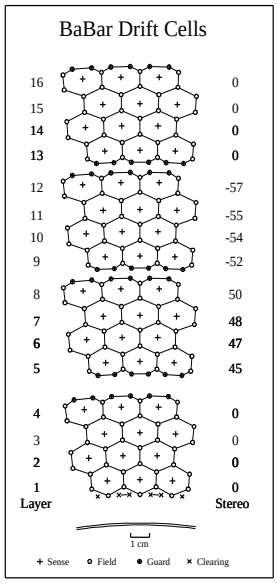

The DCH is bounded radially by the support tube at its inner radius and the DIRC at its outer radius. The center of the chamber is displaced by 36.7 cm in the forward direction due to the boost. This allows for particles emitted at polar angles of 17.2^0 to traverse at least half of the layers before exiting through the front end plate. In the backward direction, particles with a polar angle of 152.6^0 traverse at least half of the layers of the chamber.

The DCH has a total of 7,104 drift cells, arranged in 40 cylindrical layers. The layers are arranged by four into ten super layers (see 2.3.2). Each layer of a super layer has the same wire orientation and equal numbers of cells. The drift cells are hexagonal in shape, 11.9 mm and 19.0 mm along the radial and azimuthal directions, approximating a circular symmetry over a large portion of the cell.

Each cell consists of one sense wire surrounded by six field wires, shown in 2.3.2. The sense wires are made of tungsten-rhenium, 20 μm in diameter and tensioned with a 30 g weight. The field wires, made of aluminum, are held at ground potential while a positive high voltage is applied to the sense wires.

The DCH electronic system provides a measurement of the drift time and the charge, and sends a single bit to the trigger system for every wire with a signal. The electronics are compact and highly modular to accommodate the small cell size and difficult access through the DIRC support tube.

High precision position measurements are obtained from the relation between the measured drift time and drift distance. For each signal, the drift distance is estimated by computing the distance of closest approach between the track and the wire.

The energy loss, dE/dx, for charged particles traversing the chamber is found from the total charge deposited in each drift cell. The individual dE/dx measurements are truncated at 80%, and the specific energy loss per track is taken as mean of the remaining measurements. Figure 2.10 shows the distribution of dE/dx measurements as a function of track momenta. The Bethe-Bloch predictions for particles of different masses are superimposed.

2.4. DIRC

2.4.1. Purpose and Design Requirements. The Particle Identification (PID) system of Babar relies primarily on a new kind of ring-imaging Cherenkov detector

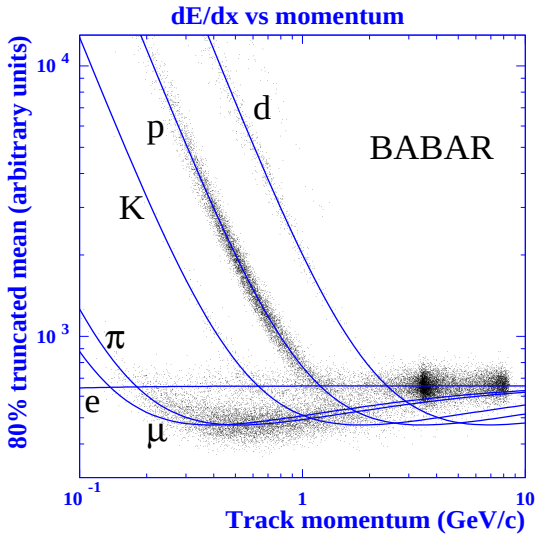

Figure 2.10: Measurement of dE/dx in the DCH as a function of track momenta. The curves show the Bethe-Bloch predictions derived from control samples of particles of different masses.

known as the DIRC. PID below 700 MeV/c is accomplished with dE/dx measurements from the SVT and DCH. The DIRC provides the ability to tag the flavor of one B meson from the cascade decay $b \to c \to s$. The momenta of the kaons used for flavor tagging extend beyond 2 GeV/c with most below 1 GeV/c. Pions and kaons from the rare two-body decays $B^0 \to \pi^+\pi^-$ and $B^0 \to K^+\pi^-$ are well separated. The DIRC provides π/K separation of 4 σ or more for all tracks from B-meson decays from the pion Cherenkov threshold of up to 4.2 GeV/c.

The DIRC is thin and uniform in terms of radiation length and small in the radial dimension, reducing the volume. Also, the system has fast signal response and operates under high backgrounds.

The DIRC geometry and radiator material is chosen so that the magnitudes of angles are maintained upon reflection from a flat surface. Figure 2.11 shows the schematic of the DIRC geometry, illustrating the principles of light production, transport and imaging. The DIRC is a three-dimensional imaging device, relying on the position and arrival time from photo-multiplier tubes (PMTs).

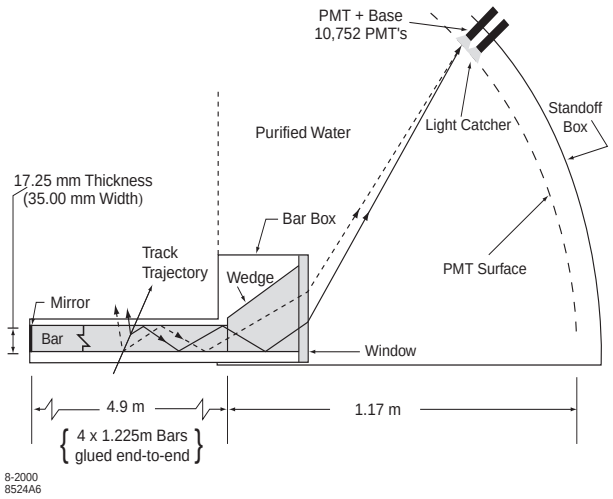

Figure 2.11: Schematic drawing of the DIRC fused silica radiator bar and imaging region

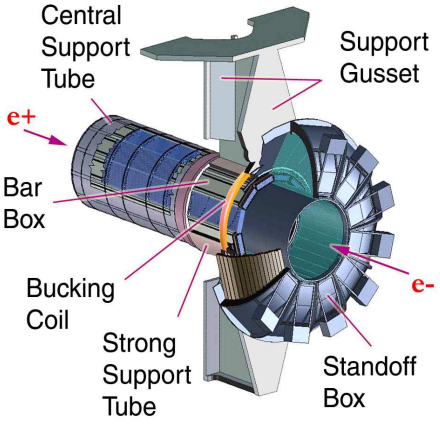

Figure 2.12: DIRC support structure

The principal components of the DIRC are shown in Figure 2.12. The radiator material of the DIRC is synthetic, fused silica in the form of long, thin bars with rectangular cross sections. The bars serve as both the radiative material and as light pipes for light trapped in the radiator due to total internal reflection. The refractive index of the bars is $n = 1.473$, and the Cherenkov angle is given by $cos\theta_C = 1/n\beta$, where $\beta = v/c$. The bars are arranged in a 12-sided polygonal barrel. Each side of the barrel contains an hermetically sealed container, known as the bar boxes. Each barbox contains 12 bars, for a total of 144 bars. The bars are 17 mm-thick, 33 mm-wide, and 4.9m long, and each bar is made of four 1.225 m pieces glued together (see Figure 2.13).

Mirrors are placed at the front end of the radiators to reflect the light to the back end. The radiator bars subtend a solid angle of about 94% of the azimuth and 83% of the c.m. polar angle.

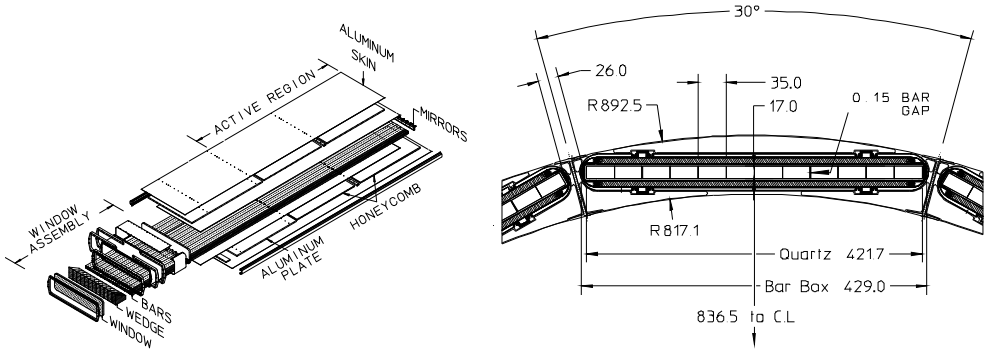

Figure 2.13: DIRC bar box assembly (left) and transverse section of bar box (right)

2.4.1.1. *Layout and Function.* A fused silica wedge is glued to the readout end of the bar to reflect photons at large angles relative to the bar axis. The wedge is nearly the same width as the bars with a trapezoidal profile. The twelve wedges in each bar box are glued to a 10 mm-thick fused silica window, providing a seal to the purified water in the standoff box.

The back end of the detector is instrumented with photon detectors, minimizing interference with other detector systems in the forward region. Once photons arrive at the instrumented end of the detector, they emerge into a water filled region known as the standoff box. The standoff box contains 6,000 liters of purified water. Water is cost effective and has nearly the same refractive index ($n = 1.346$) as the fused silica, which minimizes total internal reflection at the silica-water interface. The water volume is exchanged every ten hours to ensure purity and resistivity.

Once the photons pass through the standoff box they are detected by closely packed PMTs. The PMTs at the rear of the standoff box lie in a toroidal-shaped surface. There are 12 PMT sections, each containing 896 PMTs. The PMTs are surrounded by light catcher cones to capture light that might otherwise miss the PMT. The PMTs are located 1.2 m from the bar end. The cones provide an effective active surface area light collection fraction of 90%.

The DIRC FEE is mounted on the outside of the standoff box. The FEE measures the arrival time of each Cherenkov photon detected by the PMT array to an

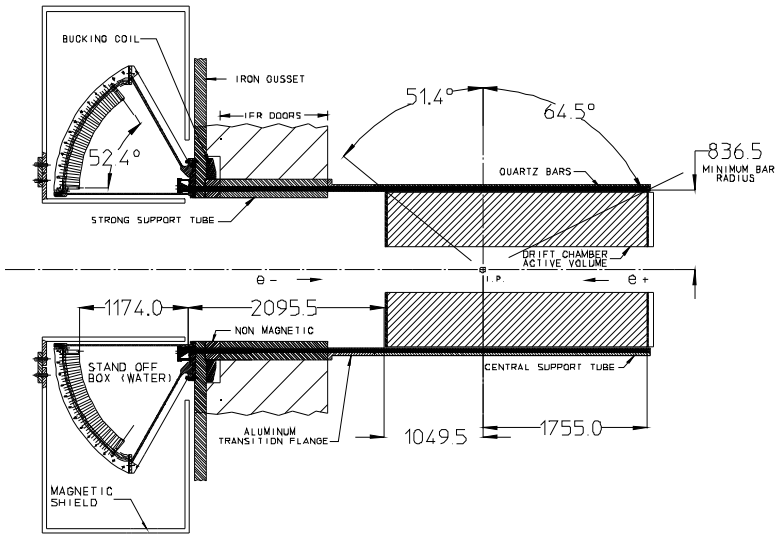

Figure 2.14: [

Elevation view of the DIRC system geometry. All dimensions are in mm.

accuracy of the transit time spread in the PMTs of 1.5 ns. The geometry of the DIRC is shown in Figure 2.14.

2.5. Electromagnetic Calorimeter

2.5.1. Purpose and Design Requirements. The EMC measures electromagnetic showers with excellent efficiency, energy resolution, and angular resolution over the energy range of 20 MeV to 9 GeV. The energy range is bounded on the upper end by QED processes, such as $e^+e^- \to e^+e^-(\gamma)$ or $e^+e^- \to \gamma\gamma$, and by the need for efficient reconstruction of B-meson decays, containing multiple π^0s and η^0s, on the low end of the energy range. This energy range of the EMC allows for detection of photons from π^0 and η decays, as well as radiative, and electromagnetic processes. The EMC contributes to flavor tagging of neutral B mesons by identifying electrons from semi-leptonic and rare decays.

The EMC's most stringent requirement is the measurement of extremely rare decays of B mesons containing π^0s, placing an energy resolution for the EMC at about 1% to 2%. The calorimeter operates reliably within the 1.5 T field of the solenoid.

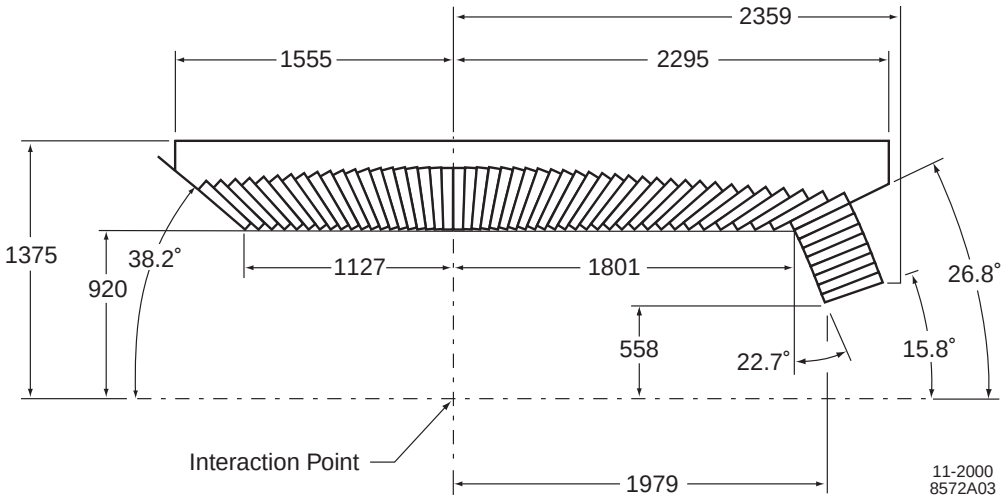

Figure 2.15: Longitudinal cross section of the EMC (top half). The detector is axially asymmetric around the z-axis.

2.5.2. EMC Layout. The calorimeter is a hermetic, total absorption device made of an array of thallium-doped cesium iodide (CsI(Tl)) crystals. The crystals' intrinsic efficiency for photon detection is nearly 100% down to a few MeV. But to ensure sensitivity to the π^0 efficiency, material at the front end of the EMC is minimized. The thallium-doped crystals provide a light yield of 50,000 γ/MeV and a Moliére radius of 3.8 cm, allowing for excellent energy and angular resolution. The crystals have a tapered trapezoidal shape, limiting the effects of shower leakage from higher energetic particles.

The EMC has a conical forward end cap and a cylindrical barrel. The detector covers the entire azimuth and extends in polar angle from 15.8^0 to 141.8^0, corresponding to a coverage of 90% in the c.m. system (see Figure 2.15). The barrel contains 5,760 crystals arranged in 48 rings with 120 crystals each. The end cap contains 6,580 crystals arranged in eight rings with 820 crystals each.

The crystals are read out with silicon photodiodes that are matched to the spectrum of scintillation light. The actual photon detector contains two silicon PIN diodes glued to a transparent polystyrene substrate which is glued to the rear face of the crystal.

The entire calorimeter is surrounded by a double Faraday shield composed of two 1 mm-thick aluminum sheets, shielding the diodes and pre-amplifiers. The EMC is maintained at constant temperature.

2.6. Detector for Muons and Neutral Hadrons

2.6.1. Purpose and Design Requirements. The outer most piece of the Babar detector is the IFR, providing a large solid angle coverage, good efficiency, and high background rejection for muons and neutral hadrons. The IFR identifies muons with high efficiency down to about 1 GeV/c, and detects neutral hadrons, primarily K_L^0 and neutrons, over a wide range of momenta and angles.

Muon detection is neccesary for tagging the flavor of the B meson from semi-leptonic decays, for the study of semi-leptonic decays involving leptons from B and D mesons and τ leptons, and also for reconstruction of vector mesons. Detection of the K_L^0 allows for the study of exclusive B decays to CP eigenstates. Detection of muons relies almost entirely on the IFR with other detector systems providing complimentary information. Charged tracks that are reconstructed in the tracking system (SVT and DCH) are extrapolated to the IFR.

K_L^0s and other neutral hadrons interact with the steel of the IFR and are identified as clusters that are not associated with a charged track.

The system is reliable and has extensive monitoring due to size and lack of accessibility.

2.6.2. Steel Flux Return and Limited Streamer Tubes. The IFR covers a total active area of about 2000 m^3, and uses the steel flux return of the magnet as a muon filter and hadron absorber. The steel flux return is segmented into 18 plates, increasing in thickness from 2 cm for the inner nine plates to 10 cm for the outer plates. In the original IFR, single gap resistive plate chamber (RPC) detectors were used. The RPCs were replaced with plastic Limited Streamer Tubes (LSTs) to detect streamers from ionizing particles.

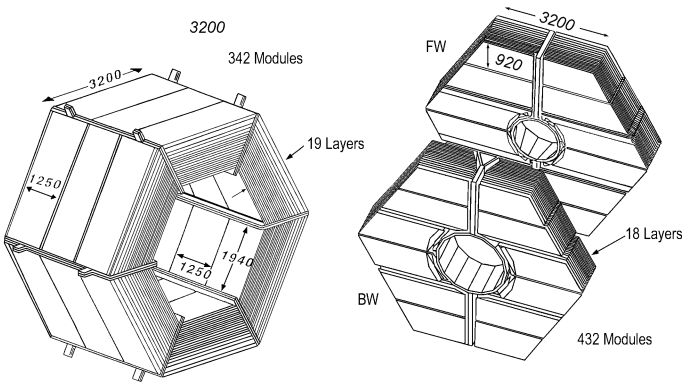

Figure 2.16: Overview of the IFR. Barrel sector and backward (BW) and forward (FW) end doors indicated here. The RPCs are replaced with the LSTs

Figure 2.17: Standard LST

The standard LST configuration consists of a silver plated 100 μm diameter wire, located at the center of a 9×9 mm^2 section. A plastic structure, or profile, contains eight cells, open on one side (Figure 2.17). The profile is coated with a resistive layer of graphite.

The IFR previously contained 19 layers of RPCs. All the layers of RPCs were removed, except for layer 19 since it is inaccessible. In layers 5, 7, 9, 11, 13, and 15, 2-cm thick brass absorber plates replaced the RPCs. The remaining layers contain the LST modules.

2.7. Trigger

The trigger system selects events of interest with a high, stable, and well-understood efficiency while rejecting background events, keeping the total event rate under 120 Hz. The total trigger efficiency must exceed 99% efficiency for all $B\overline{B}$ events and is at least 95% for continuum events. The trigger is a robust and flexible system, able to perform under extreme background conditions. The trigger contributes less than 1% to the overall dead-time.

The trigger is implemented as a two-level hierarchy, with the Level 1 (L1) hardware trigger followed by the Level 3 (L3) in software. The trigger can accommodate up to ten times the projected design luminosity of PEP-II. The L1 is set to have a typical output rate of 1 kHz, during normal operation. The L3 receives the output from L1 and performs a second stage rate reduction for the main physics sources.

2.8. Online Computing System

The computing system provides data acquisition, supporting an L1 trigger accept rate up to 2 kHz and a maximum output rate of 120 Hz. The system does not contribute more than 3% of the overall dead time. The online computing system is a set of subsystems with dedicated hardware components with a common software infrastructure. The subsystems are outlined below:

- Online Dataflow (ODF) - Communication and control of detector systems' FEEs for data acquisition and building of event data.
- Online Event Processing (OEP) - Processes complete events; performs data quality monitoring and final stage calibrations.
- Logging Manager (LM) - Selects and writes events to disk for input to the Online Prompt Reconstruction (OPR) processing.
- Online Detector Control (ODC) - Controls and monitors environmental conditions of the detector systems.
- Online Run Control (ORC) - Sequences the operations of the computing system components. Provides the graphical user interface for operator control.

Chapter 3

Conservative Estimate of Particle Identification Systematic Uncertainties

3.1. Introduction

We outline how estimates of systematic errors on PID efficiencies may be obtained and present results for the simplest cases.

First, we outline possible sources of systematic error on the PID efficiency of a signal yield:

(1) Flaws in simulation of PID-related aspects of detectors, e.g., incorrect simulation of dE/dx, DIRC photons, incorrect simulation of material interactions.

(2) MC may not simulate all runs equally well (time dependence).

(3) Dependence on event environment, such as the track multiplicity, may be somewhat different in the signal mode (analysis sample) and the PID control sample mode on which PID tables are based.

(4) Dependence on Λ, K^0_S flight length, if any, could be different in the signal mode (analysis sample) and the PID control sample mode on which PID tables are based.

(5) Possibly incorrect p, θ spectra of final state particles because the true signal PDF is not completely known, (e.g., polarization in decay).

(6) Bin-centering corrections due to differences between signal and PID sample spectra within bins.

(7) Problems intrinsic to the PID tweaking procedure.

Items 1, 2 should be covered by errors in the PID tweaking / weighting procedures. Items 3, 4 can be examined using data if signal is copious, from similar copious decay modes in data, or from MC.

In this note, we focus on items 1-4. Items 5, 6 must necessarily be handled by the analyst by varying the true pdf. Item 7 can be addressed by adjusting the PID tweaking procedure: this could be a project for someone eager to improve existing PID selectors.

3.2. Alternative PID tables

In this section we describe how alternative PID tables are obtained for the various particle types.

(1) e and μ: We use leptonic decays of the J/Ψ in $B \to J/\Psi K^{(*)}$ decays. The statistical precision of these tables is far poorer than the standard PID tables.

(2) π and K: We use the copious charm decay $D^+ \to K^-\pi^+\pi^+$. The statistical precision of these tables is comparable to the standard PID tables derived from $D^0 \to K^-\pi^+$ decays where the D^0 arises from D^{*+} decays.

(3) p: We use $\Lambda_c^+ \to pK^*$ and $\Lambda_c^+ \to pK_S^0$ decays. [Yet to be implemented].

3.3. Procedures for estimating Systematic Errors

We will describe the procedures by referring to one or more of the tables that constitute the results of this note. Consider Table Table 3.1. The table lists estimates of systematic errors for the PID efficiency for a given selector, typically LH for the hadrons, NN for muons and Micro for electrons, at different tightness levels indicated by the column heading. The table is derived for a given sample of tracks. Currently we use electrons and muons from J/Ψ decay in the $B \to J/\Psi K^{(*)}$ mode, and kaons and pions from D^0 decay in the $B \to D^0\pi$ mode.

Note that we refer to one or more of three distinct samples in this note. The "PID control sample" (or "fine" binned sample) is the standard control sample used by the PID group. The "alternative PID sample" (or "coarse" binned sample) is the alternative PID sample mentioned in the section above. Finally, we pretend to be analysts finding an average PID efficiency and use an "analysis sample" (typically from signal MC) to define the (p, θ, ϕ) spectrum of the particles being studied.

The first row of errors is simply the statistical error due to the PID table statistics. Even with an infinitely large sample, the PID efficiency errors will make a finite contribution.

The second row reflects the statistics of the analysis sample.

The third row is an estimate of the error due to the statistics of the PID tweaking procedure.

The remaining rows are all derived from the difference in efficiency obtained from the standard PID table and from an alternative PID table. For leptons, the alternative PID table is obtained from a data sample of $B \to J/\Psi K^{(*)}$ decays. Since this has limited statistics, the binning of these tables is necessarily coarse. For this reason, in the following, we shall often refer to the alternative PID table as the "coarse binned" table, and the regular PID table as the "fine binned" table (even though for K and π the binning is the same). For K and π the alternative PID table is derived from $D^+ \to K^-\pi^+\pi^+$ decays.

Rows 4 through 6 are estimated from the slope of the (coarse - fine) difference vs. momentum, theta and time respectively. For time, we use the integrated luminosity, normalized to 1.

Row 7 lists the difference of average efficiencies. In all cases, we only use bins where the coarse-binned table has non-zero entries for comparison.

Adding all rows in quadrature implies double counting. Therefore, we take only the largest of the last 4 rows in quadrature with the first three to form the total error.

The expressions used for the various errors are as follows. The average efficiency is defined by

$$\langle \epsilon \rangle = \sum_i f_i \epsilon_i \tag{3.3.1}$$

where f_i is the fraction of events in bin i and ϵ_i is the efficiency in that bin. Note that the index i runs over all bins and is "multi-dimensional" in that sense. We chose not to use separate indices for p, θ and ϕ. Of course, since there are many runs, labeled by $j = 1 \ldots n_R$, we should write

$$\langle \epsilon \rangle = \sum_j l_j \sum_i f_{ji} \epsilon_{ji} \tag{3.3.2}$$

where l_j is the fractional integrated luminosity in each run: $\sum_j l_j = 1$. In actual practice, the efficiency is only averaged over bins in which both the "fine" and "coarse" binning values exist; such bins are labeled by i' to distinguish them from all bins.

The error on this average efficiency is defined by

$$\Delta\langle \epsilon \rangle = \sqrt{\sum_j l_j^2 \sum_{i'} [(\Delta f_{ji'})^2 \epsilon_{ji'}^2 + f_{ji'}^2 (\Delta \epsilon_{ji'})^2]} \tag{3.3.3}$$

Similarly, the error on the difference between average efficiencies $\delta\epsilon \equiv \epsilon_1 - \epsilon_2$ based on two different PID tables (1 and 2) is given by

$$(\Delta(\delta\epsilon))^2 = \sum_j l_j^2 \sum_{i'} [(\Delta f_{ji'})^2 (\delta\epsilon_{ji'})^2 + f_{ji'}^2 (\Delta(\delta\epsilon_{ji'}))^2] \tag{3.3.4}$$

The error due to the tweaking procedure is defined by

$$(\Delta\epsilon_{tw})^2 = \sum_j l_j^2 \sum_{i'} [(f_{ji'}\epsilon_{ji'}^{MC})^2 \Delta r_{i'}^2] \tag{3.3.5}$$

where $\epsilon_{ji'}^{MC}$ is the MC efficiency in a bin and $\Delta r_{ji'}$ is the error on the ratio $\epsilon_{ji'}^{MC}/\epsilon_{ji'}$. For purposes of error estimation, we replace $\epsilon_{ji'}^{MC}$ in equation (3.3.5) above with $\epsilon_{ji'}$.

For the momentum, angle and time dependence, we plot the difference defined above vs. the relevant quantity and fit a straight line to this plot. The probability p_{sl} for the slope to be non-zero is defined as the χ^2-derived probability, using $\chi^2 = (a/\Delta a)^2$, where a is the slope and 1 degree of freedom. Then, the error is defined as

$$\Delta\epsilon = (1 - p_{sl}) a \sigma \tag{3.3.6}$$

where σ is the rms of the independent variable (momentum, angle or time).

Why use this formula and where did it come from? Initially, we chose to examine the χ^2/DF for the constant difference hypothesis (no dependence) and assign a systematic error when the χ^2/DF exceeded unity. However, this caused the errors to jump from being zero to significantly non-zero values for selectors of different tightness. The formula above seeks to avoid such behavior.

This formula was our best guess. We knew that a low probability implied we should assign a systematic error, and a high probability meant we shouldn't, but didn't know how to smoothly go from one extreme to the other. This formula is something we just invented. We're still looking for a better one, so if you have a better argument, we can change it.

3.4. Conclusions and Remaining Issues

We find that the **electron** (and positron) errors are ∼1%. Considering all the problems the other particles display, this may be considered surprisingly good. In any case, it assures us that the code, which is essentially the same for all particle types, does not automatically create large systematic errors.

The **muon** alternative tables do not agree with the standard tables to better than 5%. The effect seems real since it can be reproduced by an independent program. Perhaps there is a magical cut one can apply to bring the numbers closer. Our search for a significant hadronic peaking background did not yield a positive result.

We have checked that the difference in muon efficiencies is not a simple programming error. First, one of us doing the analysis wrote separate programs to check the difference in the average efficiency for the full sample of μ^+ using the VeryLoose selector. They gave exactly the same result. Then, we had different people repeat the efficiency calculation for this same sample using yet other programs, one each for the "fine" and "coarse" binned samples. Once again, they obtained exactly the same numerical values for the PID efficiencies.

Pions and **Kaons** agree very well for the usual selectors (VL, L, T, VT) but not for the GLH Tight selector. It seems that the GLH Tight selector standard PID tables are a lot different from those for the usual Tight selector, so perhaps the problem lies with the GLH Tight selector. One remaining issue with the pions is why the momentum dependence is peculiar above 1.5 GeV.

Proton statistics are poor, and the alternative tables are ∼10% different from the standard tables. The only cut which gives a clear mass peak for the $\Lambda_c^+ \to pK_S^0$ channel is the proton PID cut, so fits without this cut tend to exhibit all the ills of poor statistics. Perhaps we should switch to the $\Lambda_c^+ \to pK^-\pi^+$ mode where PID cuts on the charged kaon can be made.

3.5. Appendix I: Tables

Table 3.1: Summary of systematic errors in % for e^-.

	PidLH	VLoose	Loose	Tight	VTight
PID Efficiency Statistics	0.00	0.00	0.00	0.00	0.00
Analysis Sample Statistics	0.00	0.00	0.00	0.00	0.00
Data/MC Effy. Ratio statistics	0.00	0.00	0.00	0.00	0.00
Momentum dependence	0.11	0.26	0.39	0.12	0.33
Theta dependence	1.03	0.32	0.12	1.08	0.41
Run dependence	0.85	0.78	1.26	0.27	0.26
Other PID table	0.84	1.35	2.51	2.27	2.46
Total	1.03	1.35	2.51	2.27	2.46

Table 3.2: Summary of systematic errors in % for e^+.

	PidLH	VLoose	Loose	Tight	VTight
PID Efficiency Statistics	0.00	0.00	0.00	0.00	0.00
Analysis Sample Statistics	0.00	0.00	0.00	0.00	0.00
Data/MC Effy. Ratio statistics	0.00	0.00	0.00	0.00	0.00
Momentum dependence	0.18	0.15	0.08	0.02	0.01
Theta dependence	0.00	0.18	0.01	0.29	0.11
Run dependence	0.18	0.37	0.44	0.37	0.07
Other PID table	0.69	0.07	0.08	0.34	0.37
Total	0.69	0.37	0.44	0.37	0.37

Table 3.3: Summary of asymmetries and errors in % for e.

	PidLH	VLoose	Loose	Tight	VTight
Fine Asymmetry	0.31 ± 0.02	2.44 ± 0.03	0.20 ± 0.03	0.05 ± 0.03	0.12 ± 0.03
Coarse Asymmetry	0.21 ± 0.12	2.88 ± 0.06	0.93 ± 3.15	0.41 ± 0.47	0.72 ± 0.15
CrsAsym - FineAsym	-0.09 ± 0.12	0.43 ± 0.07	0.73 ± 3.15	0.36 ± 0.47	0.61 ± 0.15

Table 3.4: Summary of systematic errors in % for μ^-.

	MinIon	VLoose	Loose	Tight	VTight
PID Efficiency Statistics	0.00	0.00	0.00	0.00	0.00
Analysis Sample Statistics	0.00	0.00	0.00	0.00	0.00
Data/MC Effy. Ratio statistics	0.00	0.00	0.00	0.00	0.00
Momentum dependence	0.20	0.35	0.12	0.30	0.00
Theta dependence	1.14	0.01	0.00	0.66	1.25
Run dependence	0.05	1.52	1.80	0.20	0.08
Other PID table	2.45	4.61	5.20	4.53	5.11
Total	2.45	4.61	5.20	4.53	5.11

Table 3.5: Summary of systematic errors in % for μ^+.

	MinIon	VLoose	Loose	Tight	VTight
PID Efficiency Statistics	0.00	0.00	0.00	0.00	0.00
Analysis Sample Statistics	0.00	0.00	0.00	0.00	0.00
Data/MC Effy. Ratio statistics	0.00	0.00	0.00	0.00	0.00
Momentum dependence	0.04	0.01	0.05	0.03	2.24
Theta dependence	0.85	0.42	0.94	2.89	0.83
Run dependence	0.02	0.05	2.21	0.94	0.06
Other PID table	0.59	3.68	5.08	3.99	3.17
Total	0.85	3.68	5.08	3.99	3.17

Table 3.6: Summary of asymmetries and errors in % for μ.

	MinIon	VLoose	Loose	Tight	VTight
Fine Asymmetry	0.02 ± 0.03	1.25 ± 0.02	1.24 ± 0.02	1.50 ± 0.03	1.56 ± 0.03
Coarse Asymmetry	1.36 ± 0.05	1.87 ± 0.17	1.40 ± 1.71	2.00 ± 1.21	3.15 ± 0.18
CrsAsym - FineAsym	1.35 ± 0.06	0.62 ± 0.17	0.16 ± 1.71	0.51 ± 1.21	1.60 ± 0.18

Table 3.7: Summary of systematic errors in % for π^-.

	VLoose	Loose	Tight	VTight
PID Efficiency Statistics	0.00	0.00	0.00	0.00
Analysis Sample Statistics	0.01	0.01	0.00	0.00
Data/MC Effy. Ratio statistics	0.00	0.00	0.00	0.00
Momentum dependence	1.11	0.47	0.48	0.78
Theta dependence	0.53	0.37	0.00	0.24
Run dependence	0.03	0.00	0.20	0.03
Other PID table	0.27	0.05	0.01	0.00
Total	1.11	0.47	0.48	0.78

Table 3.8: Summary of systematic errors in % for π^+.

	VLoose	Loose	Tight	VTight
PID Efficiency Statistics	0.00	0.00	0.00	0.00
Analysis Sample Statistics	0.01	0.01	0.00	0.00
Data/MC Effy. Ratio statistics	0.00	0.00	0.00	0.00
Momentum dependence	0.94	0.45	0.52	0.87
Theta dependence	0.44	0.25	0.30	0.32
Run dependence	0.19	0.01	0.26	0.25
Other PID table	0.02	0.00	0.00	0.00
Total	0.94	0.45	0.52	0.87

Table 3.9: Summary of asymmetries and errors in % for π.

	VLoose	Loose	Tight	VTight
Fine Asymmetry	-0.03 ± 0.04	0.13 ± 0.04	0.05 ± 0.03	-0.34 ± 0.03
Coarse Asymmetry	0.02 ± 0.01	0.39 ± 0.00	0.25 ± 0.00	-0.20 ± 0.00
CrsAsym - FineAsym	0.05 ± 0.04	0.26 ± 0.04	0.20 ± 0.03	0.14 ± 0.03

Table 3.10: Summary of systematic errors in % for K^-.

	VLoose	Loose	Tight	VTight
PID Efficiency Statistics	0.00	0.00	0.00	0.00
Analysis Sample Statistics	0.00	0.00	0.00	0.00
Data/MC Effy. Ratio statistics	0.00	0.00	0.00	0.00
Momentum dependence	0.62	0.15	0.18	0.30
Theta dependence	0.41	0.52	0.68	0.73
Run dependence	0.02	0.07	0.00	0.00
Other PID table	0.00	0.55	1.98	2.05
Total	0.62	0.55	1.98	2.05

Table 3.11: Summary of systematic errors in % for K^+.

	VLoose	Loose	Tight	VTight
PID Efficiency Statistics	0.00	0.00	0.00	0.00
Analysis Sample Statistics	0.00	0.00	0.00	0.00
Data/MC Effy. Ratio statistics	0.00	0.00	0.00	0.00
Momentum dependence	0.48	0.15	0.01	0.11
Theta dependence	0.19	0.83	0.87	0.91
Run dependence	0.15	0.04	0.00	0.00
Other PID table	0.00	0.26	1.46	1.56
Total	0.48	0.83	1.46	1.56

Table 3.12: Summary of asymmetries and errors in % for K.

	VLoose	Loose	Tight	VTight
Fine Asymmetry	0.32 ± 0.04	0.22 ± 0.04	0.31 ± 0.04	0.29 ± 0.04
Coarse Asymmetry	0.11 ± 0.00	0.21 ± 0.00	0.39 ± 0.00	0.39 ± 0.00
CrsAsym - FineAsym	-0.20 ± 0.04	-0.01 ± 0.04	0.08 ± 0.04	0.10 ± 0.04

Table 3.13: Summary of systematic errors in % for p^-.

	GLHT	VLoose	Loose	Tight	VTight
PID Efficiency Statistics	0.00	0.00	0.00	0.00	0.00
Analysis Sample Statistics	0.00	0.00	0.00	0.00	0.00
Data/MC Effy. Ratio statistics	0.00	0.00	0.00	0.00	0.00
Momentum dependence	0.01	0.89	4.05	4.74	0.67
Theta dependence	4.63	0.00	0.55	0.14	0.85
Run dependence	4.94	7.59	9.42	7.53	6.37
Other PID table	1.10	5.30	10.93	10.13	7.77
Total	4.94	7.59	10.93	10.13	7.77

Table 3.14: Summary of systematic errors in % for p^+.

	GLHT	VLoose	Loose	Tight	VTight
PID Efficiency Statistics	0.00	0.00	0.00	0.00	0.00
Analysis Sample Statistics	0.00	0.00	0.00	0.00	0.00
Data/MC Effy. Ratio statistics	0.00	0.00	0.00	0.00	0.00
Momentum dependence	0.01	1.42	0.28	0.01	1.14
Theta dependence	0.03	3.00	4.15	4.82	4.64
Run dependence	8.85	0.59	2.39	3.39	0.86
Other PID table	3.29	15.75	12.57	9.37	8.32
Total	8.85	15.75	12.57	9.37	8.32

Table 3.15: Summary of asymmetries and errors in % for p.

	GLHT	VLoose	Loose	Tight	VTight
Fine Asymmetry	2.20 ± 0.01	2.75 ± 0.02	2.03 ± 0.01	1.66 ± 0.01	0.82 ± 0.01
Coarse Asymmetry	0.91 ± 0.07	-3.65 ± 0.11	1.25 ± 0.09	2.40 ± 0.06	0.50 ± 0.07
CrsAsym - FineAsym	-1.29 ± 0.07	-6.40 ± 0.11	-0.78 ± 0.09	0.73 ± 0.07	-0.33 ± 0.07

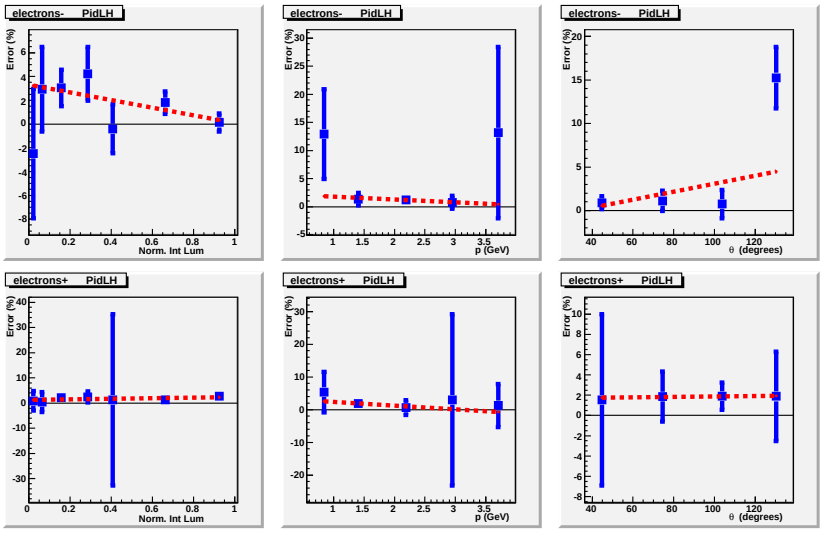

Figure 3.1: p, θ and run dependence of differences in PID efficiencies for electrons (NotPi).

3.6. Appendix II: Figures

We include here all the figures showing the momentum, angle and time dependence of differences between PID efficiencies obtained using two different control samples. In all cases the quantity plotted is the standard PID efficiency minus the alternative PID efficiency, in %. Only point-to-point statistical errors are shown and used in the linear fit, with the correlated errors removed.

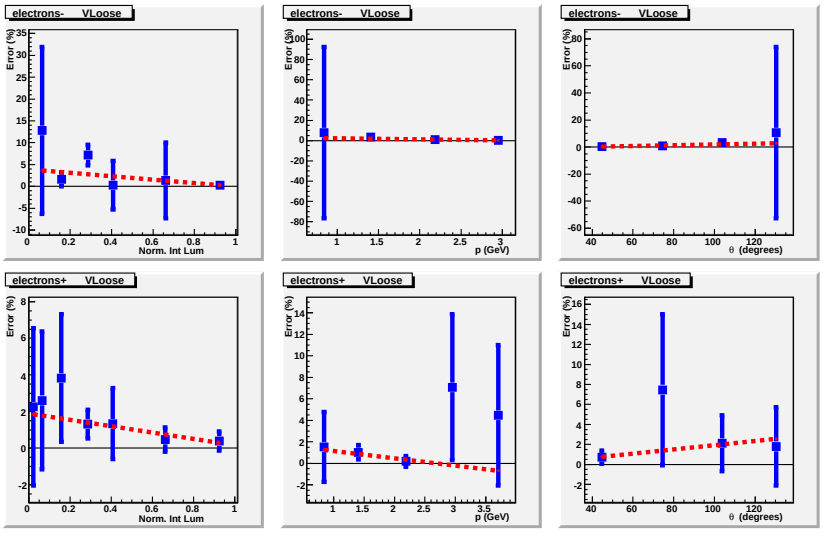

Figure 3.2: p, θ and run dependence of differences in PID efficiencies for electrons (VLoose).

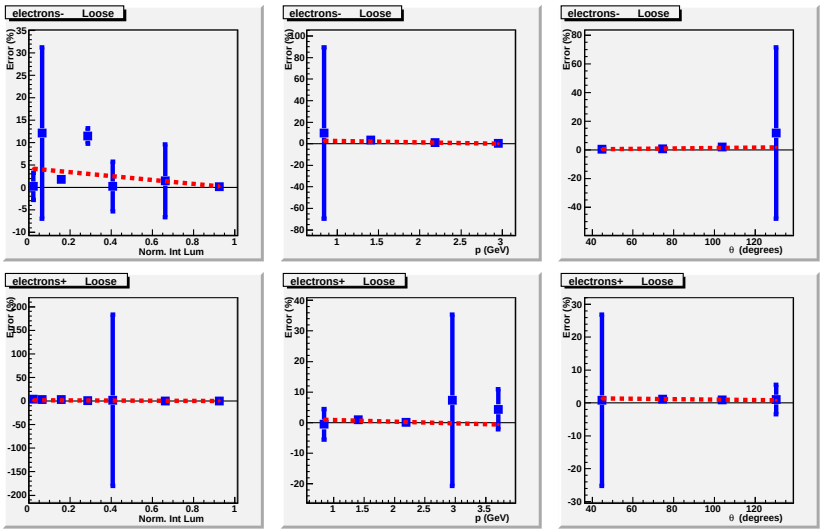

Figure 3.3: p, θ and run dependence of differences in PID efficiencies for electrons (Loose).

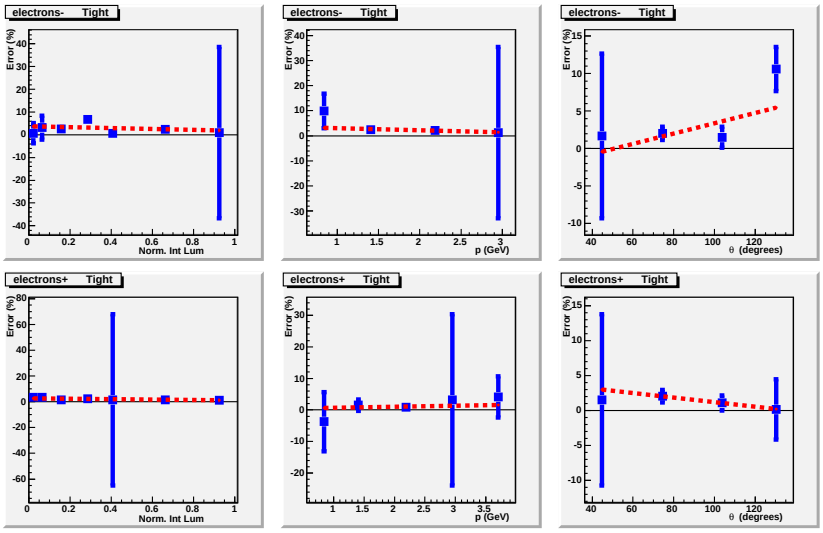

Figure 3.4: p, θ and run dependence of differences in PID efficiencies for electrons (Tight).

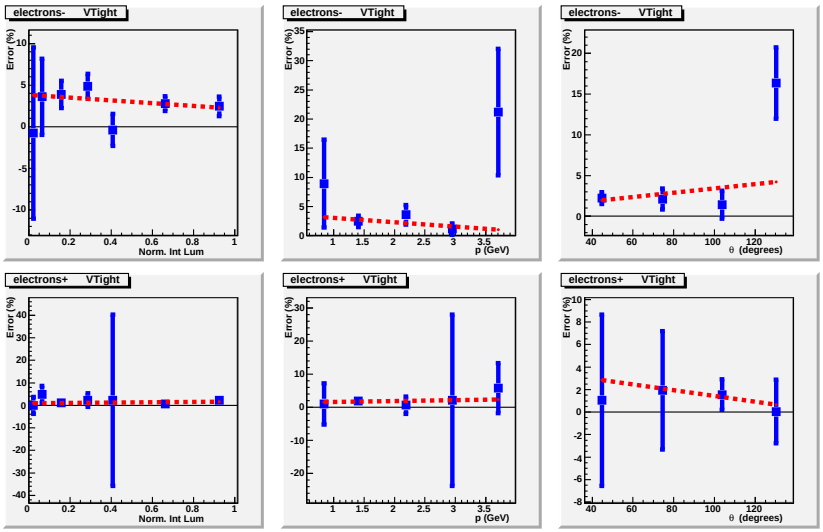

Figure 3.5: p, θ and run dependence of differences in PID efficiencies for electrons (VTight).

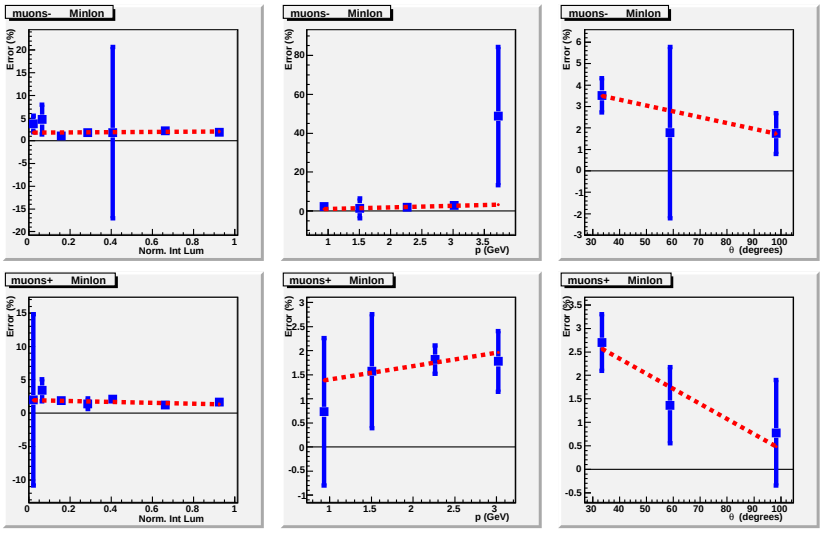

Figure 3.6: p, θ and run dependence of differences in PID efficiencies for muons (MinIon).

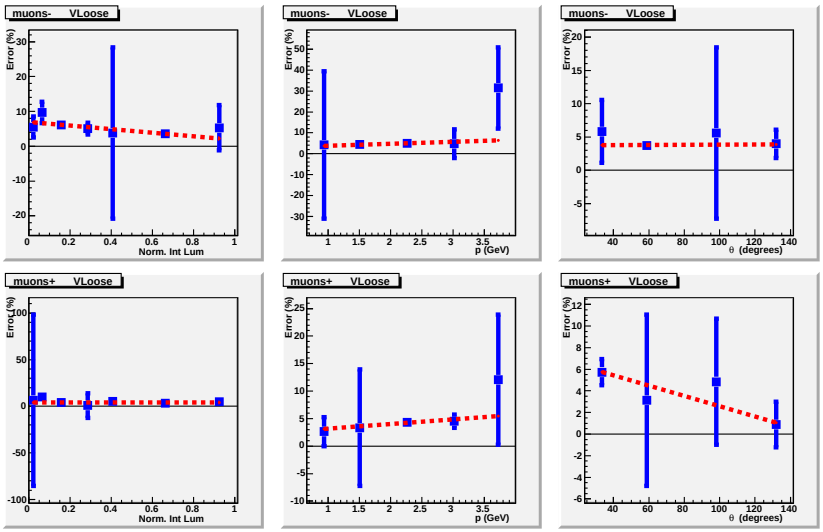

Figure 3.7: p, θ and run dependence of differences in PID efficiencies for muons (VLoose).

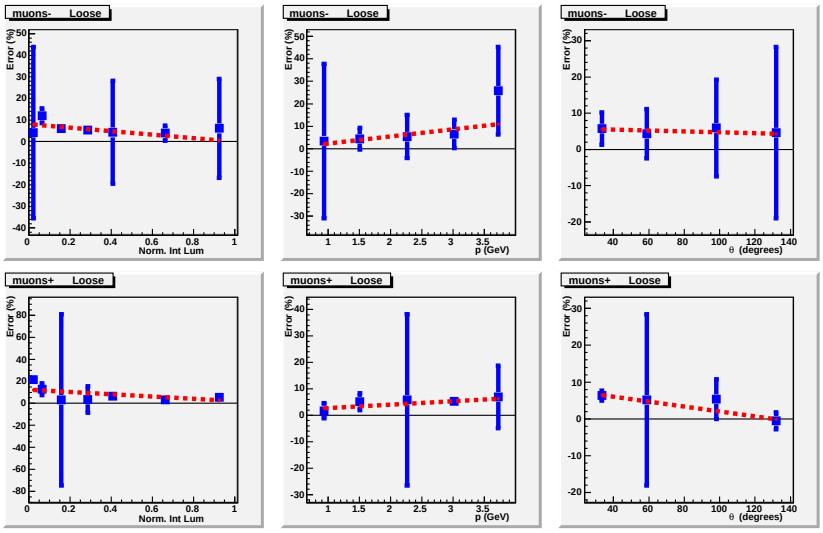

Figure 3.8: p, θ and run dependence of differences in PID efficiencies for muons (Loose).

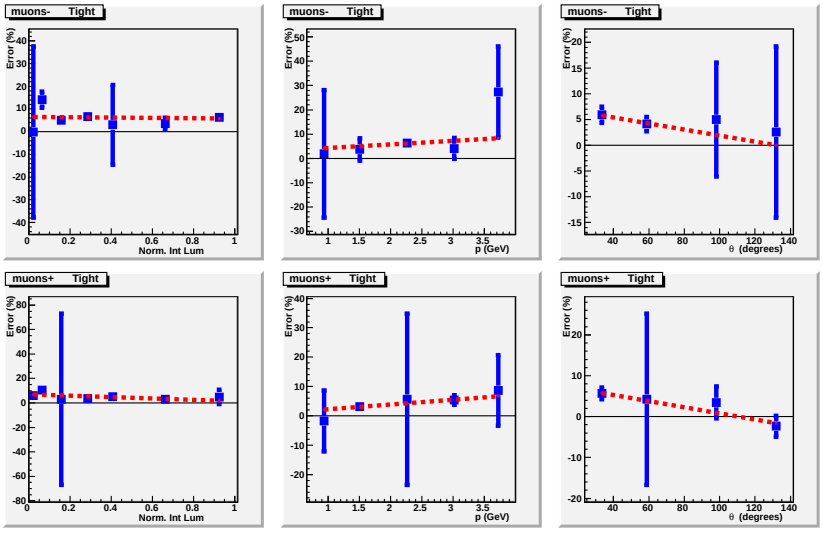

Figure 3.9: p, θ and run dependence of differences in PID efficiencies for muons (Tight).

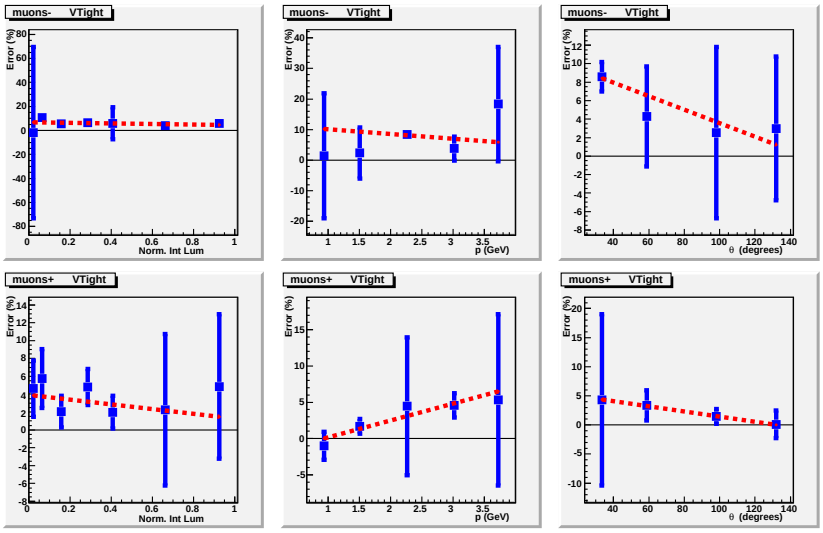

Figure 3.10: p, θ and run dependence of differences in PID efficiencies for muons (VTight).

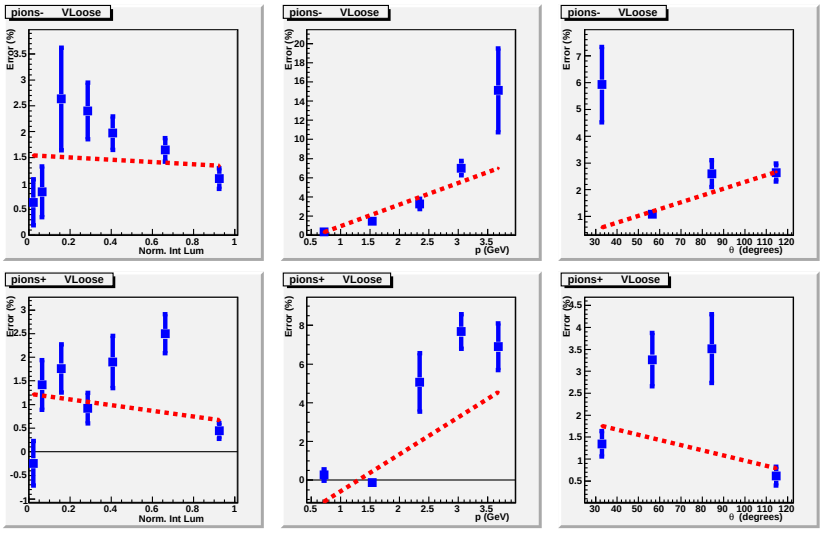

Figure 3.11: p, θ and run dependence of differences in PID efficiencies for pions (VLoose).

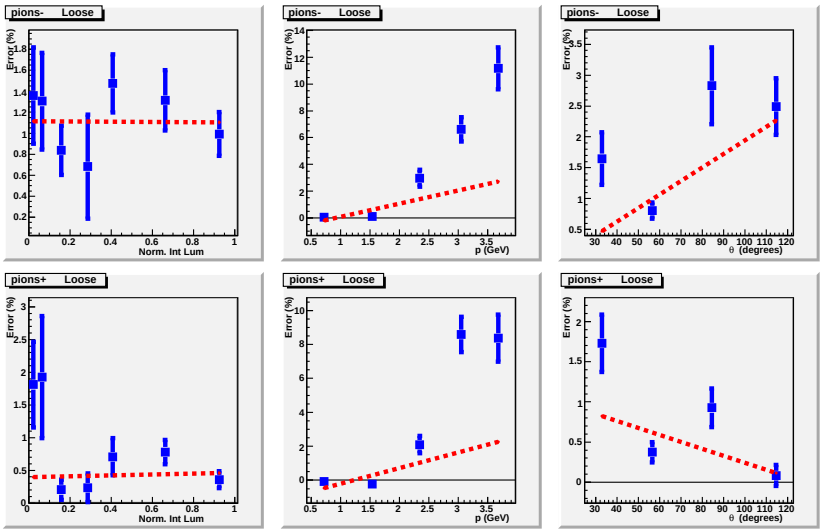

Figure 3.12: p, θ and run dependence of differences in PID efficiencies for pions (Loose).

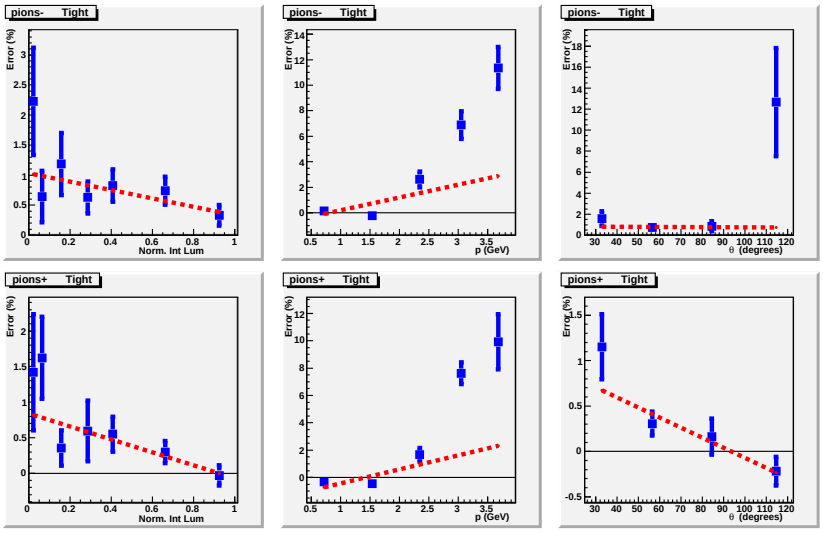

Figure 3.13: p, θ and run dependence of differences in PID efficiencies for pions (Tight).

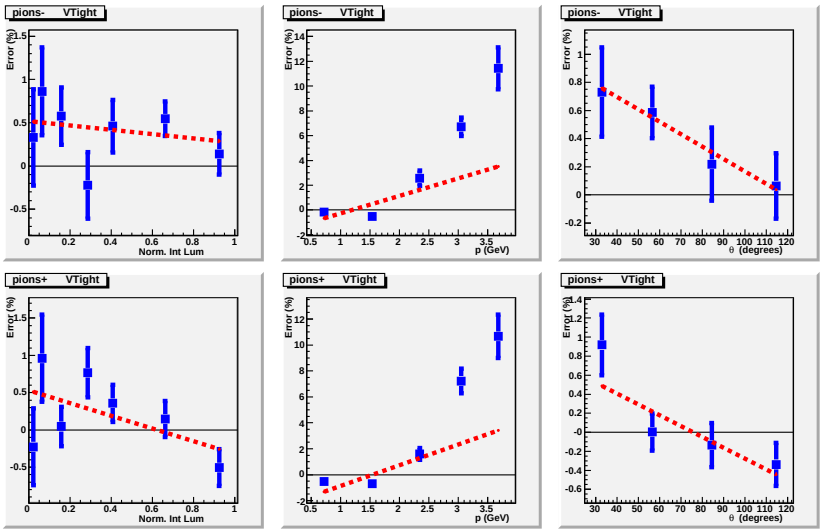

Figure 3.14: p, θ and run dependence of differences in PID efficiencies for pions (VTight).

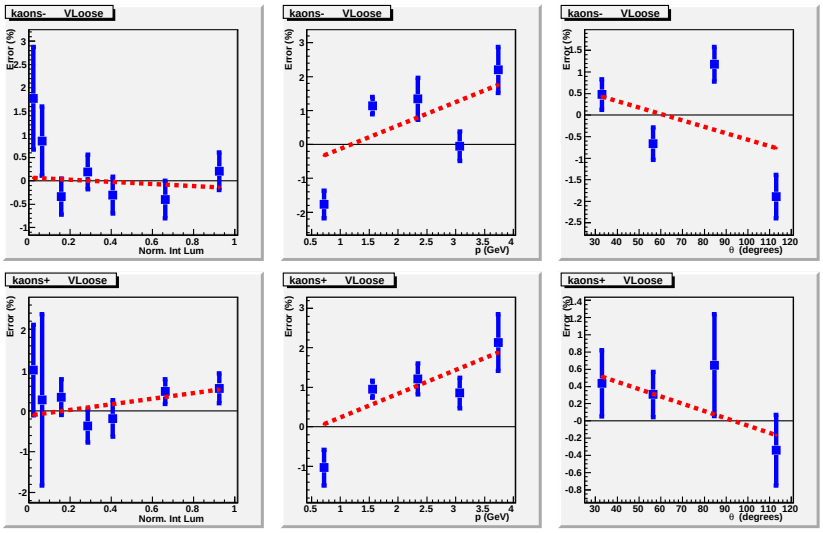

Figure 3.15: p, θ and run dependence of differences in PID efficiencies for kaons (VLoose).

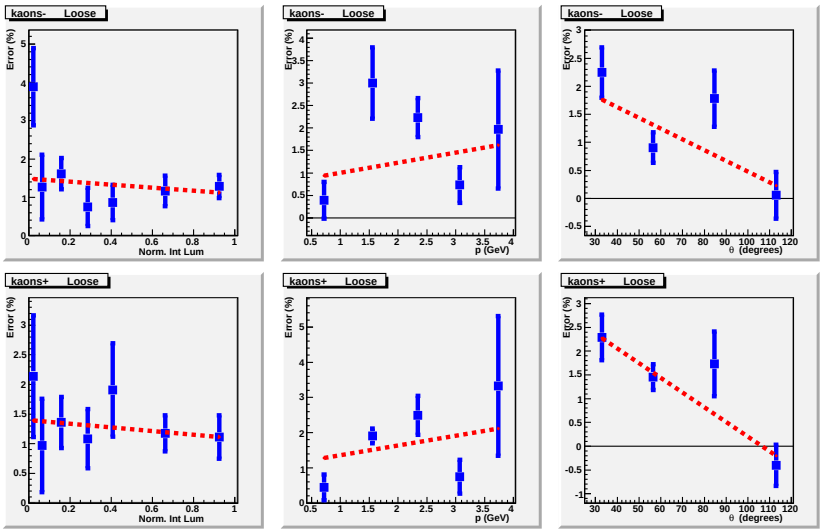

Figure 3.16: p, θ and run dependence of differences in PID efficiencies for kaons (Loose).

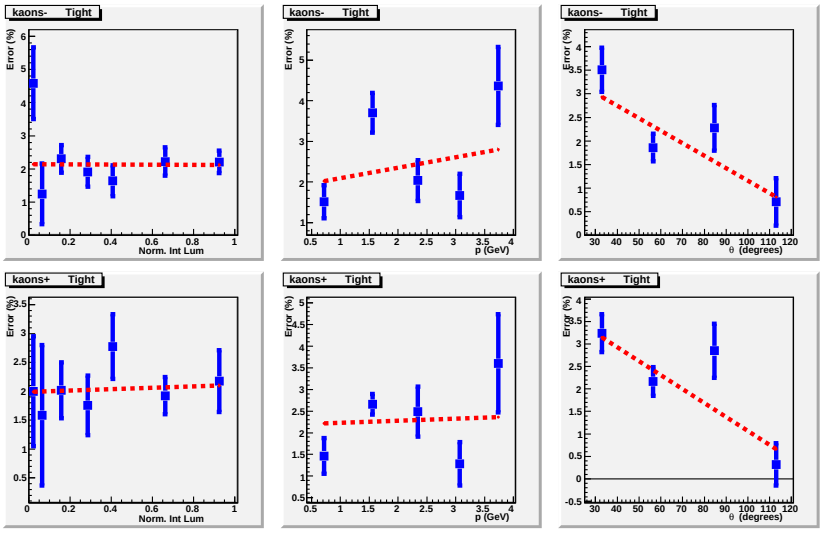

Figure 3.17: p, θ and run dependence of differences in PID efficiencies for kaons (Tight).

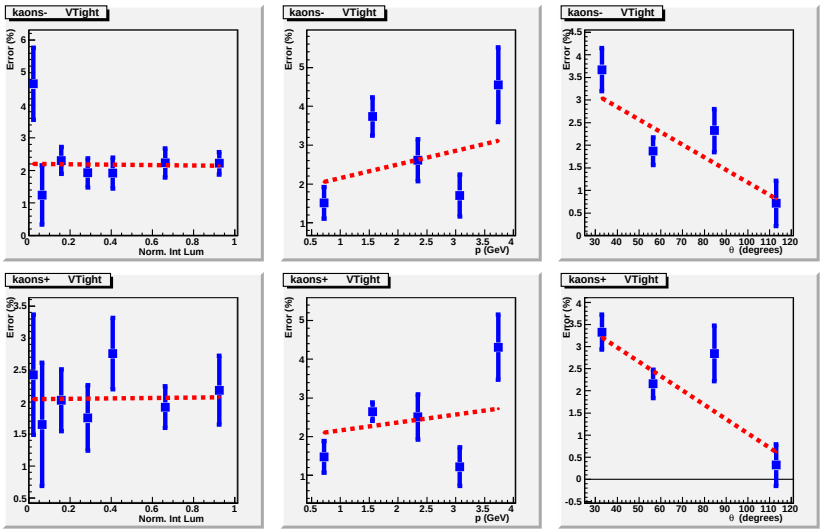

Figure 3.18: p, θ and run dependence of differences in PID efficiencies for kaons (VTight).

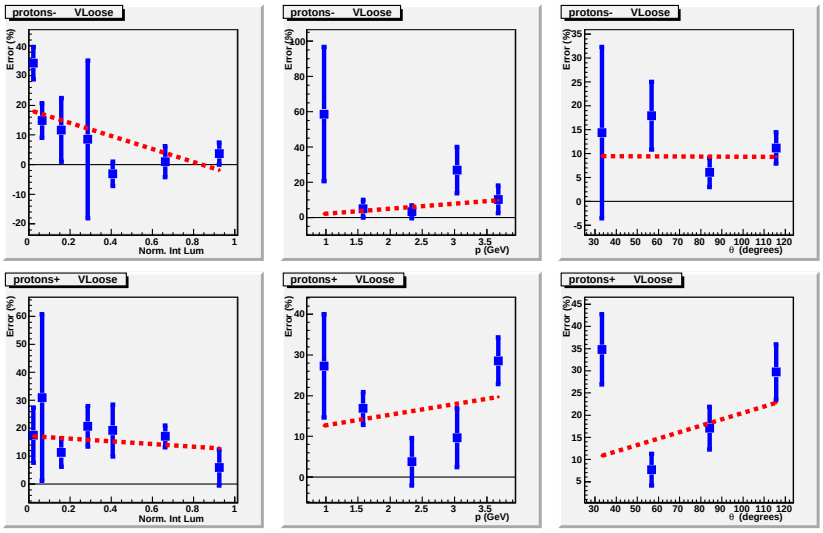

Figure 3.19: p, θ and run dependence of differences in PID efficiencies for protons (VLoose).

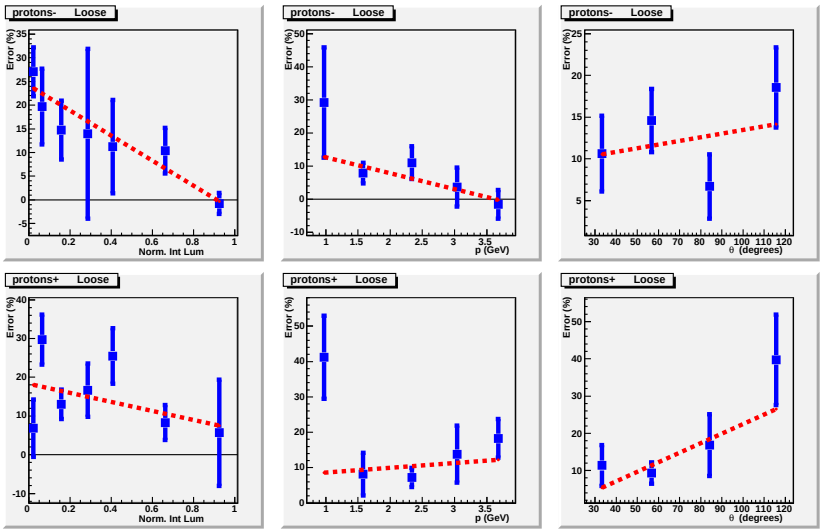

Figure 3.20: p, θ and run dependence of differences in PID efficiencies for protons (Loose).

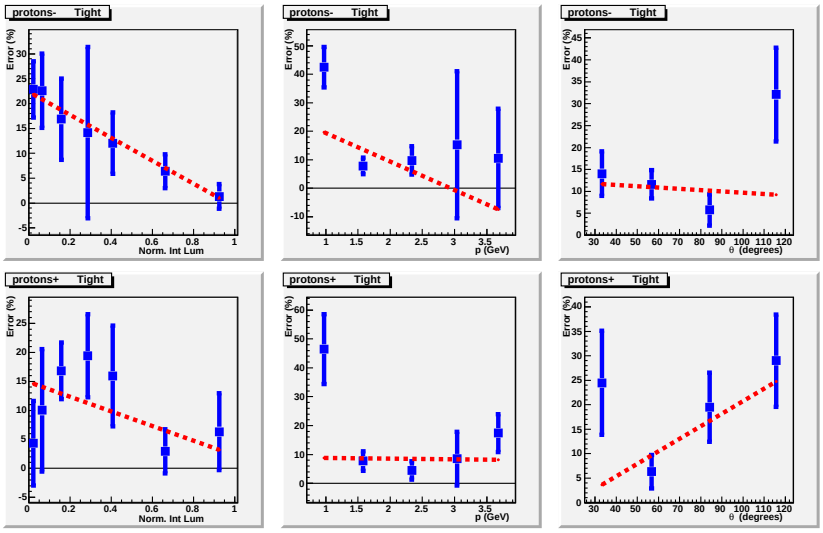

Figure 3.21: p, θ and run dependence of differences in PID efficiencies for protons (Tight).

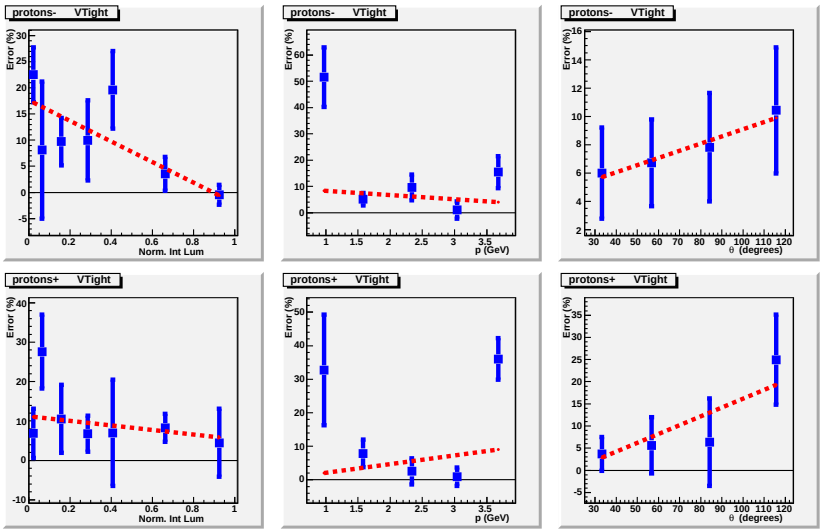

Figure 3.22: p, θ and run dependence of differences in PID efficiencies for protons (VTight).

3.7. Appendix III: Alternative Control Samples

The following section describes the event selection for the skims, cuts used to produce the control samples, and the additional cuts used to produce the efficiency tables. Additional variables stored in the ntuple that are not previously documented are described as well.

3.7.1. Lepton Control Sample. We use the already existing BaBar skim Jpsitoll. Refer to the FilterTools sequence in JpsitollPath.tcl. The skim provides us with one lepton track identified with PID, while the other track does not have PID requirements.

The lepton control sample comes decays of J/Ψ, where the J/Ψ originates from various B decays:

•$B^+ \rightarrow J/\Psi K^+$

•$B \rightarrow J/\Psi K_s$

•$B \rightarrow J/\Psi K^*$

The selection criteria for the sample is as follows:

•Electron from eBremRecoELNC

•Muon from muNNVeryLoose

•Other lepton from GoodTracksLoose

•K^+ from KLHLoose

•K_s from KsDefault

•K^* from KstarKPiDefaultPID

•BGFMultiHadron

•ntracks > 4

•R2 < 0.7

•2.9 $GeV/c^2 < m(J/\Psi) < 3.2\ GeV/c^2$

•5.2 $GeV/c^2 < mES < 5.3\ GeV/c^2$

•-0.15 $GeV/c^2 < \Delta E < 0.15\ GeV/c^2$

To increase the purity of the control samples before the efficiency tables are made, tighter requirements are placed on the pid identified lepton track, the mass of the J/Ψ, and the event helicity.

The following cuts required for the electron sample:

•$Prob(vertex\chi^2) > 0.02$

•2.95 $GeV/c^2 < m(J/\Psi) < 3.14\ GeV/c^2$

•-0.05 $GeV/c^2 < \Delta E < 0.05\ GeV/c^2$

•Require the identified electron to be PidLHElectron

•-0.7 < Helicity < 0.7

The following cuts required for the muon sample:

•$Prob(vertex\chi^2) > 0.02$

•3.06 $GeV/c^2 < m(J/\Psi) < 3.14\ GeV/c^2$

•-0.05 $GeV/c^2 < \Delta E < 0.05\ GeV/c^2$

•Require the identified electron to be MuNNTight

•-0.7 < Helicity < 0.7

Below are the variables stored in the ntuple tress for $B \rightarrow J/\Psi K$ decays.

The tree associated with the electron is identified as ntp901.

•otherp: Pid identified electron track's momentum

•othertheta: Pid identified electron track's polar angle

•otherphi: Pid identified electron track's azimuthal angle

•othercharge: Pid identified electron track's charge

•otheriselh: Pid identified electron also passes PidLHElectron selector

•kmass: Kaon mass

•kmode: Decay type, K^+ decay = 1, $K_s = 2$, K^* decay = 3

•kp: Kaon track's momentum

•mPsi: Mass of J/Ψ candidate

•mES: Energy substituted mass

•deltaE: ΔE

•R2: Second to zeroth Fox-Wolfram moment

•nTrk: Number of charged tracks in the event

•helicity: Angle between one of the lepton daughters and the $K_{(s)}^{(+,*)}$ in the J/Ψ rest frame

The tree associated with the muon is identified as ntp902.

•otherp: Pid identified muon track's momentum

•othertheta: Pid identified muon track's polar angle

•otherphi: Pid identified muon track's azimuthal angle

•othercharge: Pid identified muon track's charge

•otherismunnt: Pid identified muon also passes MuNNTight selector

•kmass: Kaon mass

•kmode: Decay type, K^+ decay = 1, K_s = 2, K^* decay = 3

•kp: Kaon track's momentum

•mPsi: Mass of J/Ψ candidate

•mES: Energy substituted mass

•deltaE: ΔE

•R2: Second to zeroth Fox-Wolfram moment

•nTrk: Number of charged tracks in the event

•helicity: Angle between one of the lepton daughters and the $K_{(s)}^{(+,*)}$ in the J/Ψ rest frame

3.7.2. $D^+ \to K^-\pi^+\pi^+$ **Control Sample.** In order to obtain a high statistics sample of kaons and pions, which do not come from D^0 decays, the most copius mode available are charged D meson decays. There was no existing charm skim for such a decay. In FilterTools, the skim is defined in DcToKPiPiPromptNoPidPath.tcl and the selection criteria for the skim is described here:

•GoodTracksVeryLoose for all tracks

•Cascade vertexer

•Geometric constraint

•$p^* > 2.7\ GeV/c$

•$1.7\ GeV/c^2 < m(D^+) < 2.1\ GeV/c^2$

•$\chi^2(vertex) > 0.005$

The decays of charmed D mesons provide a relatively high statistics control sample for kaons and pions. With the use of DTaggingTools, we are able to provide a high purity sample. We require at least 3 charged tracks in the event along with the following requirements:

•BGFMultiHadron

•R2 > 0.2

•Sphericity < 0.5

•Thrust > 0.7

We obtain the likelihood from DTaggingTools for the Beam fit and the Dalitz fit. Both likelihoods are stored in the ntuple, but we only cut on the Beam fit likelihood which is required to be greater than 1.

To further increase the purity of the sample before creating the efficiency tables, we impose an additional cut using the Dalitz likelihood cut from DTaggingTools.

•likelihdDalitz > 3.5

Below are the variables stored in the $D^+ \to K^-\pi^+\pi^+$ trees

The tree associated with the kaon track is identified as ntp401.

•dpcms: D center of mass momentum

•likelihdDalitz: Value of likelihood from Dalitz fit in DTaggingTools

•likelihdBeam: Value of likelihood from Beam fit in DTaggingTools

•nTrk: Number of charged tracks in the event

•kpi1Mass: kaon and first pion daughters' pair mass

•kpi2Mass: kaon and second pion daughters' pair mass

•pi1pi2Mass: pion daughters' pair mass

The tree associated with the first pion daughter is identified as ntp402, and the second pion daughter tree is identified as ntp403.

3.7.3. Proton Control Sample. We use protons from $\Lambda_c^+ \to pK^-\pi^+$, however, in an effort to achieve a pure sample we require that the Λ_c candidates come

from decays of $\Sigma_c^{++,0} \rightarrow \Lambda_c^+ \pi^{+,-}$. The skim defined in SigmaCToLambdaCNoPid-ProtonPath.tcl includes the $pK\pi$ decay mode along with the pK_s decay mode. The latter is not used as part of the control sample due to such low statistics.

•K_s default list

•$0.455\ GeV/c^2 < m(K_s) < 0.54\ GeV/c^2$

•GoodTracksVeryLoose for proton track

•Kaon and pion tracks from LHTight lists

•Cascade vertexer for Λ_c

•Geometric constraint

•$p^*(\Lambda_c) > 2.7\ GeV/c$

•$2.18\ GeV/c^2 < m(\Lambda_c) < 2.38\ GeV/c^2$

•Add4 Λ_c and pion

•$p^*(\Sigma_c) > 2.7\ GeV/c$

•$m(\Sigma_c) - m(\Lambda_c) < 300\ MeV/c^2$

The Σ_c candidate is formed by simply adding the four vectors of the Λ_c candidate, which has the same requirements as the skim, with a pion from a tight Pid list. To remove Λ_c candidates that do not come from Σ_c we place cuts on the p^* of the Σ_c candidate and the mass difference between the Σ_c and the Λ_c:

•$p^*(\Sigma_c) > 3.2\ GeV/c$

•$160\ MeV/c^2 < m(\Sigma_c) - m(\Lambda_c) < 175\ MeV/c^2$

The Λ_c candidates may contain reflections from charm mesons D^+, D_s, or D^* which may affect proton efficiency. To look for reflections we recalculate the proton track's energy either with a kaon or pion hypothesis (denoted as K_p or π_p) and form either a D^+ or D_s. A D^0 may be formed using the kaon track with the proton track as a pion(π_p), we can then find the q value of the D^* decay. Efficiency tables were produced with and without removing the reflections. The reflections can be removed using the following cuts:

•$1.859\ GeV/c^2 < m(K\pi\pi_p) < 1.879\ GeV/c^2$

•$4\ MeV/c^2 < m(K\pi\pi_p) - m(K\pi_p) - m(\pi) < 8\ MeV/c^2$

•1.959 $GeV/c^2 < m(K\pi K_p) < 1.979\ GeV/c^2$

Below are the variables stored in the ntuples for the $\Lambda_c \rightarrow pK\pi$ tree. This control sample contains just one tree for the proton track, identified as ntp501.

•LambdaCpcms: Λ_c center of mass momentum

•SigmaCpcms: Σ_c center of mass momentum

•massDiff: m(Σ_c) - m(Λ_c)

•KKpiMass: Recalculated mass of Λ_c daughters using a kaon hypothesis for the proton track

•KpipiMass: Recalculated mass of Λ_c daughters using a pion hypothesis for the proton track

•Qvalue: $m(K\pi\pi_p) - m(K\pi_p) - m(\pi)$

3.7.4. Mass Distributions.

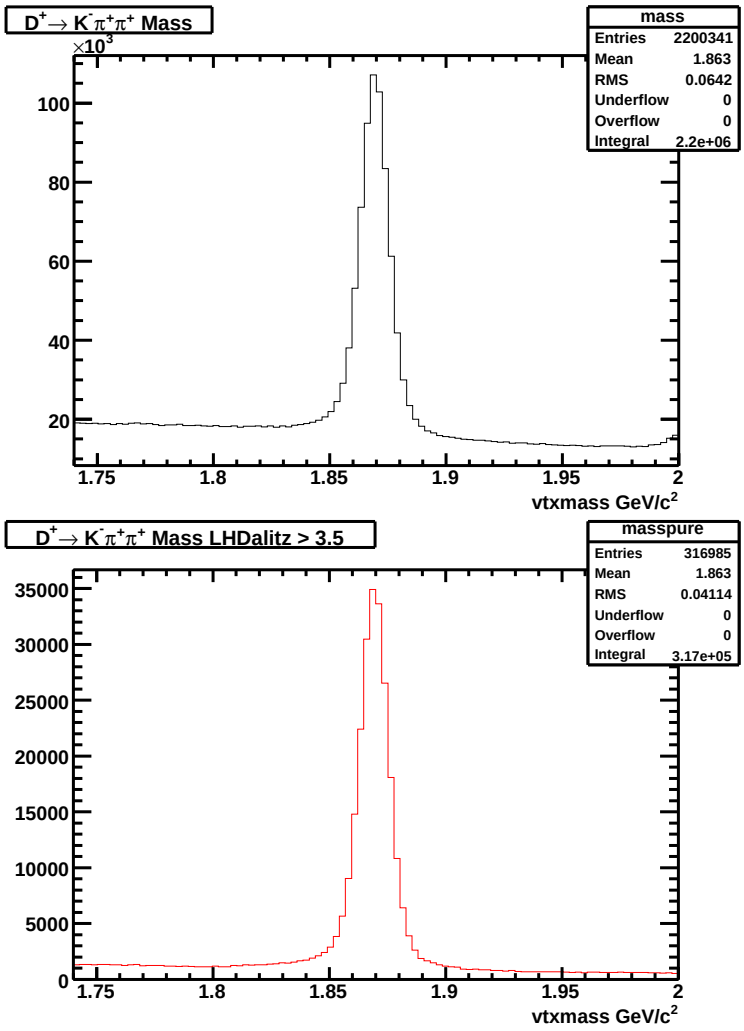

Figure 3.23: **Top: D^+ mass distribution at the ntuple level; Bottom: D^+ mass distribution with Dalitz likelihood cut imposed for producing efficiency tables; taken from Run4 OnPeak data**

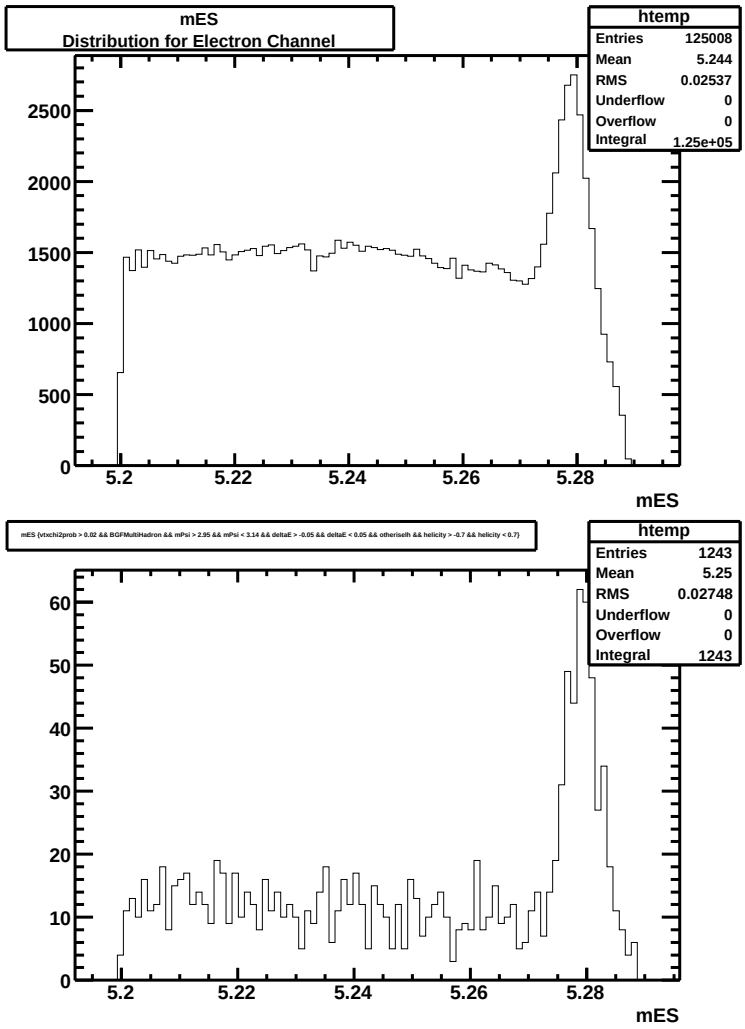

Figure 3.24: **Top: mES Distribution for $J/\Psi \to e^+e^-$ Bottom: mES Distribution with further cuts imposed for producing efficiency tables; taken from Run4 OnPeak data**

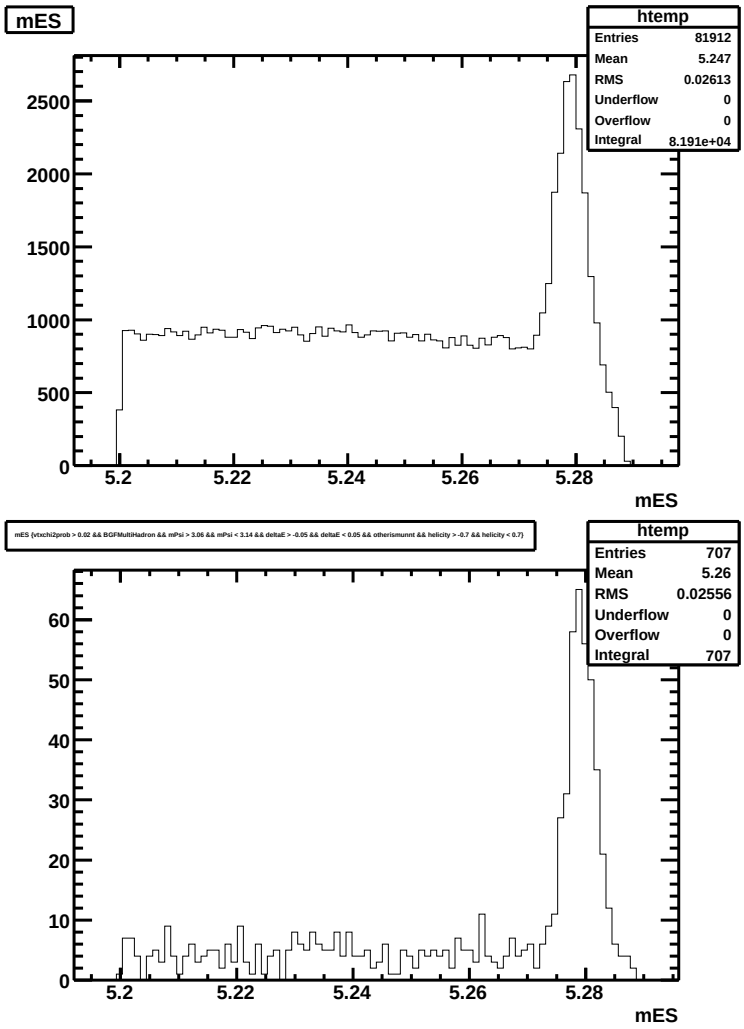

Figure 3.25: **Top: mES Distribution for $J/\Psi \to \mu^+\mu^-$ Bottom: mES Distribution with further cuts imposed for producing efficiency tables; taken from Run4 OnPeak data**

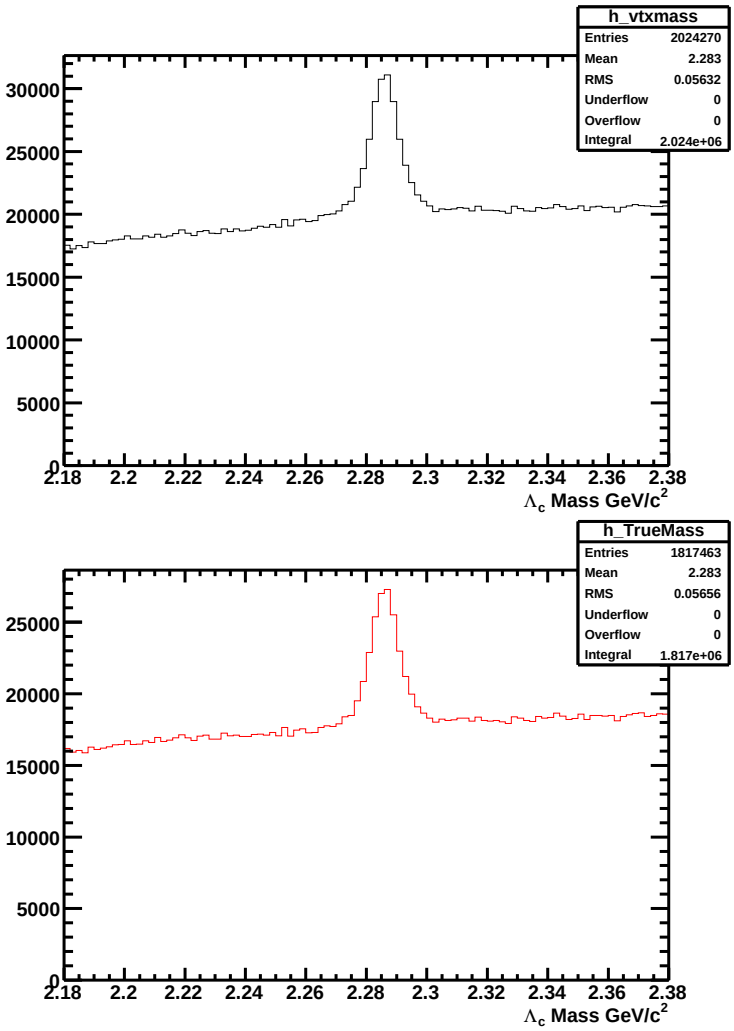

Figure 3.26: **Top: Mass distribution of Λ_c candidate Bottom: Λ_c mass distribution after cutting out the reflections; taken from the entire dataset**

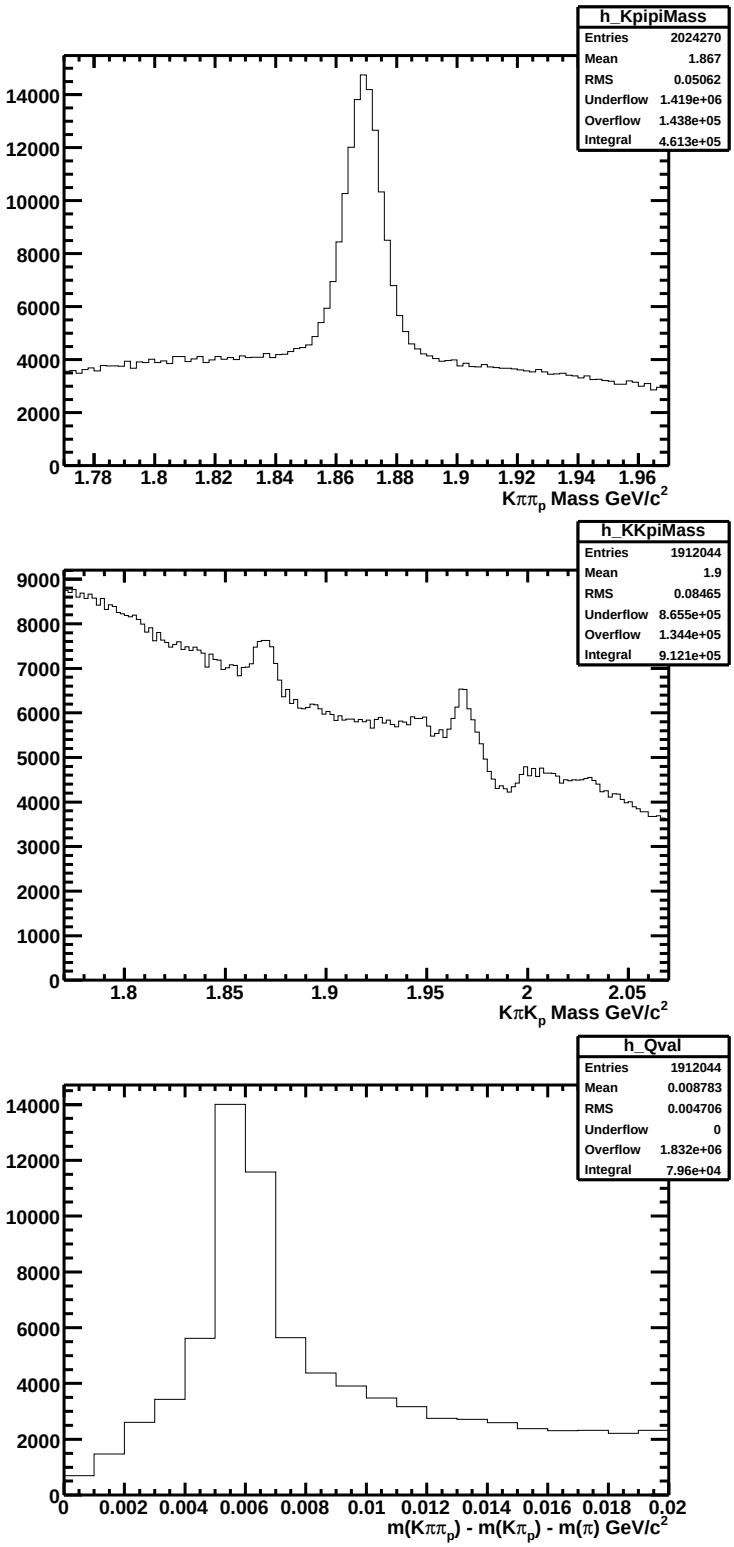

Figure 3.27: **Recalculated mass of Λ_c daughters using either kaon or pion hypothesis for the proton track. The $K\pi K_p$ and q value are plotted after a cut around the D^+ mass peak from $K\pi\pi_p$**

Chapter 4

Charged Pion Tracking Efficiency and Asymmetry

4.1. Introduction

The goal of the study described in this note is to measure the asymmetry in the pion tracking efficiency as a function of lab momentum directly from data. This asymmetry is the dominant systematic uncertainty for direct CP asymmetry measurements. Two methods from different types of physics events provide us with the tracking asymmetry as a function of lab momentum. The first method relies upon decays of τ leptons to 3 hadron tracks, denoted as Tau31, and also provides a measurement of the absolute tracking efficiency. The second method exploits rotational invariance in the form of isotropy of two-body decays of spin-zero mesons. While we use flavor-tagged $D^0 \to \pi^+\pi^-$ decays in principle any two-body decays (such as from K-shorts, B^0, D^+ etc.) can be used. The method provides the tracking asymmetry as a function of any desirable quantity, such as the pion lab momentum.

This study is essential for our study of direct CP violation in charm decays where we aim for sensitivity below 1%, a level now possible with BaBar's data set of 540 fb^{-1} of integrated luminosity. New physics would be indicated for direct CP asymmetries greater than 1%. Additional asymmetries arise from detector asymmetries, particle identification, and tracking.

4.2. Charge Asymmetry in Pion Tracking Efficiency from Monte Carlo

Although our methods measure the efficiency and asymmetry directly from data, we begin by displaying the asymmetry obtained directly using the BaBar Monte Carlo. One reason for this is that in our meson decay method we assume that the asymmetry at high lab momenta (> 2 GeV) is zero, or even if slightly non-zero, the Monte Carlo can be trusted because we are out of the region of rapidly oscillating cross-sections as a function of energy. Above 2 GeV in pion lab momentum we enter the slowly-varying regime. The major uncertainty in asymmetry determined from Monte Carlo at high energies is in the amount and nature of detector material; a 20% systematic error should cover that. The average tracking asymmetry from the Monte Carlo is $-6 \times 10^{-5} \pm 0.00023$.

Another reason for studying the MC-derived asymmetry is to establish a baseline, an expectation for the result from data.

Finally, by plotting and fitting the MC asymmetry (which has higher statistics than data) to various functions we can select a function that fits well but whose parameters can then be determined directly from a fit to data. We finally chose to parameterize the efficiency with the following formula:

$$\epsilon(p_{Lab}) = 1 - A_0 e^{\frac{(p_{Lab}-p_0)}{\tau_0}} - B_0 e^{\frac{(p_{Lab}-p_1)}{\tau_1}} \tag{4.2.1}$$

Figures Figure 4.1, Figure 4.2 show the pion track efficiency and asymmetry respectively. Here and elsewhere in the document the asymmetry is defined as

$$a(p_{Lab}) \equiv \frac{\epsilon(p_{\pi^+}) - \epsilon(p_{\pi^-})}{\epsilon(p_{\pi^+}) + \epsilon(p_{\pi^-})} \tag{4.2.2}$$

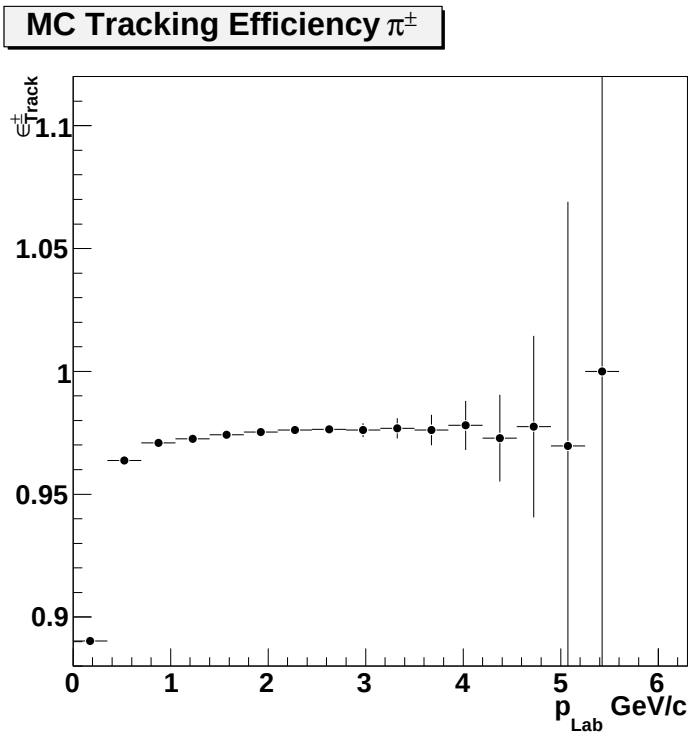

Figure 4.1: Monte Carlo Tracking Efficiency for π^+ and π^-

4.3. Methods

4.3.1. The Tau31 Method. BAD 931 describes how tracking efficiency can be measured using "Tau31" decays, i.e., decays in which one of two taus decays to a lepton (the "1" in Tau31) and the other to 3 prongs. The leptonic decay is used to tag the event as a tau-tau event. Some of the 3-prongs are missing a track due to tracking inefficiency and the tracking efficiency can be estimated by diviing the number of two-prongs by the total number of 2- and 3-prong decays.

Unfortunately, when a hadronic track is missing, we do not know its 3-momentum, making the efficiency determination as a function of momentum and angle difficult. The best one can do is to estimate the track's angles from the visible remaining tracks, and a momentum scale from the missing momentum or missing pt. We call these variables pseudo-theta (and pseudo-phi) and ptmiss.

The Tau31 decays can be used to determine the efficiency as a function of p and theta by creating an acceptance-transfer matrix from the true momenta to the

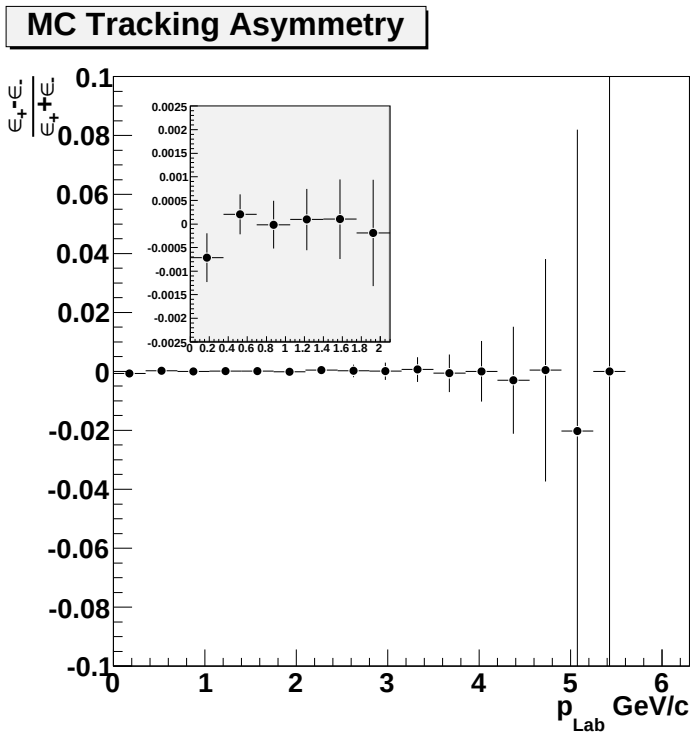

Figure 4.2: Monte Carlo Tracking Asymmetry as a function of lab momentum. The inset plot shows the asymmetry up to 2 GeV, where our measurements from data are applicable.

observed quantities using MC, and thereby determining the true distribution of momenta as well as the efficiency from data.

We realized there is an easier way: if a track has an efficiency ϵ, the probability for the event to be 2-prong is proportional to $\epsilon^2(1-\epsilon)$, while the probability for it to be a 3-prong is proportional to ϵ^3, assuming all tracks are distinguishable. Therefore, we could populate a 2-dimensional ptmiss-pseudo-theta histogram for 2-prongs by starting with the 3-prong sample and weighting every event by the ratio $(1-\epsilon)/\epsilon$, where epsilon can be parameterized as a function of the observed 3-momentum of the third prong. The resulting matrix can then be fit to the observed, binned, 2-prong events. To the extent that the background in 2-prongs is due to inefficiency in the 3-prong background, this automatically takes care of the background and reduces background subtraction issues.

Unfortunately, there are substantial backgrounds in the tau samples. This makes it difficult to directly implement the method described above. The problems were

eventually circumvented by first developing an understanding of these backgrounds using MC and focusing on parts of the ptmiss-pseudo-theta space where contamination is lower. Details can be found in the sections below, particularly in section 4.7.

4.3.2. The Method of Two-body Decays of Spinless Mesons.

4.4. Monte Carlo and Data sets

We briefly summarize the various Monte Carlo samples used for the study and the final data sets used to measure the tracking efficiency and asymmetry. All data and Monte Carlo samples are produced from Release-24 series skims. The Tau data and MC are taken from R24a2-v03 tags, and the charm samples are from R24c-v07 tags.

4.4.1. Signal Monte Carlo. We obtain Monte Carlo tracking efficiencies and asymmetries using signal Monte Carlo events of $D^+ \to K^+K^-\pi^+$. The sample contains 25 million generated events for both D^+ and D^-, using the release-24 SP10. The decays are modeled using phase space only.

4.4.2. Tau31. Tau31 data was obtained from the tracking group which generates ntuples from Tau31Tracking skim. Runs 1-6 R24a2-v03 On and Off peak data were used. For the Monte Carlo, we use the corresponding B^+B^- Generic, $B^0\bar{B}^0$ Generic, $e^+e^- \to \mu^+\mu^-\gamma$ (KK2F), $e^+e^- \to \tau^+\tau^-\gamma$ (KK2F), $e^+e^- \to u\bar{u}/d\bar{d}/s\bar{s}$, $e^+e^- \to c\bar{c}$ MC samples scaled to the luminosity of the full data set.

4.4.3. Two-Body Charm Samples. Two-body charm decays are available from the Charm mixing group, which uses the D0To2ProngDcj skim as input for both tagged and untagged D^0 decays. R24c-v07 data sets for runs 1 through 6 On and Off peak were recently made available. Monte Carlo samples were not used in this part of the study.

4.5. Event Selection

Event selection criteria for both methods are based on analyses performed by the BaBar tracking group (BAD 931) and the BaBar charm mixing group (BAD 1754). Differences or additions to the original selection criteria are indicated below.

4.5.1. Tau31 Event Selection. The event selection for Tau31 decays is based upon the selection that is described in BAD 931. The primary difference between the event selection for R24 data and what is currently being used by the Tau group is additional criteria to limit contamination of lepton tracks into the 3-prong side of the event. We limit ourselves to a maximum number of four tracks in the event. We only search for $\tau \rightarrow \mu$ to tag the event. On the 3-prong side, we search for events with two oppositely-charged tracks consistent with the mass of the ρ^0.

Only events with 3 or 4 Charged tracks and a total charge of +1, 0, or -1 are analyzed. The total charge requirement suppresses backgrounds from beam gas events. Contamination from photon conversions and K_s decays are suppressed. Photon conversions are suppressed by rejecting events containining two charged tracks with an invariant mass less than 100 MeV where one of the tracks passes the Electron Super Loose KM selector. K_s decays are suppressed by rejecting events which contain two tracks with a vertex more than 2 cm from the beam spot, a $\chi^2 > 0.01$, and an invariant mass within 10 MeV of the K_s mass.

The events that passed the initial selection criteria are now required to have either 4 tracks (3-prong) or 3 tracks (2-prong). We search for the most isolated track with a minimum of 120^0 in the center-of-mass frame from all other tracks in the event. We further isolate the track by requiring that no neutral clusters, with an energy of 100MeV, be within 90^0 of the track in the lab frame. The isolated track is also constrained to have a lab momentum between 20% and 80% of the beam energy. Next, we search for only good quality muon tracks, such that they satisfy GoodTracksLoose requirements, have a transverse momentum of greater than 200

MeV, and have both a transverse impact parameter less than 1mm and a z impact parameter less than 3 cm. Finally, the track must satisfy a tight muon ID selector.

Once the muon tag of the 1-prong τ decay is identified, we search for decays of $\tau^+ \to \rho h^+$, where h is a hadron. We search for two oppositely charged tracks which have a dE/dx pull less than 3σ. The total missing momentum of the two pion tracks and the lepton is constrained by requiring that the -0.80 $< cos(\theta_{miss}) <$ 0.80 defined as follows.

Using

$$\vec{p}(\pi\pi\mu) \equiv \vec{p}(\pi^+) + \vec{p}(\pi^-) + \vec{p}(\mu^+) \tag{4.5.1}$$

we define

$$cos(\theta_{miss}) = \frac{p_z(\pi\pi\mu))}{p(\pi\pi\mu)} \tag{4.5.2}$$

and that the transverse component is greater than 300 MeV. The mass of the two pion tracks is required to be consistent with that of the ρ^0 within 100 MeV.

The following criteria, which were not used in the original Tau31 study, are applied to further reduce our backgrounds. We veto events where either of the ρ^0 daughter tracks are consistent with a loose muon or loose electron particle ID to reduce contamination from lepton tracks. Finally, we require tracks to have a minimum DCH dE/dx of 300.

4.5.2. $D^0 \to \pi^+\pi^-$ **tagged** $D^{*+} \to D^0\pi^+_{slow}$**.** $D^0 \to \pi^+\pi^-$ events are obtained from samples provided by the Charm mixing group. This sample uses slow pions associated with the decay of D^{*+} to tag the flavor of the D^0 meson and reduce background. The event selection is described in detail in BAD 1754. The final sample we obtain by skimming the "primary" ntuples generated from the D0To2ProngDcj skim. The sample has already passed the initial reskimming selection criteria with super loose PID requirements on two-body decay tracks.

•1.78 GeV $<$ m(D^0) $<$ 1.94

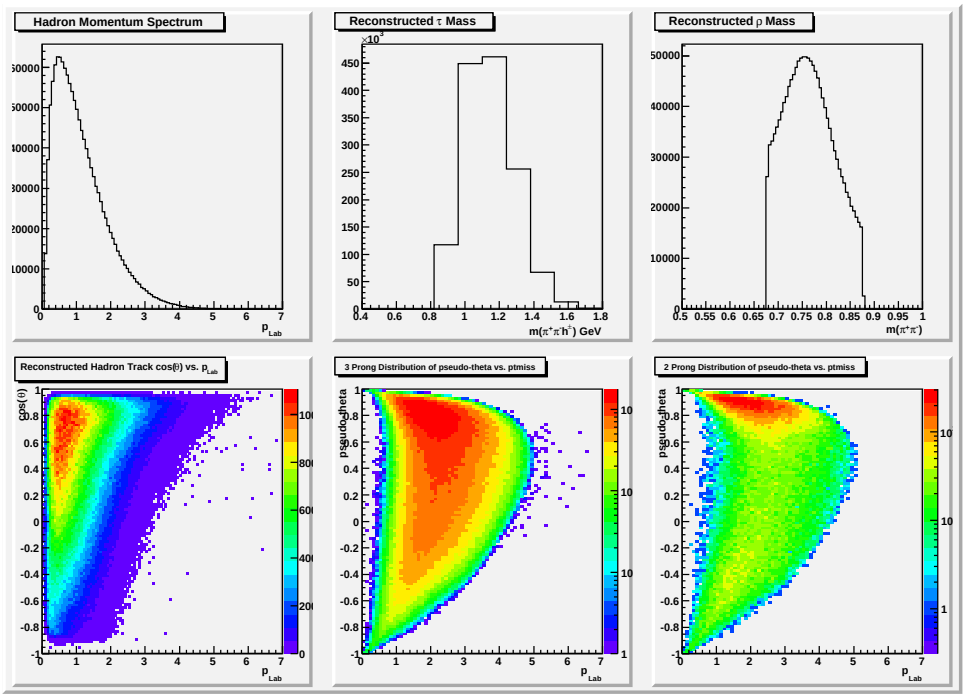

Figure 4.3: Distribution of events for 2-prong and 3-prong after event selection

•χ^2 Probability, $P(\chi^2)$, from the D^0 vertex fit to satisfy $0.001 < P(\chi^2) < 1$

•$p^*(D^0) > 2.5$ GeV

•Require a minimum of 12 hits in the drift chamber for each daughter track

•Require the D^0 decay time error,σ_t, (obtained from TreeFitter vertex fit) to be > 0.5 psec.

The following criteria are required for the tagged sample:

•0.14 GeV $< \Delta$m $<$ 0.16 GeV

•Momentum of slow pion, $p_{\pi_s} > 100$ MeV

•The minimum number of SVT and DCH hits on the slow pion track, $N_{\pi_s}^{SVT}$ and $N_{\pi_s}^{DCH}$, must satisfy $N_{\pi_s}^{SVT} \geq 6$ and $N_{\pi_s}^{DCH} > 0$.

•The slow pion must be inconsistent with an electron ID. Refer to section 4.4 in BAD 1754 for further description

The following criteria required for asymmetry measurement:

•One of the daughter tracks satisfy $p_{Lab} > 2$ GeV, while the opposite charged track satisfy $p_{Lab} < 2$ GeV

4.6.1. Tau31. In order to correctly model the 2-prong distribution of events by weighting the 3-prong events, the 2-prong backgrounds must be well-understood. Using the Tau31 generic MC, we use the truth information to classify events. The backgrounds found in the 2-prong distributions are entirely from feed-up of 1-prong tau decays (Table 4.1). The dominant backgrounds typically occur when one of the reconstructed tracks is the 1-prong daughter track while the other track is a lepton associated with a γ conversion or the decay of a π^0.

Type	% Events
True $\tau^{\pm} \rightarrow \rho h^{\pm}_{miss}$	93%
$\gamma \rightarrow e^+e^-$	5%
$\pi^0 \rightarrow e^+e^-(\gamma)$	1%
Material Interactions	$< 1\%$
Other	$< 1\%$

Table 4.1: Composition of generic 2-prong decays, which survive all cuts listed above, from the Monte Carlo truth information

Signal events in the 2-prong distribution are the result of either tracking inefficiency or acceptance loss. Using the MC, we determine the percentage of events where the hadron track is generated outside the acceptance of the detector (Table 4.2).

Generated Angle	% Events
$25^\circ < \theta(\text{hadron}) < 147^\circ$	30%
$\theta(\text{hadron}) < 25^\circ$	54%
$\theta(\text{hadron}) > 147^\circ$	16%

Table 4.2: Composition of true 2-prong tau decays, which survive all the cuts listed above, with respect to the detector acceptance

We further categorize the acceptance loss events into the signal types of events generated in the MC (Table 4.3). We obtain distributions of acceptance loss events from generic tau MC which are separated into the various tau decays either through the a_1 resonance, via the $W^{\pm}$ boson or through another channel.

MC Decay	% Events
$\tau \rightarrow a_1$	85%
$\tau \rightarrow W$	14%
other	1%

Table 4.3: Composition of Acceptance Loss events in generic tau MC

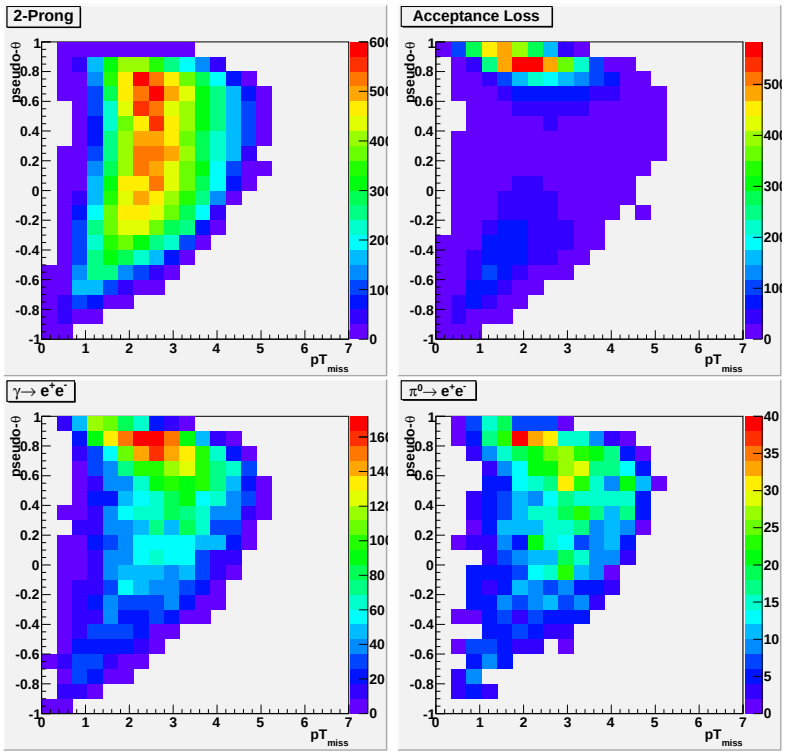

Figure 4.4: Monte Carlo Distributions

Selection Criteria	N(τ MC)	N(Generic MC)	N(Data)	ϵ (τ MC)	ϵ(Generic MC)	ϵ(Data)
Reject Conversions	74740426	30794057	115526215	94.73	98.44	81.47
Reject Ks	74540987	30360638	114869656	99.73	98.59	99.43
Isolated tracks	60655230	9697066	68382228	81.37	31.94	59.53
No Neutral Clusters	31980972	453555	33924680	52.73	4.68	49.61
Beam energy cut	31970522	449413	33660732	99.97	99.09	99.22
Tight PID muons	9586402	28692	6056028	29.99	6.38	17.99
MultiProng Events	3973991	4634	2015038	41.45	16.15	33.27
e veto $\pi(\rho^0)$	3229750	3548	1646054	81.27	76.56	81.69
mu veto $\pi(\rho^0)$	3229750	3548	1646054	100.00	100.00	100.00
dE/dx > 300 $\pi(\rho^0)$	3229750	3548	1646054	100.00	100.00	100.00
3prong	3069630	2866	1559962	95.04	80.78	94.77
e veto (hadron track)	3036008	2733	1540412	98.90	95.36	98.75
mu veto (hadron track)	2824468	2507	1441170	93.03	91.76	93.56
proton veto (all prongs)	2753076	2219	1398801	97.47	88.52	97.06
dE/dx > 300 (hadron track)	2694417	2161	1365922	97.87	97.38	97.65
2prong	160120	682	86092	4.95	19.22	5.23

Table 4.4: Relative selection efficiencies for τ Monte Carlo, generic background Monte Carlo (luminosity weighted), and data. ϵ is the relative efficiency w/ respect to the previous selection criteria. The relative efficiency for 2 prong events is compared to the selection dE/dx > 300 on pions from rho0.

4.6.2. Dalitz Re-weighting of Tau events in MC. Hadronic decays of tau leptons are not well understood, and the distribution of events in Monte Carlo does not properly model the data. Using the the 3-prong distribution of events in data, we can re-weight the acceptance loss events from Monte Carlo which are used to model the acceptance loss in the data.

To correctly account for the differences in Monte Carlo and data, an iterative procedure is used to re-weight the Monte Carlo events as a function the tau mass, the ρ^0 mass $m_{12}(\pi^+_\rho \pi^-_\rho)$, and $m_{23}(\pi^-_\rho h^+_{missing})$ The final weight applied to the Monte Carlo events is the product of three weights: 3π mass, ρ mass, and $\pi^- h^+$ mass. When re-weighting the acceptance loss events, the true MC track four-vector of the missing hadron is used when calculating $m_{23}(\pi^-_\rho h^+_{missing})$.

$$w_i = w_{3\pi} \times w_\rho \times w_{\pi^- h^+} \tag{4.6.1}$$

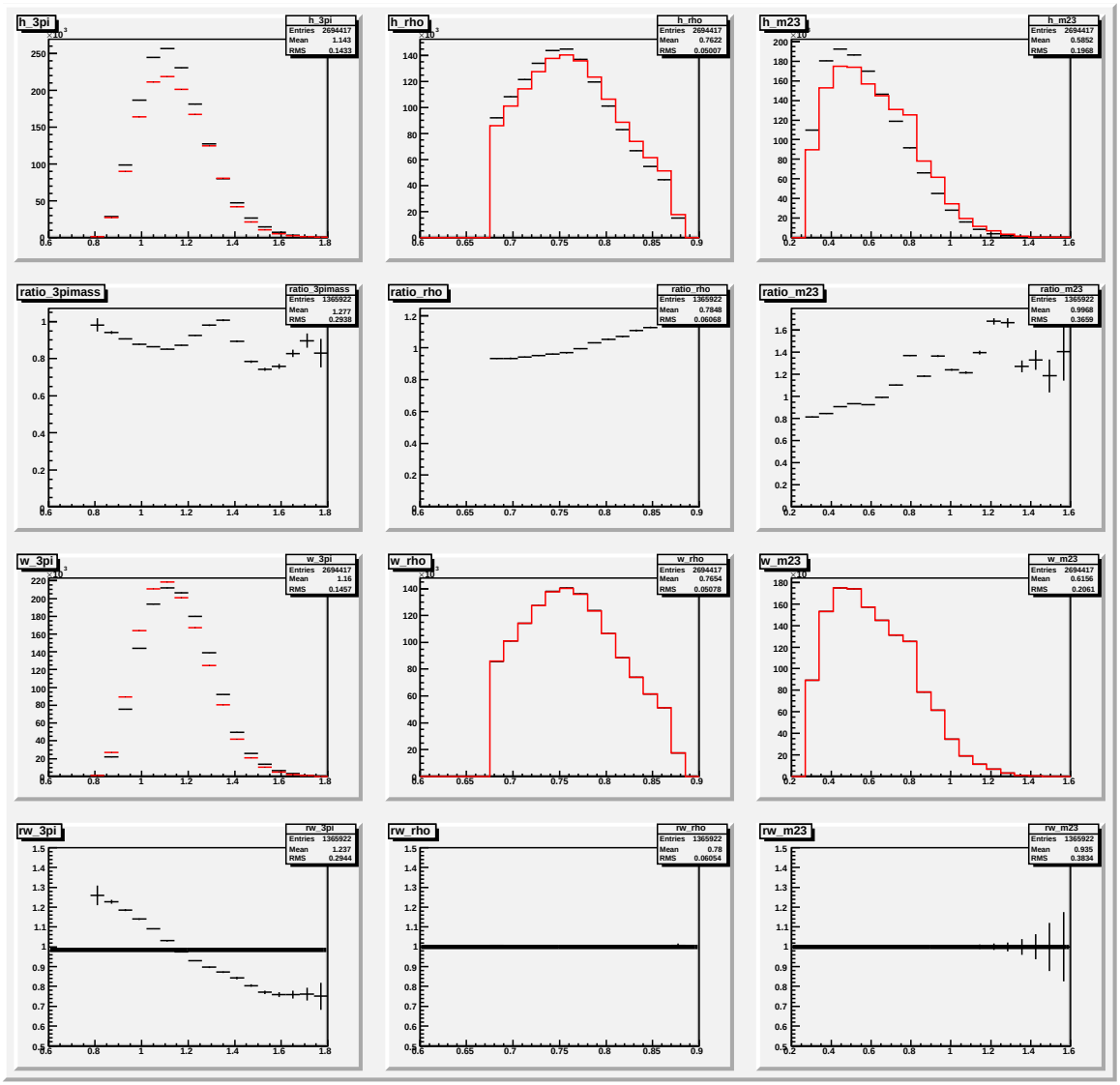

Figure 4.5: Data versus Monte Carlo events before re-weighting

4.6.3. $D^0 \to \pi^+\pi^-$**.** The dominant background in $D^0 \to \pi^+\pi^-$ is $D^0 \to K^-\pi^+$, which typically can be removed with the application of particle identification. In our case, we must restrict the use of particle ID since we want to know the tracking asymmetry. Another method to remove the $K\pi$ background is to cut on the reflected mass of the D^0 by assuming the kaon mass for one of the tracks and cut out the reflection (Figure 4.8). The long tail of the background still remains under the signal region, and therefore must still be accounted for. To resolve this, we take the shape of the $K\pi$ background directly from data by applying tight kaon particle

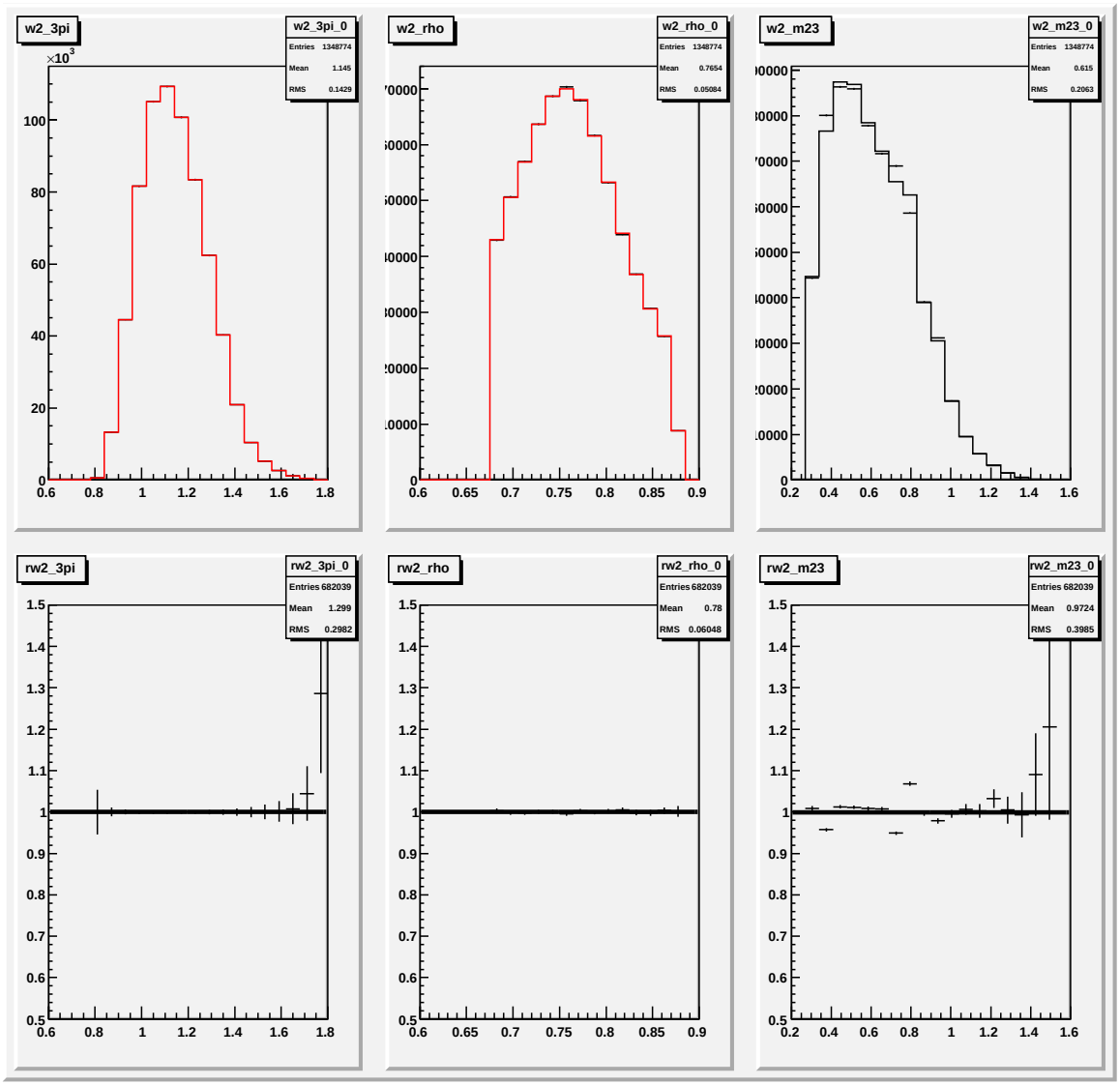

Figure 4.6: τ^+ Data versus Monte Carlo events after re-weighting

identification. The mass peak of $D^0 \to \pi^+\pi^-$ is removed, but the large signal of $K\pi$ remains. The shape is used in the fit with an overall scale factor floated and we do not remove the reflection with a kinematic cut. The reflection only appears when the faster track is the right-sign kaon. For D^0 decays, the $K^-\pi^+$ background appears when the faster track is negative; for $\bar{D}^0$ decays, the $K^+\pi^-$ reflection appears when the faster track is positive.

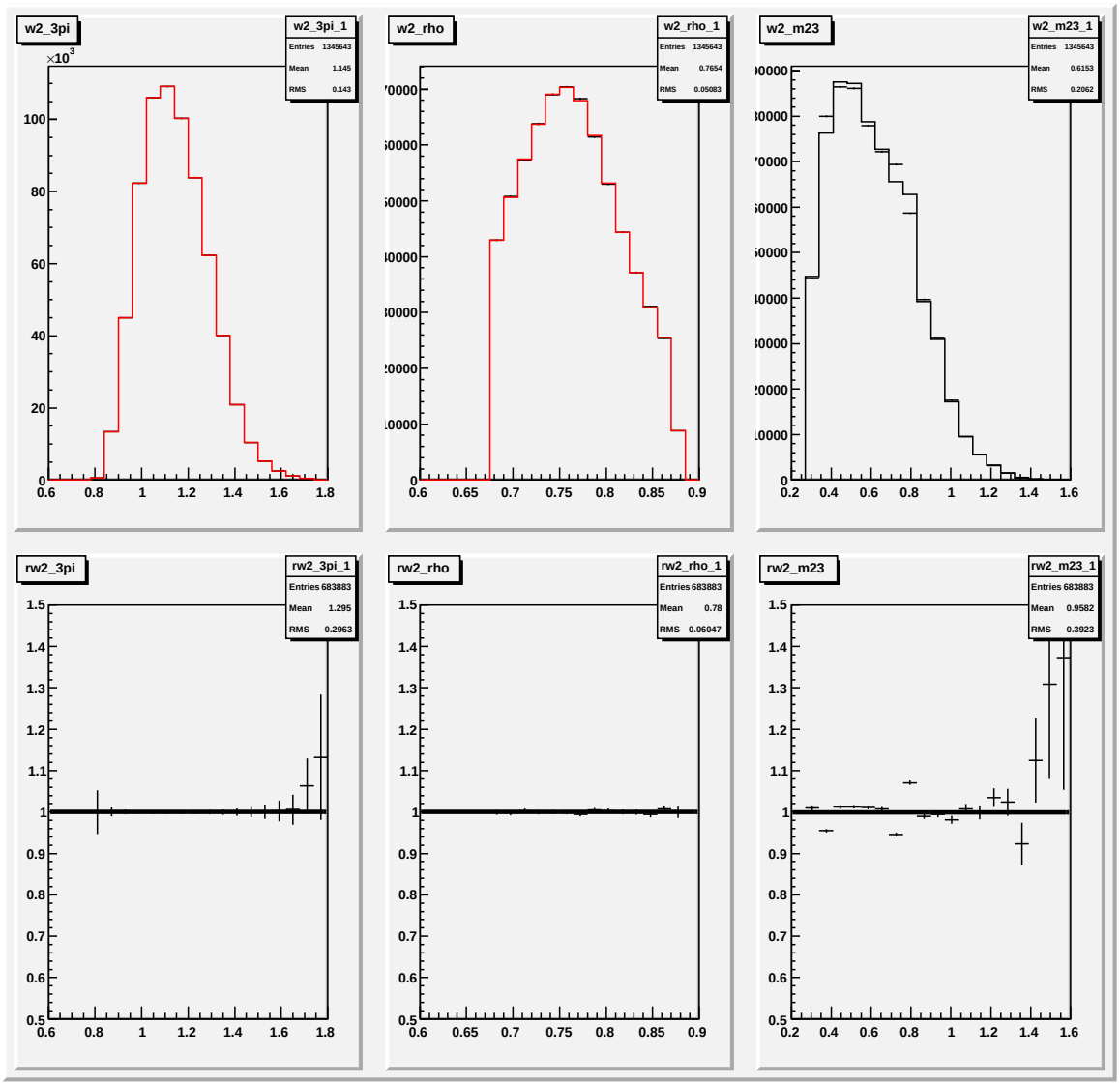

Figure 4.7: τ^- Data versus Monte Carlo events after re-weighting

4.7. Fit Methodology

In this section, we briefly summarize the various components in each model and the minimization strategy.

4.7.1. Tau31. The model for tau31 decays is made of three components: 3-prong events which are reconstructed as 2-prong due to tracking inefficiency, 3-prong events which are reconstructed as 2-prong events because one track is missing due to detector acceptance loss, and 1-prong backgrounds found only in the 2-prong events.

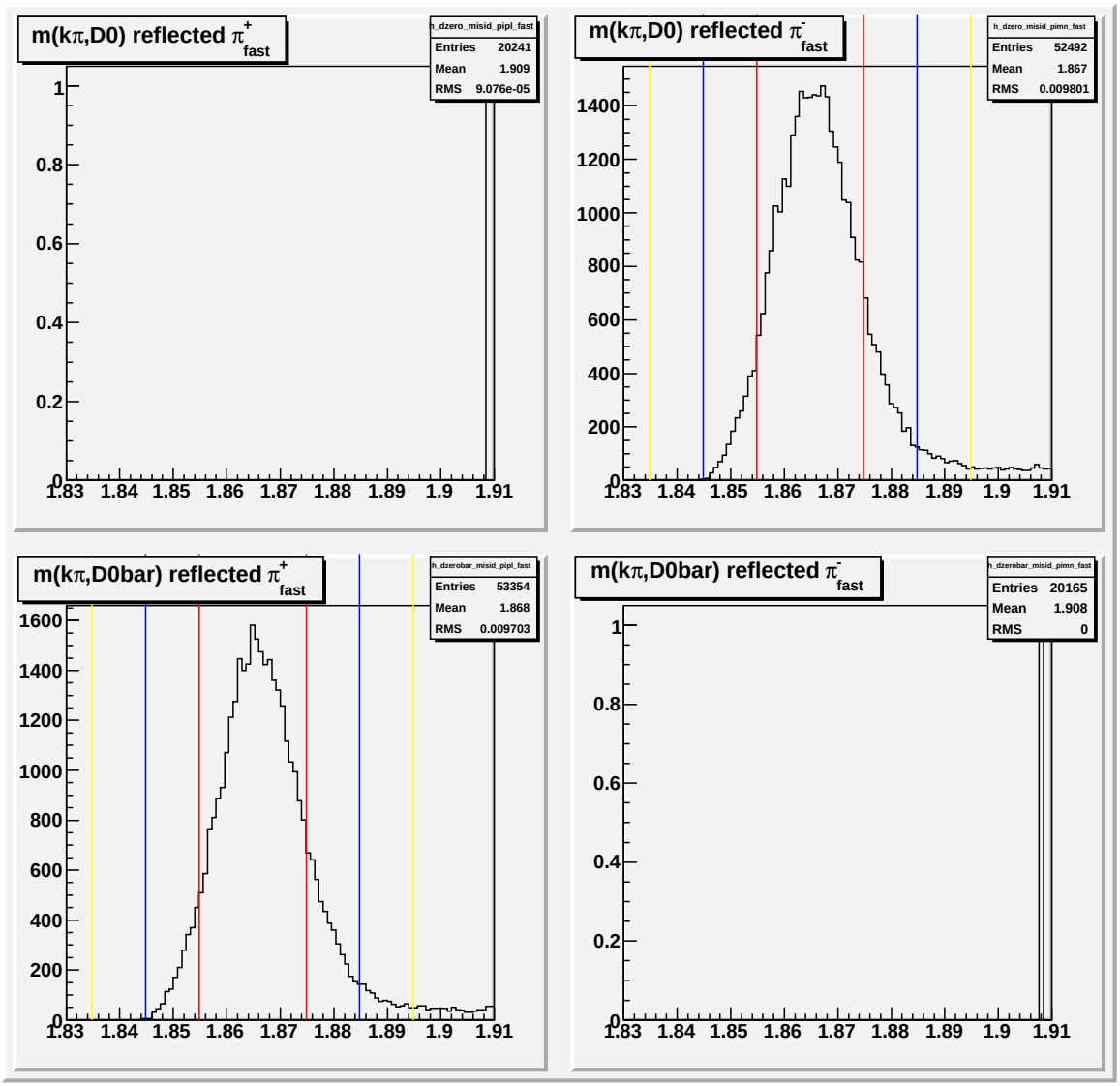

Figure 4.8: Reflected $K\pi$ mass for D^0 and $\bar{D}^0$ decays when we assume a kaon mass hypothesis for the faster track.

Any extra part of the 2-prong background is assumed to be described by MC. Low acceptance regions are excluded by kinematic cuts on the visible prongs and opposite-side lepton.[*] Optimal cuts are determined from MC. A similar procedure yields the fake rate using 4-prong events.

Errors on the number of events in each bin need to be evaluated correctly since most of the weights are far from 1 (in the 0.05 - 0.15 range typically). Bins are chosen to populate the histogram uniformly. A piecewise-linear interpolation in momentum is used to parameterize the tracking efficiency.

We define the efficiency for positive and negative tracks

$$\epsilon^{\pm}(p_{Lab}) = \epsilon_{p_{Lab}}(1 \pm a_i) \tag{4.7.1}$$

where a_i is the asymmetry at momentum bin edge i, and $\epsilon_{p_{Lab}}$ is the six parameter efficiency as a function of the lab momentum taken from the MC. We assume a piecewise linear function of the lab momentum for the asymmetry using interpolation between bin edges. To obtain the expected distribution of 2-prong events which are due to tracking inefficiency, we weight each 3-prong event. The weight, w_ϵ, is defined as

$$w_\epsilon = \frac{1 - \epsilon^{\pm}_{hadron}}{\epsilon_{\pi_1^{\pm}} \times \epsilon_{\pi_2^{\mp}} \times \epsilon_{hadron^{\pm}}} \tag{4.7.2}$$

Acceptance loss events are modeled using the distributions taken from the Monte Carlo. Different shapes are used for positive and negative events, and we have three shapes associated with the different type of signal events: $\tau \to a_1$, $\tau \to W$, and remaining signal events that are not classified. The overall scale of the distribution for each type of acceptance loss event is floated in the fit.

The background shapes are taken from the MC for positive and negative tracks and split into two categories. The dominant background of $\gamma \to e^+e^-$ is one distribution while the remaining background categories are combined into a single distribution.

Additional distributions from generic $b\bar{b}$, $c\bar{c}$, and uds MC are also included in the fit but fixed to the relative luminosity. These contributions are small.

We minimize a two-dimensional χ^2 function in pseudo-theta (θ') and pt_{miss} over 20x20 bins as the sum of χ^2 for τ^+ events and τ^- events:

$$\chi^2 = \sum_i \left[\frac{N_{observed} - N_{expected}}{\Delta_{expected}} \right]^2 \tag{4.7.3}$$

where the expected number of events is comprised of the number of events due to tracking inefficiency, the number of events due to acceptance loss, and the number of events due to 1-prong backgrounds.

We find θ' and pt_{miss} from the two reconstructed tracks on the 2-prong side of the event.

Using

$$\vec{p}(\pi\pi) \equiv \vec{p}(\pi^+) + \vec{p}(\pi^-) \tag{4.7.4}$$

$$\cos(\theta') = \frac{p_z(\pi\pi)}{p(\pi\pi)} \tag{4.7.5}$$

$$pt_{miss} = p_T(\pi\pi) \tag{4.7.6}$$

The distribution of 2-prong events with the bins overlaid can be seen in Figure 4.9.

The total error in each bin for the expected number of events is given by

$$\sigma^2_{Total} = \sum_{i=1}^{n_{background}} w_i^2 + \sum_{i=1}^{N_{acceptance}} w_i^2 + N_\epsilon \tag{4.7.7}$$

The minimization of the χ^2 function is performed using MINUIT, with a total of 20 free parameters and 780 degrees of freedom.

4.7.2. $D^0 \to \pi^+\pi^-$**.** To measure the tracking asymmetry in two body decays, we assume that the asymmetry for faster tracks, $p_{Lab} > 2$ GeV, is zero as indicated from Monte Carlo. With this assumption, we find the yield of $D^0(\bar{D^0})$ events for the slower daughter track in bins of momentum up to 2 GeV. We obtain two measurements of tracking asymmetry for each momentum bin, since the pion asymmetry is measured from either D^0 or $\bar{D^0}$.

For each slower pion momentum bin we fit for yield of D^0 by minimizing χ^2 over the 1-dimensional mass plot, for a D^0 mass between 1.78 GeV and 1.94 GeV.

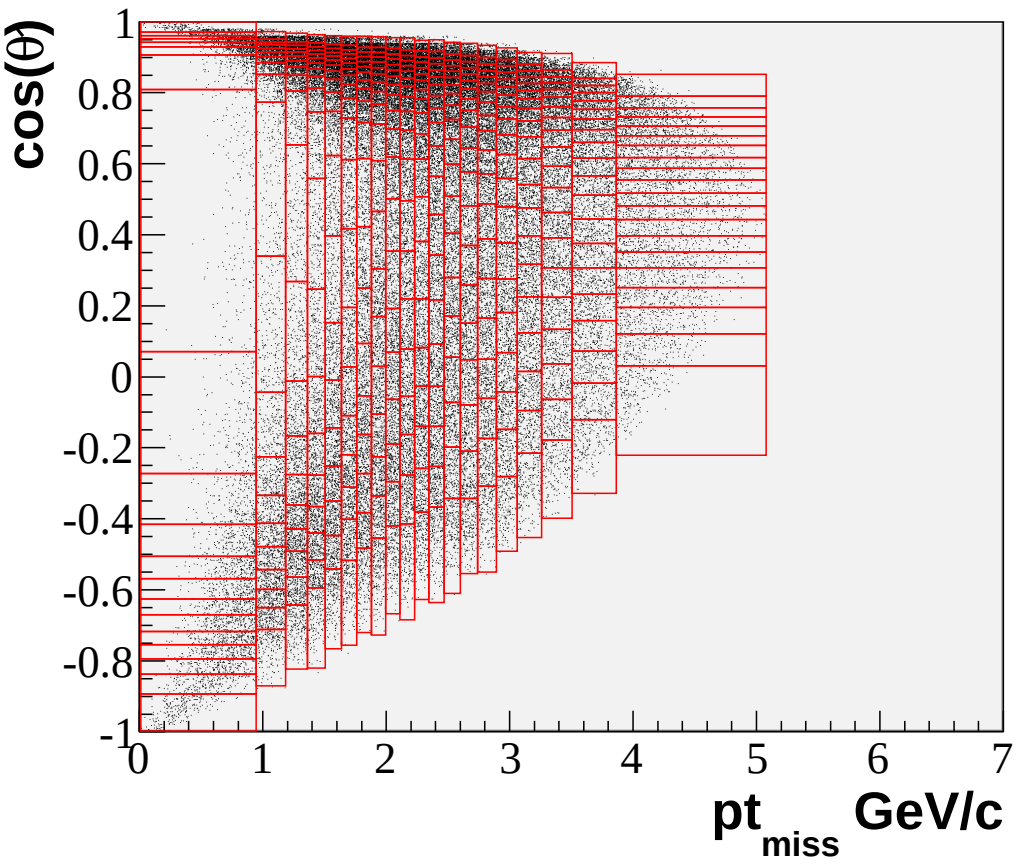

Figure 4.9: Distribution of the observed 2-prong events for the full BaBar data set. The bins, shown in red, are chosen such that the number of events in each bin is statistically equivalent. Each bin contains approximately 215 events.

The background includes an overall scale factor for the $K\pi$ background plus an additional linear term to fit the remaining combinatorial background. The signal function is a double-Gaussian function where the two Gaussians share a mean. The $K\pi$ background distribution is a histogram of the D^0 mass in each momentum bin with tight kaon particle id applied to the faster track.

We measure the asymmetry for D^0 and $\bar{D}^0$

$$A_\epsilon = \frac{N(D^0_{\pi^+_{slower}}) - N(D^0_{\pi^-_{slower}})}{N(D^0_{\pi^+_{slower}}) + N(D^0_{\pi^-_{slower}})} \tag{4.7.8}$$

4.8. Results

The results for the average asymmetry for Tau31, D^0 and $\bar{D}^0$ are listed below and are found to be consistent with zero (Table 4.5).

Table 4.5: Average Tracking Asymmetry

Mode	Asymmetry (%)
Tau31	0.10 ± 0.26
$D^0 \to \pi^+\pi^-$	0.24 ± 0.72
$\bar{D}^0 \to \pi^+\pi^-$	-0.46 ± 0.69
MC	-0.006 ± 0.023

4.8.1. Tau31 Results. The MINUIT output is included in appendix A.

Parameter description:

```
A_0, p0, tau, B_0, p1, tau_prime

 a_0

a_1

a_2

a_3

plus(minus)_acceptanceloss

plus(minus)_acceptancelosscat1

plus(minus)_acceptanceloscat2

plus(minus)_conversions

plus(minus)_bgd

plus(minus)_uds

plus(minus)_cc

plus(minus)_bb
```

The final result for the tracking efficiency versus lab momentum is shown in Figure 4.10, and the tracking asymmetry at four momentum points is found in Figure 4.10. The black curve in Figure 4.10 indicates the equation 1 with the

parameters taken from the fit. The red curves indicate the 1 sigma error bands obtained from the correlation error matrix with respect to the six parameters of the tracking efficiency function. We do not include correlations from the other parameters in the fit.

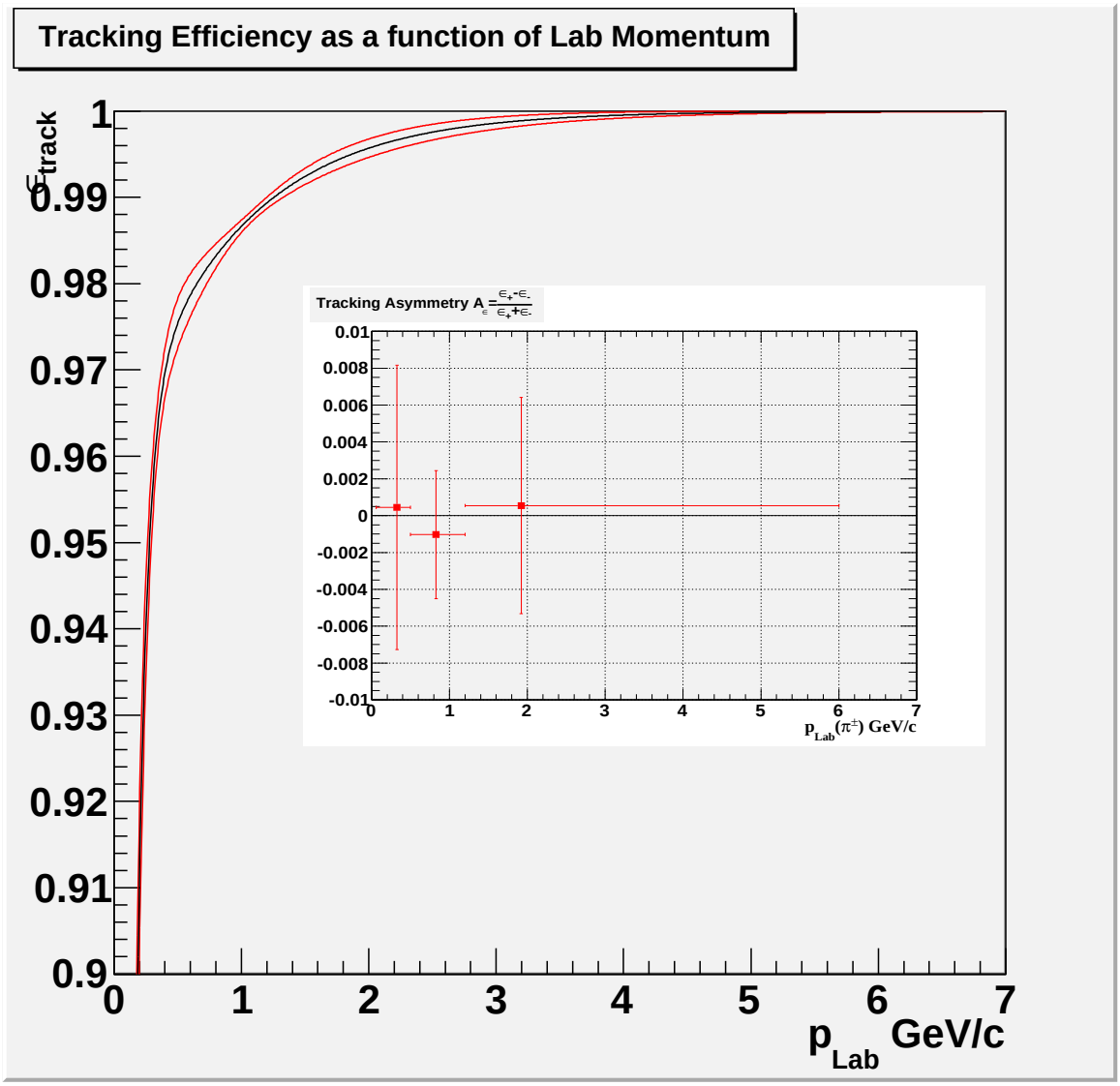

Figure 4.10: Tracking Efficiency as a function of Lab Momentum with 1 sigma error bands shown in red. The Tracking Asymmetry as a function of Lab Momentum is inset.

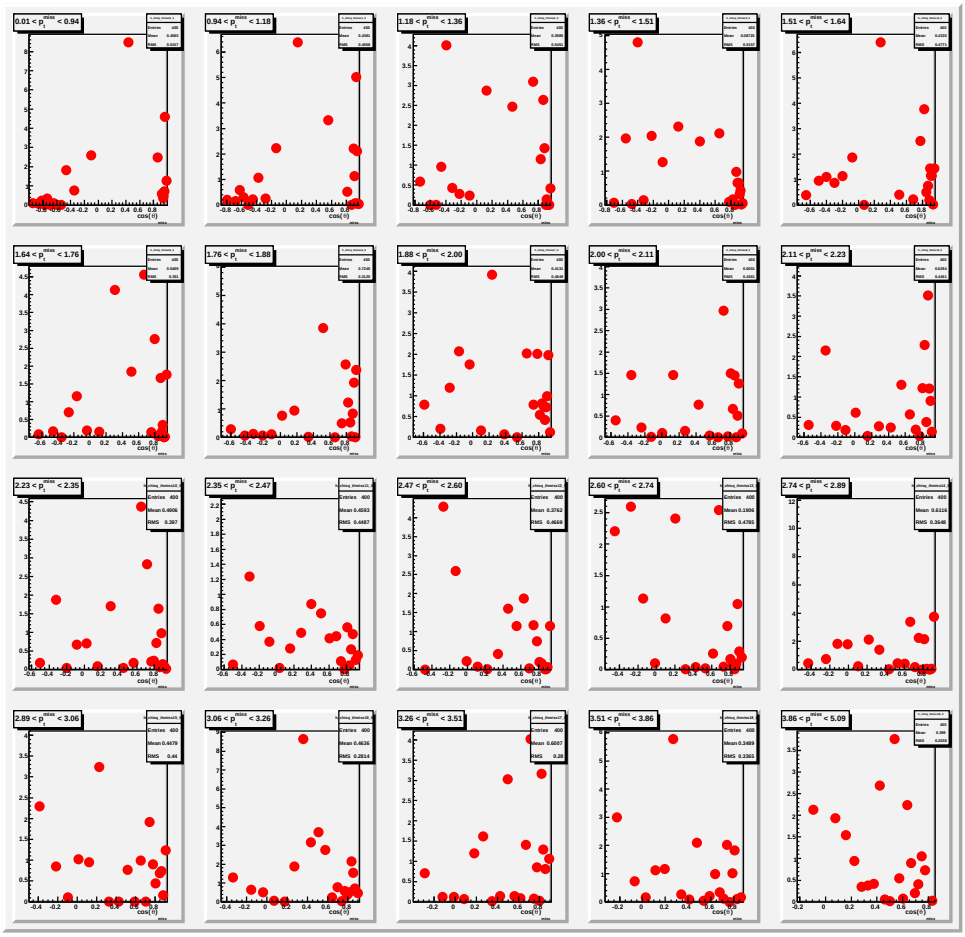

Figure 4.11: τ^+ χ^2 distribution as a function of $cos(\theta)$ prime in bins of p prime

4.8.2. $D^0 \to \pi^+\pi^-$.

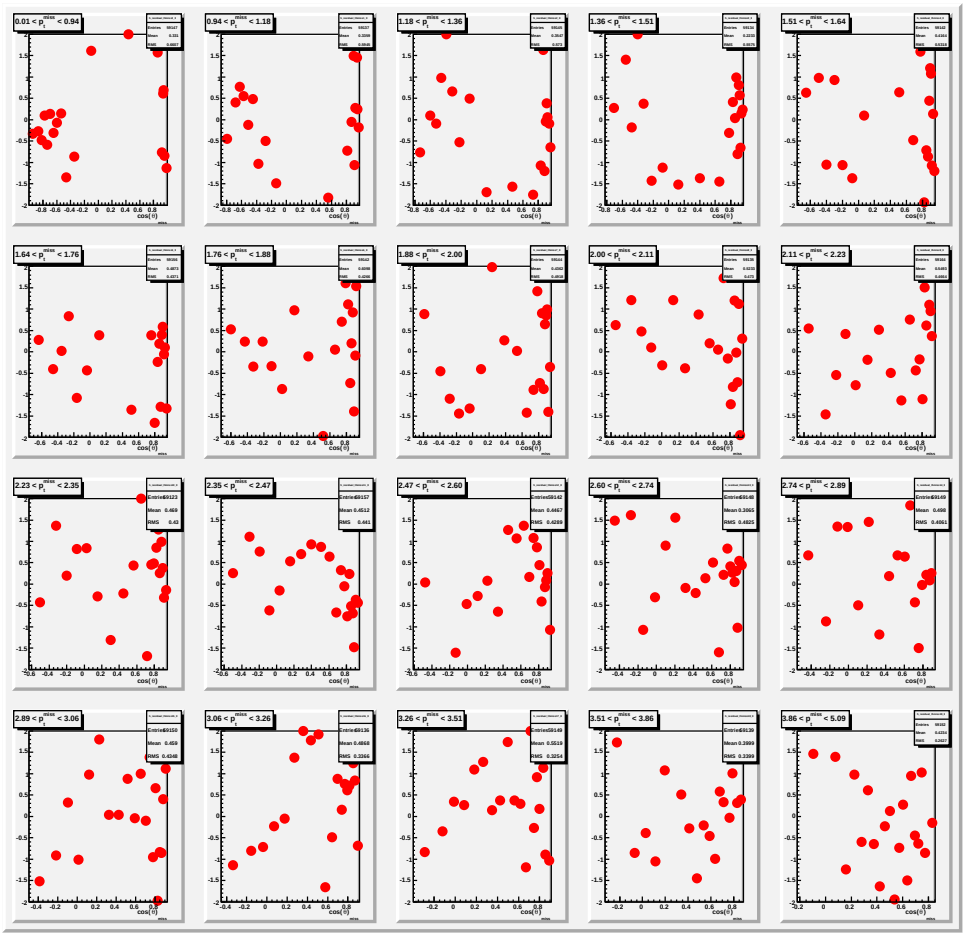

Figure 4.12: Fit result for τ^+ residual distributions as a function of $cos(\theta)$ prime in bins of p prime

4.8.3. Expected Tracking Asymmetries based on known nuclear cross section measurements.

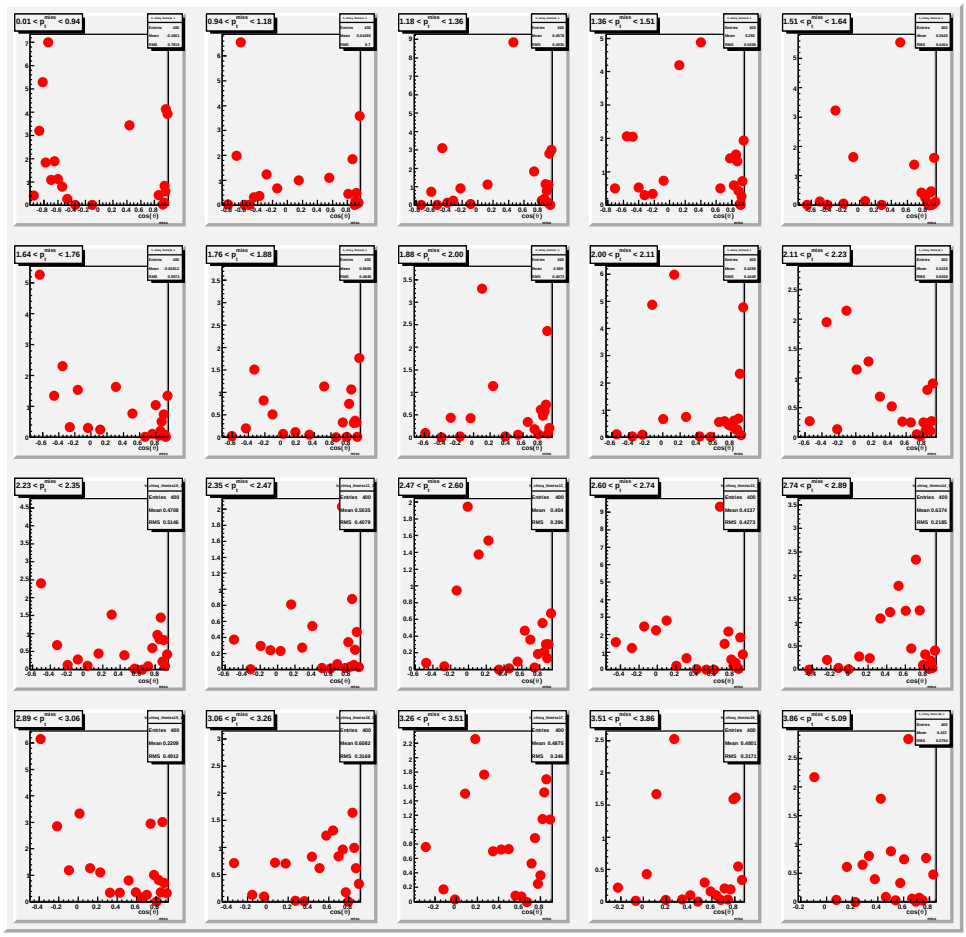

Figure 4.13: Fit result for τ^- χ^2 distribution as a function of $cos(\theta)$ prime in bins of p prime

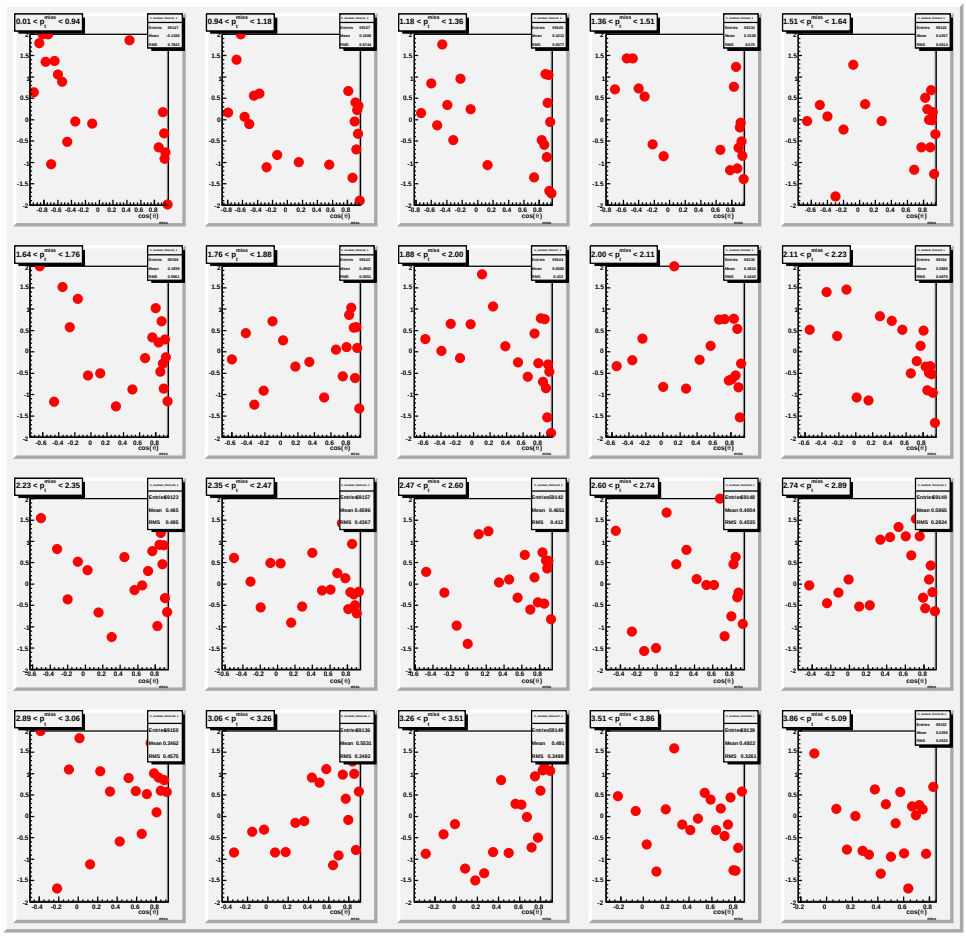

Figure 4.14: Fit result for τ^- residual distributions as a function of $cos(\theta)$ prime in bins of p prime

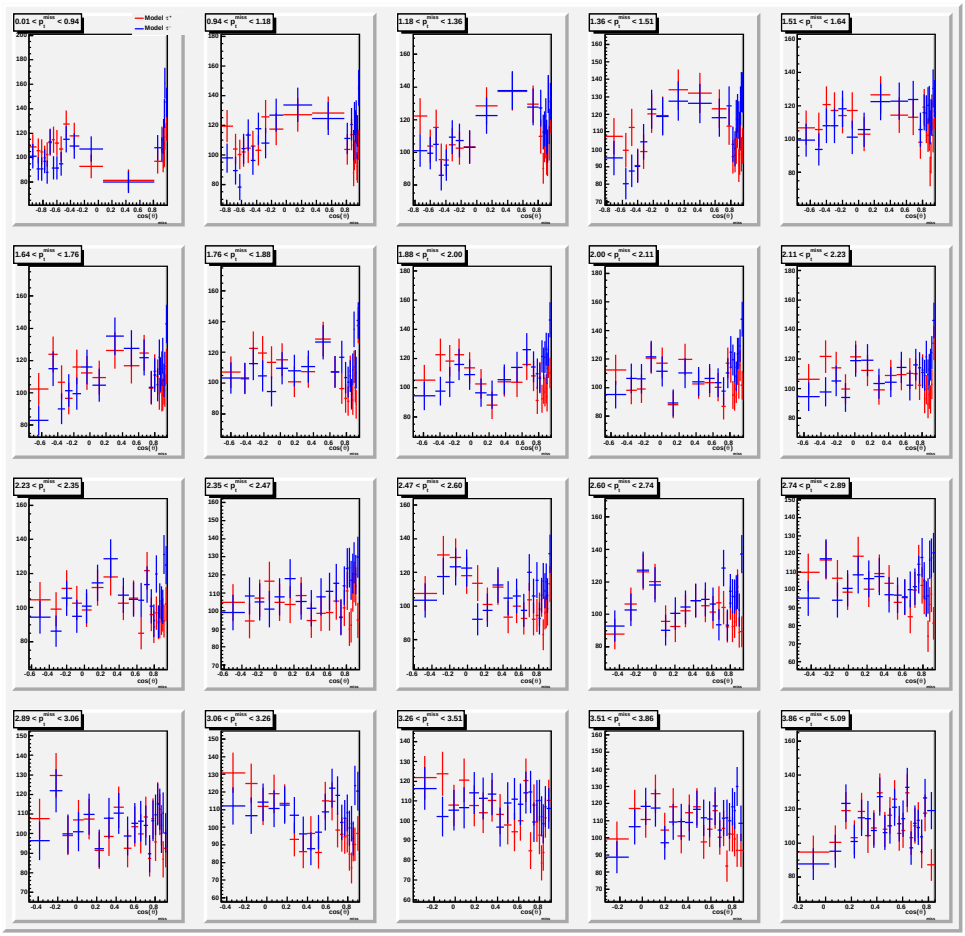

Figure 4.15: Model using parameters of final fit for π^+ and π^- distribution as a function of $cos(\theta)$ prime in bins of p prime

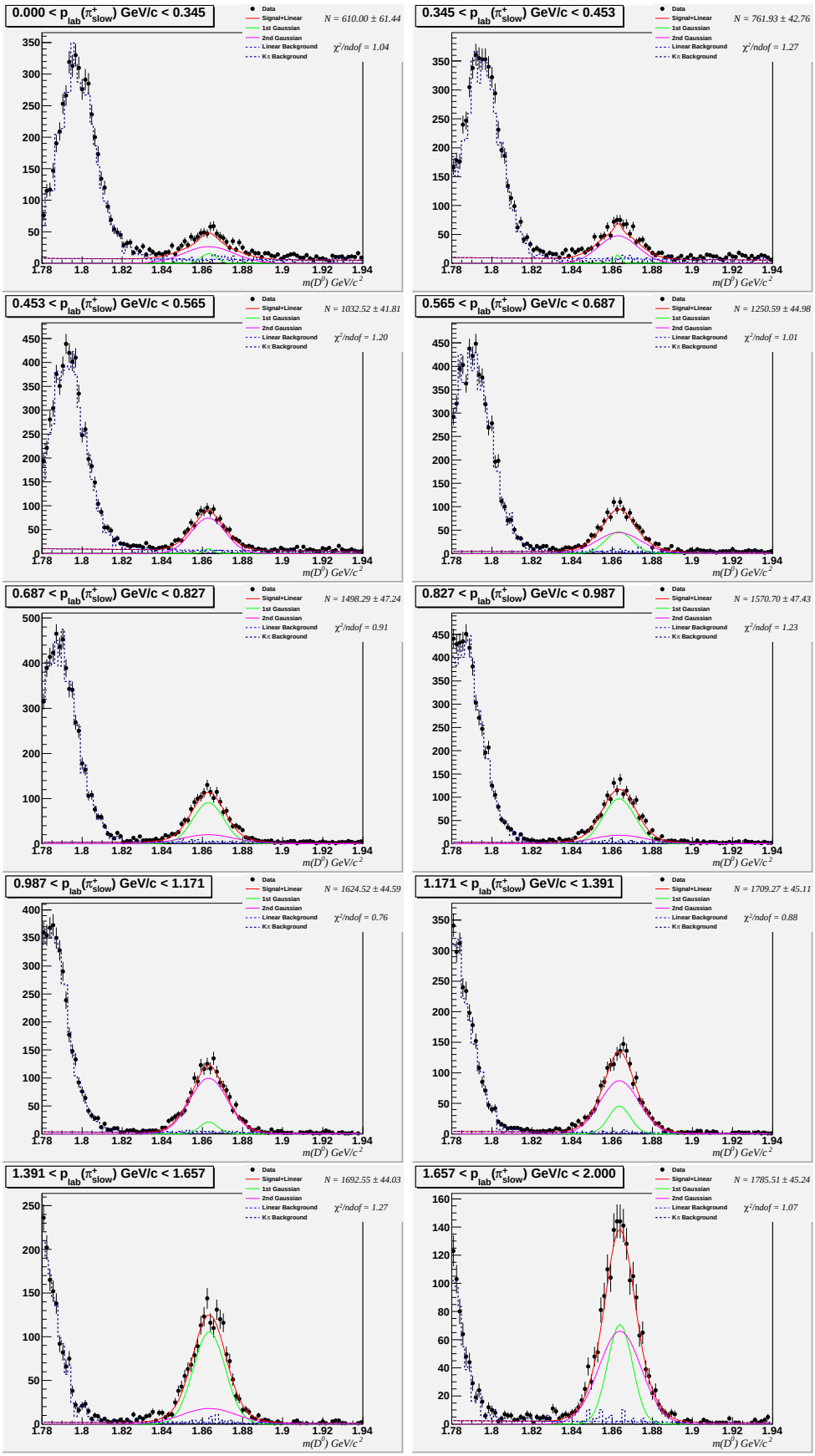

Figure 4.16: Fits to D^0 mass in bins of lab momentum of slower π^+ track.

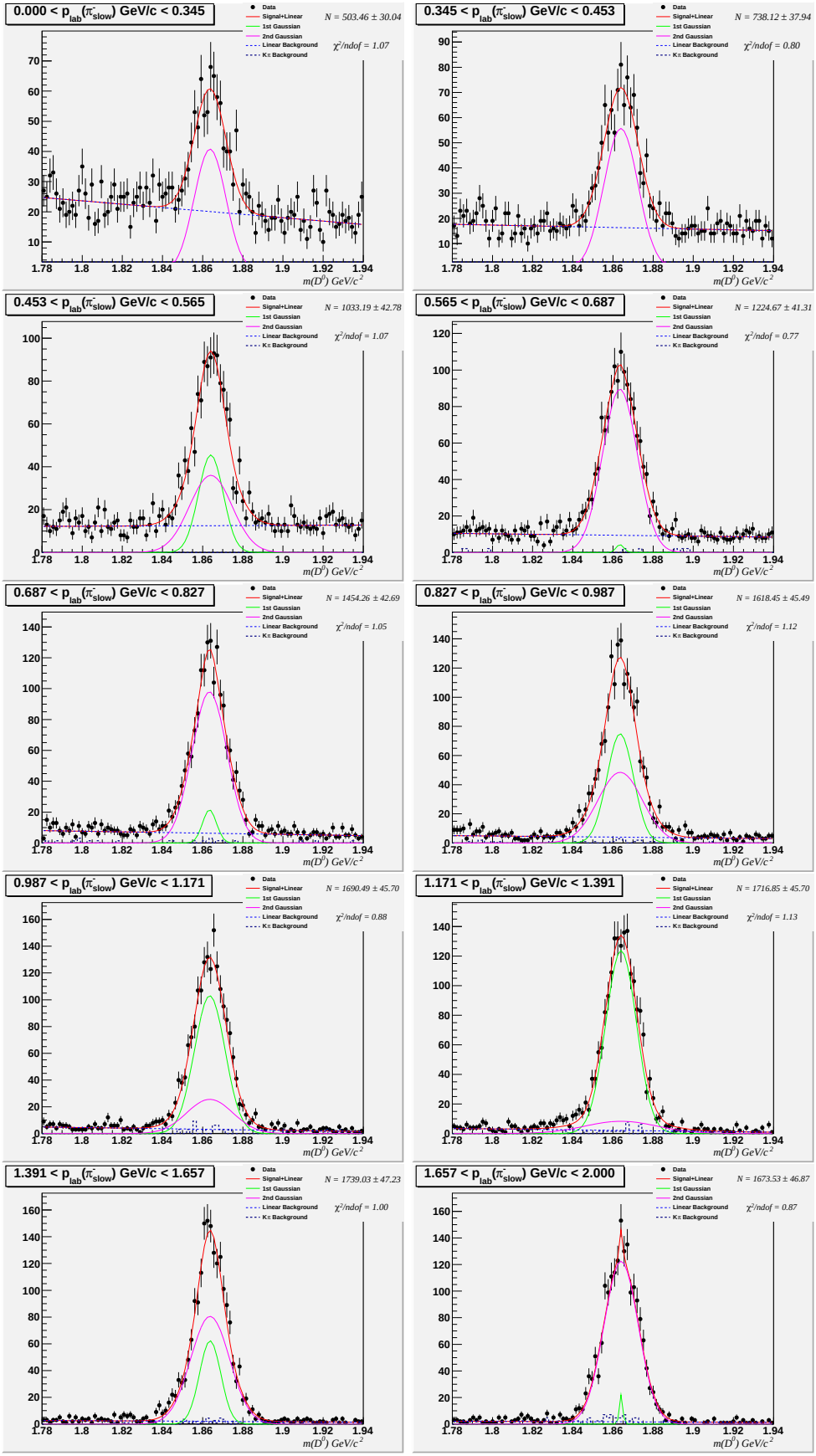

Figure 4.17: Fits to D^0 mass in bins of lab momentum of slower π^- track.

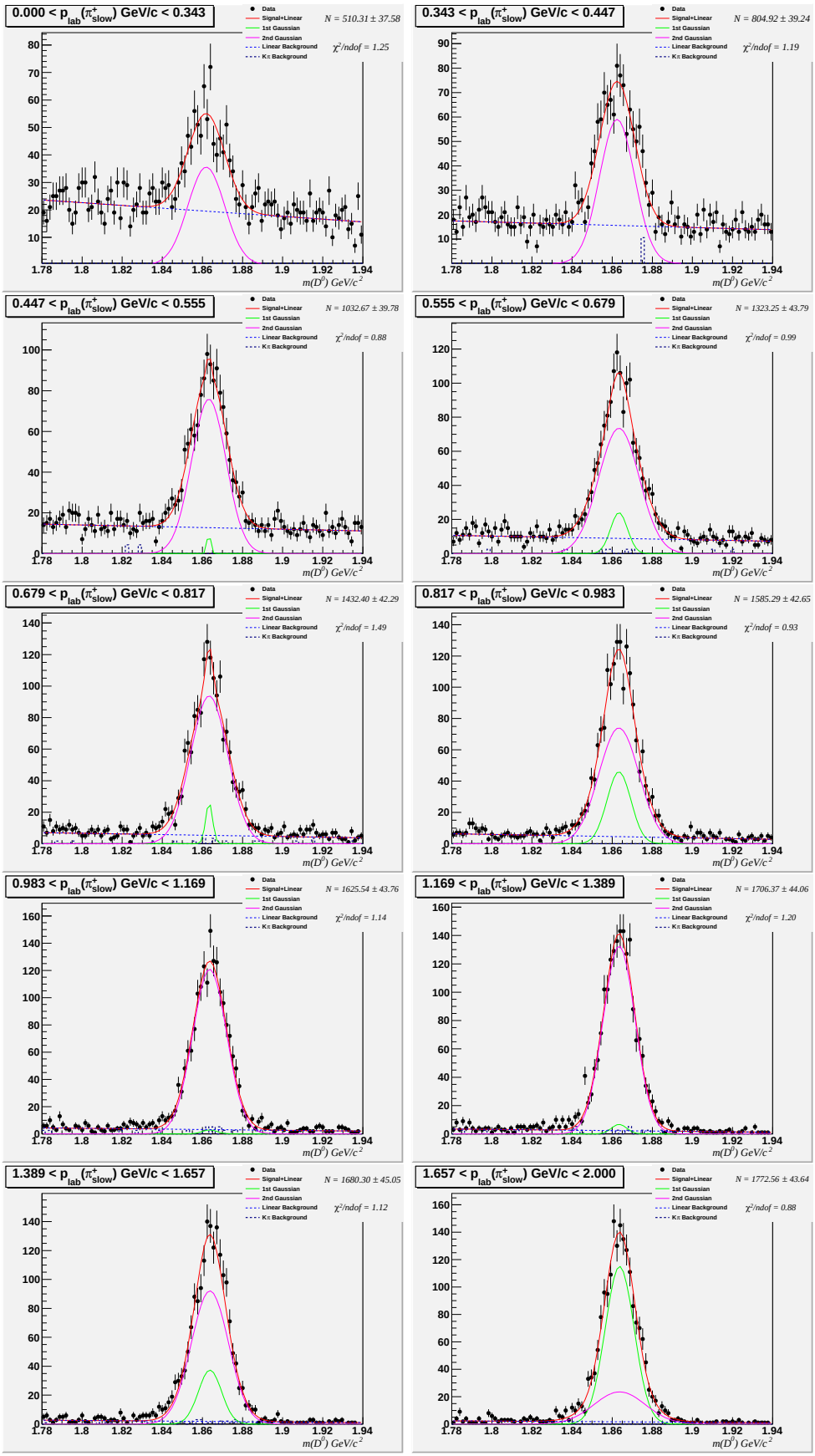

Figure 4.18: Fits to $\bar{D}^0$ bar mass in bins of lab momentum of slower π^+ track.

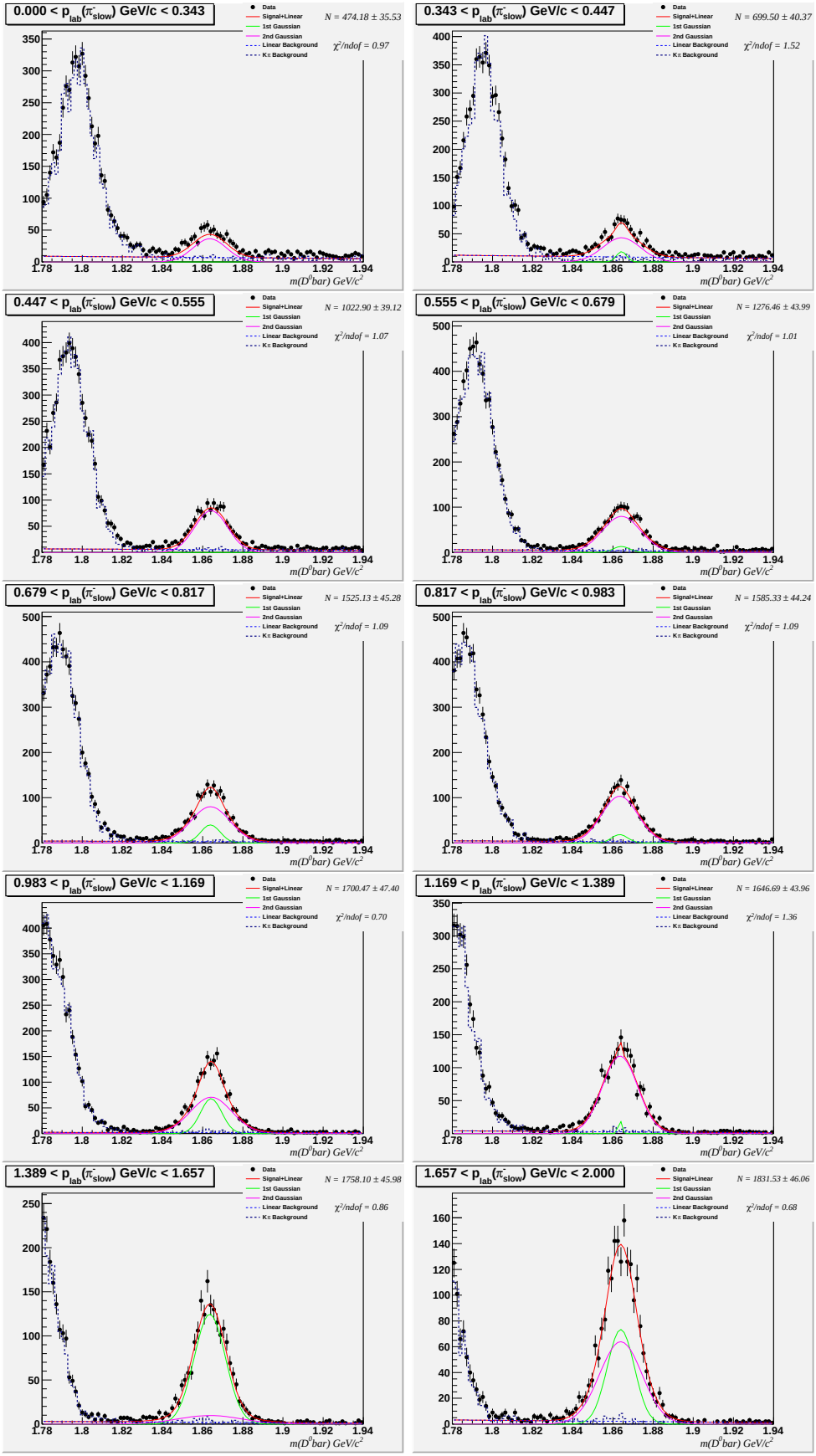

Figure 4.19: Fits to $\bar{D}^0$ mass in bins of lab momentum of slower π^- track.

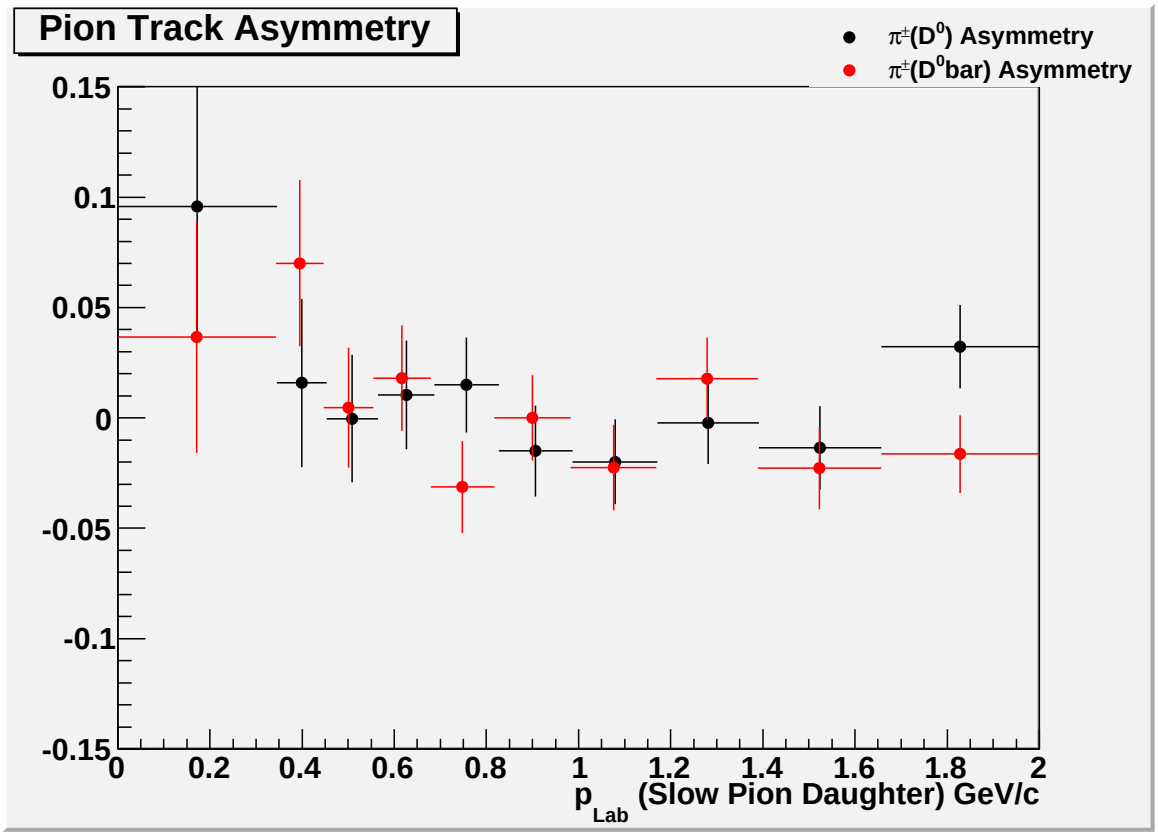

Figure 4.20: Tracking Efficiency Asymmetry as a function of Lab Momentum for pion tracks originating from D^0 and $\bar{D}^0$

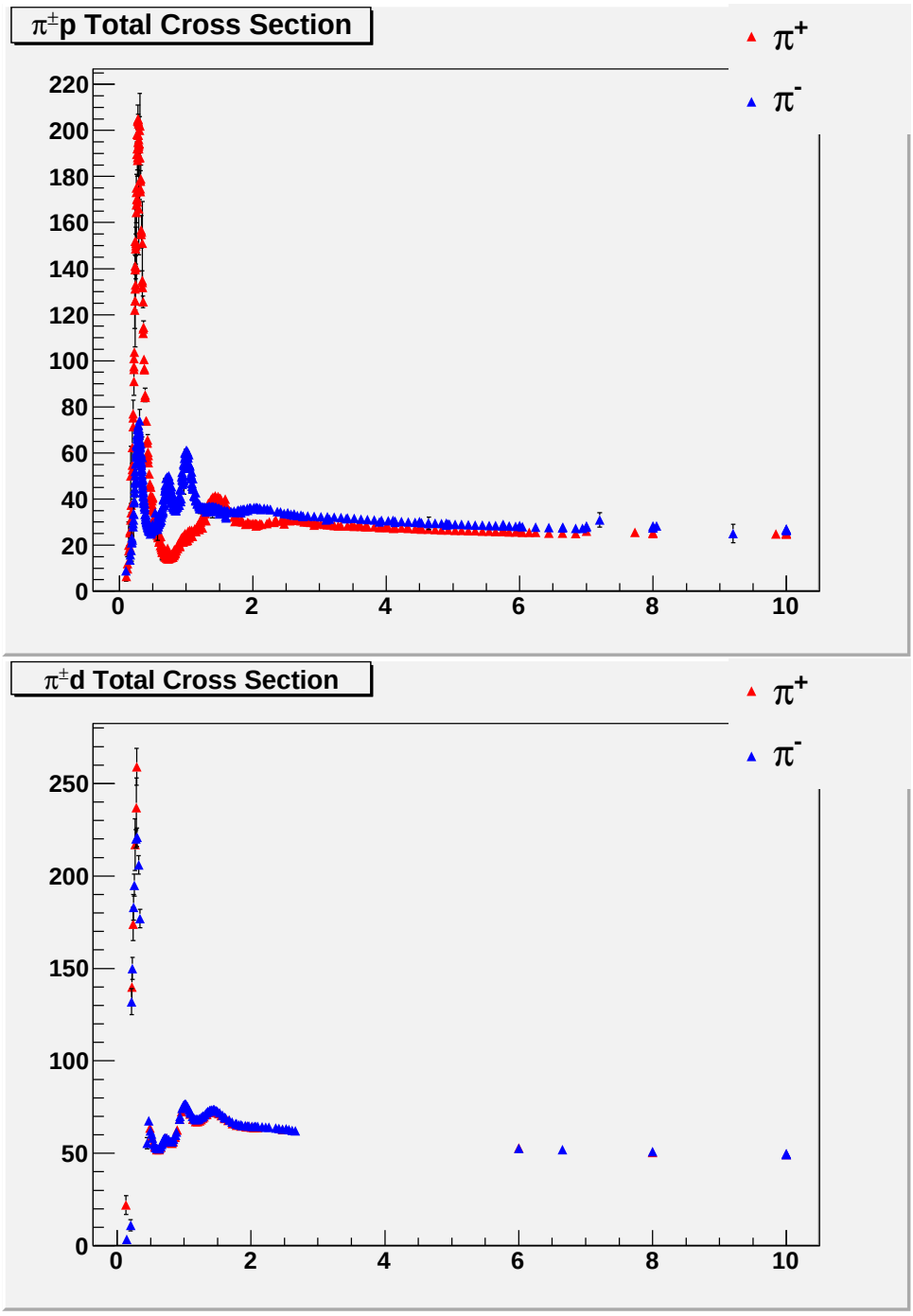

Figure 4.21: Nuclear cross section measurements for pion on proton and pion on deteurium as a function of lab momentum

Chapter 5

Measurment of Direct CP Asymmetry in the decay of $D^+ \to K^+K^-\pi^+$

5.1. Data sets and Event Selection

The data used are all from runs 1-6, including both on-resonance and off-resonance running. We also use "Signal" MC (generated useing a phase space decay model), a 2xData R24 generic MC and a 5xData R26 generic MC.

Data and Monte Carlo collections for this analysis were produced from the Release-24 series, using analysis-51 and con24boot09 conditions. Additional generic Monte Carlo for $c\bar{c}$ and $b\bar{b}$ events are available in the Release-26 series. We combine R24 and R26 Monte Carlo to increase statistics for modeling the background as a function of the Dalitz plot position. Refer to Table 5.1 for data luminosity and equivalent MC luminosity for these data sets.

Collection	Luminosity (fb^{-1})
PR Data R24c-v07	476.083
uds SP Data R24c-v07	1133.063
$c\bar{c}$ SP Data R24c-v07	951.183
$c\bar{c}$ SP Data R26a-v02	3659.497
B^+B^- SP Data R24c-v07	1347.204
$B^0\bar{B}^0$ SP Data R24c-v07	1364.227
B^+B^- SP Data R26a-v02	1731.983
$B^0\bar{B}^0$ SP Data R26a-v02	1570.589

Table 5.1: Integrated luminosity collected from the BaBar experiment (PR Data) and equivalent luminosity of generic Monte Carlo data sets used in this analysis. The PR Data collection is a fully reprocessed data set which includes all of the improvements in software and tracking over the life of the experiment. The R26a SP collections are Monte Carlo collections equivalent to to R24c MC collections, however, these data sets have a significant increase in statistics for the charm Monte Carlo.

The candidate reconstruction is split into three stages, the first being the skimming of All-Events data. An official skim which selects D^+ and D_s^+ exists in the R24 skimming cycle [**14**]. The second stage is the pre-selection criteria that are imposed during the ntuple production process while running over the skimmed events. Vertexing, particle id, mass, and momentum cuts are applied to reduce background and sample size. The third stage is the Candidate selection which has requirements on track quality, and a Likelihood Ratio (LR) test is performed to discriminate between signal and background which tunes the purity and signifcance of signal events in data. Description of the discriminant can be found in appendix B.

Skim Selection [**14**]:

- •Kaon particle ID KCombinedSuperLoose
- •Pion Track: GoodTracksVeryLoose
- •$p_{CM} > 2.4$ GeV
- •Vertex Probability > 0.005
- •1.7 GeV $< m(D) < 2.1$

Pre-Selection Criteria:

- •Kaon Particle ID KaonBDTTight
- •Pion track is GoodTracksLoose
- •1.7 GeV $< m(D) < 2.1$
- •$p_{CM} > 2.4$ GeV
- •Vertex fit probability $> 0.5\%$

Candidate Selection Criteria:

- •2.4 GeV $< p_{CM} < 5$ GeV
- •1.8 GeV $< m(D) < 1.94$
- •Drift Chamber dE/dx > 300 for all daughter tracks
- •Number of DIRC photons associated with daughter tracks is at least 1
- •p_T of pion track > 300 MeV
- •q-value cut m($K^+K^-\pi^+$) - m($K^-\pi^+$) - m(π(PDG)) > 15 MeV

- D^0 mass cut —m(K^+K^-) - m(D^0(PDG)— > 5(D^0 PDG width)
- Select 1 candidate per event with largest vertex fit probability
- Dalitz boundary cut on mass-constrained Dalitz plot variables m^2_{KK} and $m^2_{K\pi}$
- Likelihood Ratio (LR) LR > 0.85

5.2. Background Studies

This section describes our preliminary look at the background and various background models that have been fit to the sideband data.

Several studies are performed on Monte Carlo and data to determine the sources of backgrounds within the signal region, the amount of asymmetry present in the background, and the distribution of background events in data. We find that while the background consists of over 40 distinct sources the amount of asymmetry in the background is small. In addition, the shape of the background does change dramatically as a function of the D^+ mass.

5.2.1. Generic Monte Carlo Background Analysis. Generic Monte Carlo is a useful tool in understanding the types of backgrounds that are present in the data. The classification of these backbrounds has been determined for the various generic MC data sets, and we provide of the breakdown of these backgrounds for D^+ and D^- events after passing all event selection criteria. The backgrounds are categorized seperately for the lower mass sideband region and upper mass sideband region and by the charge of the D meson. The detailed of the background are included in appendix B. Here, we summarize our findings of the background analysis:

- 5% electron or muon is mis-identified as a pion
- 7% kaon is mis-identified as a pion
- 3% pion is mis-identified as a kaon
- UDS MC 16% $\bar{K}^{*0}$ Resonance
- UDS MC 12% Φ Resonance
- $c\bar{c}$ MC 5% $\bar{K}^{*0}$ Resonance
- $c\bar{c}$ MC 9% Φ Resonance
- $c\bar{c}$ MC 5% D^0 Semileptonic Decays
- $c\bar{c}$ MC 5% $D^0 \to K^-\pi^+\pi^0$
- Signal decays mis-reconstructed with random pion account for 3%

5.2.2. Background Asymmetry in Sideband Data. This section shows the results of various comparisons of sideband data (using χ^2 tests) of D^+ vs D^- and for different mass regions. Before proceeding with a study of the CP asymmetry in the signal decay we need to ensure that the asymmetry in the background is negligible. To do so, we evaluate the χ^2 over 441 bins. The binning is chosen from the the reconstruction efficiency so that a comparison can also be made using background events which have been corrected by phase space and efficiency. The largest contribution to the χ^2 is from comparing the combined D^+ and D^- events for the lower mass sideband (left) to the upper mass sideband (right). The results are reported in Table 5.2.

Charge	Sideband	Correction	$\chi^2/ndof$	Probability
D^+	Left-Right	none	1.10	0.065
D^-	Left-Right	none	1.24	0.000
$D^\pm$	Left	none	0.94	0.822
$D^\pm$	Right	none	1.05	0.237
$D^\pm$	Left-Right	none	1.36	0.000
D^+	Left-Right	Phase-Space	1.10	0.066
D^-	Left-Right	Phase-Space	1.24	0.001
$D^\pm$	Left	Phase-Space	0.94	0.817
$D^\pm$	Right	Phase-Space	1.05	0.206
D^+	Left-Right	Phase-Space X Efficiency	1.10	0.067
D^-	Left-Right	Phase-Space X Efficiency	1.24	0.001
$D^\pm$	Left	Phase-Space X Efficiency	0.95	0.777
$D^\pm$	Right	Phase-Space X Efficiency	1.07	0.155

Table 5.2: Sideband asymmetry analysis for data, with and without correcting for phase-space and efficiency. The largest differences are due to comparing the upper and lower sideband data. This behavior is expected since the background varies linearly with respect to the D^+ mass. The sidebands with respect to charge do not exhibit any asymmetry over the Dalitz plot.

5.2.3. Background Slices. Profiles of background shapes are made in various dimensions with respect to the Dalitz plot m^2 variables and helicity angles. For example, course bins are chosen in $m^2(K^+K^-)$ (Figure G.1). For each bin in $m^2(K^+K^-)$ the $m^2(K^-\pi^+)$ is plotted (Figure G.3). Several of these slices are made

for the low mass and high mass sideband region with respect to the charge of the $D^{\pm}$ meson:

- slices in $m^2(K^+K^-)$ corresponding to plots in $m^2(K^-\pi^+)$ (Appendix G)
- slices in $m^2(K^+K^-)$ corresponding to plots in $cos(\theta)_{K^+K-}$ (Appendix H)
- slices in $m^2(K^-\pi^+)$ corresponding to plots in $m^2(K^+K^-)$ (Appendix G)
- slices in $m^2(K^-\pi^+)$ corresponding to plots in $cos(\theta)_{K^-\pi+}$ (Appendix H)

5.2.4. Background with Phase-Space Profiles. In addition to plotting raw distributions of background events in various dimensions, Dalitz plot projections (with phase-space events for comparison) are another useful tool in determining the structure of the background. Since the shape of phase-space is known, enhanced structure above a flat phase-space indicate which structures are significant. Plots of background events in the sideband regions for D^+ and D^- with phase-space events from signal MC (scaled to the number of events int the sideband) show structure that is not due to phase-space alone. The efficiency-corrected signal MC is also plotted, giving a clear indication of the shapes which need to be described in a background PDF.

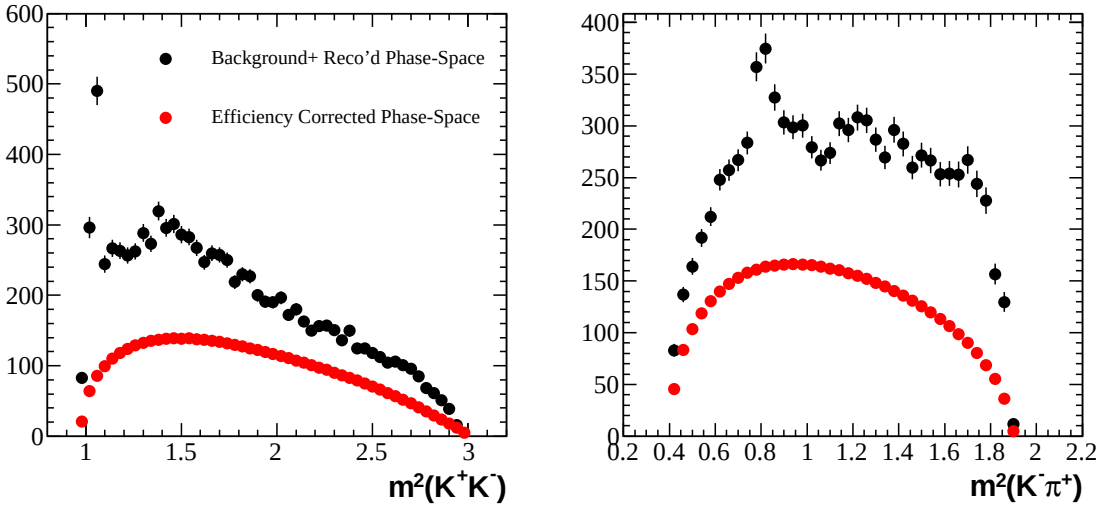

Figure 5.1: D^+ low mass sideband region Dalitz plot projections of background events and reconstructed signal MC phase-space events. Clear $\phi(1020)$ and $\bar{K}^*(892)$ peaks are visible.

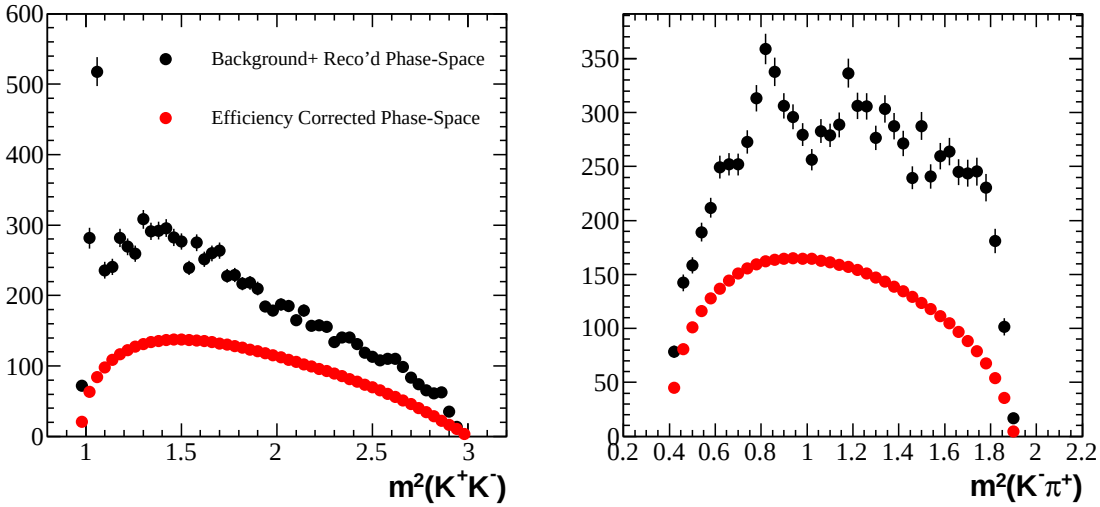

Figure 5.2: D^- low mass sideband region Dalitz plot projections of background events and reconstructed signal MC phase-space events. Clear $\phi(1020)$ and $K^*(892)$ peaks are visible.

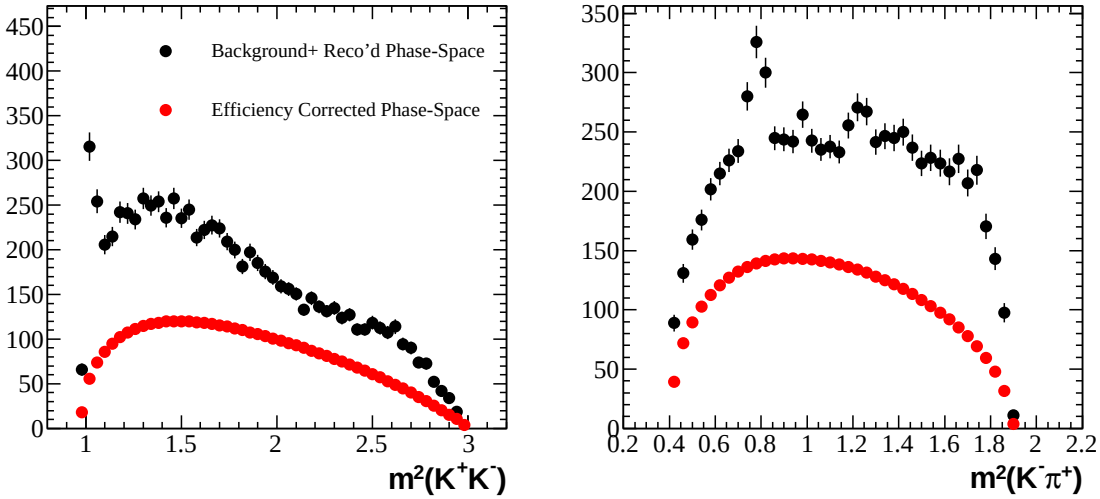

Figure 5.3: D^+ high mass sideband region Dalitz plot projections of background events and reconstructed signal MC phase-space events. Clear $\phi(1020)$ and $\bar{K}^*(892)$ peaks are visible.

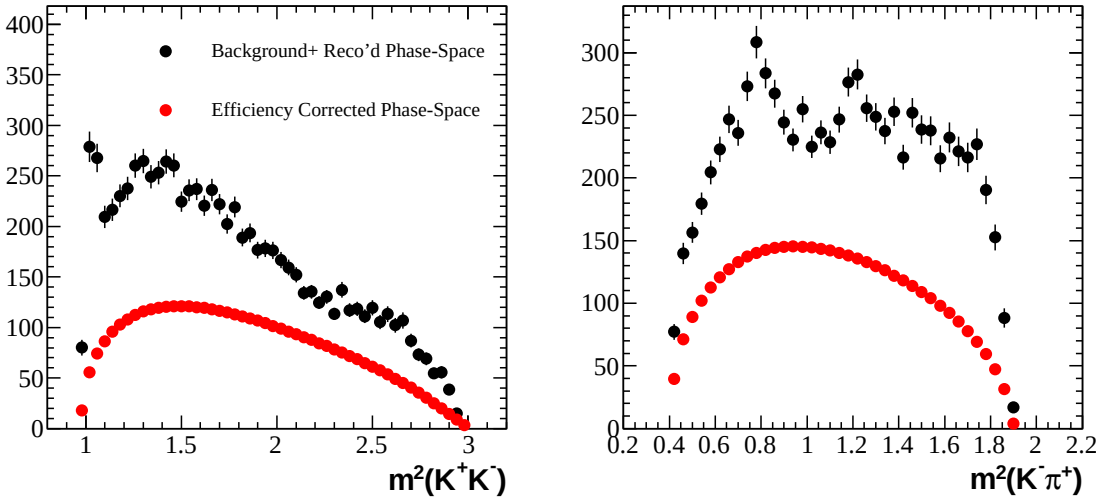

Figure 5.4: D^- high mass sideband region Dalitz plot projections of background events and reconstructed signal MC phase-space events. Clear $\phi(1020)$ and $K^*(892)$ peaks are visible.

5.2.5. Background shape as a function of D^+ mass. We compare the Dalitz plot projections of sideband data in slices of the D^+ mass to look for variation within each sideband. The comparisons are shown in Figure 5.5,Figure 5.6, Figure 5.7, and Figure 5.8. The mass windows extend as far away as 8σ from the mean of D^+ down to 4.5σ. Plots of the projections are provided for a 2σ mass window and for mass windows of 0.5σ. Qualitatively, the shape of the Dalitz plot projections do not differ from mass regions far away from D^+ signal region and close to the signal region. The charge of the D^+ is not considered in this study since the background asymmetry has been discussed in previous sections. No significant variation with mass is apparent.

5.2.6. Background Model. Several choices for the modeling of the background over the Dalitz plot within the signal region are possible. Two steps are neccesary in determining the model of the background:

- Mass dependence of the background shape
- Accurate description of sideband data over the Dalitz plot

The mass dependence of the background shape can be determined directly from data with an accurate fit of the entire D mass spectrum. From the previous section, we know that the mass dependence is linear, while the signal depends on three seperate components. However, an accurate description of the background shape over the Dalitz plot requires fitting and validating various possible models. These include using the BaBar Monte Carlo, re-normalization of the Monte Carlo to describe data or fitting directly to the sideband data. The preferred method in this analysis is to find a model which can be fit directly to the data and then be validated with data which gives a goodness-of-fit close to or equal to one. We fit the sideband with different models:

- Monte Carlo Model
- Dalitz plot model
- k Nearest Neighbor

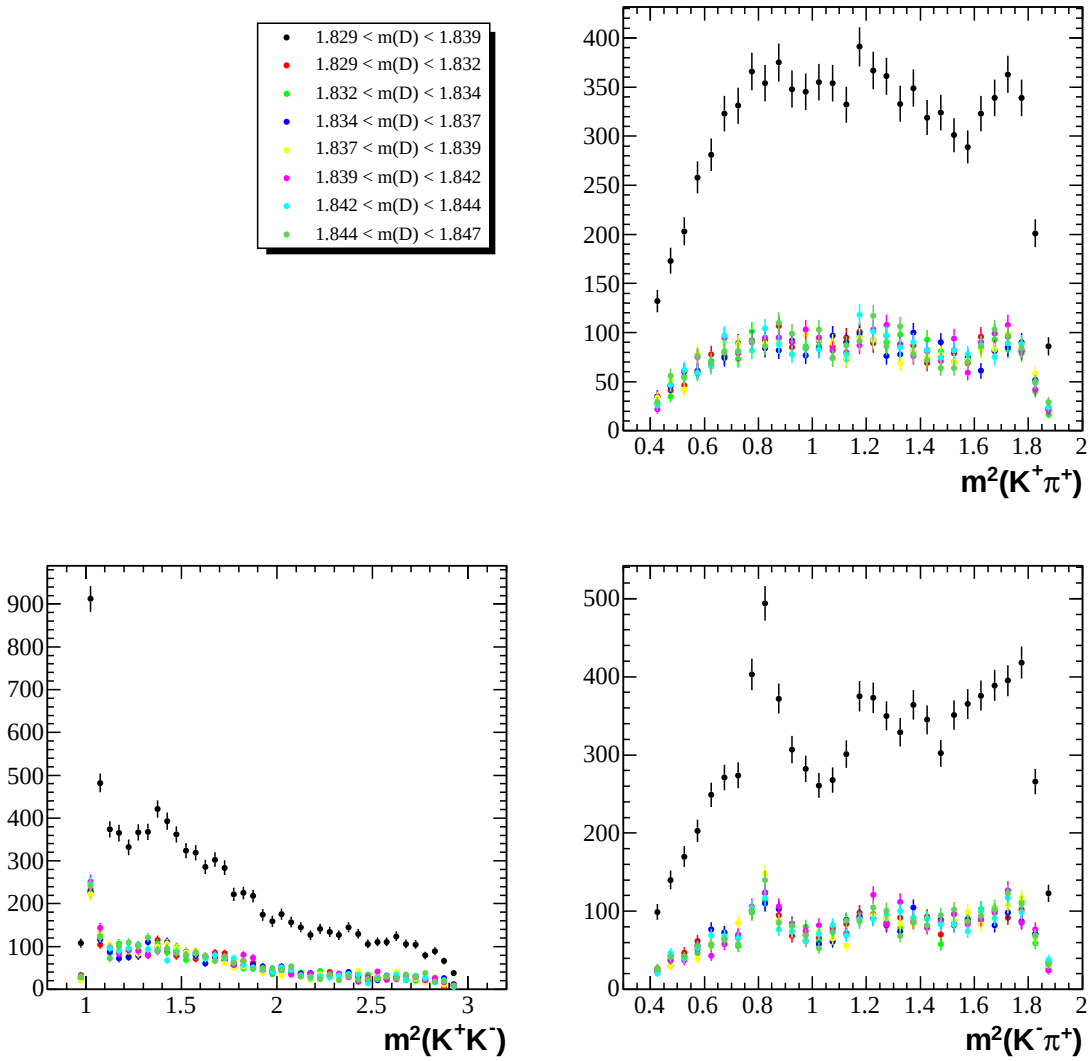

Figure 5.5: Unnormalized D low mass sideband region Dalitz plot projections of background events in slices of the D mass. The black points represent a 2σ mass, while the remaining points are taken from 0.5σ mass regions.

•3-region model

5.2.6.1. *Monte Carlo Model.* This model consists of a sum of histograms, each of which describes a particular MC component as a pdf. The pdfs we consider are 11 in number: 3 pdfs from uds MC, 6 pdfs from $c\bar{c}$ MC, 1 pdf for B^+B^- MC, and 1 pdf for $B^0\bar{B}^0$ MC. A description of these follows in Table 5.3 below.

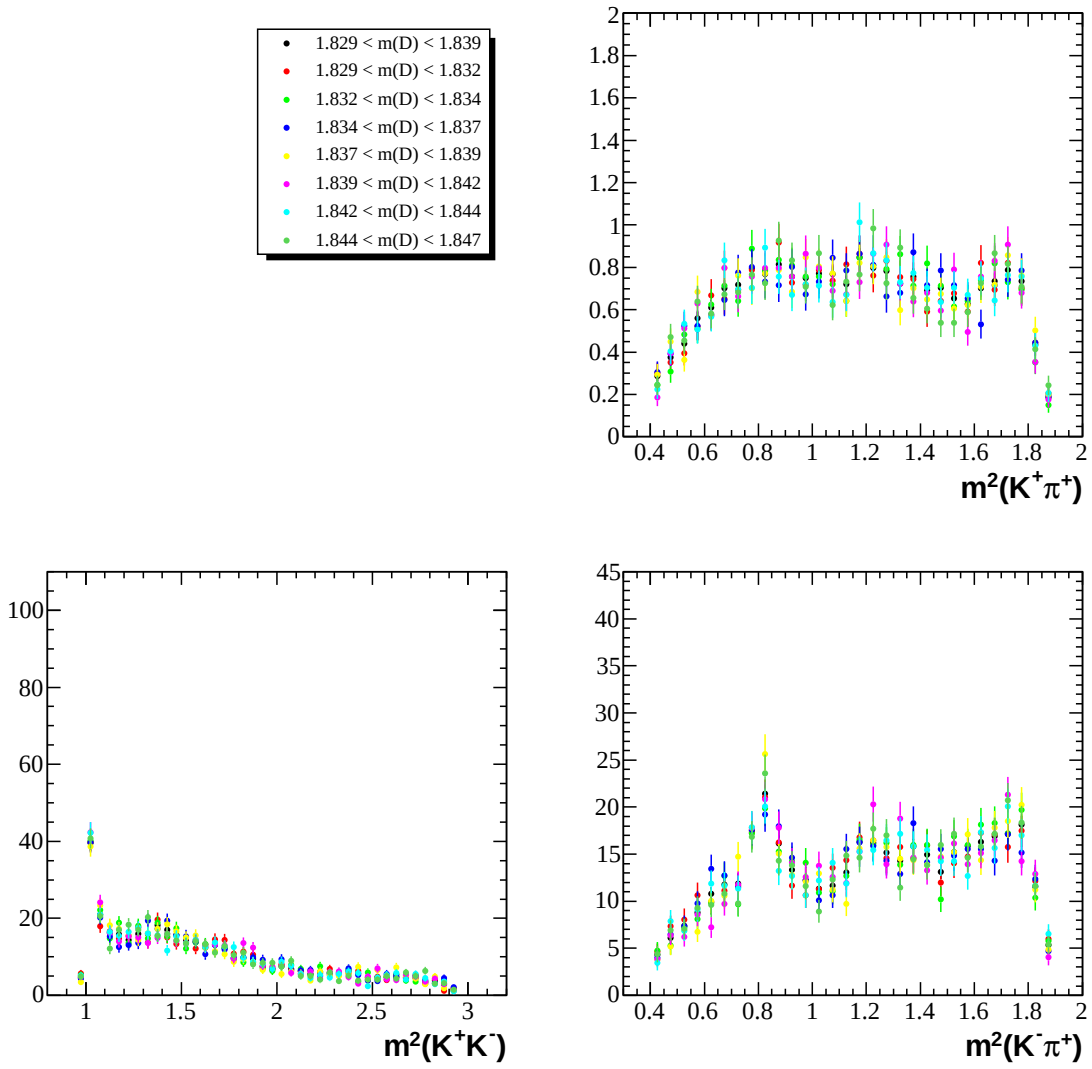

Figure 5.6: Normalized D low mass sideband region Dalitz plot projections of background events in slices of the D mass. The black points representa 2σ mass, while the remaining points are taken from 0.5σ mass regions.

Since the MC description of the data may not be perfect, we float the fractions of each pdf incoherently in our fit to sideband data and report the results in Table 5.3, Table 5.4, Table 5.5, and Table 5.6.

The results of the fits are shown in Figure 5.9, Figure 5.10, Figure 5.11, and Figure 5.12. The $\chi^2/ndof$ for the fits varies between 1.2 and 1.4. We find this unacceptably high; also, we find that the fit fractions are considerably different from the MC which further calls this model into question.

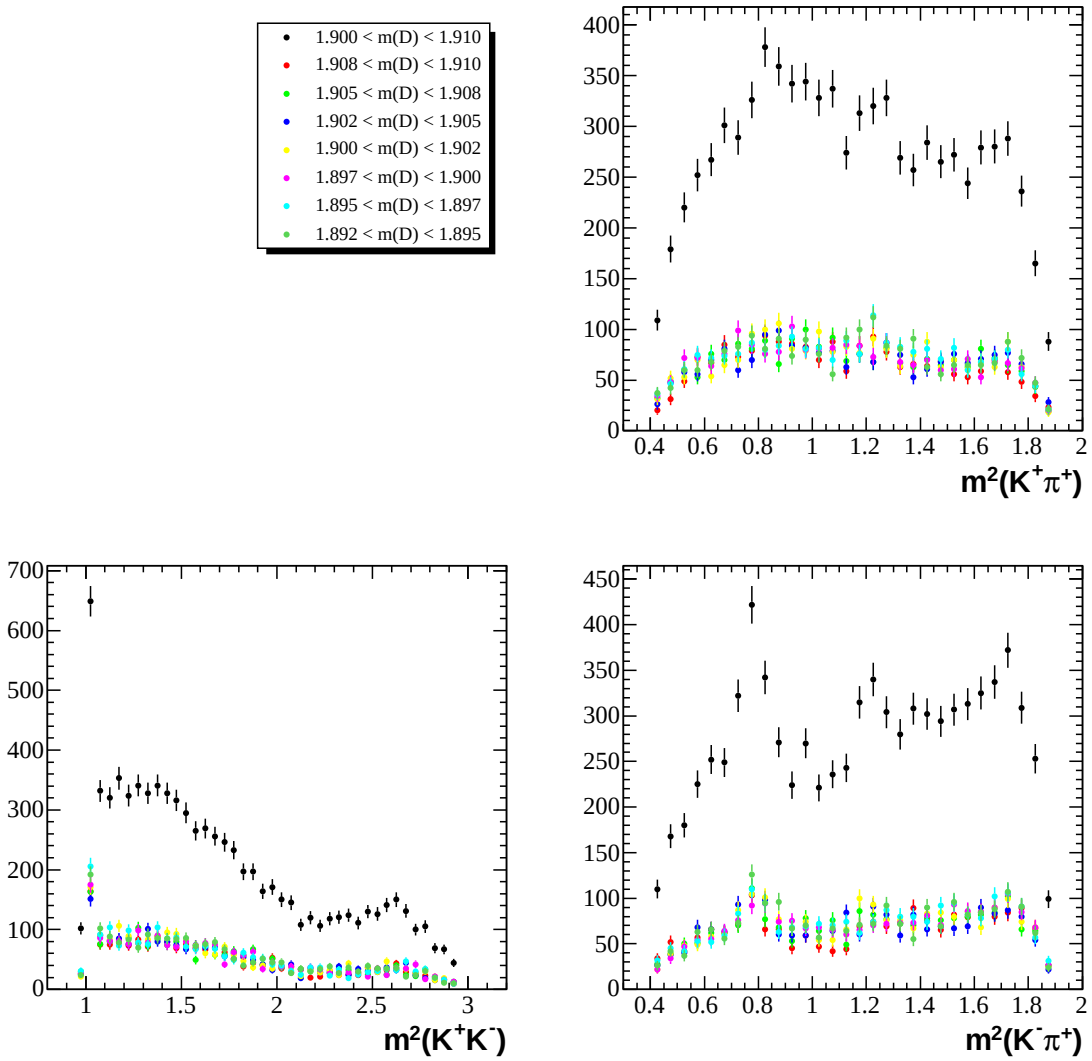

Figure 5.7: Unnormalized D high mass sideband region Dalitz plot projections of background events in slices of the D mass. The black points represent a 2σ mass, while the remaining points are taken from 0.5σ mass regions.

The sideband regions used in our fits are 2σ on the lower and upper mass regions, and since the D mass dependence is linear (determined from the integrated mass fit) we take the sum of the lower and upper parameter as the number of events corresponding to a given background pdf. We combine R24 and R26 generic Monte Carlo for $c\bar{c}$ and $b\bar{b}$ events to increase the statistics of the background. The data set for *uds* Monte Carlo is R24 only. The fit results is shown in Figure 5.13.

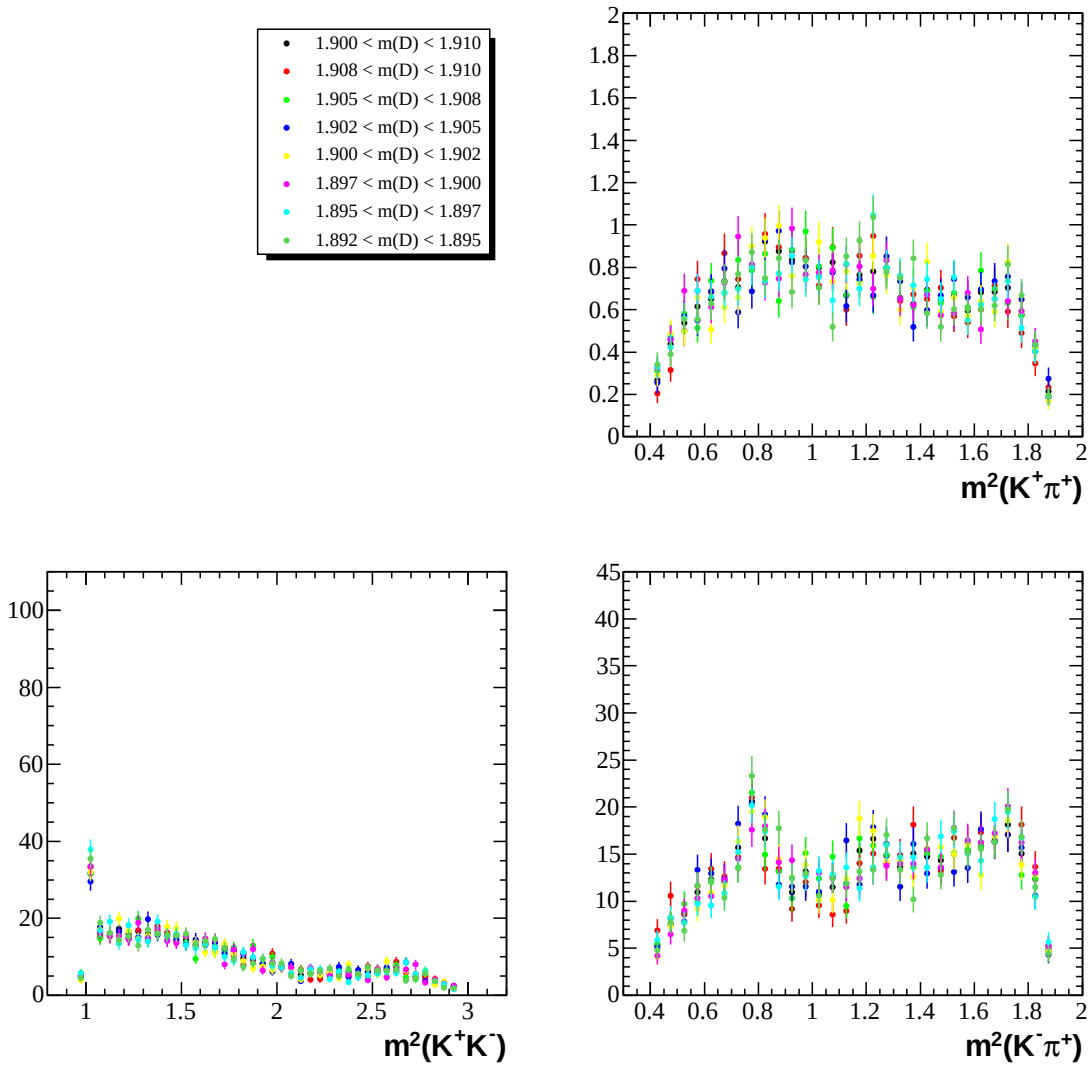

Figure 5.8: Normalized D high mass sideband region Dalitz plot projections of background events in slices of the D mass. The black points representa 2σ mass, while the remaining points are taken from 0.5σ mass regions.

To further clarify the difference in the generic Monte Carlo composition before and after the fit, we show the Dalitz plot projections with the contributions from each pdf stacked (Figure 5.14 and Figure 5.15. The backgrounds generated in the BaBar Monte Carlo do not accurately model either the overall normalization or the shape of the background.

MC background pdf	Fraction in MC (%)	Fraction in data after fit (%)
uds(other)	6.78	4.53
uds($\bar{K}^*(892)$	4.78	2.15
uds($\phi(1020)$	5.89	8.69
$c\bar{c}(D^+)$	12.77	13.55
$c\bar{c}(D_s)$	6.82	2.58
$c\bar{c}(D^0)$	12.96	6.82
$c\bar{c}(\bar{K}^*)$	9.06	18.76
$c\bar{c}(\phi(1020))$	9.21	11.94
$c\bar{c}$(other)	22.54	23.29
B^+B^-	5.28	0.00
$B^0\bar{B}^0$	3.91	7.71

Table 5.3: Fractions of pdfs in the background from MC and after a fit to the D^+ lower data sidebands.

MC background pdf	Fraction in MC (%)	Fraction in data after fit (%)
uds(other)	6.79	3.13
uds($\bar{K}^*(892)$	4.40	4.33
uds($\phi(1020)$	5.43	9.33
$c\bar{c}(D^+)$	13.36	8.05
$c\bar{c}(D_s)$	10.98	10.12
$c\bar{c}(D^0)$	13.82	25.07
$c\bar{c}(\bar{K}^*)$	7.32	10.44
$c\bar{c}(\phi(1020))$	6.91	10.00
$c\bar{c}$(other)	21.64	19.52
B^+B^-	5.59	0.00
$B^0\bar{B}^0$	3.77	0.00

Table 5.4: Fractions of pdfs in the background from MC and after a fit to the D^+ upper data sidebands.

5.2.6.2. *Alternative Models to the Monte Carlo.* As an alternative to the Monte Carlo as a description of the background, we fit the sideband data using a phenomenological model and a multivariate density estimator. The details of the phenomenological model may be found in section 5.6.4 and the k nearest-neighbor algorithm (kNN) in appendix **??**.

In brief, the phenomenological (parametric) model for the background is comprised of several resonances, such as the $\phi(1020)$ and $\bar{K}^{*0}$. In addition we allow for

MC background pdf	Fraction in MC (%)	Fraction in data after fit (%)
uds(other)	5.77	2.53
uds($\bar{K}^*(892)$	4.97	0.00
uds($\phi(1020)$	5.60	4.49
$c\bar{c}(D^+)$	12.85	0.00
$c\bar{c}(D_s)$	6.81	12.80
$c\bar{c}(D^0)$	13.06	21.84
$c\bar{c}(\bar{K}^*)$	9.28	17.62
$c\bar{c}(\phi(1020))$	9.45	12.32
$c\bar{c}$(other)	22.76	20.08
B^+B^-	5.42	0.00
$B^0\bar{B}^0$	4.03	8.33

Table 5.5: Fractions of pdfs in the background from MC and after a fit to the D^- lower data sidebands.

MC background pdf	Fraction in MC (%)	Fraction in data after fit (%)
uds(other)	6.35	0.00
uds($\bar{K}^*(892)$	4.44	6.67
uds($\phi(1020)$	5.31	9.81
$c\bar{c}(D^+)$	13.90	0.00
$c\bar{c}(D_s)$	11.08	15.02
$c\bar{c}(D^0)$	13.99	30.18
$c\bar{c}(\bar{K}^*)$	7.16	0.40
$c\bar{c}(\phi(1020))$	6.80	5.89
$c\bar{c}$(other)	21.57	17.87
B^+B^-	5.71	4.58
$B^0\bar{B}^0$	3.70	9.60

Table 5.6: Fractions of pdfs in the background from MC and after a fit to the D^- upper data sidebands.

resonances to interfere if they decay to the same final-state particles. The following resonances are included in the amplitude: $\phi(1020)$, $f_0(980)$, $f_0(1370)$, $f_0(1710)$, $\bar{K}^{*0}(892)$, and $\bar{K}^{*0}(1430)$. The total amplitude squared is

$$\begin{aligned} |A|^2 =& |A_{\phi(1020)}e^{i\phi_{\phi(1020)}}|^2 + \\ & |A_{f_0(980)}e^{i\phi_{f_0(980)}} + A_{f_0(1370)}e^{i\phi_{f_0(1370)}} + A_{f_0(1710)}e^{i\phi_{f_0(1710)}}|^2 + \\ & |A_{\bar{K}^{*0}(892)}e^{i\phi_{\bar{K}_{*0}(892)}} + A_{\bar{K}^{*0}(1430)}e^{i\phi_{\bar{K}^{*0}(1430)}}|^2 \end{aligned} \tag{5.2.1}$$

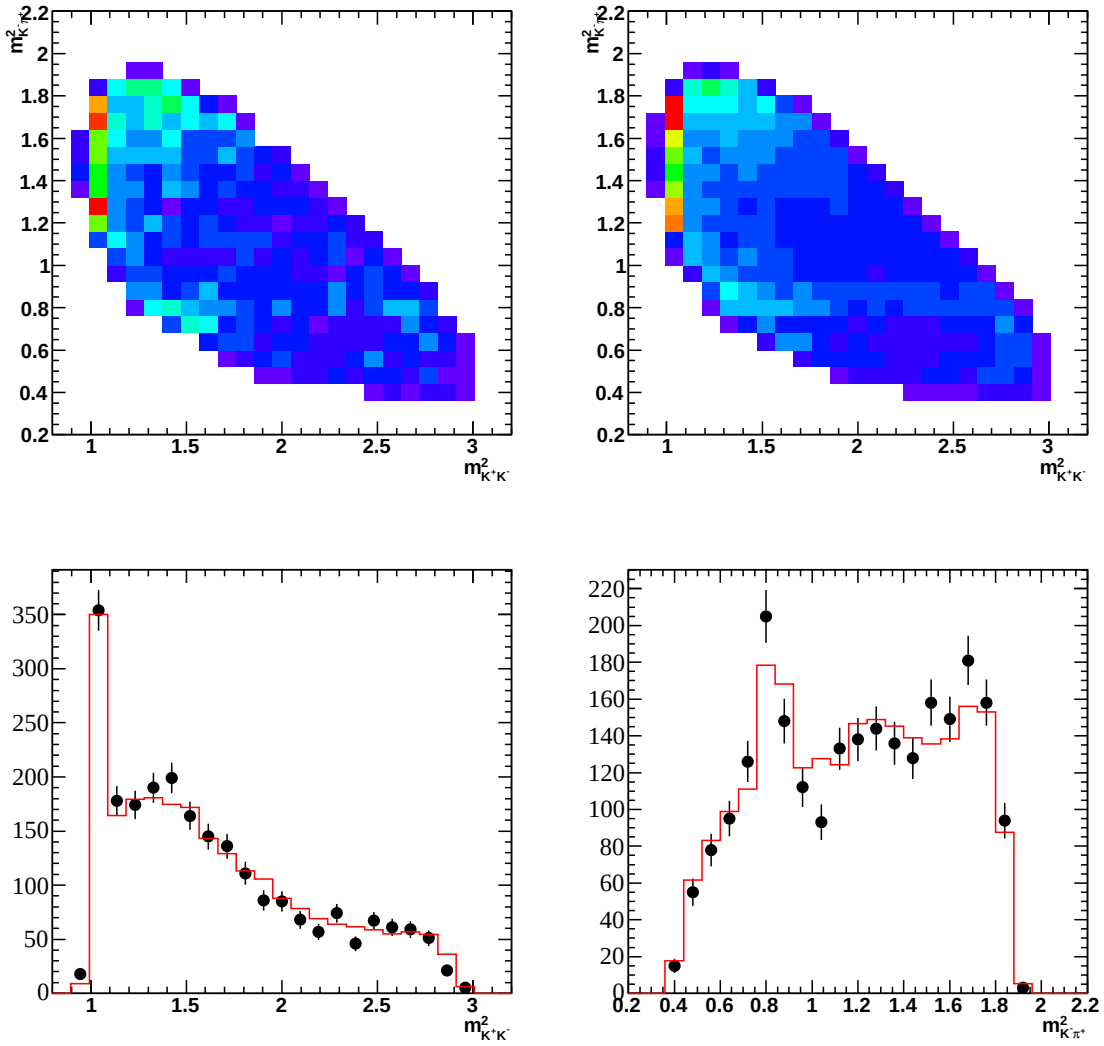

Figure 5.9: Fit results to validation sample of low mass sideband for D^+ events. The upper left plot is the data. The upper right plot is the Monte Carlo model fit result. The bottom plots show the corresponding projections of the Dalitz plot. Data are the black points, and the fit result is the red histogram.

with the magnitude and phase of $\bar{K}^{*0}$ fixed to 1,0. Due to the mass constraint imposed on the data, the dominant resonant masses are shifted by several MeV. We float the $\phi(1020)$ and $\bar{K}^{*0}$ masses in the fit and minimize the likelihood function

$$-2\ln\mathcal{L} = -2\sum_{i=1}^{N_{fit}} \ln\left(\frac{B(x_i,y_i)}{\iint B(x_i,y_i)\mathrm{d}x\mathrm{d}y}\right). \tag{5.2.2}$$

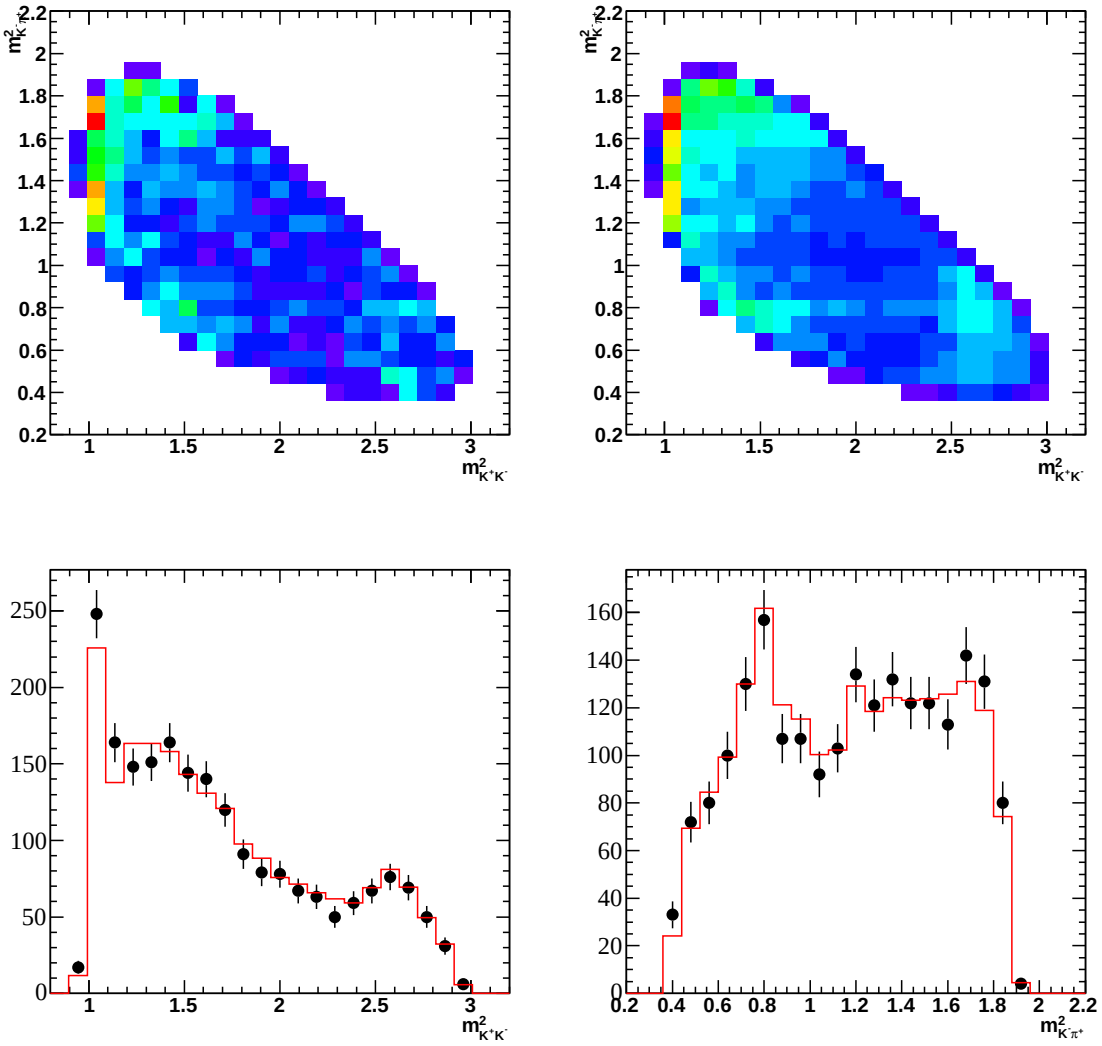

Figure 5.10: Fit results to validation sample of high mass sideband for D^+ events. The upper left plot is the data. The upper right plot is the Monte Carlo model fit result. The bottom plots show the corresponding projections of the Dalitz plot. Data are the black points, and the fit result is the red histogram.

The kNN model is a non-parametric model, based on multivariate kernel estimate techniques [**34**], which measures the density of a given data set by searching for k neighbors within a hyper-sphere of a given radius. The only parameter in the model is the number of nearest neighbors, k, to a given data point within the hyper-sphere.

To fit the sideband samples, the events are randomly split into a fitting and validation sample. We measure the χ^2 of the model and the validation sample with

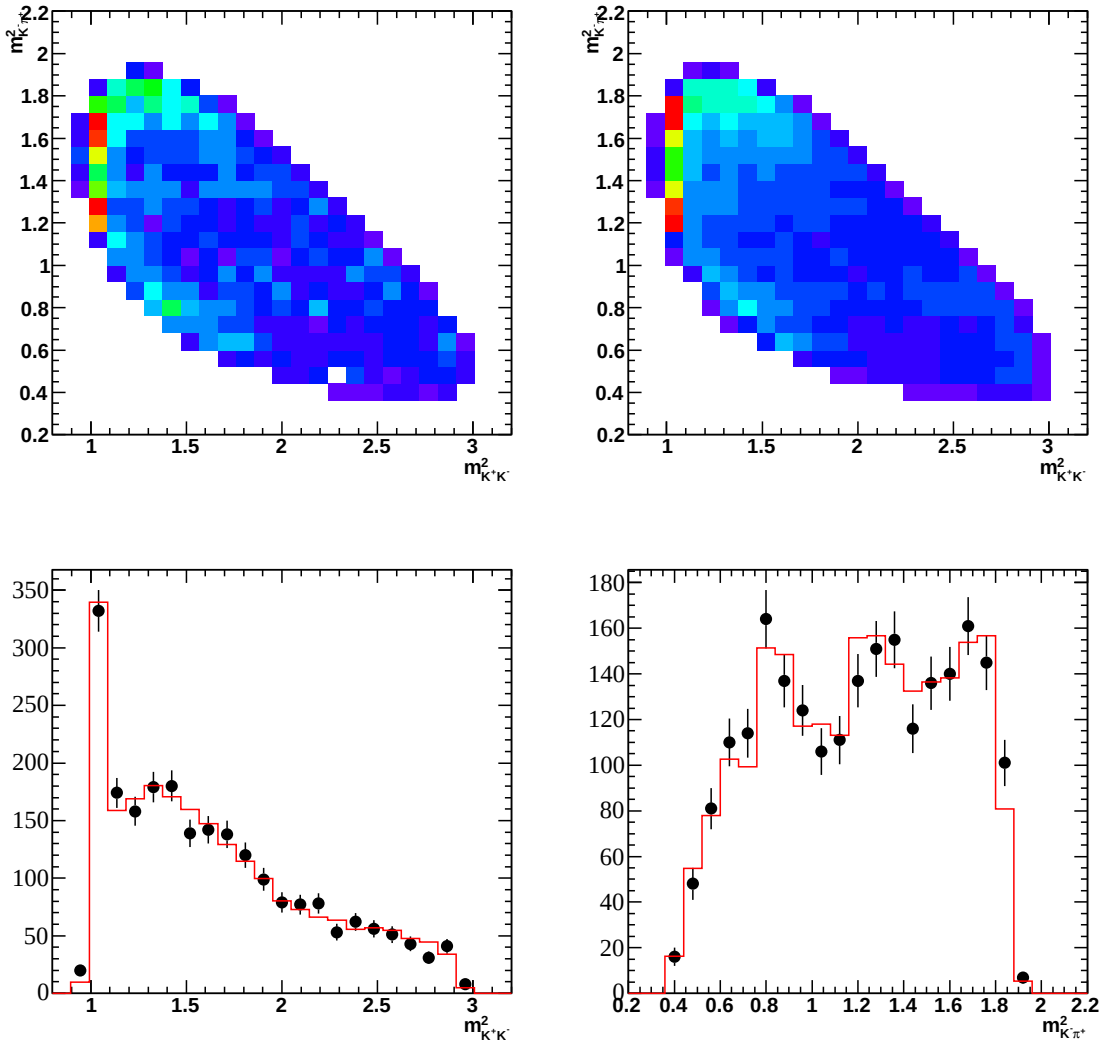

Figure 5.11: Fit results to validation sample of low mass sideband for D^- events. The upper left plot is the data. The upper right plot is the Monte Carlo model fit result. The bottom plots show the corresponding projections of the Dalitz plot. Data are the black points, and the fit result is the red histogram.

25 equally populated bins [**33**]. The χ^2 (Table 5.7) is smaller for the kNN which has only one parameter, k, the number of nearest neighbors.

$$\chi^2 = \sum_{i=1}^{Nbins} \frac{(N_i^{obs} - N_i^{pred})^2}{N_i^{pred}} \tag{5.2.3}$$

where N_i^{pred} is the number of predicted events from our model for a given bin i determined from integrating the model over the bin limits

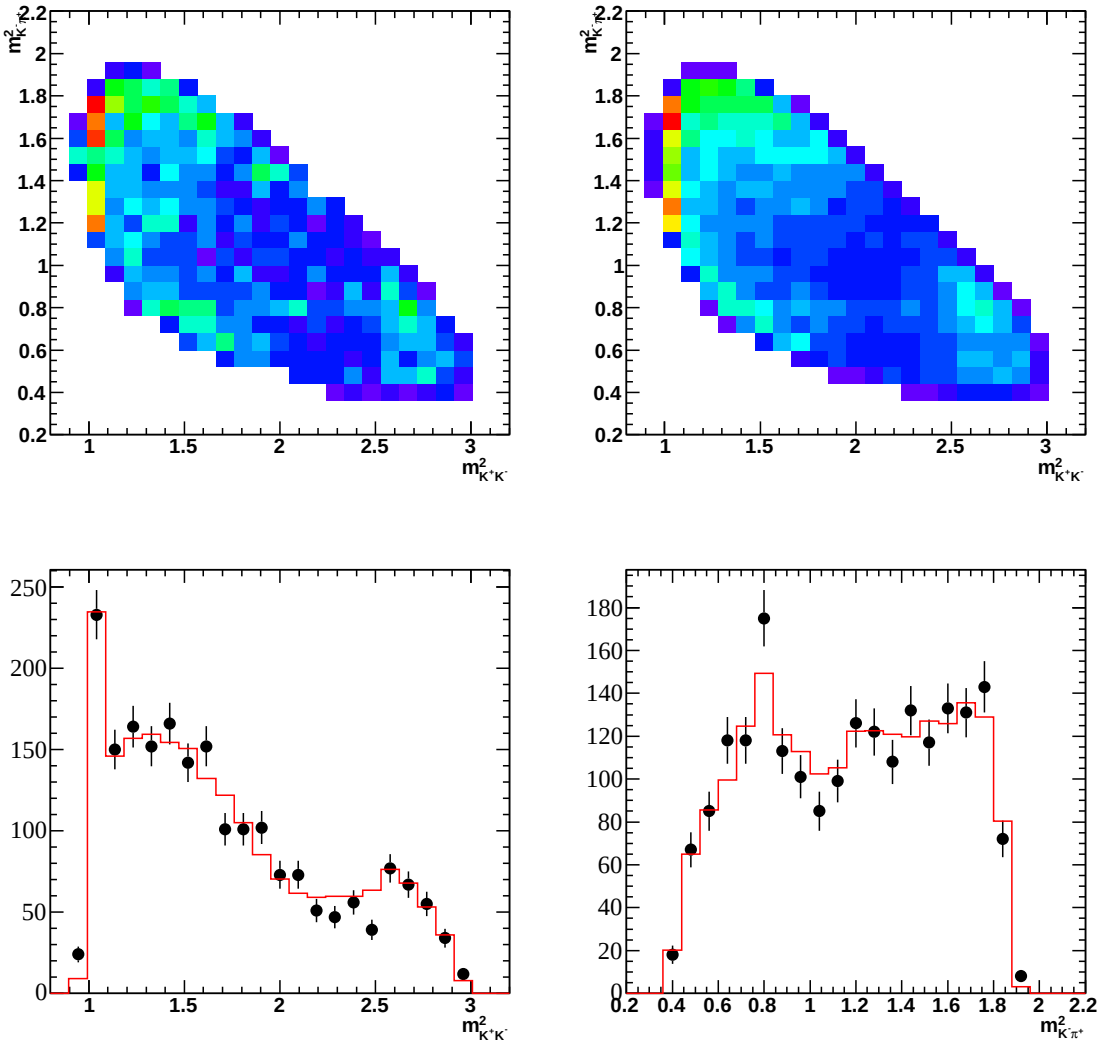

Figure 5.12: Fit results to validation sample of high mass sideband for D^- events. The upper left plot is the data. The upper right plot is the Monte Carlo model fit result. The bottom plots show the corresponding projections of the Dalitz plot. Data are the black points, and the fit result is the red histogram.

$$N_i^{pred} = \iint \mathrm{d}x\mathrm{d}y B(x,y). \tag{5.2.4}$$

5.2.6.3. *3-region Background Model.* The models described previously do not provide an accurate description over the entire region of the Dalitz plot. Our final approach was to fit sidebands using unconstrained masses in the $\phi(1020)$ and $\bar{K}^{*0}(892)$ regions with a constrained kNN model used for the rest of the Dalitz plot.

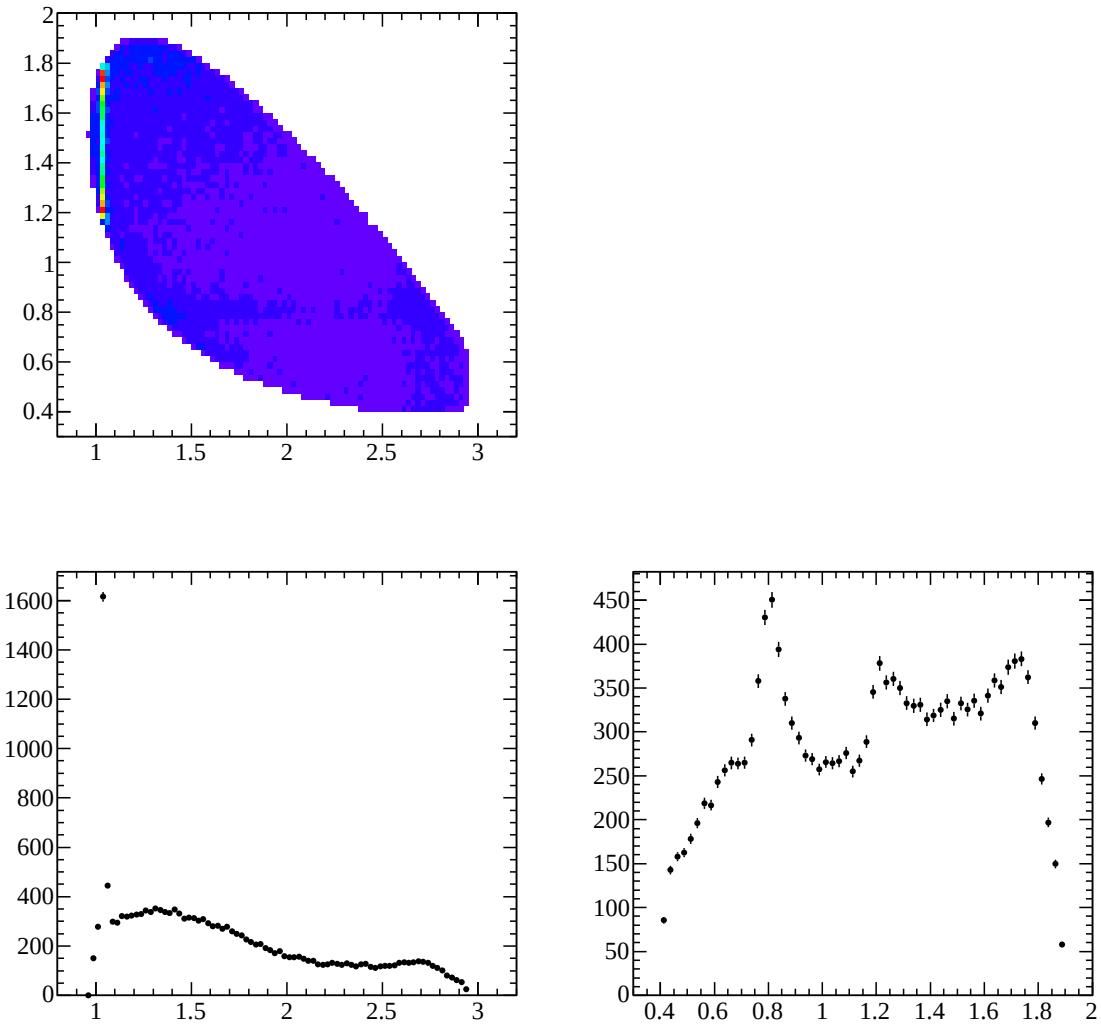

Figure 5.13: Background model and projections that results from the fit.

Model	Sideband	χ^2	Ndof
Dalitz	Low	69.96	11
kNN	Low	64.16	24
Dalitz	High	45.36	11
kNN	High	38.34	24

Table 5.7: Comparison of goodness-of-fit of sideband data fit with a phenomelogical model and kNN.

This has the advantage that the resonance regions are described by data shapes without the shifting of resonance masses that occurs with a D mass constraint. The

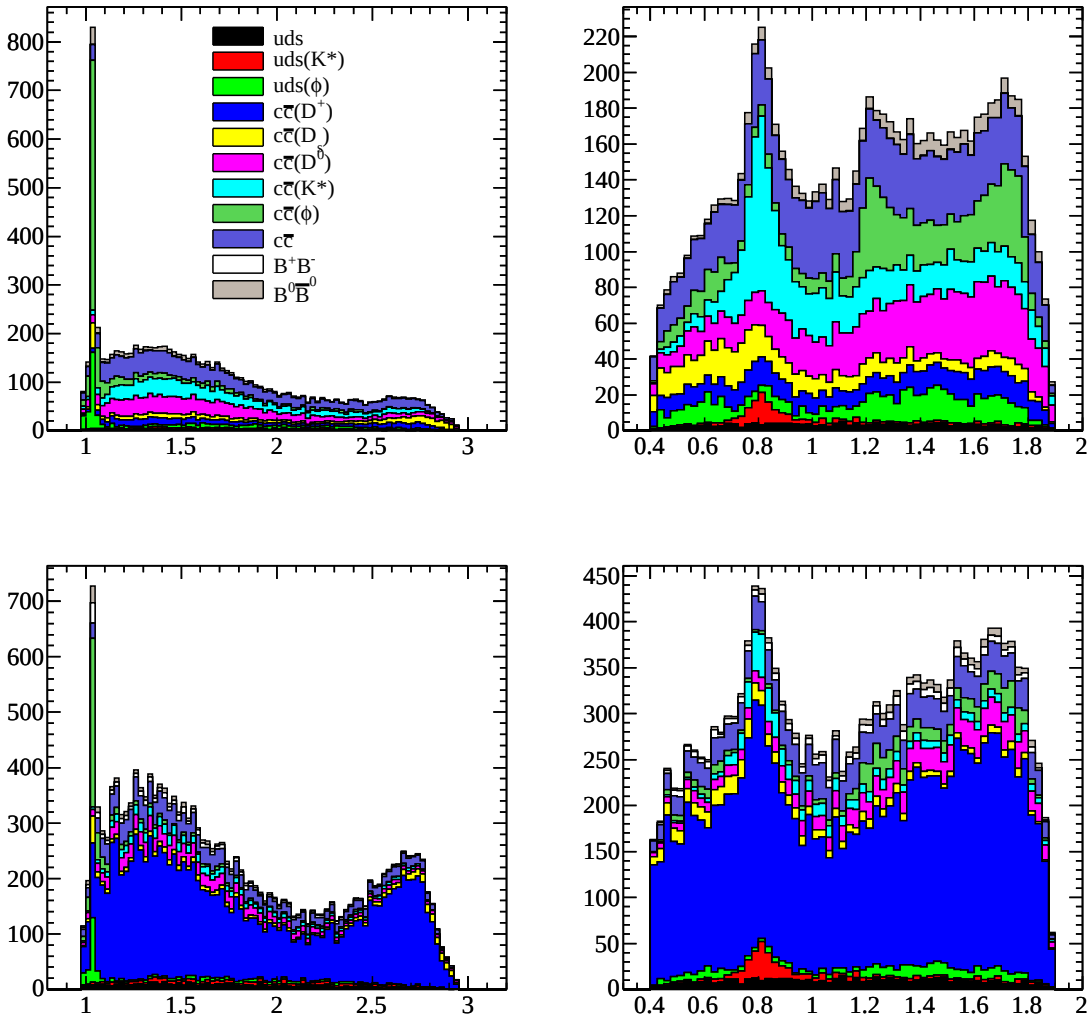

Figure 5.14: D^+ Dalitz plot projections for m_{KK} (left) and $m_{K\pi}$ (right) for the MC (top) and after the fit to the data (bottom).

rest of the Dalitz plot shows no sharp structures and is more easily described by constrained mass variables.

In the region of the $\phi(1020)$ and $\bar{K}^{*0}(892)$ we fit the "square Dalitz plot" (mass and $\cos(\theta)_{Helicity}$) region with a fit function described below. The model consists of a Breit-Wigner(BW) and a constant plus linear (BG) term in mass times a sum of Legendre polynomials plus a term linear in $\cos(\theta)_{Helicity}$. The additional term in $\cos(\theta)_{Helicity}$ allows for any forward-background asymmetry. We fit the combined data of the upper and lower sideband D mass regions, selecting events which lie

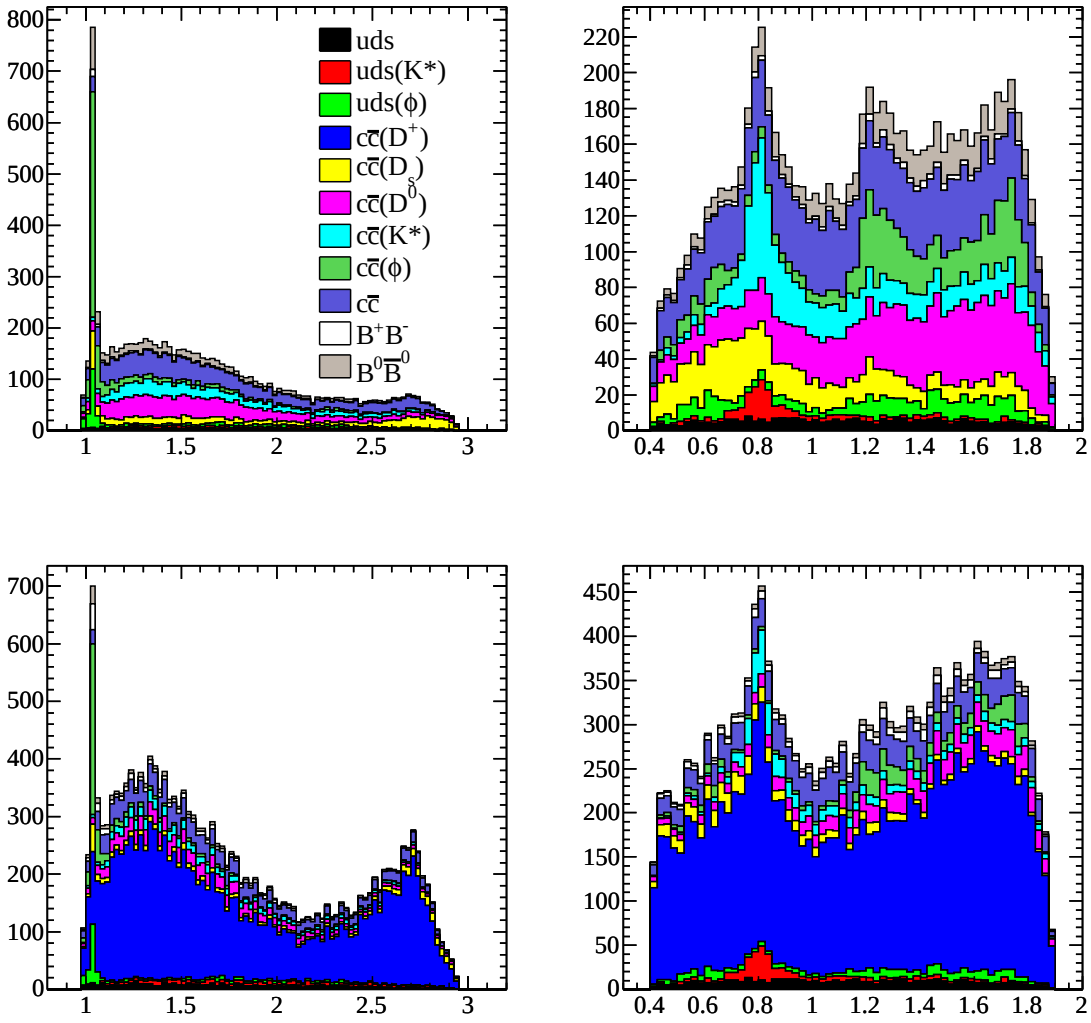

Figure 5.15: D^- Dalitz plot projections for m_{KK} (left) and $m_{K\pi}$ (right) for the MC (top) and after the fit to the data (bottom).

within 2σ of the PDG mass of the ϕ and the $\bar{K}^{*0}$. In the case of the $\bar{K}^{*0}$ region, the coefficients of the Legendre polynomials and the mass terms are the same. However, this does not work for the $\phi(1020)$ and so we allow the coefficients to be different in this case. The masses and widths of the ϕ and $\bar{K}^{*0}$ are floated in the fit. A penalty term is added to the likelihood function when floating the resonant masses and widths; this term constrains these quantities to be consistent with the PDG. The MINUIT fit results are found in appendix K.

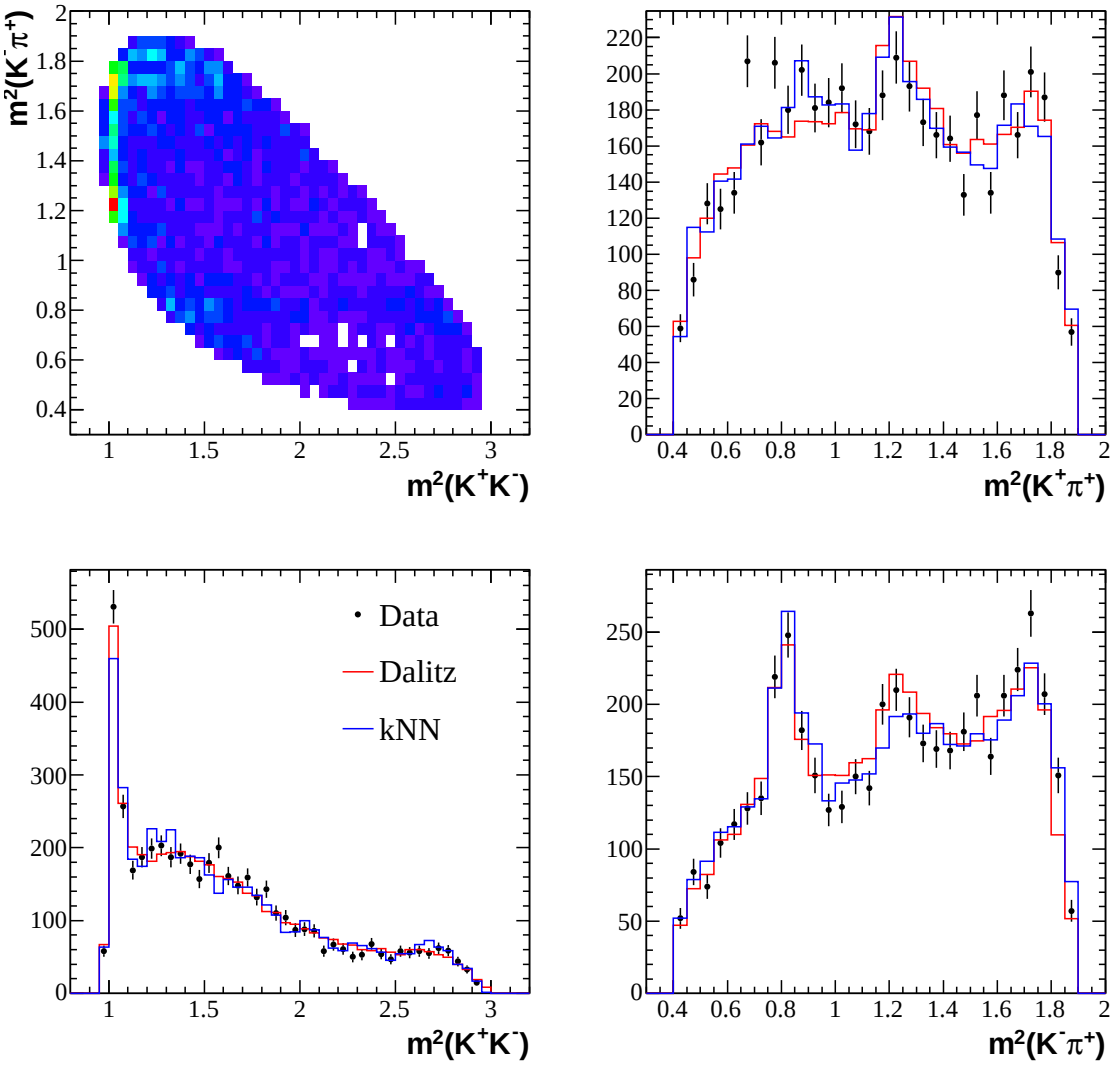

Figure 5.16: $D^{\pm}$ Dalitz plot projections for each background fitted to the data.

$$|A_{BW}|^2 = \frac{\Gamma}{(m_{KK,K\pi} - m_{\phi,\bar{K}^{*0}})^2 + (\Gamma/2)^2} \tag{5.2.5}$$

$$P_0 = 1 \tag{5.2.6}$$

$$P_1 = \cos(\theta)_{Helicity} \tag{5.2.7}$$

$$P_2 = \frac{3\cos^2(\theta)_{Helicity} - 1}{2} \tag{5.2.8}$$

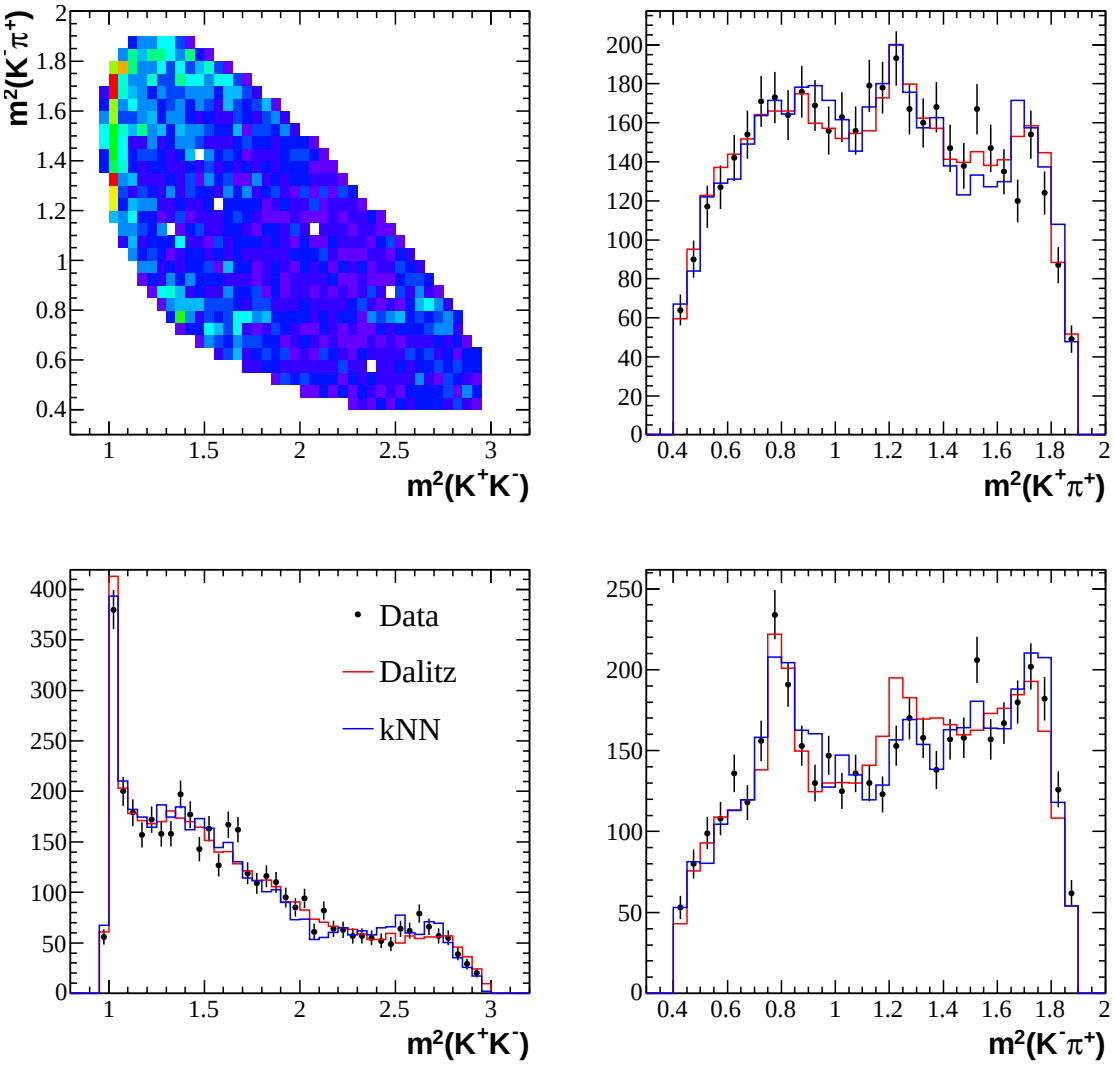

Figure 5.17: $D^{\pm}$ Dalitz plot projections for each background fitted to the data.

$$BW = \left[\frac{|A_{BW}|^2}{\int |A_{BW}|^2 dm}\right] \frac{P_0^2 + bw_{11}P_1^2 + bw_{22}P_2^2 + bw_{01}P_0P_1 + bw_{02}P_0P_2 + bw_{21}P_2P_1 + bw_{\cos(\theta)}\cos(\theta)}{2(1 + bw_{11}/3 + bw_{22}/5)} \tag{5.2.9}$$

$$BG = \left[\frac{1}{\int dm} + a(m - m_{\phi,\bar{K}^{*0}})\right] \frac{P_0^2 + p_{11}P_1^2 + p_{22}P_2^2 + p_{01}P_0P_1 + p_{02}P_0P_2 + p_{21}P_2P_1 + p_{\cos(\theta)}\cos(\theta)}{2(1 + p_{11}/3 + p_{22}/5)} \tag{5.2.10}$$

$$\chi^2_{penalty} = \frac{(m_R - m_R^{PDG})^2}{(\Delta m_R^{PDG})^2} + \frac{(\Gamma_R - \Gamma_R^{PDG})^2}{(\Delta \Gamma_R^{PDG})^2} \tag{5.2.11}$$

$$-2\ln\mathcal{L} = -2\left[\sum_{i=1}^{N_{fit}} \ln(N_{BW}BW + N_{BG}BG) - (N_{BW}+N_{BG})\right] + \frac{[(N_{BW}+N_{BG}) - N_{fit}]^2}{N_{BW}+N_{BG}} + \chi^2_{penalty} \tag{5.2.12}$$

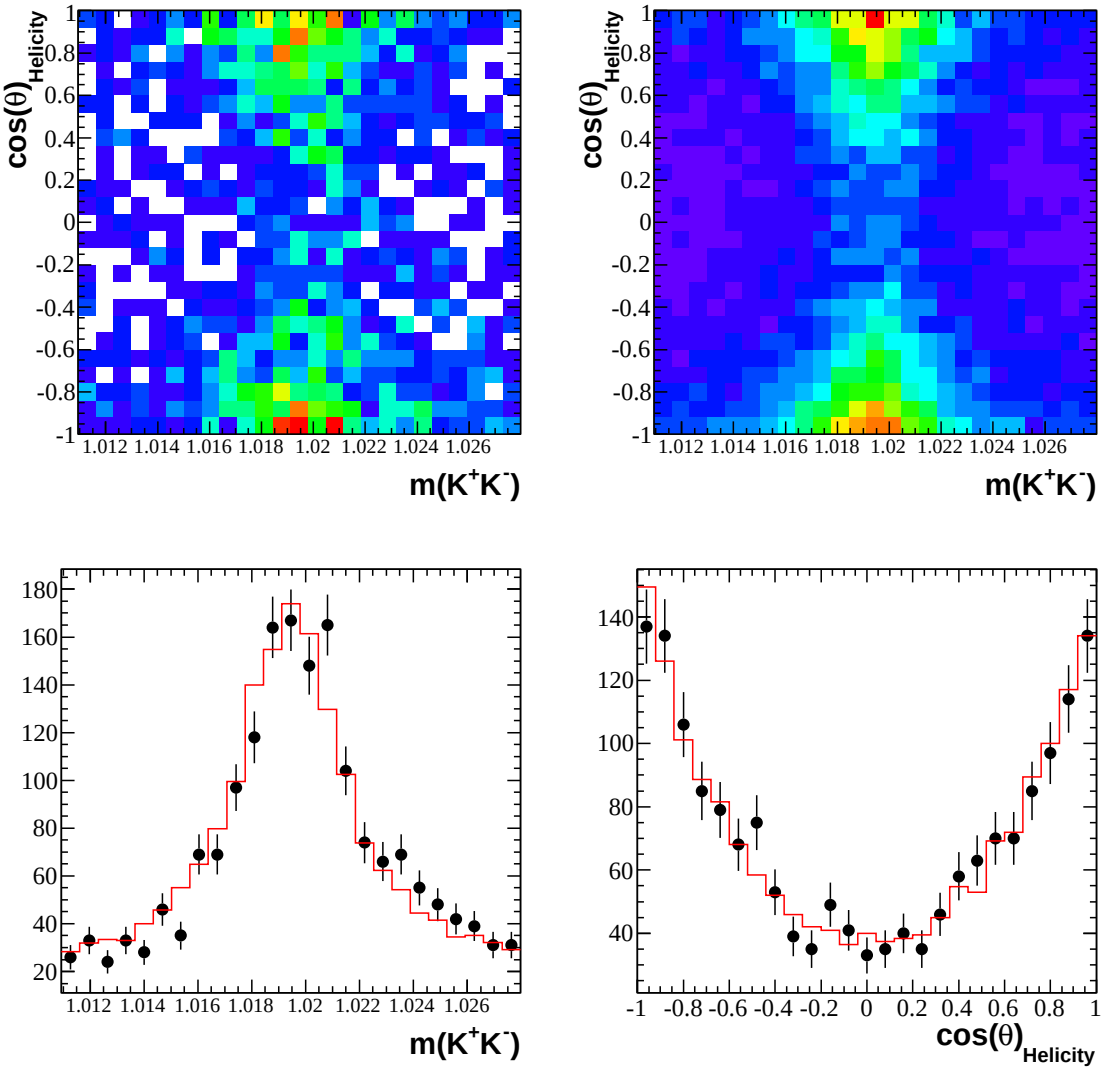

Figure 5.18: Square Dalitz plot of combined sideband data within 2σ of the ϕ mass (top left). No mass constraint is imposed on the data, therefore, the fitted mass of the ϕ is close to the PDG value, 1.01947 ± 0.00002 GeV. The upper right plot is the square dalitz plot of generated events (10X data) of the fitted model. Projections are shown in the bottom plots, where the data is indicated with black points and error bars, while the model is shown as a red histogram. The coefficients of the Legendre polynomials are floated for the background term (BG) and the Breit-Wigner term (BW).

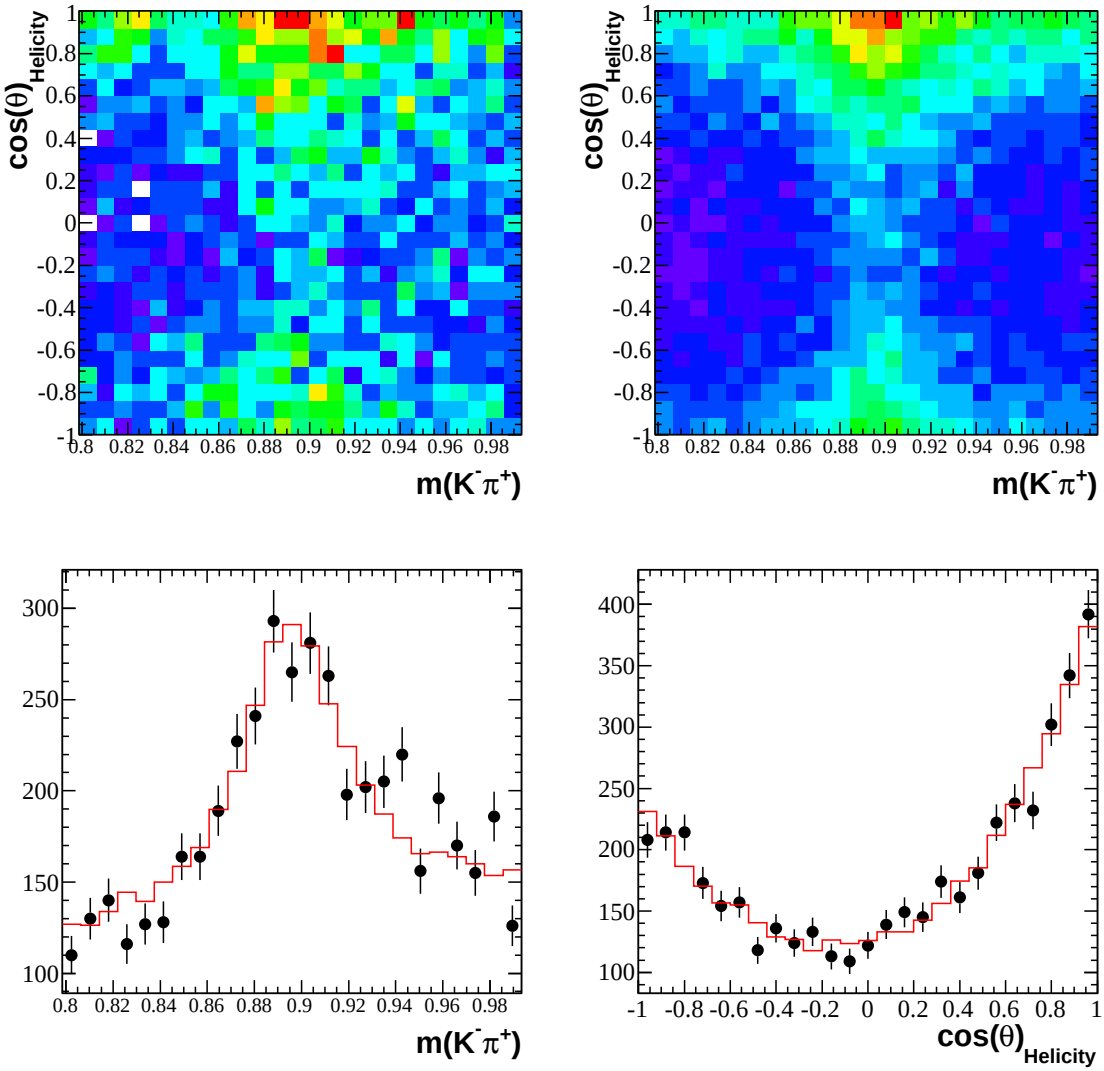

Figure 5.19: Square Dalitz plot of combined sideband data within 2σ of the $\bar{K}^{*0}$ mass (top left). No mass constraint is imposed on the data, therefore, the fitted mass of the $\bar{K}^{*0}$ is close to the PDG value, 0.896016 ± 0.00022 GeV. The upper right plot is the square dalitz plot of generated events (10X data) of the fitted model. Projections are shown in the bottom plots, where the data is indicated with black points and error bars, while the model is shown as a red histogram. The coefficients of the Legendre polynomials are common to the background term (BG) and the Breit-Wigner (BW) term.

5.3. Reconstruction Efficiency

In this section we describe the components of the reconstruction efficiency function used in the Dalitz plot fit. This function derives from the phase space Monte Carlo and is parameterized using a neural net as described below. The efficiency

from the MC is first obtained as a binned (21x21) histogram. The events in this histogram are weighted by the product of two ratios: a ratio of production distributions (data/MC in 10x10 bins of $p^* \times \cos\theta^*$) and of tracking efficiencies (which are functions of lab momenta only, but include charge asymmetry) obtained as described in a subsection below.

5.3.1. Dalitz Plot Efficiency. Our measurement of the CP asymmetry is a function of the Dalitz plot position; therefore we require that our reconstruction efficiency be known as a function of the Dalitz plot position. Since the efficiency varies slowly over the Dalitz plot, an articial neural network (ANN) is used to provide a precise determination of the efficiency as a function of the Dalitz plot position. Here we use the ANN to approximate the efficiency as a continuous function using a linear combination of sigmoid functions.

We estimate the efficiency in 441 bins over the Dalitz plot, using 24 million generated events for both D^+ and D^-. The estimated efficiency at the bin centers provide the artifical neural network an output target value which is required to be a softmax function. The resulting function as a position of the Dalitz plot position has a value between 0 and 1. To train and test the neural network, the ROOT class TMultiLayerPerceptron [**42**] is used. The training and testing sample input values and output efficiencies are determined first from randomly splitting the Monte Carlo sample.

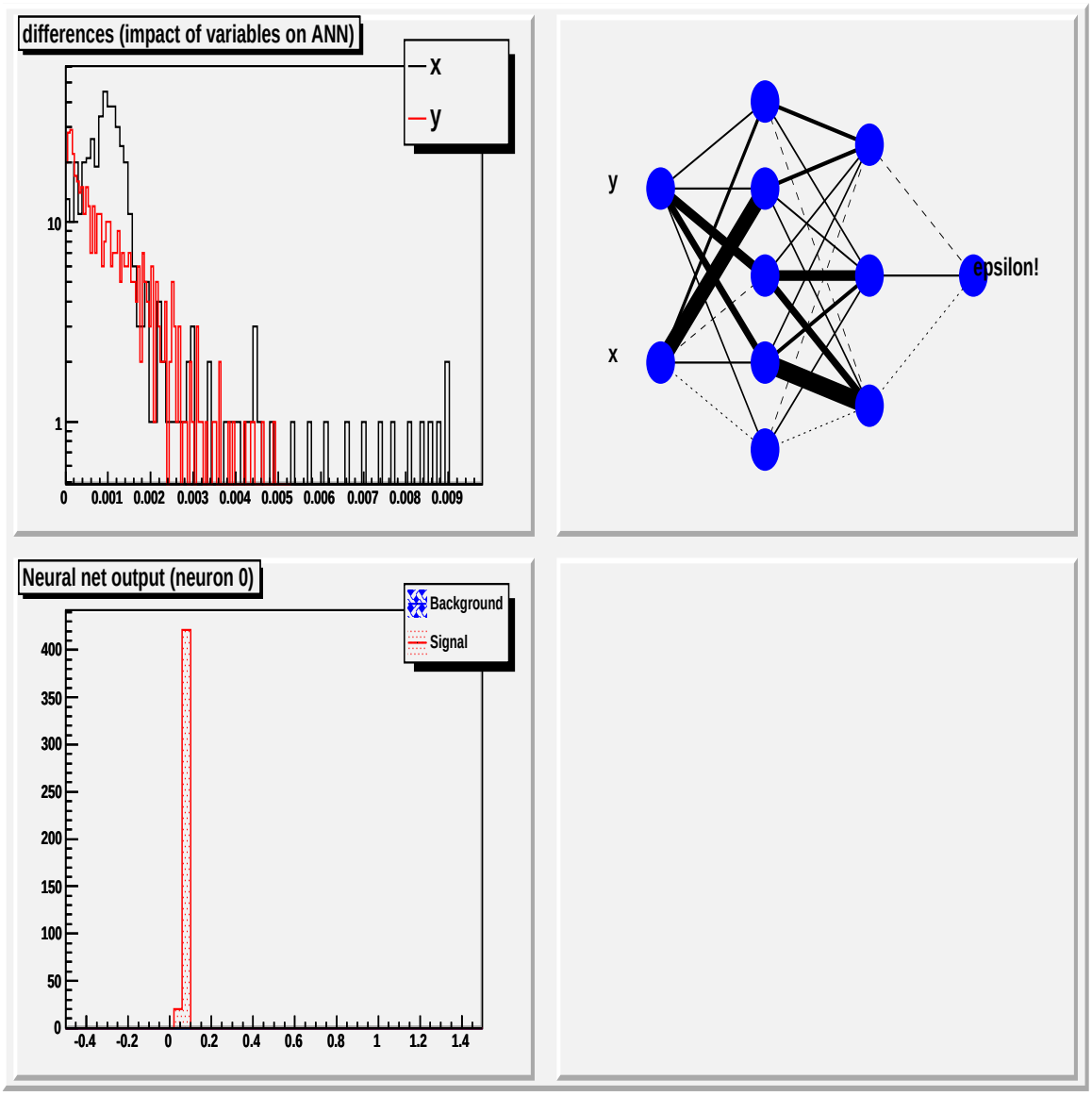

Figure 5.20: The plots are produced from TMultiLayerPerceptronAnalyzer. D^+ MultiLayerPerceptron input variables and architecture. The input variables x and y correspond to the Dalitz plot variables $m^2(K^+K^-)$ and $m^2(K^-\pi^+)$.

5.3.2. Tracking Efficiency. The overall reconstruction efficiency is a product of tracking efficiency for each daughter track of the D meson, vertexing efficiency, detector acceptance, and the remaining efficiency is due to candidate selection. The tracking efficiency is known from data [**37**], The final results of the study are shown in Figure 5.24. the remaining efficiencies are taken from the Monte Carlo.

$$\epsilon_{MC} = \epsilon(\overrightarrow{p}_{K_1})\epsilon(\overrightarrow{p}_{K_2})\epsilon(\overrightarrow{p}_{\pi})\epsilon_{Vertex}A\epsilon_{other}(\overrightarrow{p}_{K_1}, \overrightarrow{p}_{K_1}, \overrightarrow{p}_{\pi}) \tag{5.3.1}$$

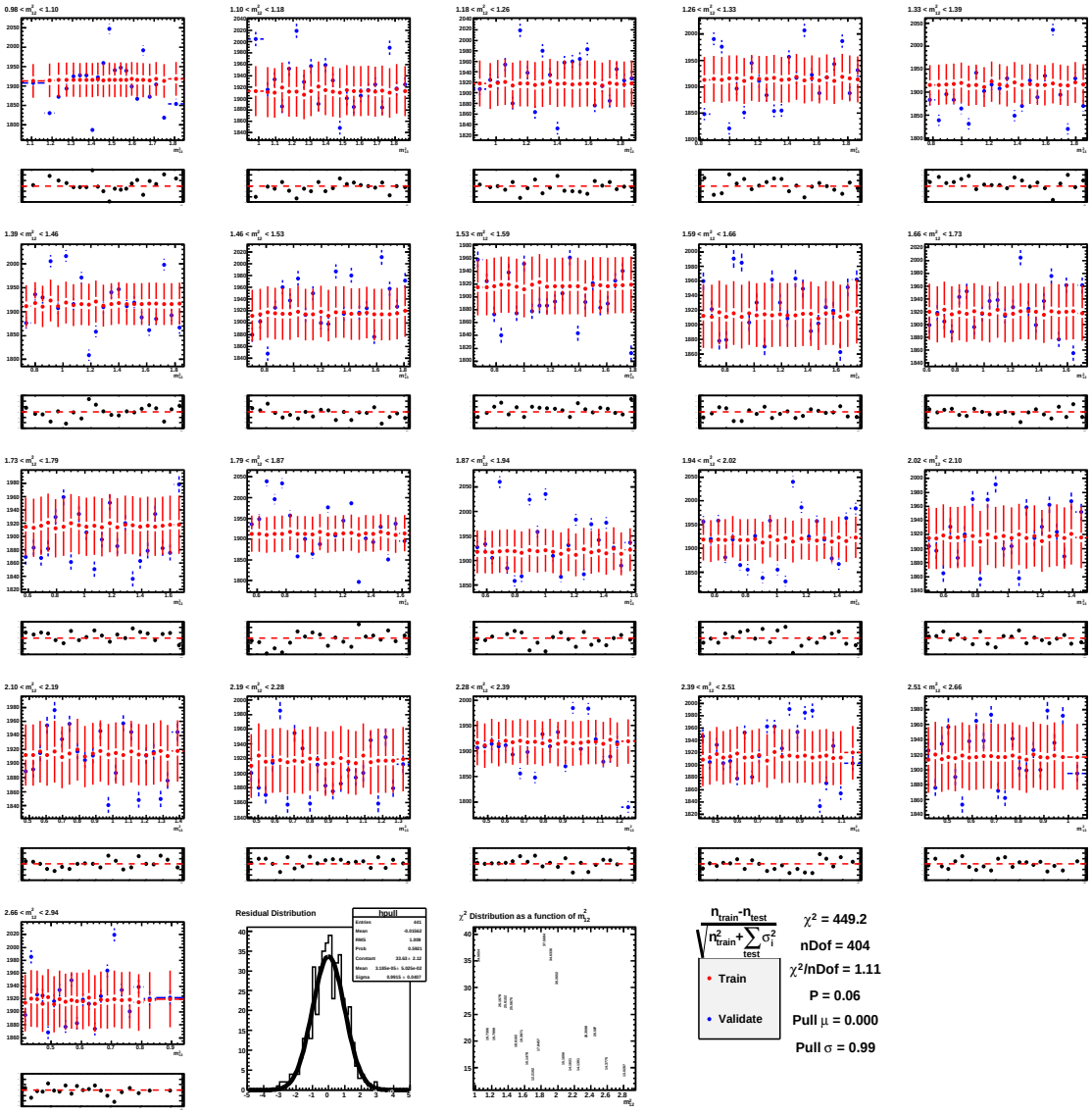

Figure 5.21: D^+ MultiLayerPerceptron Validation. A χ^2 test is performed over 441 bins. The histograms are in bins of $m^2(K^+K^-)$ and are functions of the $m^2(K^-\pi^+)$. The normalized residual distribution with a Gaussian fit is obtained.

In this section we describe detailed studies of tracking efficiencies and vertexing probabilities as a function of the Dalitz plot position. The tracking efficiency as a function of Dalitz plot position (Figure 5.25) is determined by weighting phase-space MC events with the product of the daughter track efficiencies, $\epsilon(\overrightarrow{p}_{K_1})\epsilon(\overrightarrow{p}_{K_2})\epsilon(\overrightarrow{p}_{\pi})$, which are known from Figure 5.24. The projections in $m^2(K^+K^-)$ and $m^2(K^-\pi^+)$ are flat. We find the ratio of the tracking efficiency and the overall reconstruction efficiency, $\epsilon_{Reconstruction}/\epsilon_{Tracking}$, shown in Figure 5.26.

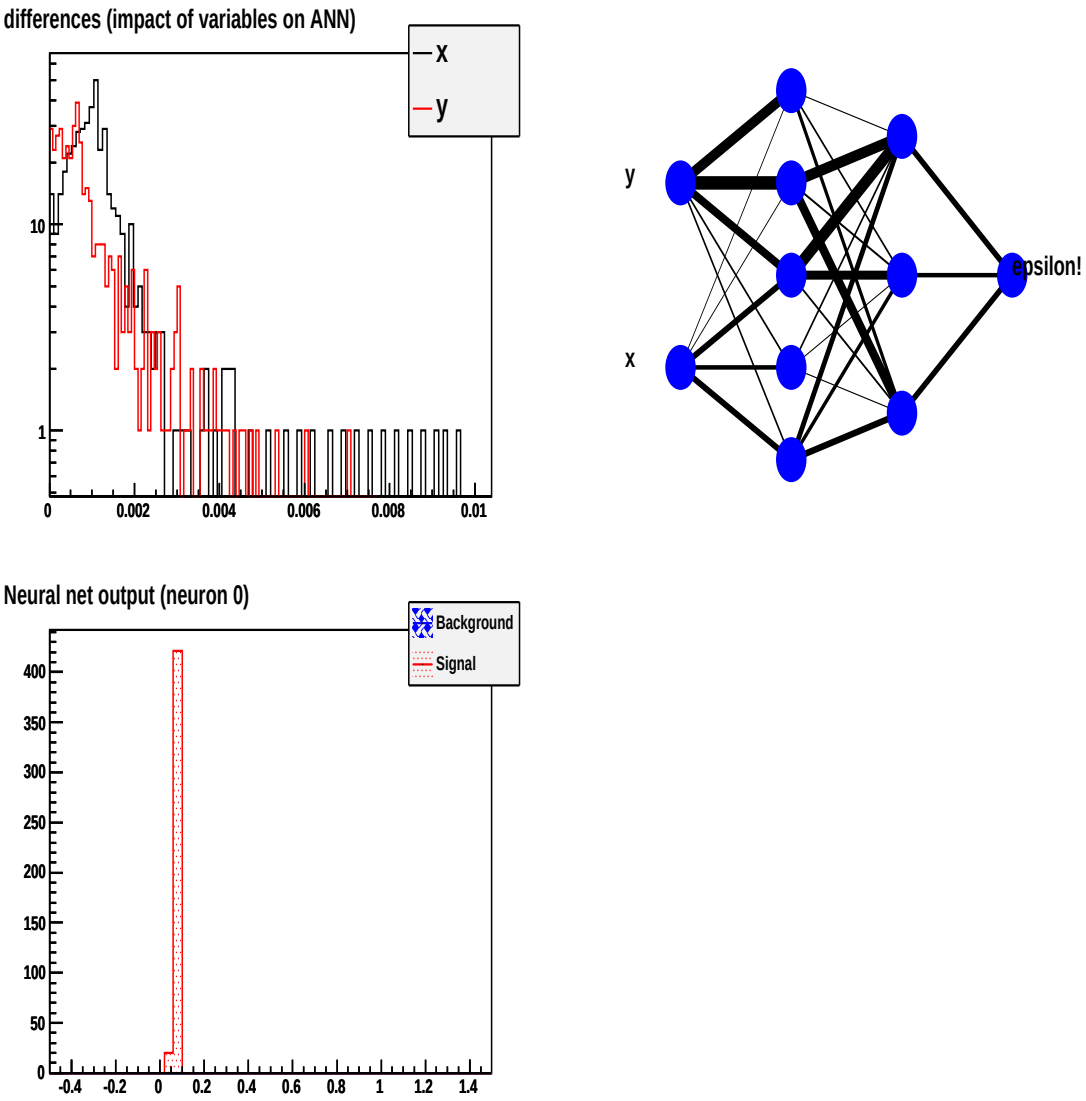

Figure 5.22: The plots are produced from TMultiLayerPerceptronAnalyzer. D^- MultiLayerPerceptron input variables and architecture. The input variables x and y correspond to the Dalitz plot variables $m^2(K^-K^+)$ and $m^2(K^+\pi^-)$.

5.3.3. Efficiency as a function production angle. In order to measure the integrated CP asymmetry and forward-backward asymmetry, we need the reconstruction efficiency as a function of production angle bin. We measure the efficiency in bins of $\cos(\theta)_{CM}$ after correcting for tracking and production. The error on the efficiency is given by the following:

$$\Delta\epsilon = \sqrt{\frac{\epsilon(1-\epsilon)}{N}} \tag{5.3.2}$$

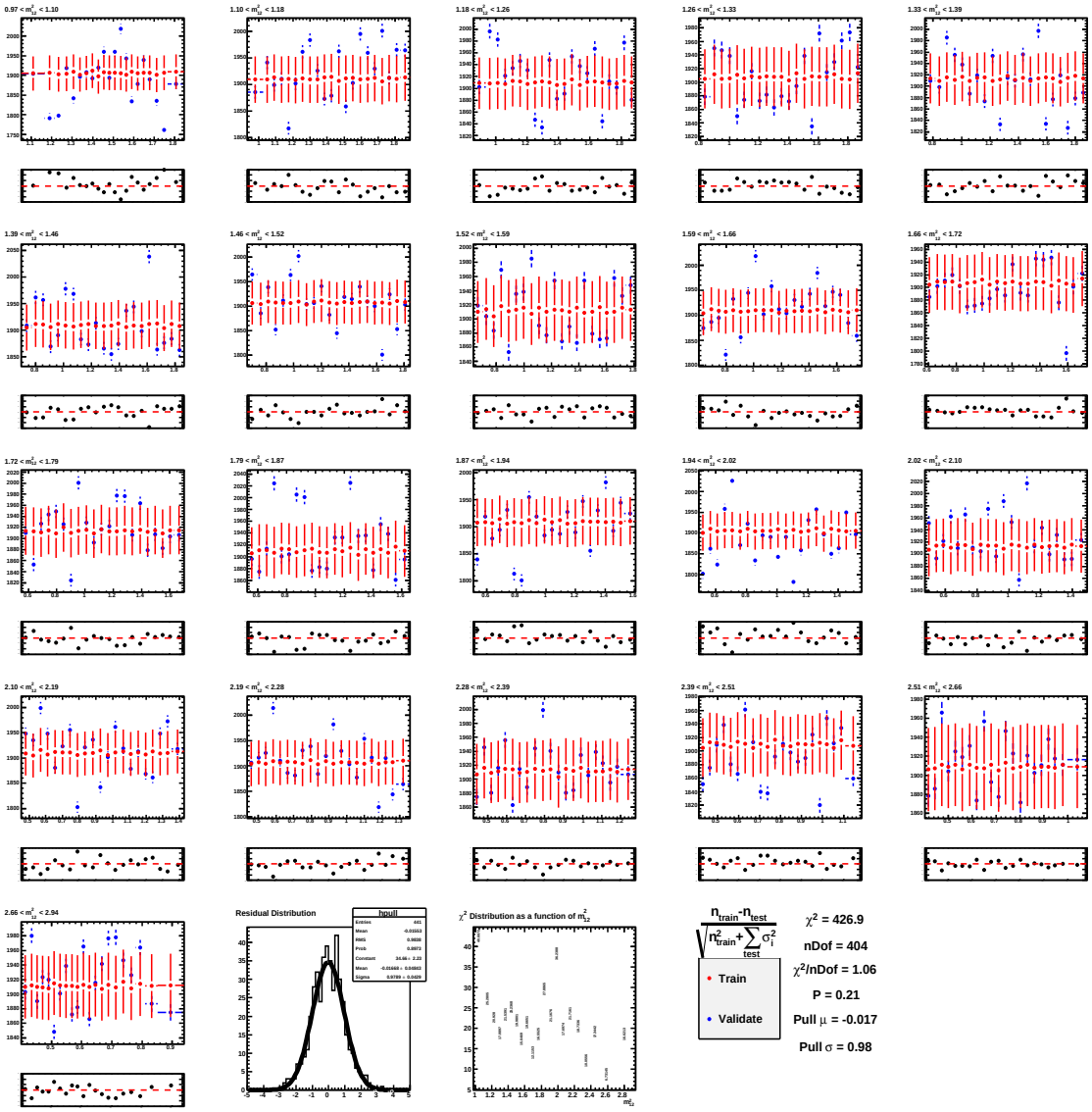

Figure 5.23: D^- MultiLayerPerceptron Validation. A χ^2 test is performed over 441 bins. The histograms are in bins of $m^2(K^-K^+)$ and are functions of the $m^2(K^+\pi^-)$. The normalized residual distribution with a Gaussian fit is obtained.

5.4. D^+ Mass Fit

5.4.1. Radiative Decays in Monte Carlo. Using BaBar Monte Carlo, we study the radiative decays of the D^+ and D_s^+ mesons. The Monte Carlo provides the radiated photon energy either due to a direct radiative decay or due to bremsstralung of one the daughter particles of the D meson. Bremsstranlung radiation does not significantly affect the mass distribution, but the radiative decays create a long tail

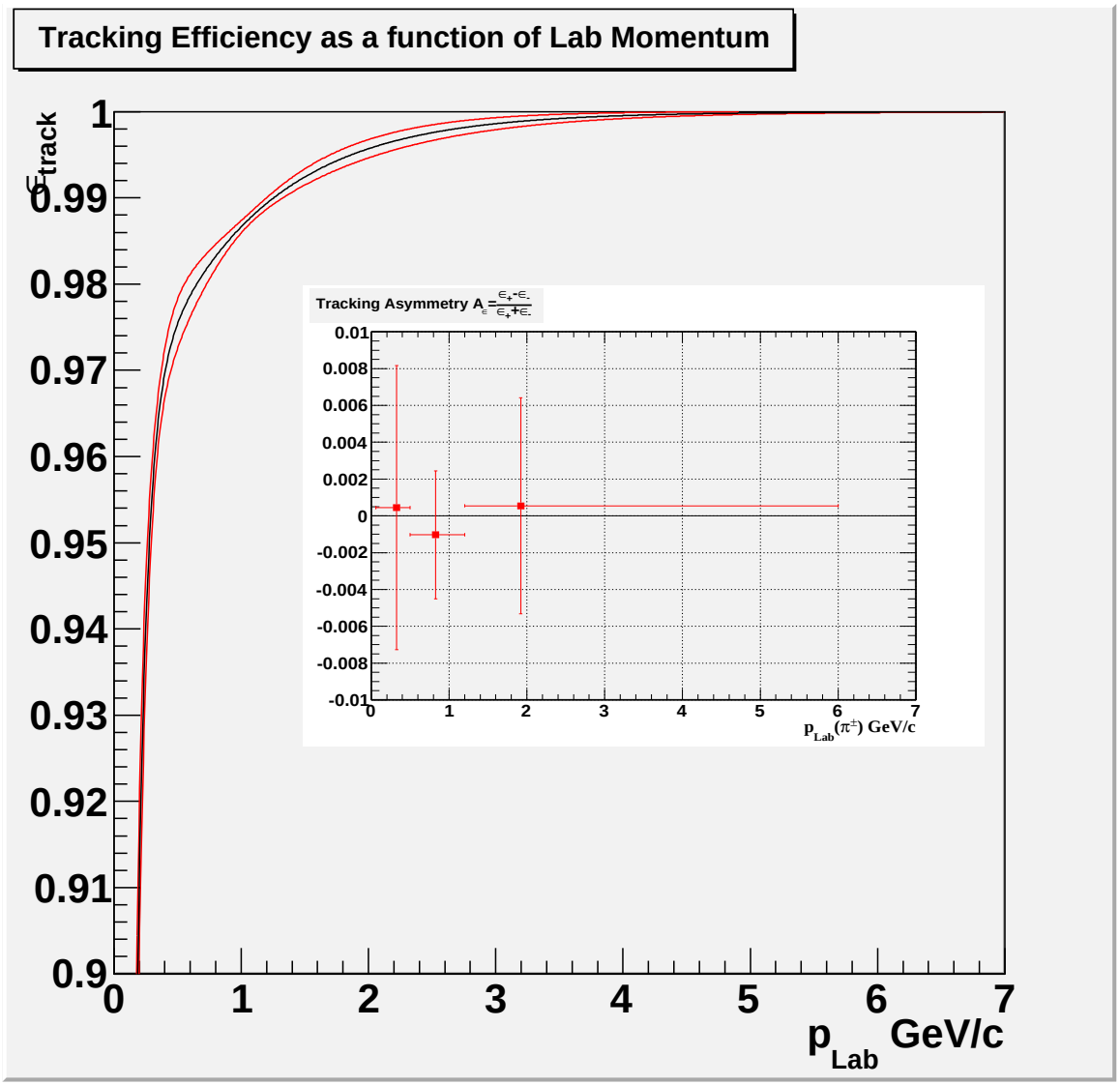

Figure 5.24: The final Results of the tracking study using decays of τ leptons. The details of the analysis can be found in BAD 2258 [**37**]. The analysis allows us to measure the tracking efficiency and asymmetry as a function of lab momentum. The black curve is the efficiency with the 1σ contour bands shown in red. The inset plot is the asymmetry measured in 3 momentum bins.

in the lower mass due to the missing energy carried away from the photon. We study the mass distribution as a function of photon energy and the angle between the daughter tracks and the radiated photon. In addition, we estimate the mass resolution of the D meson to correct the Monte Carlo.

We measure the full width at half maximum (FWHM) in data (Figure 5.29) and Monte Carlo (Figure 5.30) to determine the resolution smearing width needed to

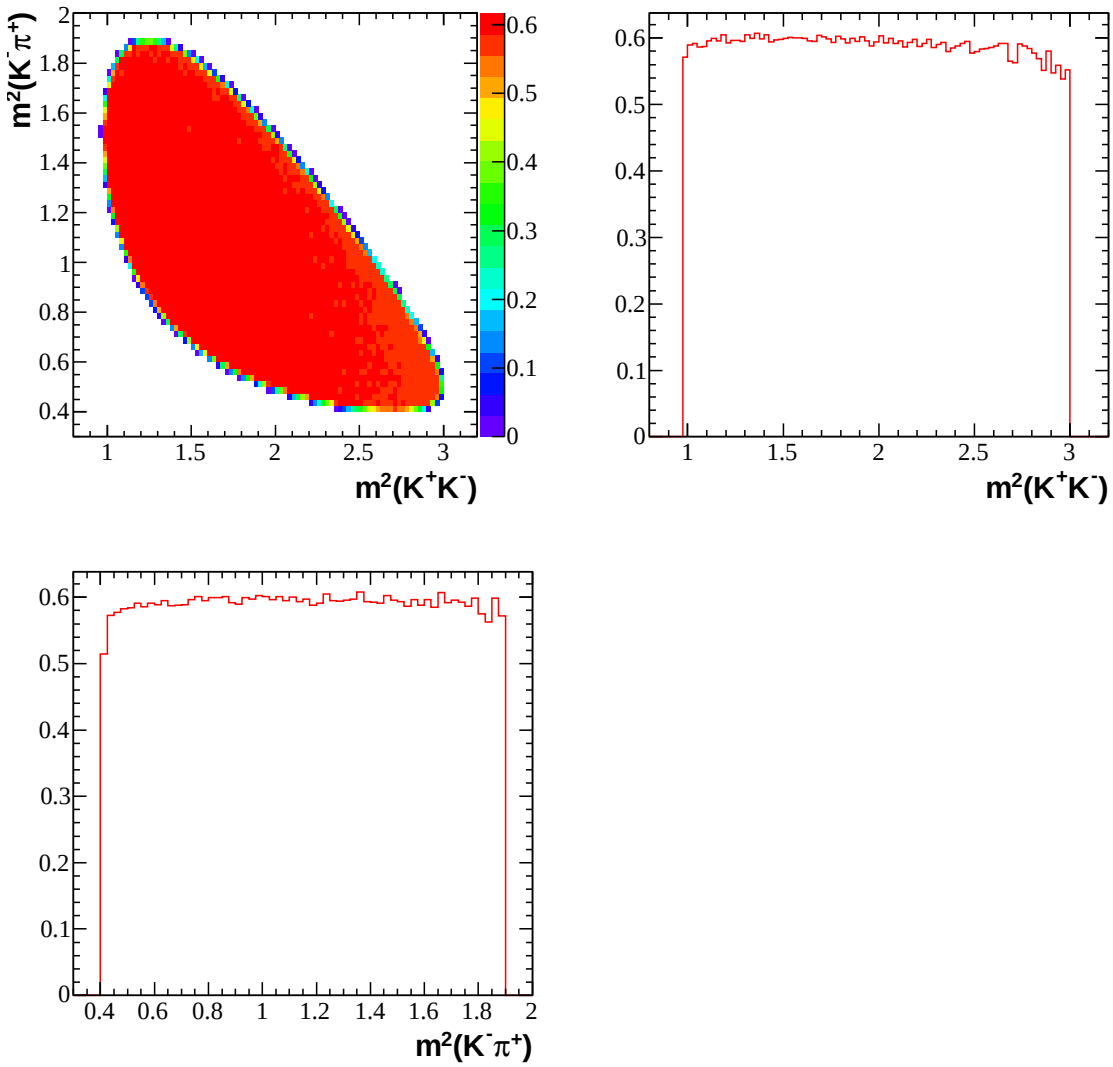

Figure 5.25: Product of the daughter particle tracking efficiency as a function of the Dalitz plot. Given the tracking efficiency determined from the τ_{31} study, we weight the generated Phase-Space Monte Carlo events to arrive at the overall tracking efficiency.

correct the Monte Carlo. To do so, we use bins of 0.1 MeV in width for data and 0.01 MeV in width for phase-space generated Monte Carlo. The maximum of the peak in data and MC is determined by fitting a gaussian in the vicinity of the peak, taking the maximum of the gaussian as the maximum for the FWHM measurement. In MC, the half maximum of the peak is taken from zero, while in data we determine the background level from a linear fit of the sideband regions and extrapolating through the signal region. In data, we find that the FWHM is 11.40 MeV and the

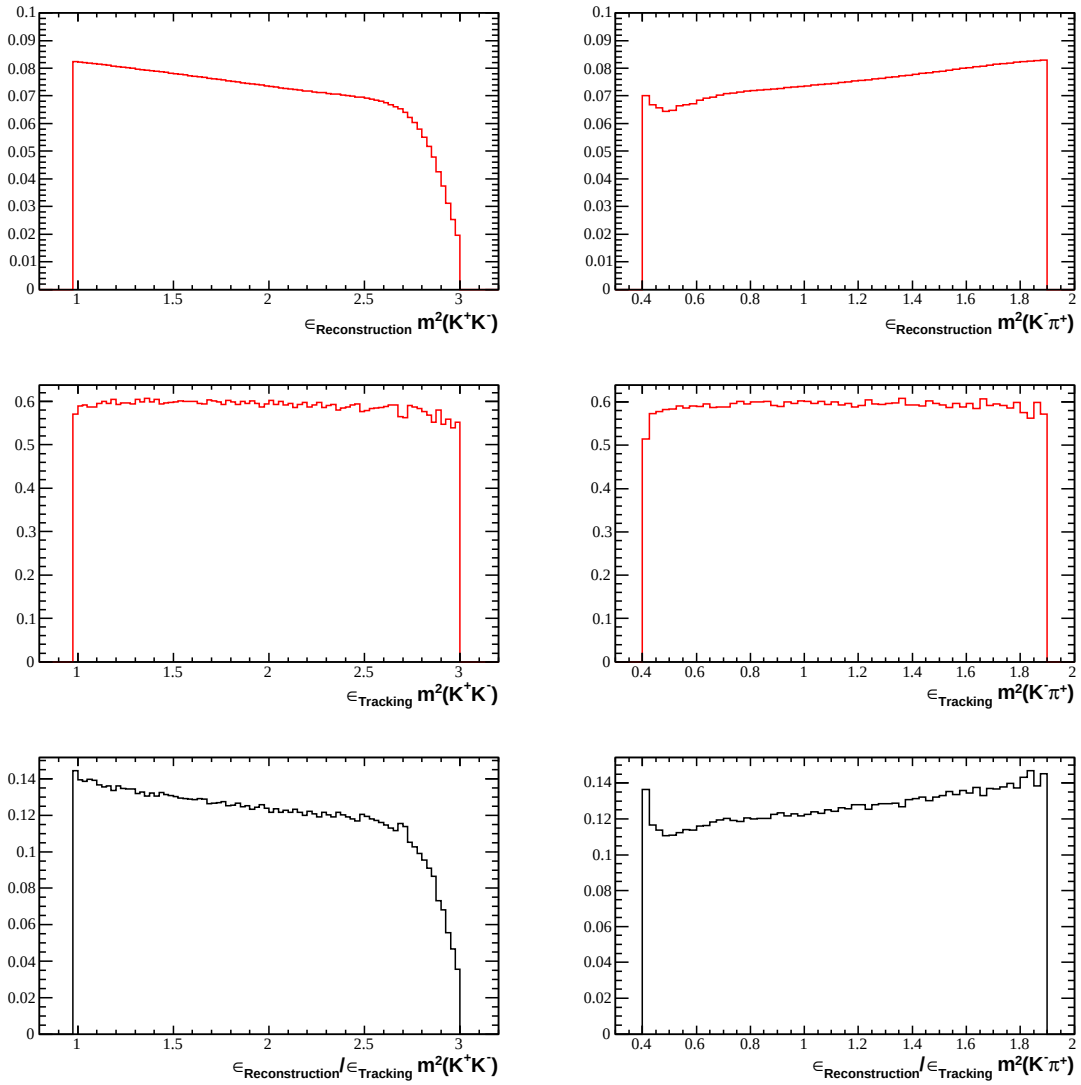

Figure 5.26: Comparison of the overall reconstruction efficiency, the tracking efficiency (Figure 5.25), and the ratio of reconstruction efficiency and tracking efficiency. A clear structure in the projections of the efficiency ratio indicates there is an additional effect in the Monte Carlo that requires further study, specifically the vertexing.

Monte Carlo is narrower at 10.08 MeV. As a result, the resolution smearing factor is 2.26 MeV. The same selection criteria is applied to data and Monte Carlo when measuring the FWHM.

The distributions of the mass for radiative decays are studied in signal phase-space MC (Figure 5.31) and in generic phase-space (Figure 5.32) events in MC. We select events in both datasets which produce non-resonant K^+, K^-, π^+ daughters

$\cos(\theta)_{CM}$	$\epsilon(D^+)$ (%)	$\Delta\epsilon(D^+)$ (%)	$\epsilon(D^-)$ (%)	$\Delta\epsilon(D^-)$ (%)
-1.00 to -0.60	5.27	0.01	5.29	0.01
-0.60 to -0.40	12.10	0.02	12.16	0.02
-0.40 to -0.20	13.78	0.02	13.82	0.03
-0.20 to 0.00	14.85	0.03	14.81	0.03
0.00 to 0.20	14.95	0.03	15.06	0.03
0.20 to 0.40	13.09	0.02	13.13	0.02
0.40 to 0.60	8.41	0.02	8.48	0.02
0.60 to 1.00	0.64	0.00	0.64	0.00

Table 5.8: Reconstruction efficiency as a function of the production angle. Tracking and production corrections are included in these results.

with a single radiated photon from the D. These events are also selected for $D(s)$ decays in the generic Monte Carlo. The photon energy is the generated energy in the Monte Carlo, and the angle between the daughter tracks is also measured from the generated momenta of the particles. We find that the photons are not colinear with any of the daughter tracks.

The mass distribution of phase-space generated single photon radiative decays for $E_\gamma > 1$ MeV is a model that is included as an additional pdf in the mass fit to data. The Monte Carlo distribution is corrected for resolution by smearing the distribution by 2.26 MeV with a gaussian for each mass reconstructed in the Monte Carlo. We generated an additional 1000 events for each MC event. The original disrtibution from MC, the smeared distribution, and the PDF generated with an additional 1000 randomly generated points are shown in Figure 5.33.

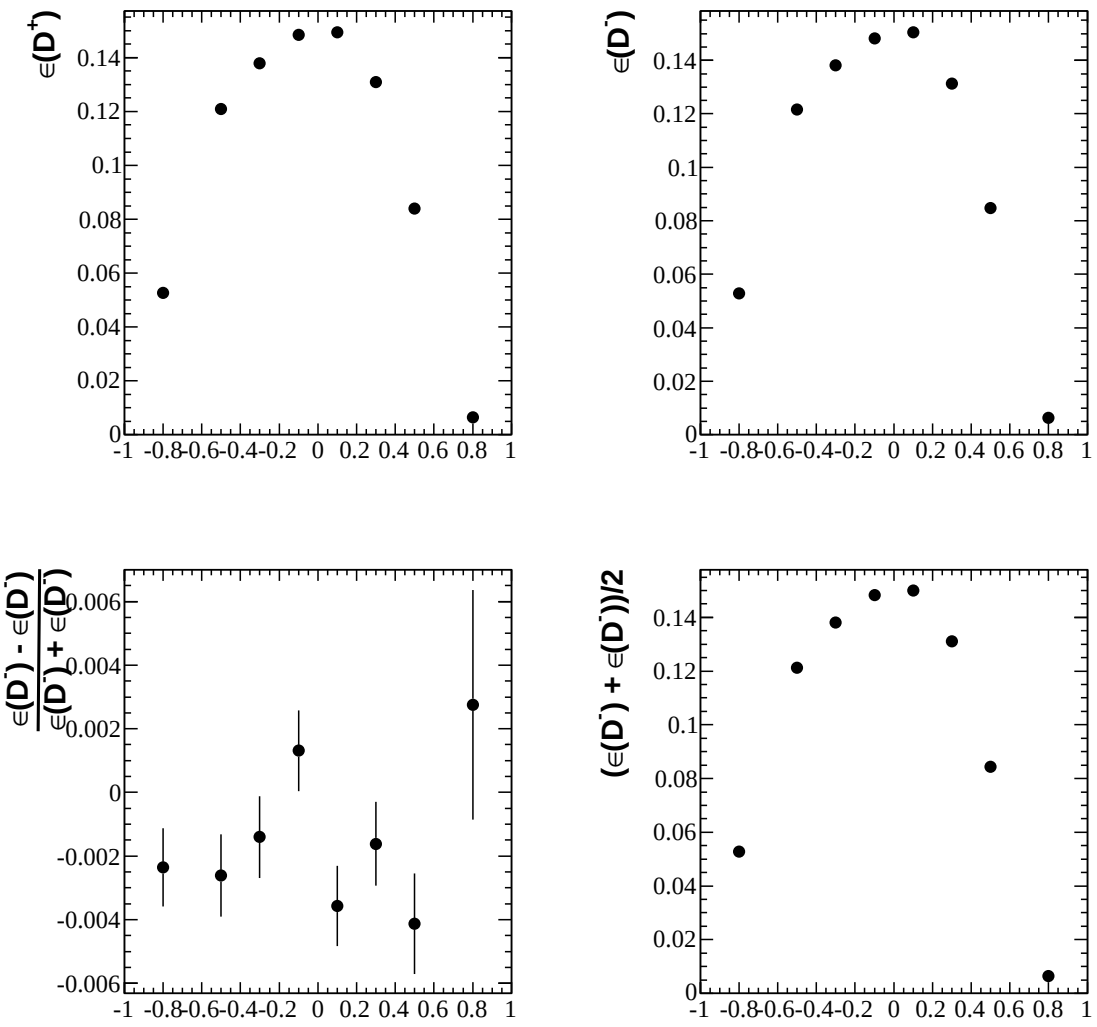

Figure 5.27: Reconstruction efficiency as a function of the production angle ($\cos(\theta)_{CM}$). Tracking and production corrections are included in these measurements. The top plots are the efficiencies for D^+ and D^-. The bottom left plot is the asymmetry in the efficiency, and the bottom right plot shows the average efficiency.

5.4.2. Integrated Mass Fit. We perform an unbinned extended maximum likelihood fit of the $D^{\pm}$ mass spectrum from 1.82 GeV^2 to 1.92 GeV^2. The model is composed of three components:

•Shape of radiative decays (Figure 5.33)

•Gaussian signal shape (double gaussian with same mean)

•Background polynomial (linear background)

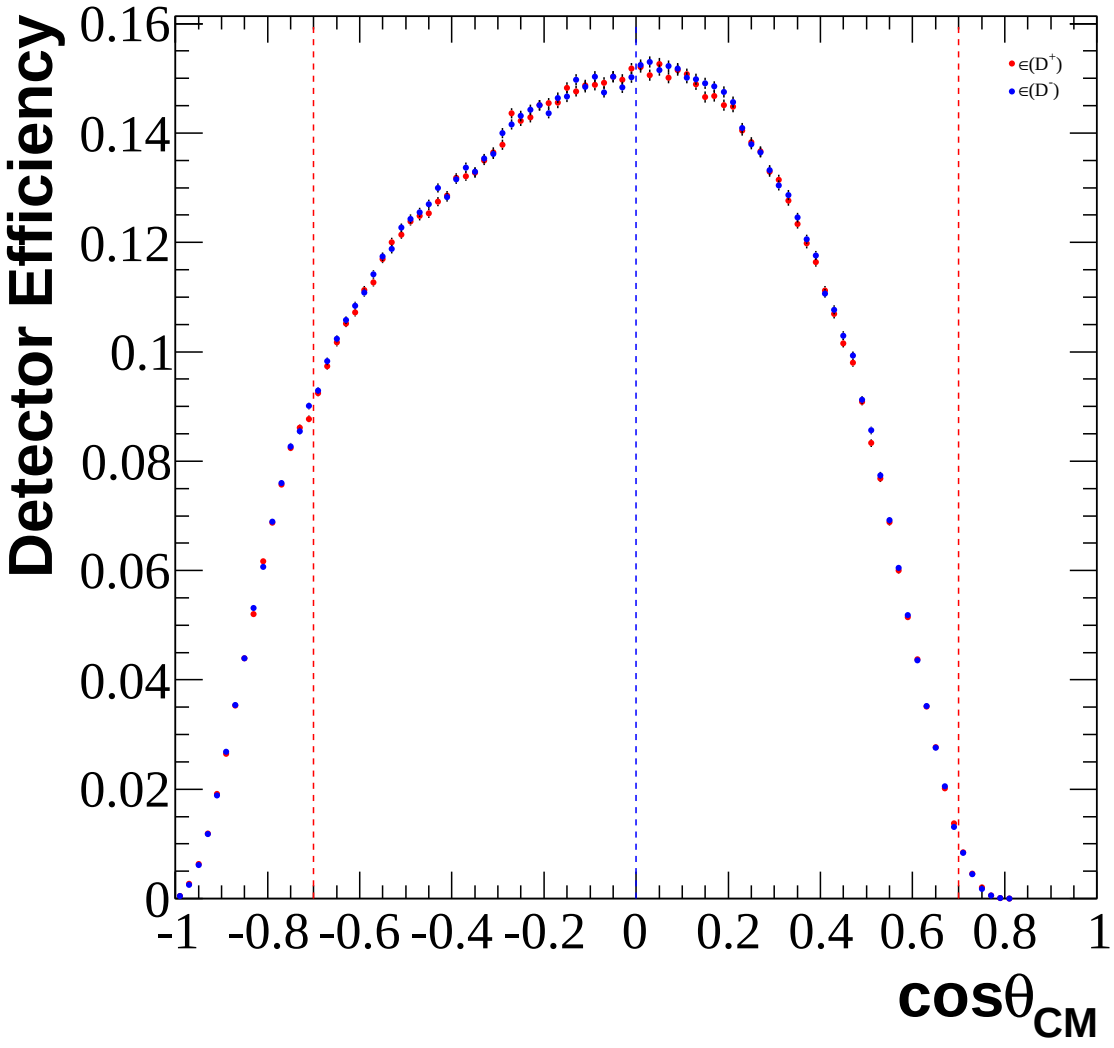

Figure 5.28: Reconstruction efficiency as a function of the production angle ($\cos(\theta)_{CM}$). Tracking and production corrections are included in these measurements. The efficiency is estimated in 100 bins over the entire production range. The lines at ± 0.7 correspond to the symmetric range which we can ensure that D mesons are reconstructed efficiently.

We use phase-space generated signal MC events to obtain the shape of radiative decays. We search for reconstructed candidates which contain a single radiative photon. We apply various cuts on the generated energy of the radiated photon to find the shape associated with the lower tail of the D mass for hard photons which significantly affect the signal shape (Figure 5.31). For photons with energy greater

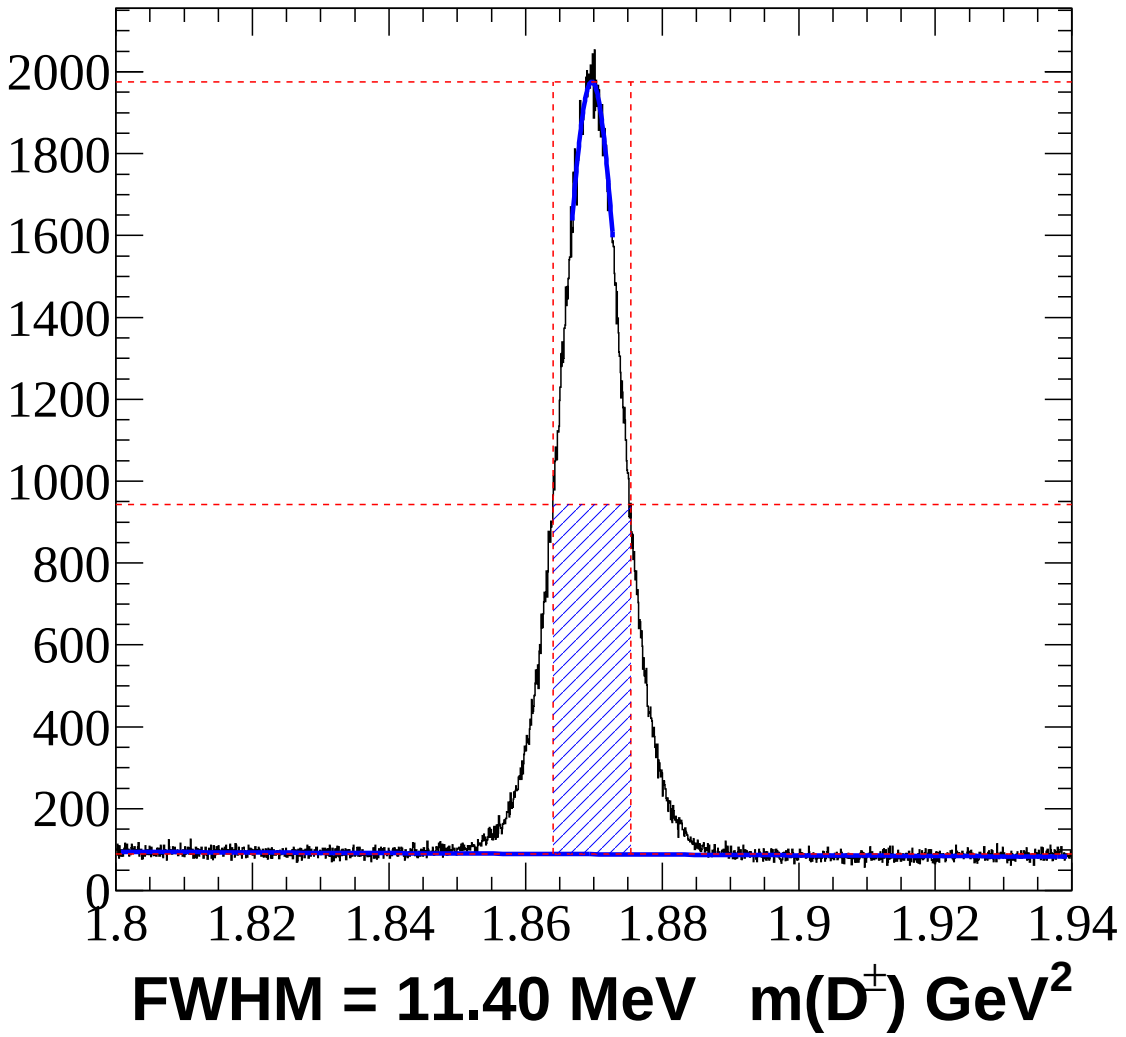

Figure 5.29: Full width at half maximum measured in data. The dashed red lines indicate the minimum, maximum, and half-maximum values. While the verticle lines indicate the FWHM. The sideband fit to the background is indicated in the blue linear curve, and the blue gaussian curve is the fit to determine the maximum.

than 10 MeV, we use the histogram with the MC mass smeared from the smearing resolution gaussian as the pdf (Figure 5.33) of the radiative events.

The model gives a χ^2/ndof = 1.05 and a fit probability of 35%. The results are shown in (Figure 5.34). The number of events due to each signal and background component are found in Table 5.9.

The fit is re-performed to measure the total number of signal events. The parameters for each signal component are fractions that vary between 0 and 1. We

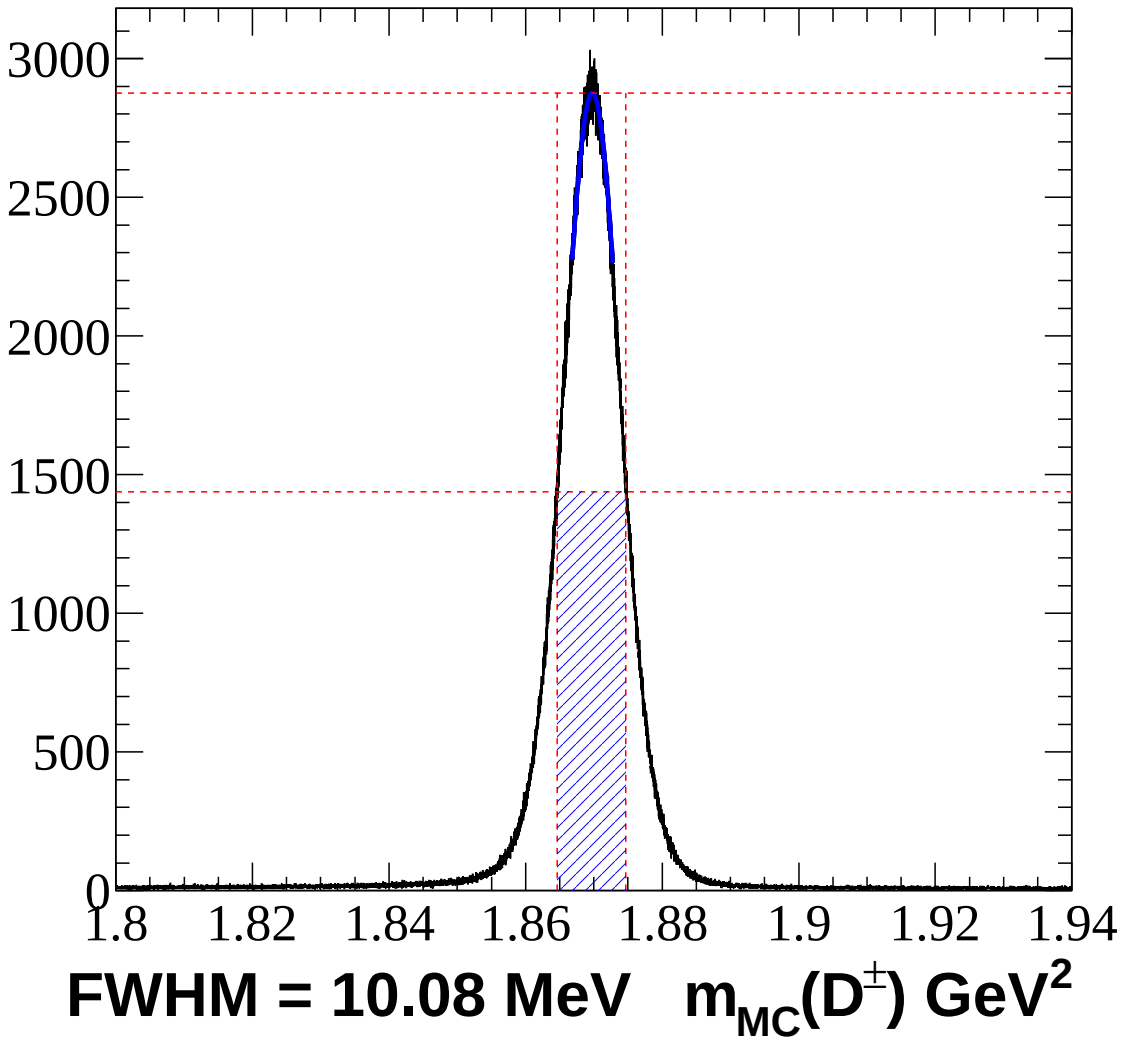

Figure 5.30: Full width at half maximum measured in signal Monte Carlo. The dashed red lines indicate the maximum, and half-maximum values. While the verticle lines indicate the FWHM. The blue gaussian curve is fit to the peak to estimate the maximum.

find an equivalent χ^2 per degree of freedom of 1.05 and a probability of 35%. The results of the fit are summarized in Table 5.10. The MINUIT output for both fits is included in appendix J.

We select the signal and background regions from the total width and the mean of the two gaussians. The signal region lies between $\pm 2\sigma$ of the fitted D mass, and the background regions lie between 6σ and 8σ of the D mass on the upper on lower

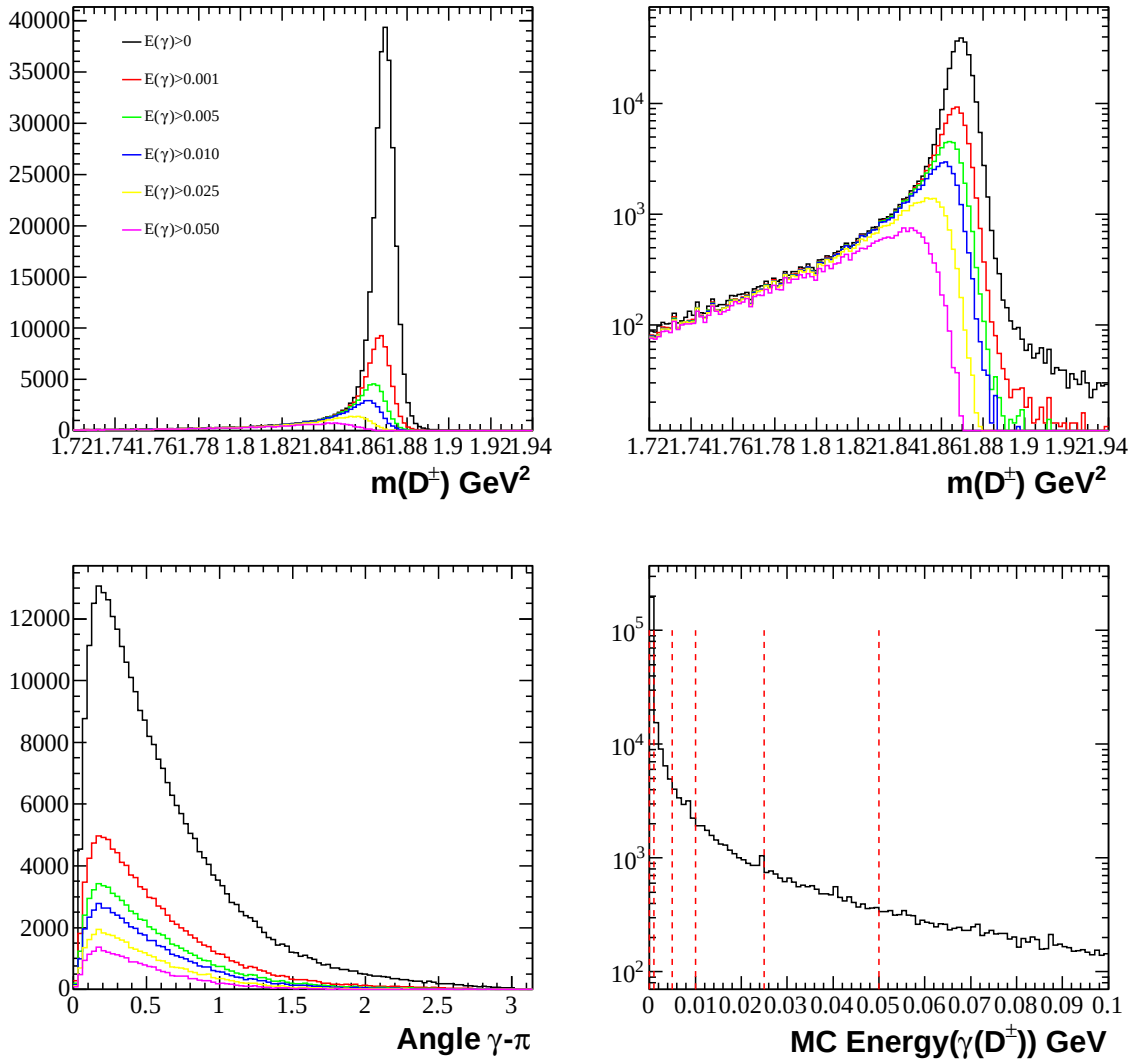

Figure 5.31: Radiative $D^+ \to K^+K^-\pi^+\gamma$ in phase-space generated signal MC. The upper left plot shows the D mass distribution for various cuts on the radiated photon energy. The lower left plot is the angle between the radiated photon and the pion track. The lower right plot indicates the various energy cuts on the photon in dashed-red lines.

mass sideband regions (Table 5.11). These are shown in Figure 5.35. The signal region contains 227,874 events and the purity of events is 92%.

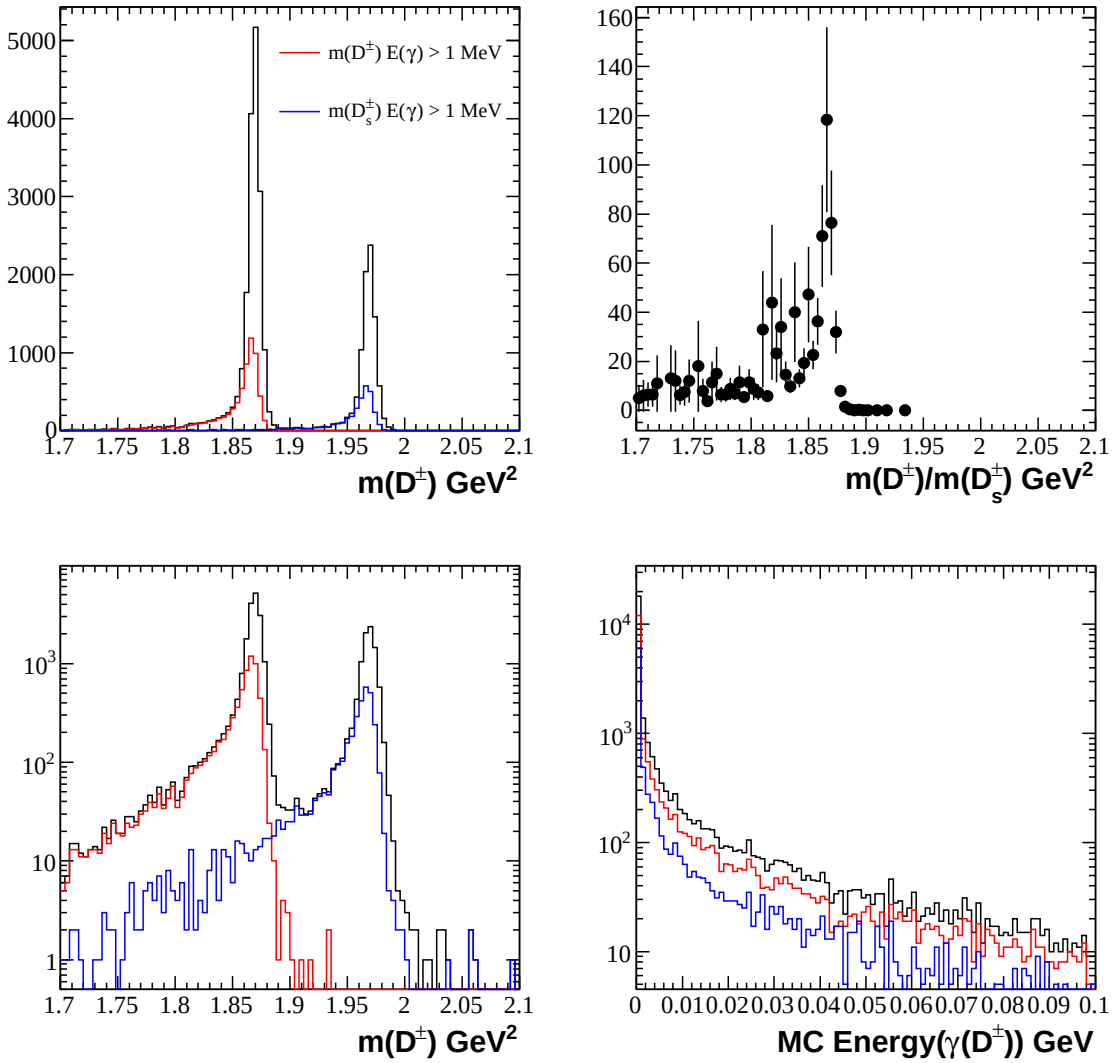

Figure 5.32: Radiative D^+,$D_s^+ \to K^+K^-\pi^+\gamma$ in generic $c\bar{c}$ MC. The upper left plot shows the D mass without any photon energy cut and the D^+ (red) and $D_S{}^+$ (blue) for E(γ) > 1 MeV. The upper right plot is the ratio of D^+ to D_s^+ radiative decays. Contamination of D_s decays in the signal region of D^+ is negligiable.

5.5. CP Asymmetry Measurement in Decay

We describe and report measurements of the CP asymmetry A, where

$$A = \frac{N(D^+)/\epsilon(D^+) - N(D^-)/\epsilon(D^-)}{N(D^+)/\epsilon(D^+) + N(D^-)/\epsilon(D^-)} \tag{5.5.1}$$

using various methods, both model-dependent and model-independent.

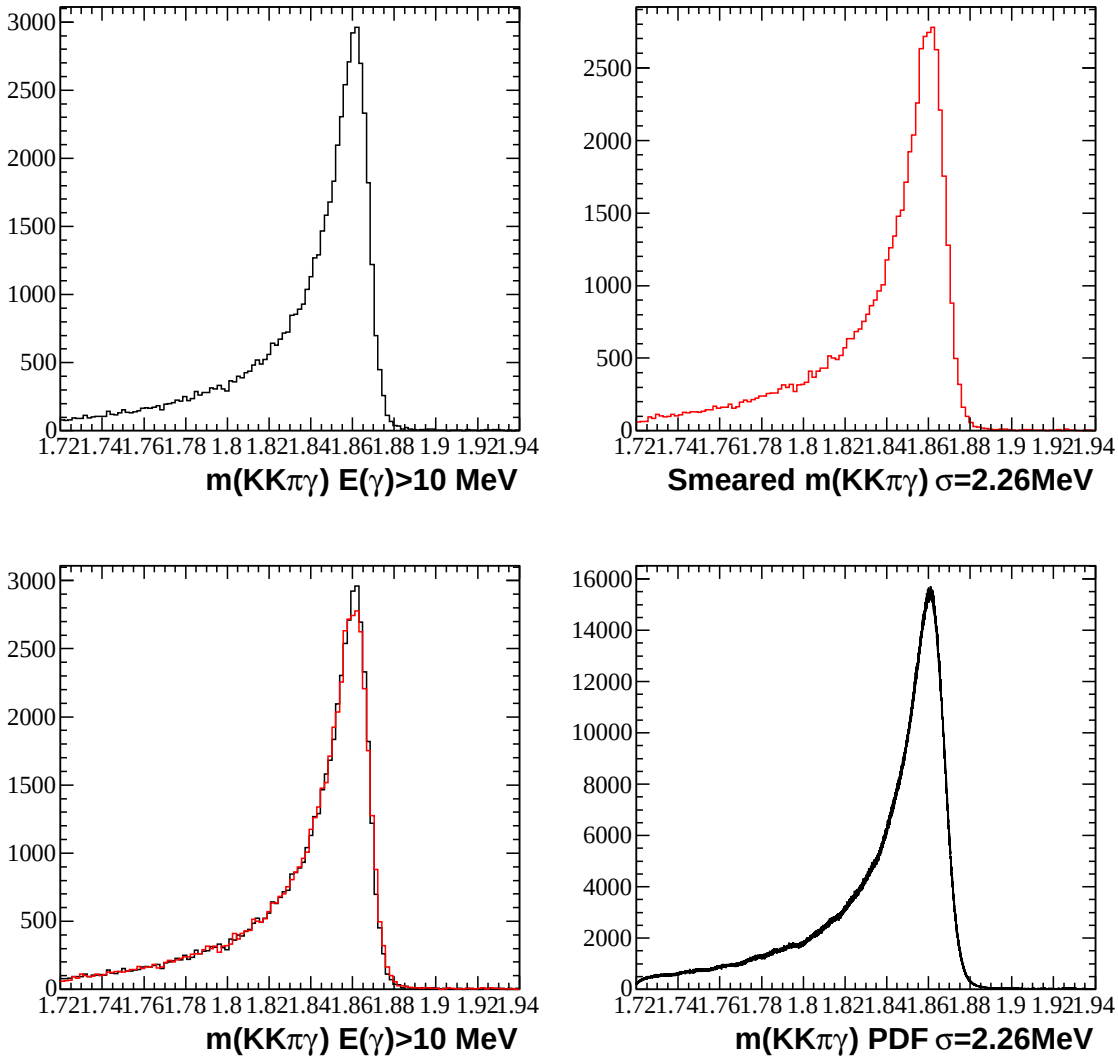

Figure 5.33: Radiative $D^+ \to K^+K^-\pi^+\gamma$ in phase-space generated signal MC. The upper left plot shows the D mass distribution for $E_\gamma > 1$ MeV. The MC distribution is smeared with a gaussian with $\sigma = 2.26$ MeV. The lower right plot has an additional 1000 points randomly generated from the resolution smearing gaussian for each MC event.

•CP asymmetry as a function of the production angle $\cos(\theta)_{CM}$ (the average of or fit to which yields the integrated asymmetry A_{CP}).

•CP Asymmetry in 2-dimensional bins of the Dalitz Plot.

•Comparison of the Legendre moments in D^+ and D^-.

•CP asymmetry in resonance amplitudes from a Dalitz plot fit.

Component	N	Error
Gaussian 1	79465	6382
Gaussian 2	141194	6486
Radiative	3226	343
Background	86726	486

Table 5.9: Signal and Background yields from the integrated mass fit. The signal yields are reported for each signal component

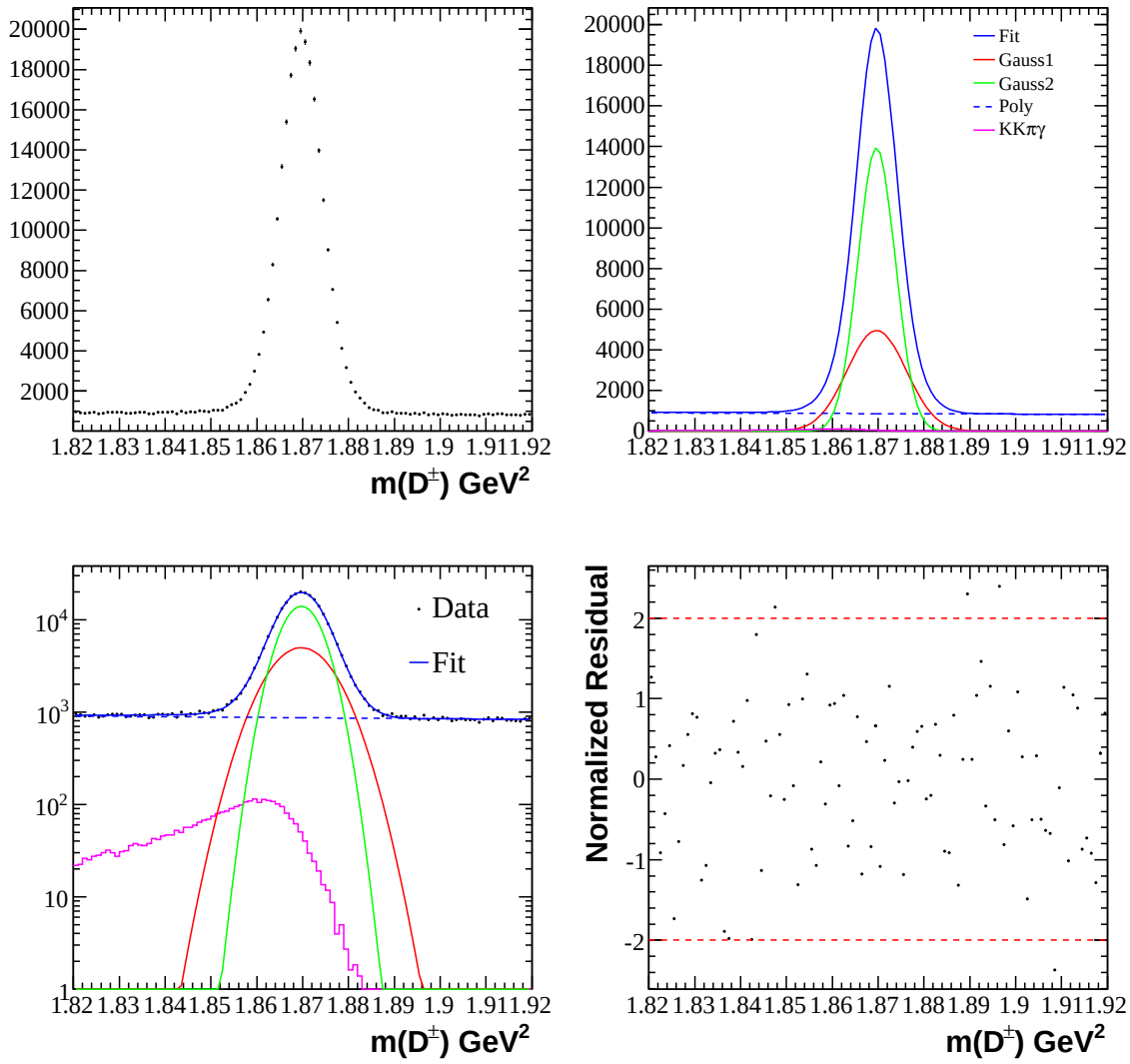

Figure 5.34: Results of the fit to integrated mass of $D^{\pm}$. The normalized residual at a given mass is shown in the lower right plot. The model gives a χ^2/ndof = 1.05 and a fit probability of 35%.

Component	Value	Error
N Signal	223881	586
Gaussian Fraction	0.638	0.043
Radiative Fraction	0.014	0.0028
Background	86733	530

Table 5.10: Signal and Background yields from the integrated mass fit. We measure the total yield for signal and background, while each signal component is a fraction of the total.

Signal Region (GeV^2)	Low Mass Sideband (GeV^2)	High Mass Sideband (GeV^2)
1.85961 to 1.87978	1.82936 to 1.83944	1.89995 to 1.91004

Table 5.11: Signal and Background regions determined from fit to reconstructed D mass. The mean and RMS of the two gaussians selects the mass windows.

5.5.1. CP Asymmetry measured as a function of $\cos(\theta)_{CM}$. We measure the asymmetry, A, in bins of the production angle. The yields and errors for D^+ and D^- are obtained from binned χ^2 fits of the D^+ and D^- mass. The fits are shown in Figure 5.38, Figure 5.39, Figure 5.40, and Figure 5.41. Given the asymmetry in each production bin, we measure the CP asymmetry as

$$A_{CP}(\theta) = \frac{A(\cos(\theta)_{CM} > 0) + A(\cos(\theta)_{CM} < 0)}{2}. \tag{5.5.2}$$

and the foward-backward asymmetry as

$$A_{FB}(\theta) = \frac{A(\cos(\theta)_{CM} > 0) - A(\cos(\theta)_{CM} < 0)}{2}. \tag{5.5.3}$$

The integrated CP asymmetry is measured as the average of the A_{CP} in each bin.

The forward-backward asymmetry, A_{FB}, and the integrated CP asymmetry can be measured simultaneously by fitting the asymmetry as a function of polar angle to the following form [**32**]:

$$A(\cos(\theta)_{CM}) = A_{CP} + A_{FB}\frac{8}{3}\frac{\cos(\theta)_{CM}}{1+\cos^2(\theta)_{CM}} \tag{5.5.4}$$

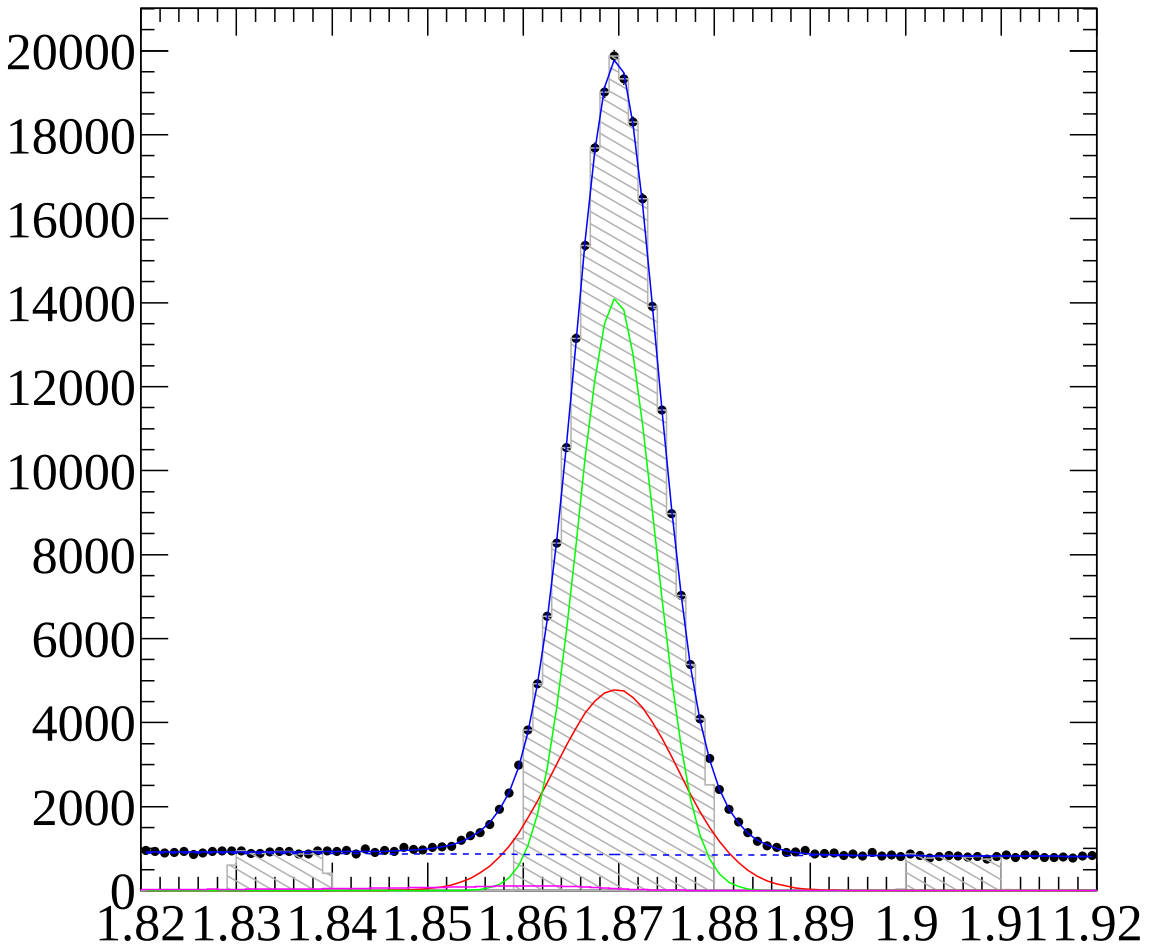

Figure 5.35: Integrated mass fit with the signal and sideband regions shown in grey. The signal region contains a total of 227,874 events.

In addition to binning the data in several production angle bins, we also measure the asymmetry in the forward and backward regions, taking the average of asymmetries as A_{CP}. We measure the asymmetry in a single bin for $\cos\theta_{CM}$ between -0.7 to 0. in the backward region of the detector and in the forward region we measure the asymmetry between 0. and 0.7. This ensures that we only consider events in regions where we can reconstruct the D^+ meson. In addition, the efficiency is taken into account by weighting each event and fitting for the efficiency-corrected yields. The efficiency as a function of production angle is shown in Figure 5.28. A summary

Average $\cos\theta$ Asymmetry	A_{CP}[%]
Average of $A_{CP}(\theta)$	-0.14 ± 0.62
8 bins in $\cos\theta_{CM}$	-0.17 ± 0.60
6 bins in $\cos\theta_{CM}$	-0.05 ± 0.53

Table 5.12: Mean integrated CP asymmetry measured from 16 independent MC samples. The RMS of these measurements is 0.2% larger than the statistical error on each sample.

Method	A_{CP}[%]	A_{FB}[%]
FB regions A_{CP}	1.12 ± 0.35	-2.12 ± 0.35
Average of $A_{CP}(\theta)$	1.13 ± 0.30	NA
From fit to $A(\cos(\theta)_{CM})$	1.12 ± 0.30	-2.92 ± 0.33

Table 5.13: Integrated CP asymmetry and forward-backward asymmetries measured in data. The results of A_{CP} are consistent from the three methods. The central values for the A_{CP} measurement are blinded by adding an unknown random number generated from a uniform distribution between -1 and 1. The FB asymmetry is not a blinded result.

of the asymmetries in data is found in Table 5.13, where the A_{CP} measurement is blinded.

We validate the procedure using 16 independent generic $c\bar{c}$ MC samples. We measure the CP asymmetry in a single bin for the forward and backward region, taking the average CP asymmetry measured from 8 bins in $\cos\theta_{CM}$, and taking the average CP asymmetry measured from 6 bins in $\cos\theta_{CM}$. The results of the validation study are shown in Table 5.12. The statistical error on each of the MC samples is 0.42%.

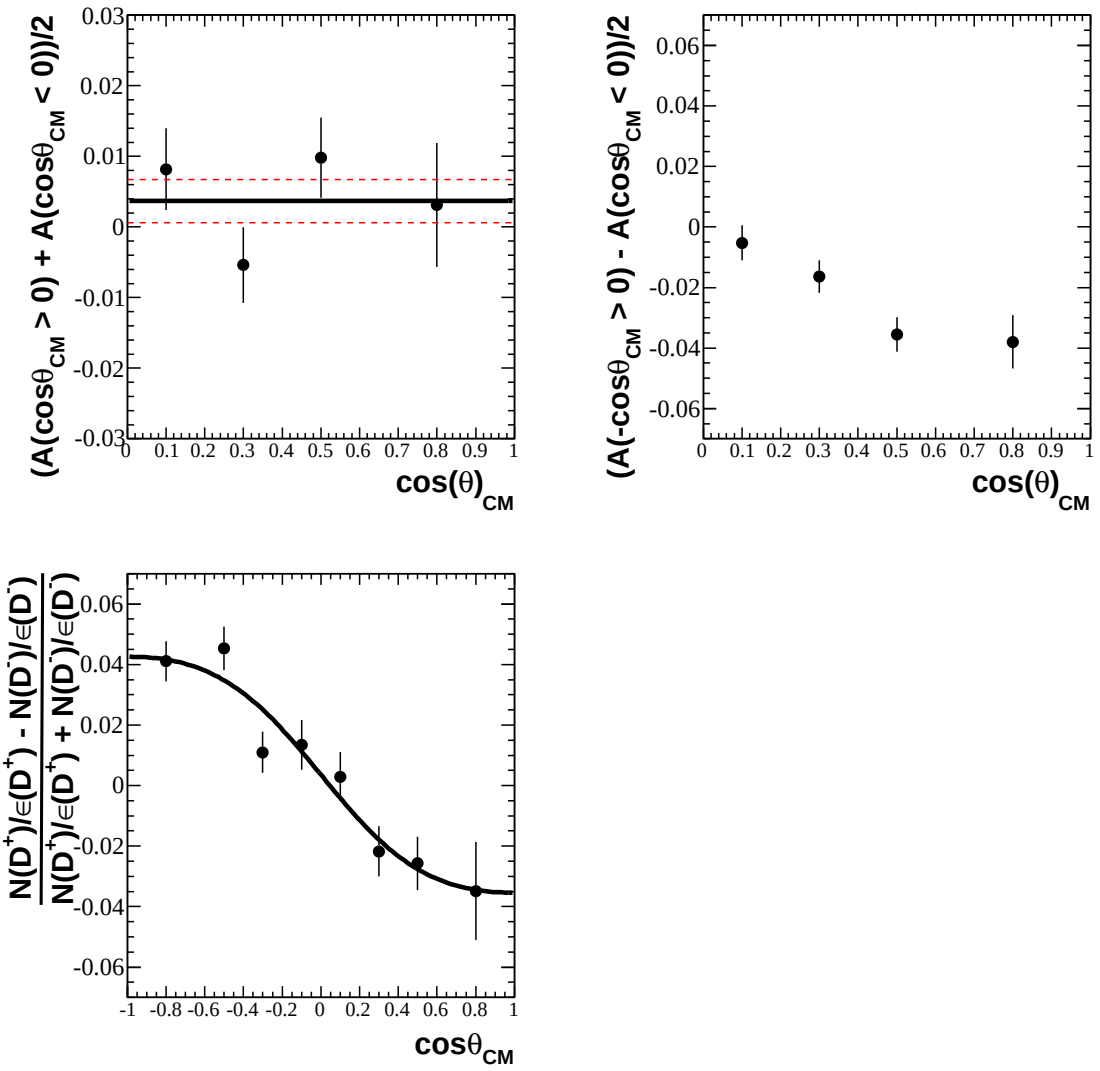

Figure 5.36: Integrated CP asymmetry and forward-backward asymmetry.

5.5.2. CP Asymmetry in bins of the Dalitz plot. In addition to fitting for the yields of D^+ and D^- in bins of the production angle, we also fit for the yields in bins of the Dalitz plot. We split the Dalitz plot into four bins:

- $\phi(1020)$ region;
- $\bar{K}^{*0}(892)$ region;
- Below the $\bar{K}^{*0}(892)$ region;
- Above the $\phi(1020)$ and $\bar{K}^{*0}(892)$ region.

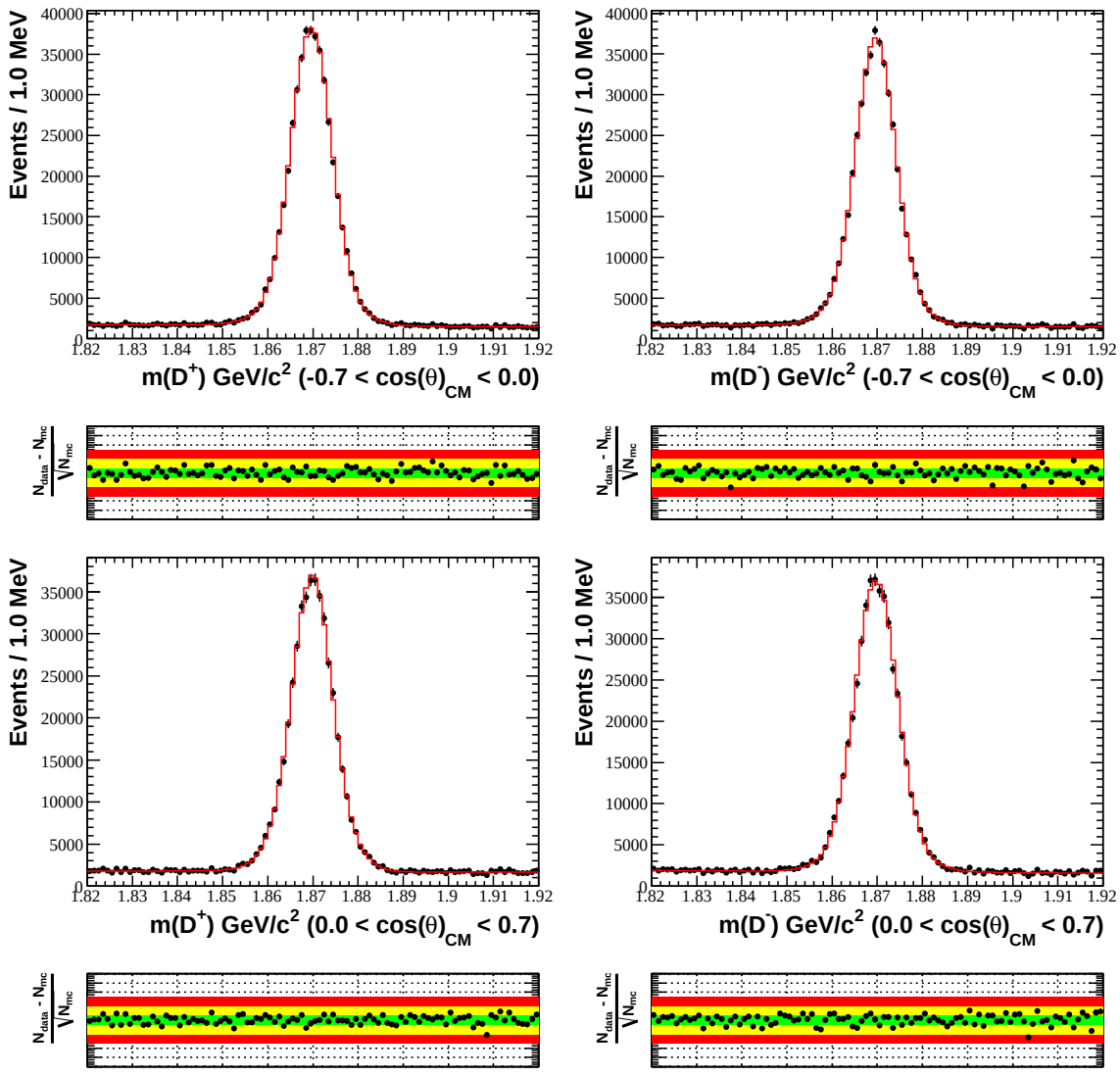

Figure 5.37: Fit results for the efficiency corrected D^+ and D^- mass in the backward production bin (upper plots) and the forward production bin (lower plots). We consider only candidates which have a production between -0.7 and 0.7.

•The entire Dalitz plot. The efficiency in each bin is determined from integrating the ANN efficiency (which included the tracking and production corrections).

The analysis is performed on 16 independent R24c generic $c\bar{c}$ MC and results are reported in Table 5.14. We report the mean and RMS of the measurements after adding a random number.

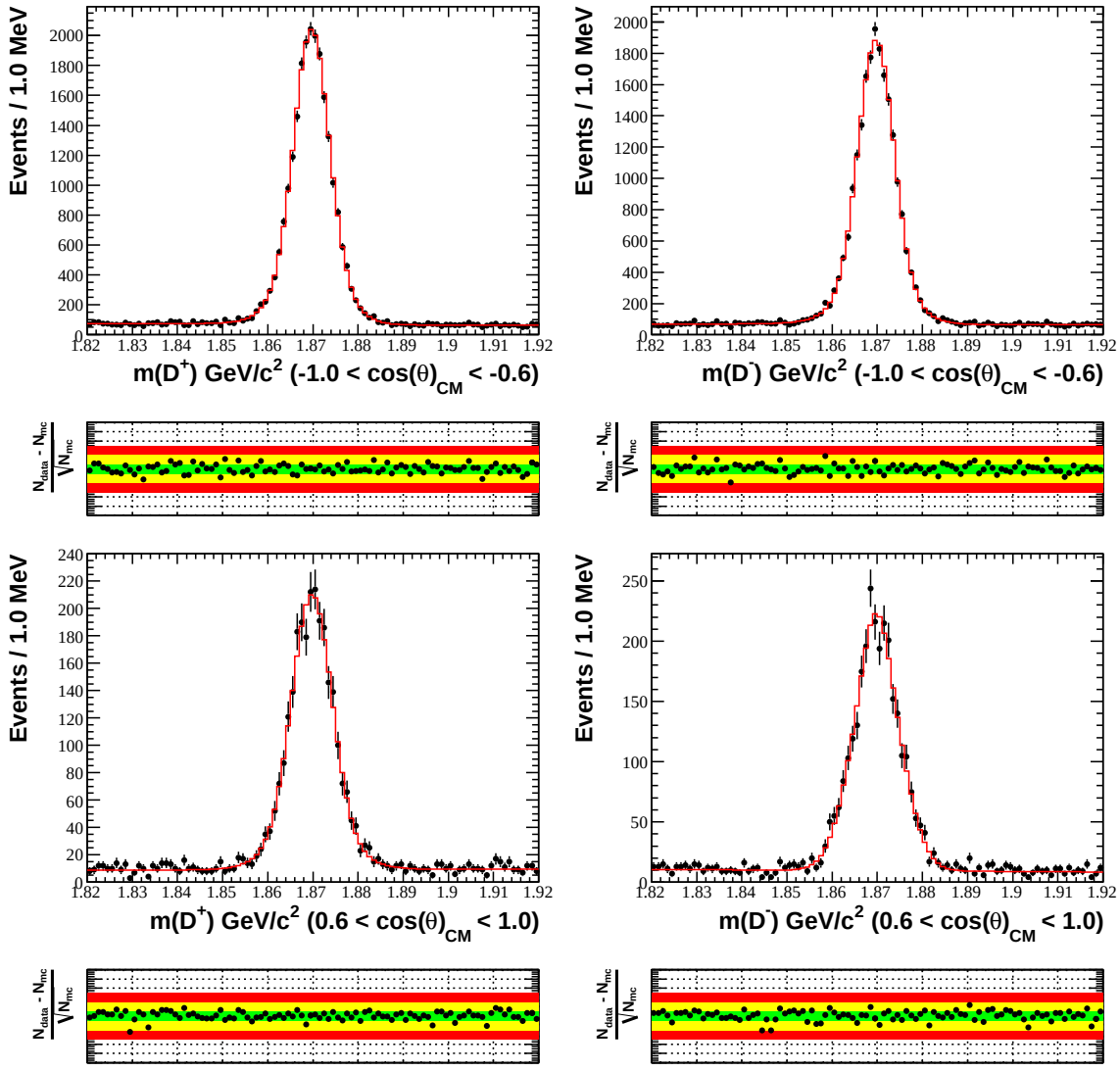

Figure 5.38: Fit results for the D^+ and D^- mass in the backward production bin (upper plots) and the forward production bin (lower plots).

Bin	$m^2(KK)$ (GeV^2)	$m^2(K\pi)$ (GeV^2)	A_{CP}[%]	A_ϵ[%]
1	1.5 to 3	0.35 to 0.6	0.45 $\pm$ 1.22	0.26
2	0.95 to 3	0.6 to 1.	-0.13 $\pm$ 0.45	-0.008
3	0.95 to 1.3	1. to 1.9	-0.27 $\pm$ 0.39	0.14
4	1.3 to 3.	1. to 1.9	0.27 $\pm$ 1.20	0.07
5	0.95 to 3	0.35 to 1.9	0.08 $\pm$ 0.51	0.07

Table 5.14: CP Asymmetry measured with the R24c and R26a generic $c\bar{c}$ data set. We report the mean and RMS from 16 independent measurements. The Dalitz plot is divided into four bins. The error is determined from the yields only. The last entry in the corresponds to integrating over the entire Dalitz plot.

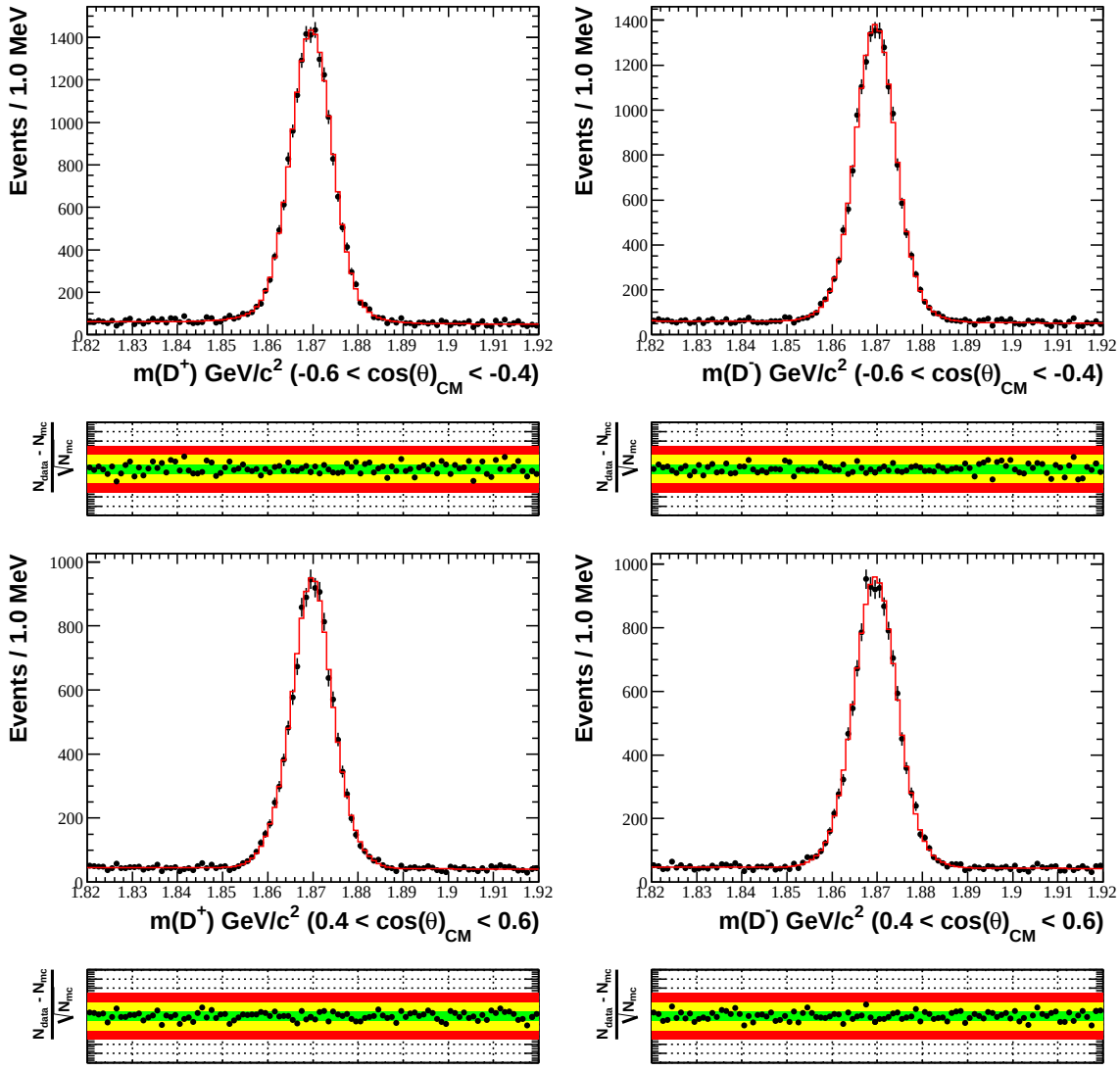

Figure 5.39: Fit results for the D^+ and D^- mass in the backward production bin (upper plots) and the forward production bin (lower plots).

5.5.3. CP Asymmetry in the Legendre Moments. We compare D^+ and D^- in KK and Kπ mass with Legendre moment weighted events. We obtain background-subtracted and efficiency corrected distributions as a function of the two-body mass. For background subtraction, we take the Legendre moment weighted mass-constrained events from the upper and lower D^+ and D^- mass sidebands and subtract these distrbutions from the signal region distributions. The distributions are then corrected for efficiency. The efficiency is computed by integrating the 2-dimensional ANN efficiency function and dividing by the area for each bin of KK

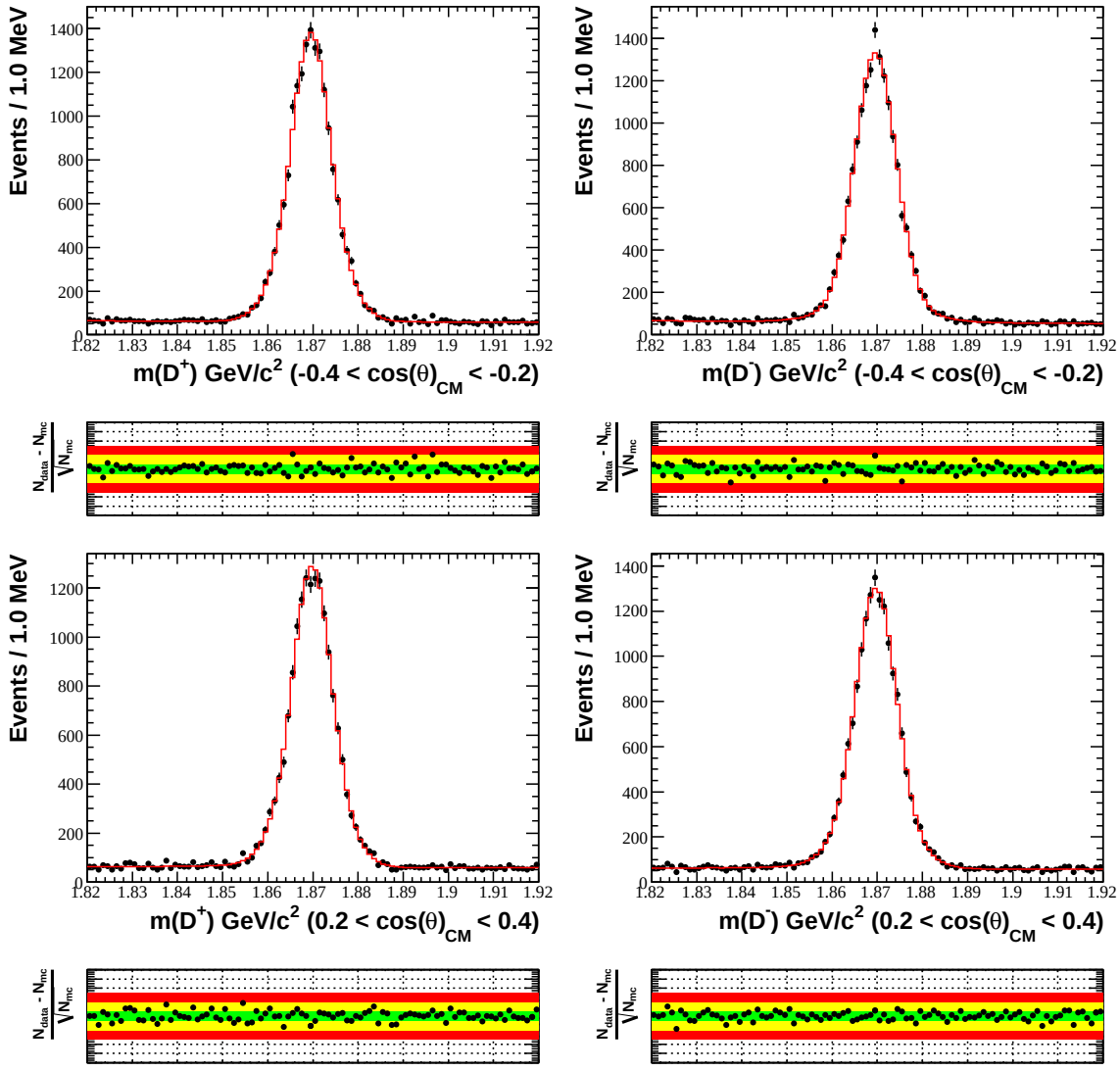

Figure 5.40: Fit results for the D^+ and D^- mass in the backward production bin (upper plots) and the forward production bin (lower plots).

mass or $K\pi$ mass. The normalized residuals are computed for each two-body mass bin and moment.

$$X_i = \frac{P_i^{D^+} - P_i^{D^-}}{\sqrt{\sigma^2_{P_i^{D^+}} + \sigma^2_{P_i^{D^-}}}} \tag{5.5.5}$$

The errors are computed from the sum of the legendre moments weights-squared and the efficiency:

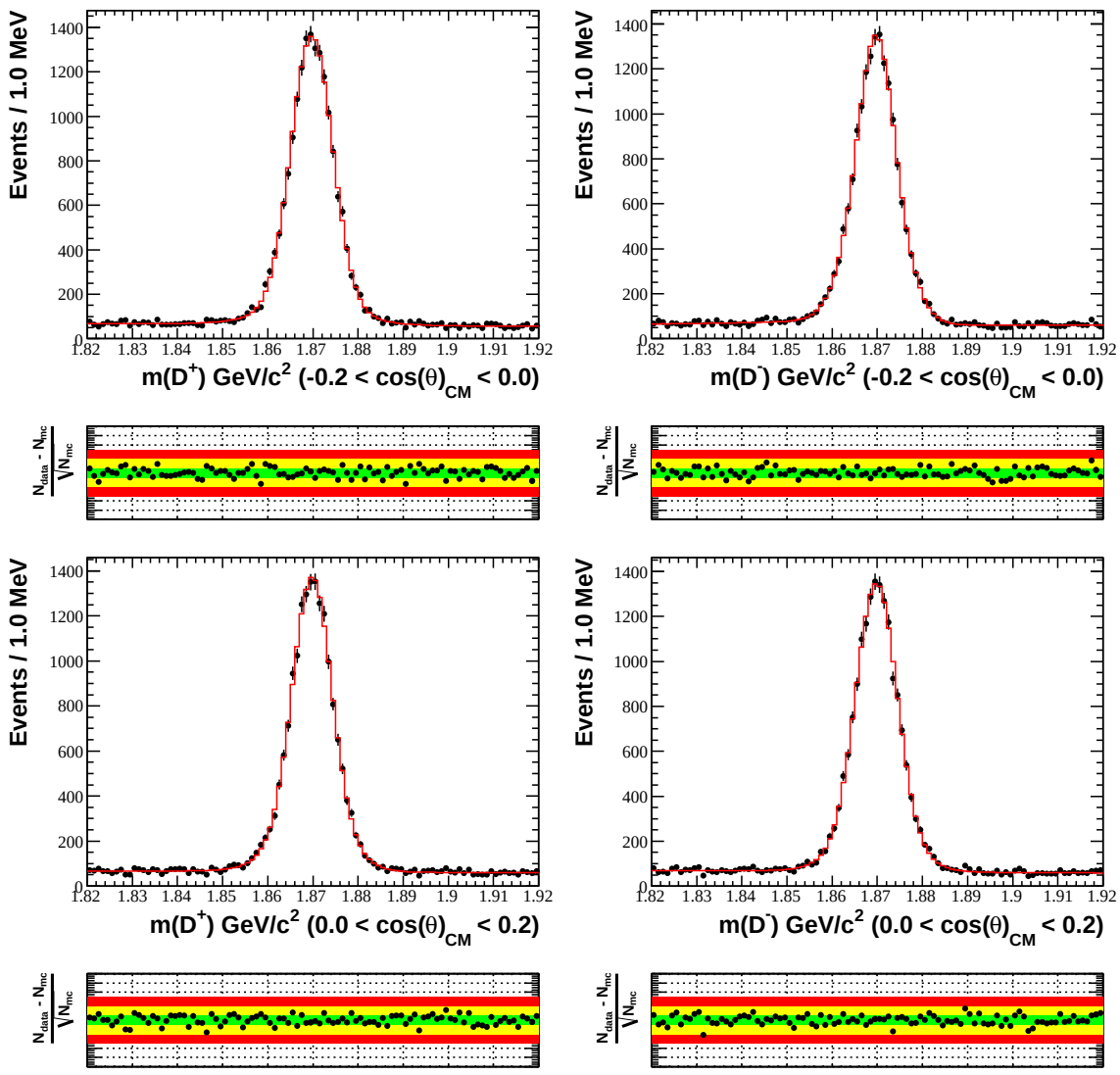

Figure 5.41: Fit results for the D^+ and D^- mass in the backward production bin (upper plots) and the forward production bin (lower plots).

$$\sigma^2_{P_i} = \frac{\sum^{Nevents} P^2_{Signal} + \sum^{Nevents} P^2_{Background}}{\epsilon_i^2} \tag{5.5.6}$$

We then calculate the $\chi^2/ndof$ over all the bins in either the KK moments or $K\pi$ moments:

$$\chi^2 = \sum_{bins} \sum_i \sum_j X_i \rho_{ij} X_j \tag{5.5.7}$$

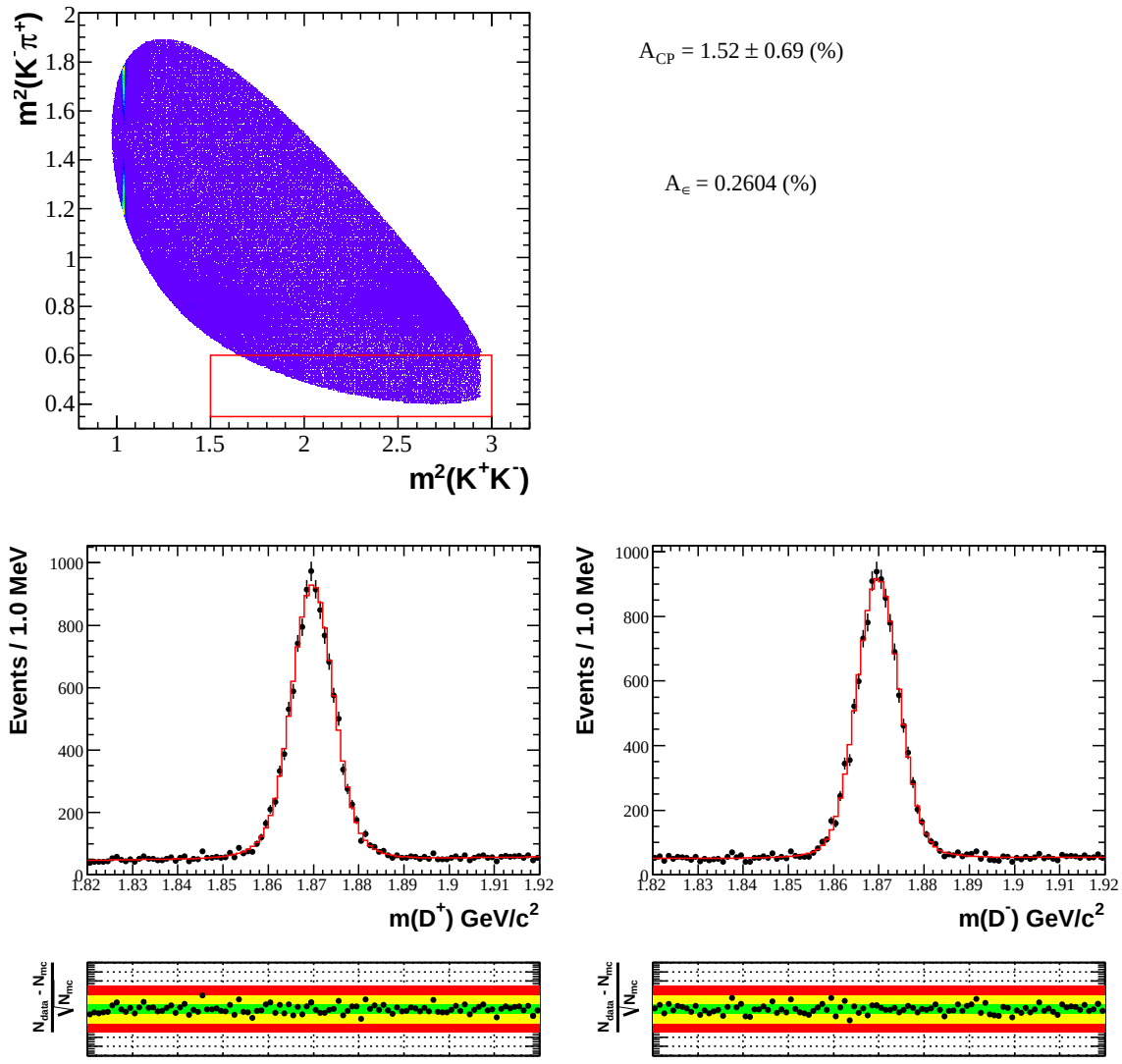

Figure 5.42: Fit results for the D^+ and D^- mass in the Dalitz plot region below $\bar{K}^{*0}(892)$.

where ρ_{ij} is the correlation coefficient for the ij moment and the number of degrees of freedom is the product of the number of bins in mass $\times$ the number of moments.

$$\rho_{ij} = \frac{\langle X_i X_j \rangle - \langle X_i \rangle \langle X_j \rangle}{\sqrt{\langle X_i^2 \rangle - \langle X_i \rangle^2}\sqrt{\langle X_j^2 \rangle - \langle X_j \rangle^2}} \tag{5.5.8}$$

The expectation values $\langle X_i \rangle$, $\langle X_i^2 \rangle$, and $\langle X_i X_j \rangle$ are evaluated from the mean of 10 measurements by splitting the sample into 10 subsamples.

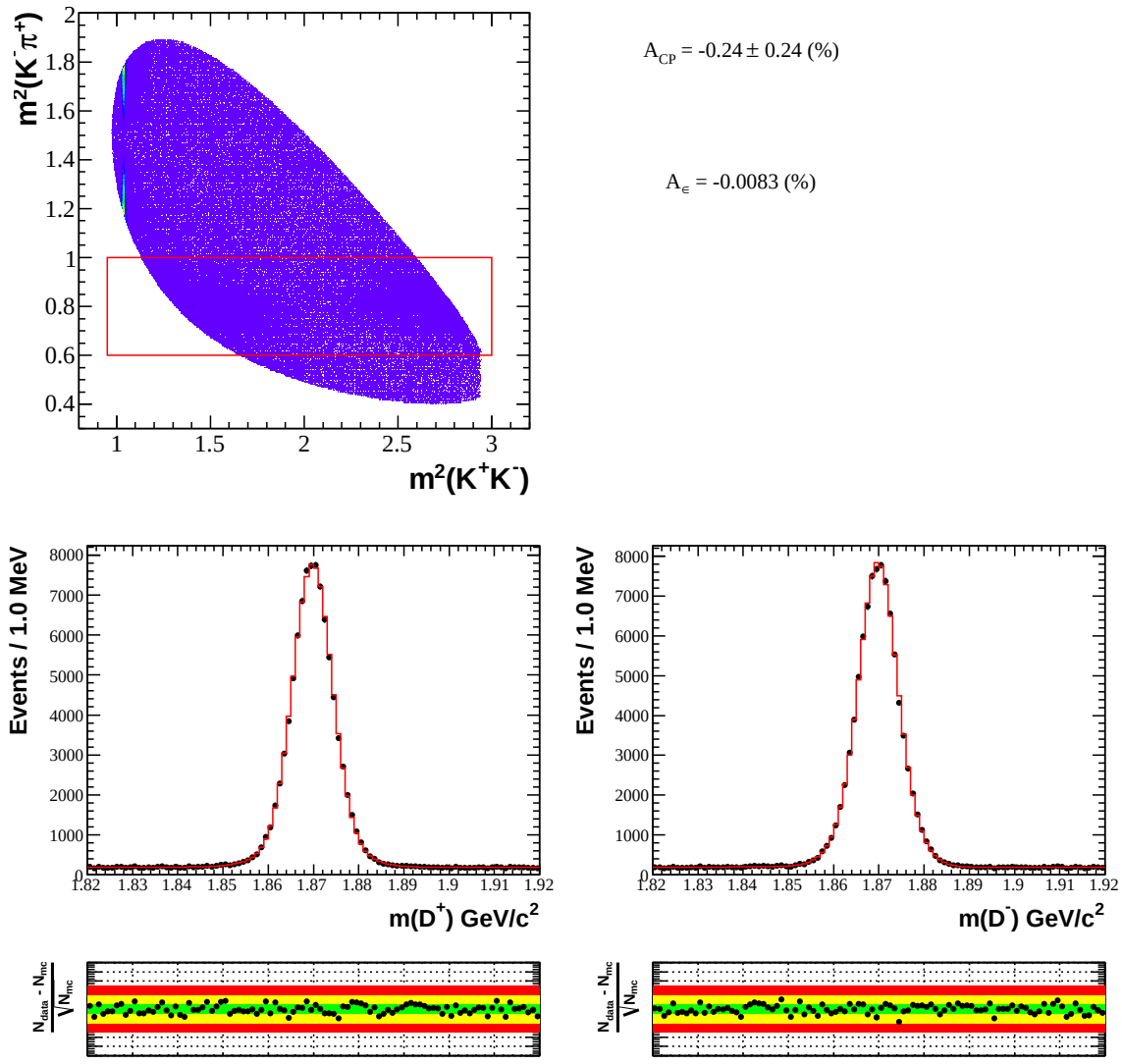

Figure 5.43: Fit results for the D^+ and D^- mass in the Dalitz plot region of $\bar{K}^{*0}(892)$.

We begin with a comparison of the charge-independent moments in the KK and $K\pi$ system for the D^+ decay and the Cabibbo-favored mode $D_s \to K^+K^-\pi^+$. The moments up to Y_7^0 for D_s are shown in Figure 5.47 and Figure 5.49 and for D^+ are shown in Figure 5.46 and Figure 5.48.

The R24c generic $c\bar{c}$ sample is analyzed here, computing the χ^2 up to the Y_7^0 moment in the KK and $K\pi$ system. The results of the analysis are found in Table 5.15.

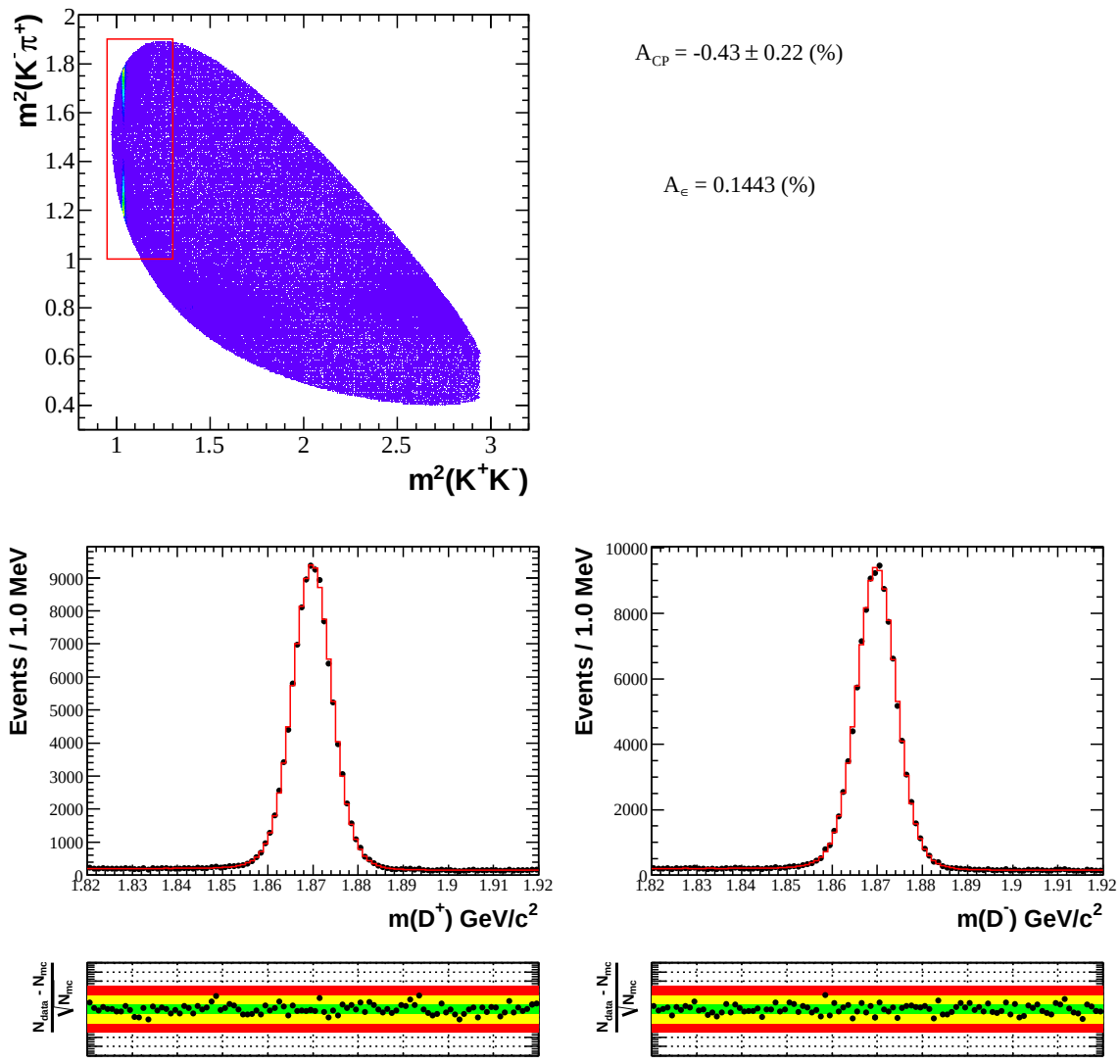

Figure 5.44: Fit results for the D^+ and D^- mass in the Dalitz plot region of the $\phi(1020)$.

System	χ^2	ndof	$\chi^2/ndof$
KK	307.5	288	1.07
$K\pi$	409.3	288	1.42

Table 5.15: Results of moments analysis with the R24c generic $c\bar{c}$ Monte Carlo data set.

5.5.4. Dalitz plot Model Dependent CP Asymmetry. We describe this measurement in the following sections.

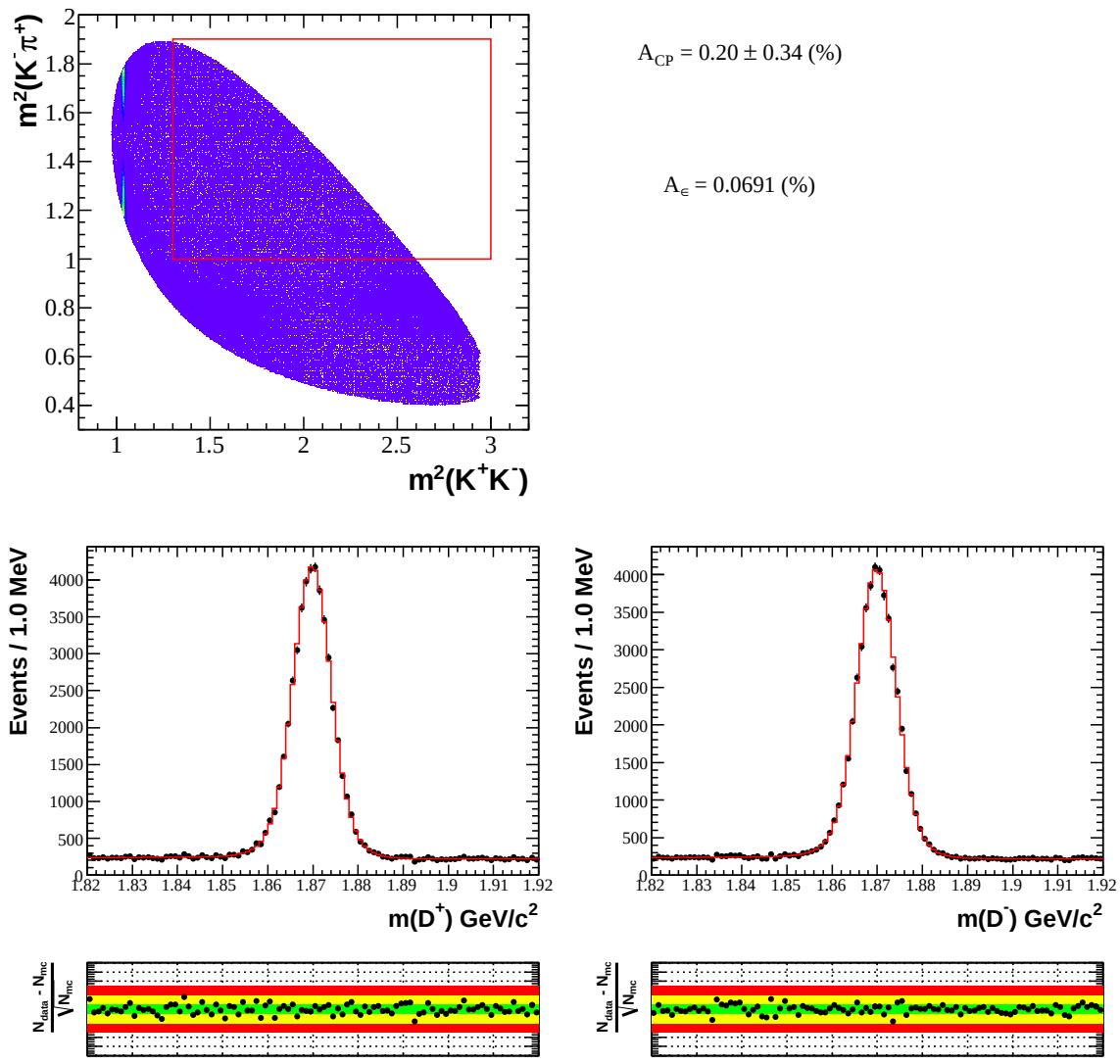

Figure 5.45: Fit results for the D^+ and D^- mass in the Dalitz plot region above the ϕ and $\bar{K}^{*0}$.

5.6. Dalitz Analysis Amplitudes

5.6.1. Overview. The analysis strategy to measure the CP asymmetry as a function of Dalitz plot position for the decay of the $D^+ \to K^+K^-\pi^+$ is similar to the typical Dalitz plot analysis. We are required to have the following:

•Model of the background as function of the Dalitz plot position (section 5.2.6)

•Detector reconstruction efficiency as a function of the Dalitz plot position (section 5.3.1)

•Model to describe the decay of D^+ meson (section 5.6.4)

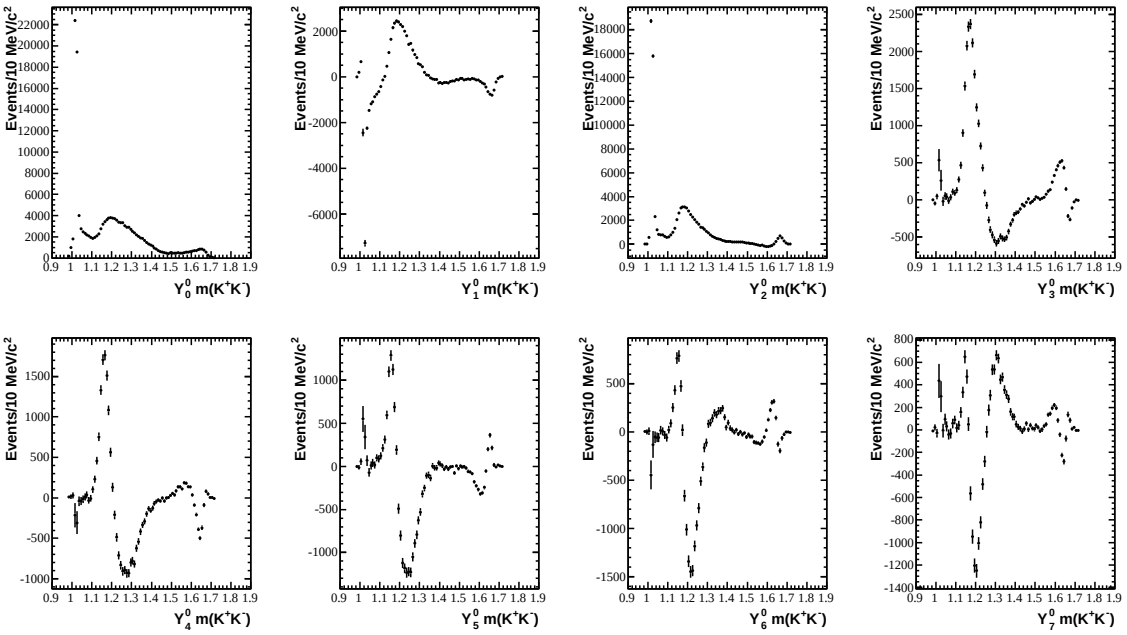

Figure 5.46: $D \to K^+K^-\pi^+$ moments in the K^+K^- system

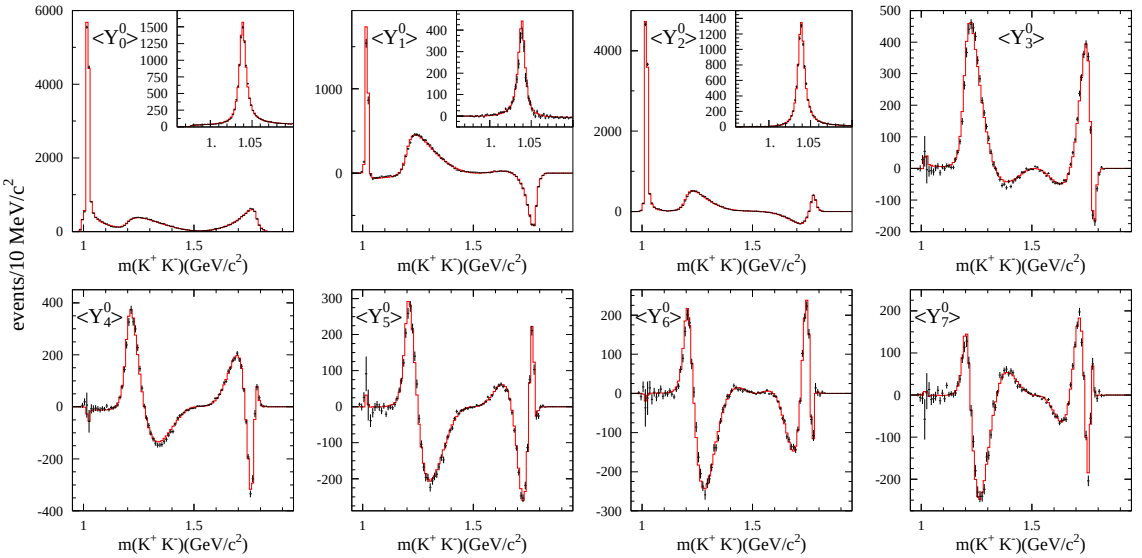

Figure 5.47: $D_s \to K^+K^-\pi^+$ moments in the K^+K^- system

In order to measure the CP asymmetry we need to account for three possible sources of systematic error

- Background Asymmetry (section 5.2.2)
- Tracking asymmetry (section 5.3.2

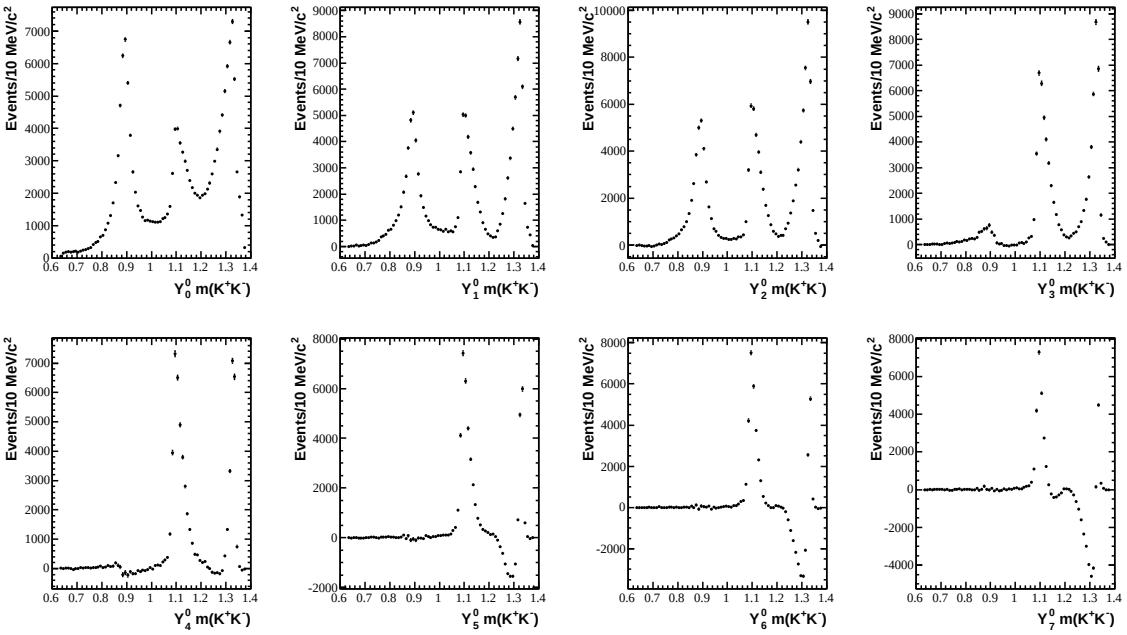

Figure 5.48: $D \to K^+K^-\pi^+$ moments in the $K^-\pi^+$ system

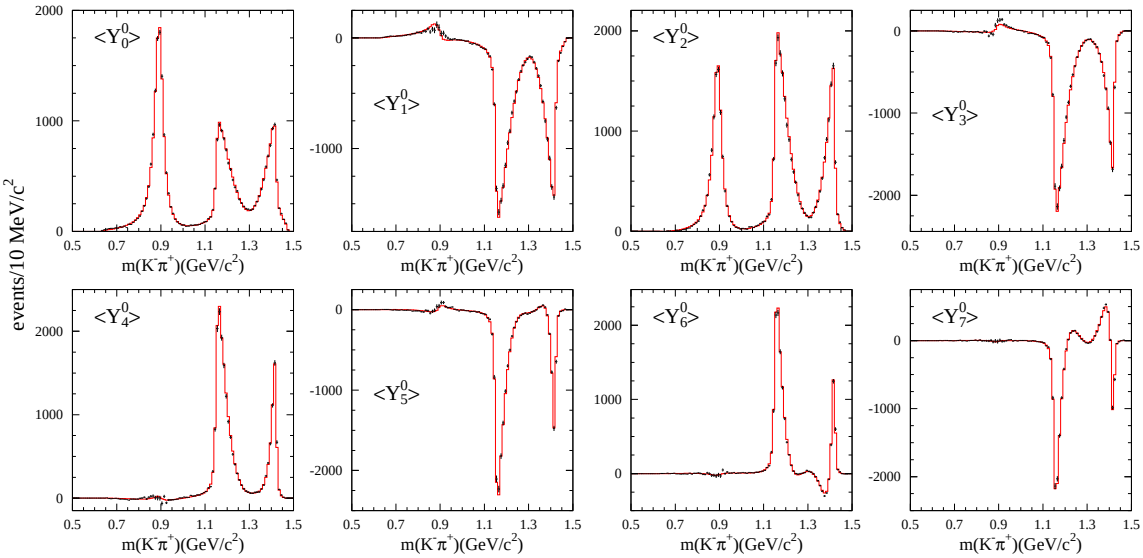

Figure 5.49: $D_s \to K^+K^-\pi^+$ moments in the $K^-\pi^+$ system

•Differences in the production distribution of the Monte Carlo (p_{CM} and $\cos(\theta)_{CM}$) and what is observed in data (section 5.6.2)

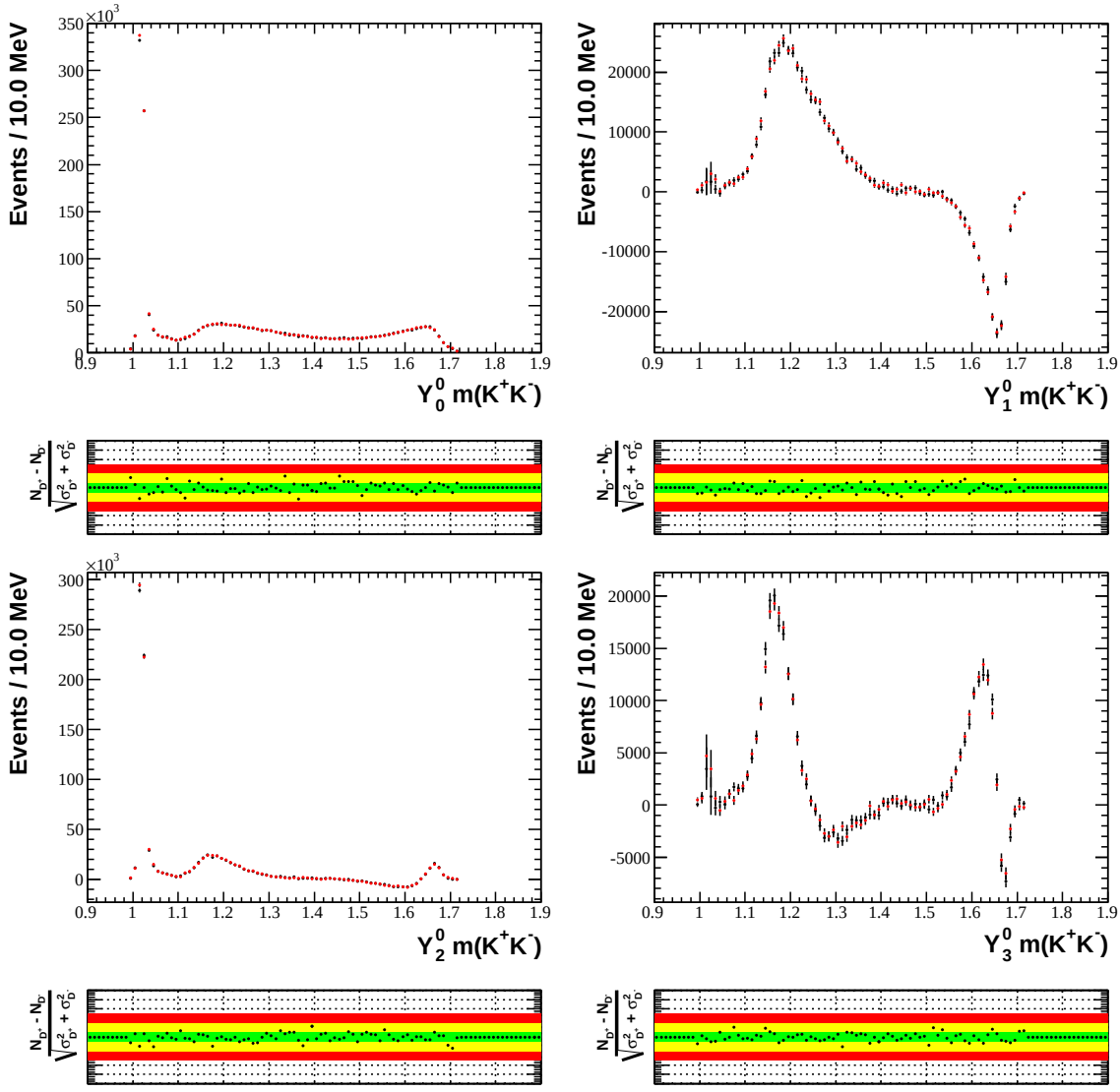

Figure 5.50: R24c generic $c\bar{c}$ $D \to K^+K^-\pi^+$ moments and residuals in the K^+K^- system for D^+ and D^- events.

The background asymmetry is removed through event selection and track quality cuts, several studies are documented to show that the asymmetry in the background is small.

We account for the two additional sources of systematic error by correcting the Monte Carlo from what we observe in data, propagating the effects throughthe Dalitz plot efficiency.

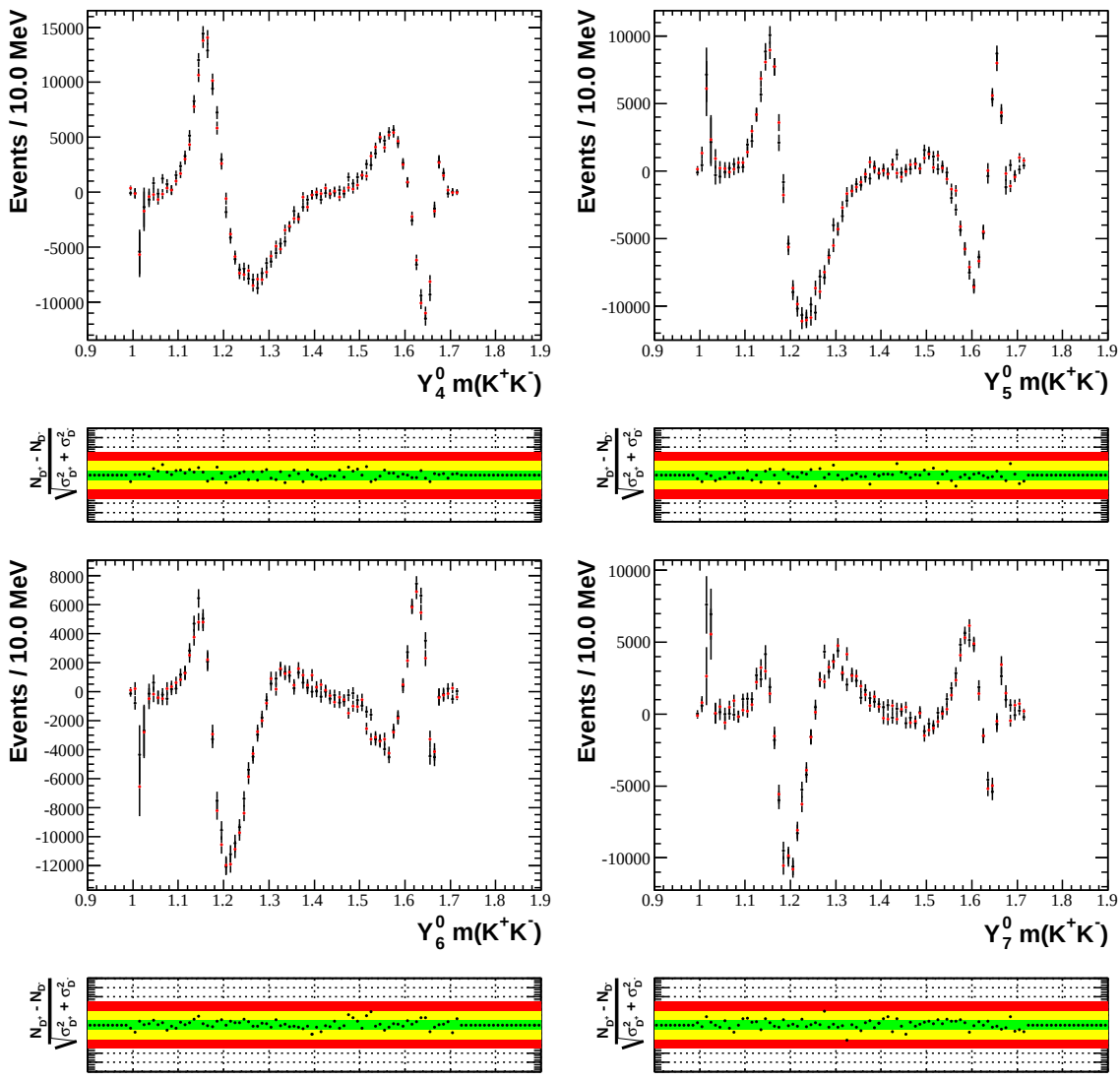

Figure 5.51: R24c generic $c\bar{c}$ $D \to K^+K^-\pi^+$ moments and residuals in the K^+K^- system for D^+ and D^- events.

Using uncontrained Dalitz plot distributions from the sideband data, we employ a k-Nearest Neighbor algorithm as an estimation of the probability density of the background in the signal region of the Dalitz plot.

The efficiency is modeled by an artificial neural network which we train from a two-dimensionally binned Dalitz plot efficiency.

As a starting point for the Dalitz plot model of D decays, we consider the Isobar model, which is the coherent sum of complex amplitudes described by Relativistic Breit-Wigner functions. All resonances up to the $f_0(1710)$ which decay either to

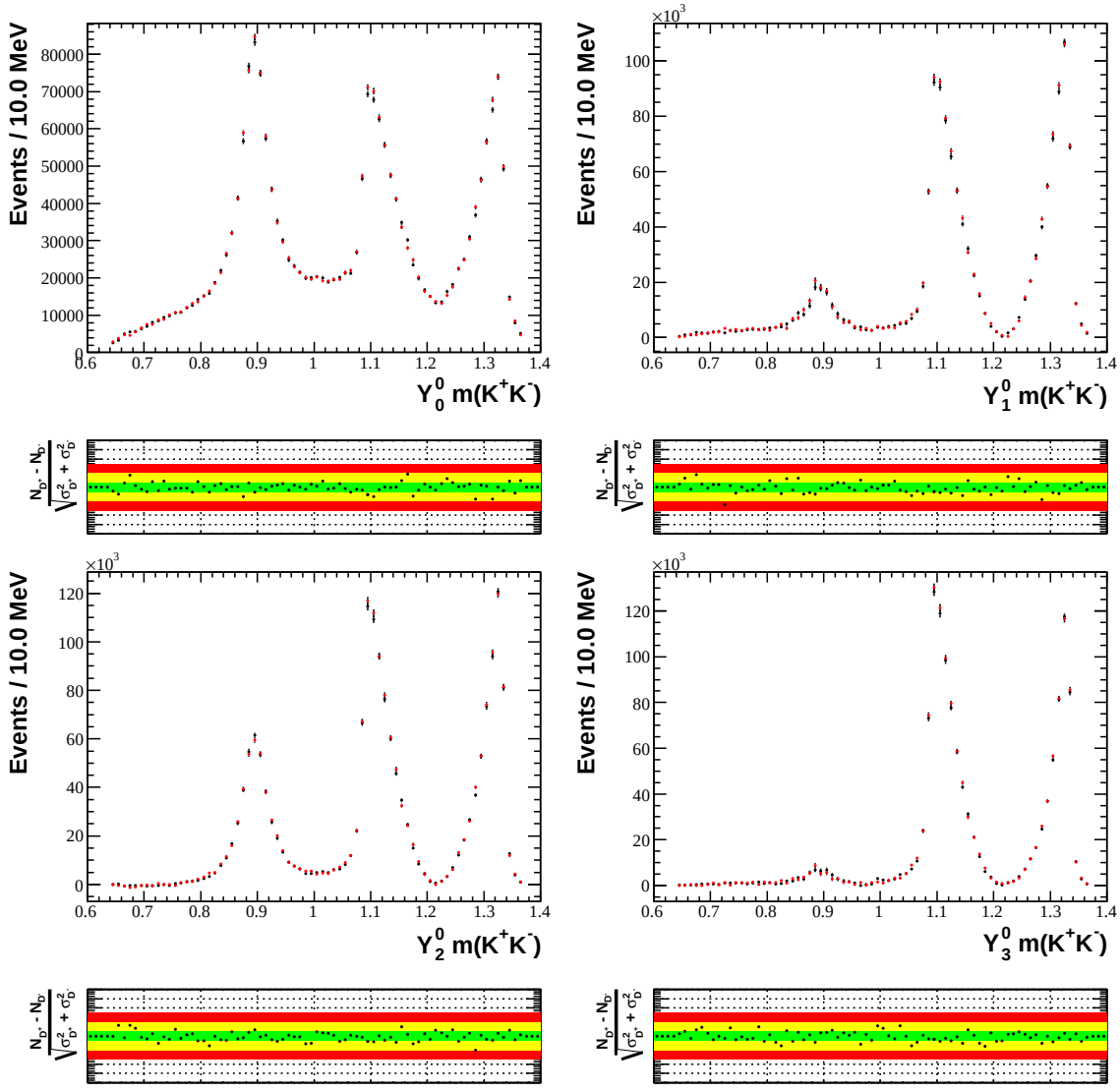

Figure 5.52: R24c generic $c\bar{c}$ $D \to K^+K^-\pi^+$ moments and residuals in the $K^-\pi^+$ system for D^+ and D^- events.

$K^-\pi^+$ or K^+K^- are included in the fit to the observed data from the entire $\Upsilon(4S)$ BaBar data set, including any additional Off-Peak data recorded during Runs 1 through 6.

5.6.2. Production Distribution of the D^+ Meson. We rely on the BaBar Monte Carlo as a model for the production of the D meson. The model is only valid if

$$N(D^+(\cos(\theta)_{CM})) = N(D^-(-\cos(\theta)_{CM})) \tag{5.6.1}$$

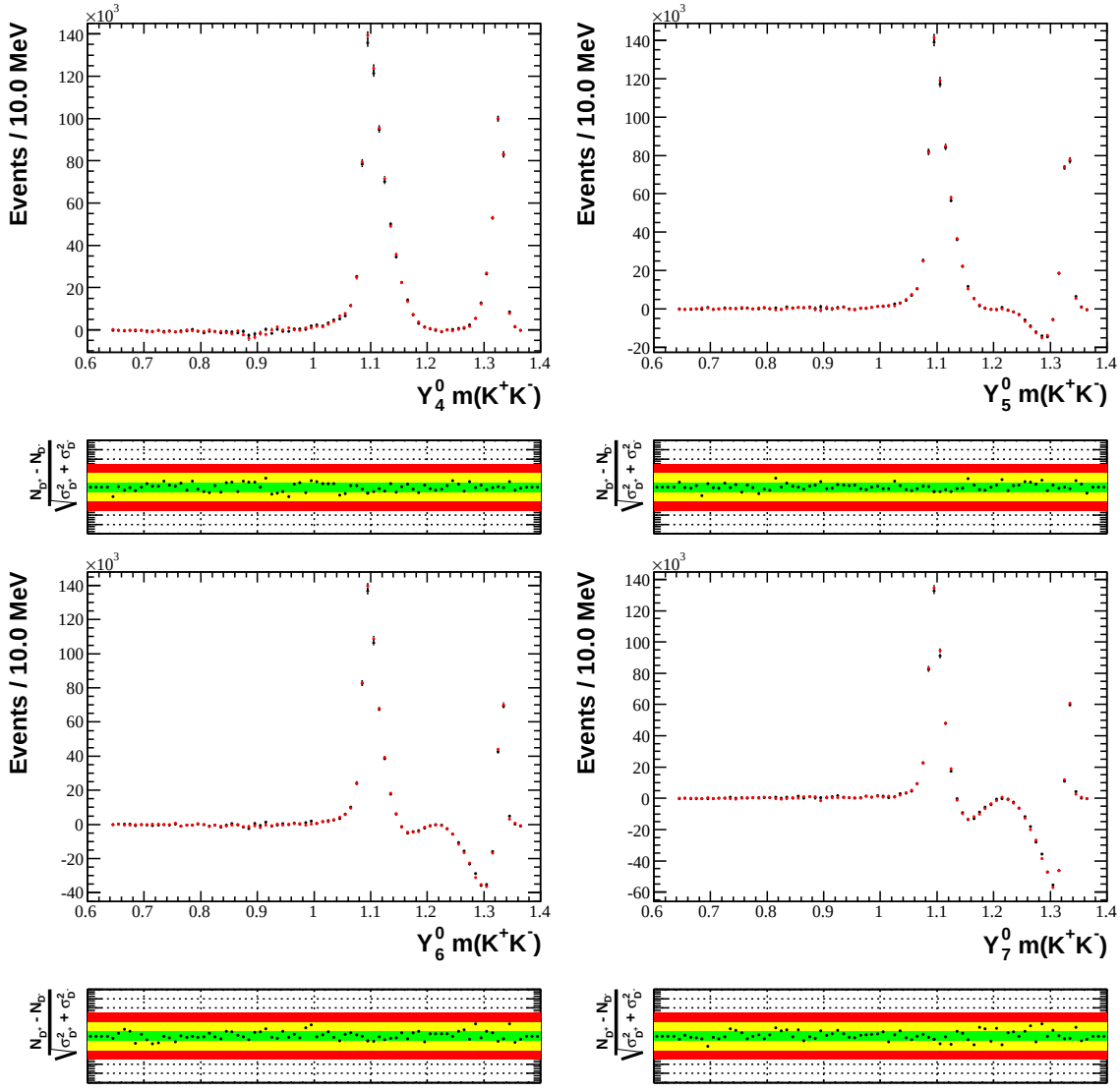

Figure 5.53: R24c generic $c\bar{c}$ $D \to K^+K^-\pi^+$ moments and residuals in the $K^-\pi^+$ system for D^+ and D^- events.

We measure the χ^2 over the two-dimensional production space (p_{CM}, $\cos(\theta)_{CM}$)), with the production angle of the D^- mapped to the D^+ production angle. The χ^2 is 3025.21 for 2500 bins. The two-dimensional residual distribution is shown in Figure 5.54. The production asymmetry before and after mapping the D^- production angle is shown in Figure 5.55.

To account for differences in the BaBar Monte Carlo production model and what is observed in data, we begin with a probability distribution function that describes

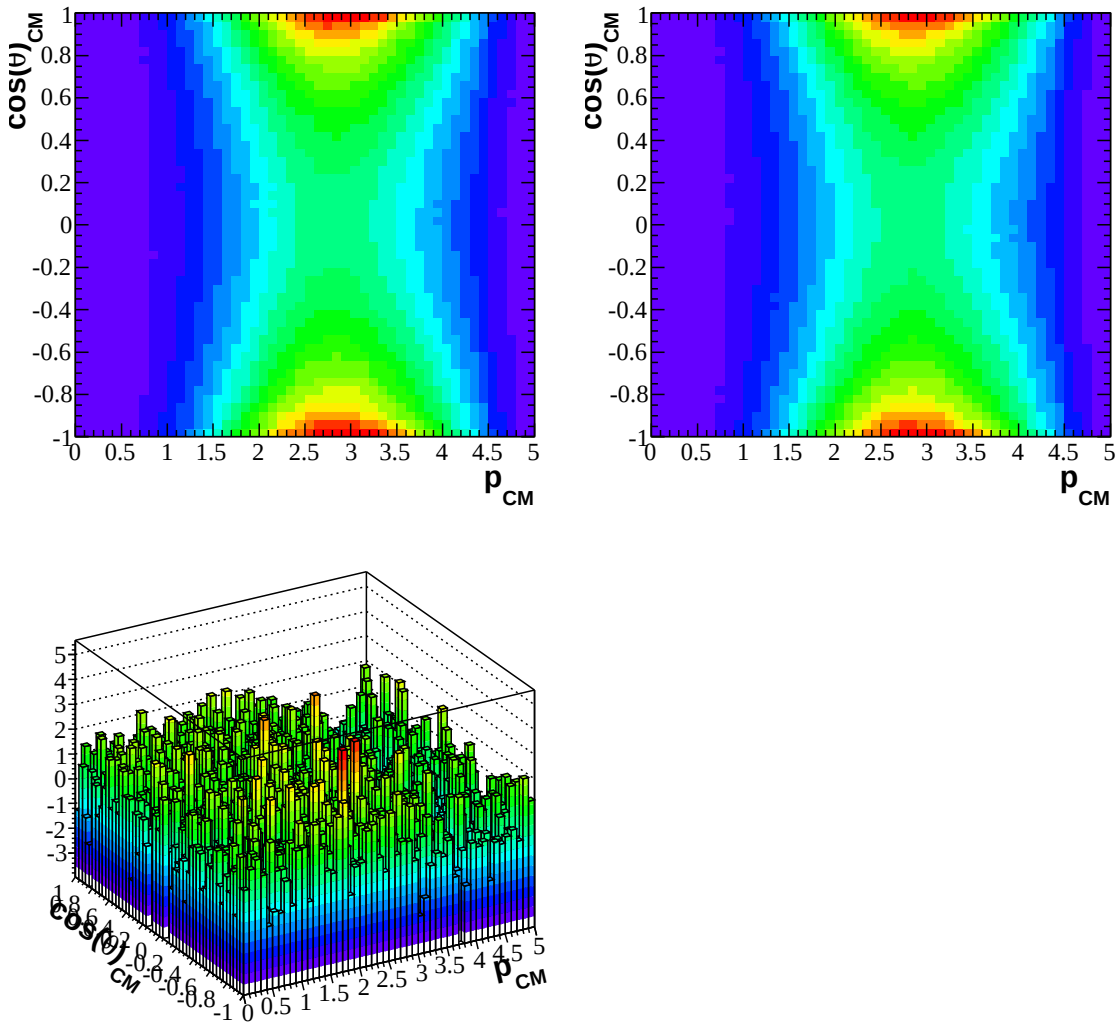

Figure 5.54: Top left plot is the production distribution for D^+ events, and the top right is the production distribution for D^- events where the production angle is taken as $-\cos(\theta)_{CM}$. The bottom shows the residual distribution of the D^+ and D^- model.

the generated BaBar Monte Carlo. We model the 2-dimensional generated distrubtion of p_{CM} and $cos(\theta)_{CM}$ with a k Nearest-Neighbor (kNN) algorithm (Purohit). We randomly select a sub-sample of 500,000 events from the 50 million generated events in our sample. We achieve a description of the production distribution in the Monte Carlo with k = 6. The Monte Carlo and kNN model are shown in Figure 5.56.

We obtain the distrbution of the production variables (p_{CM}, $\cos(\theta)_{CM}$) of signal events in data using background subtraction. The background events are taken

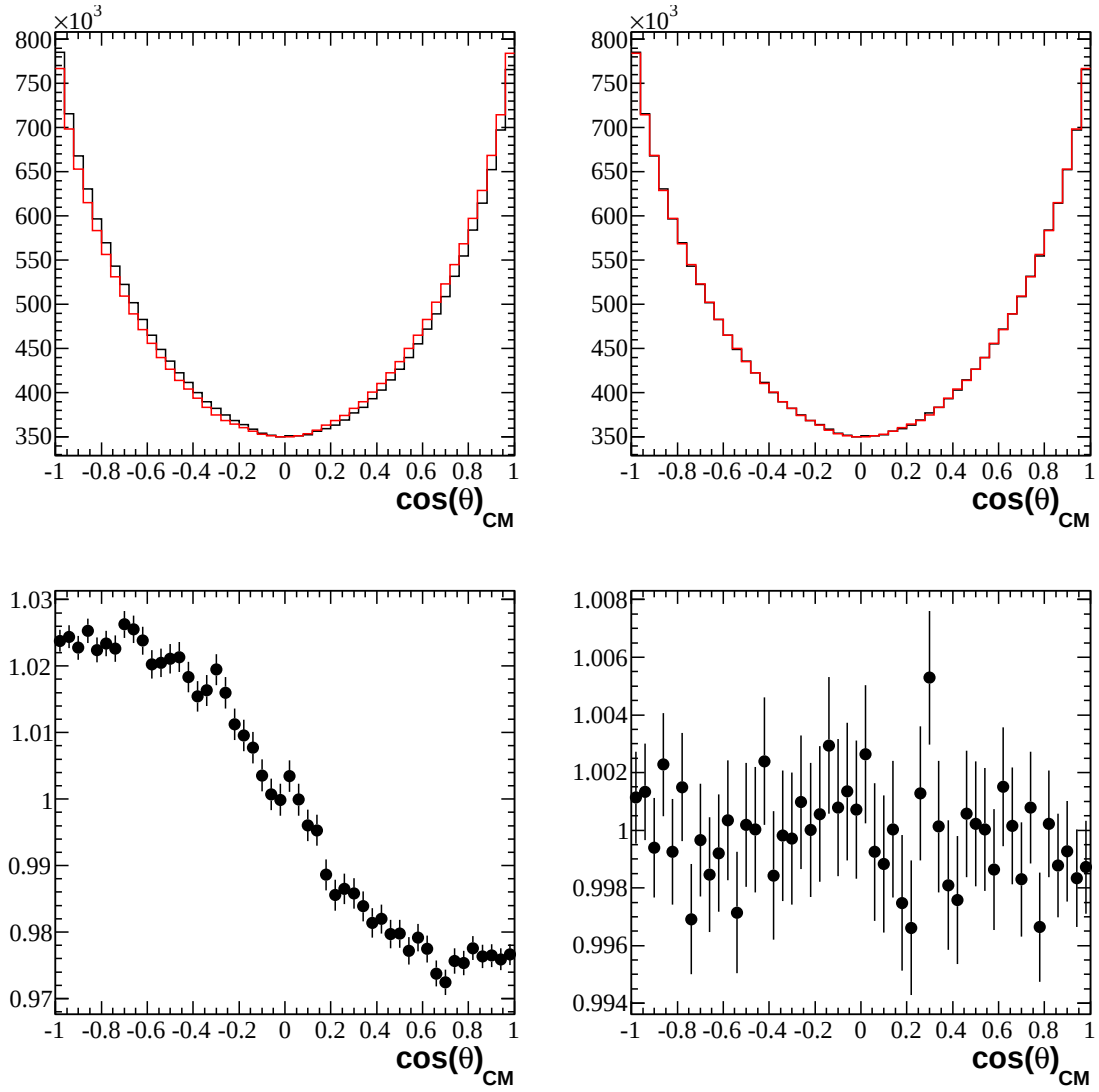

Figure 5.55: The left plots show the forward-backward asymmetry in the production of the D meson. The right plot shows the asymmetry removed after mapping the D^- production angle to $-\cos(\theta)_{CM}$.

from the upper and lower mass sideband regions, and the signal events are taken between $\pm 2\sigma$ of the mean of D. The distributions of events in the signal region (SR) ($P_{SR}(p_{CM}, \cos(\theta)_{CM})$) and in the sibeband (BR) ($P_{BR}(p_{CM}, \cos(\theta)CM)$) contain fractions of signal events α and β. α and β are known from the mass fit, using the signal pdf $S(m(D))$ and the background pdf $B(m(D))$. We can obtain the signal (S) ($P_S(p_{CM}, \cos(\theta)_{CM})$ and background (B) ($P_B(p_{CM}, \cos(\theta)_{CM})$ distributions from the following relationship:

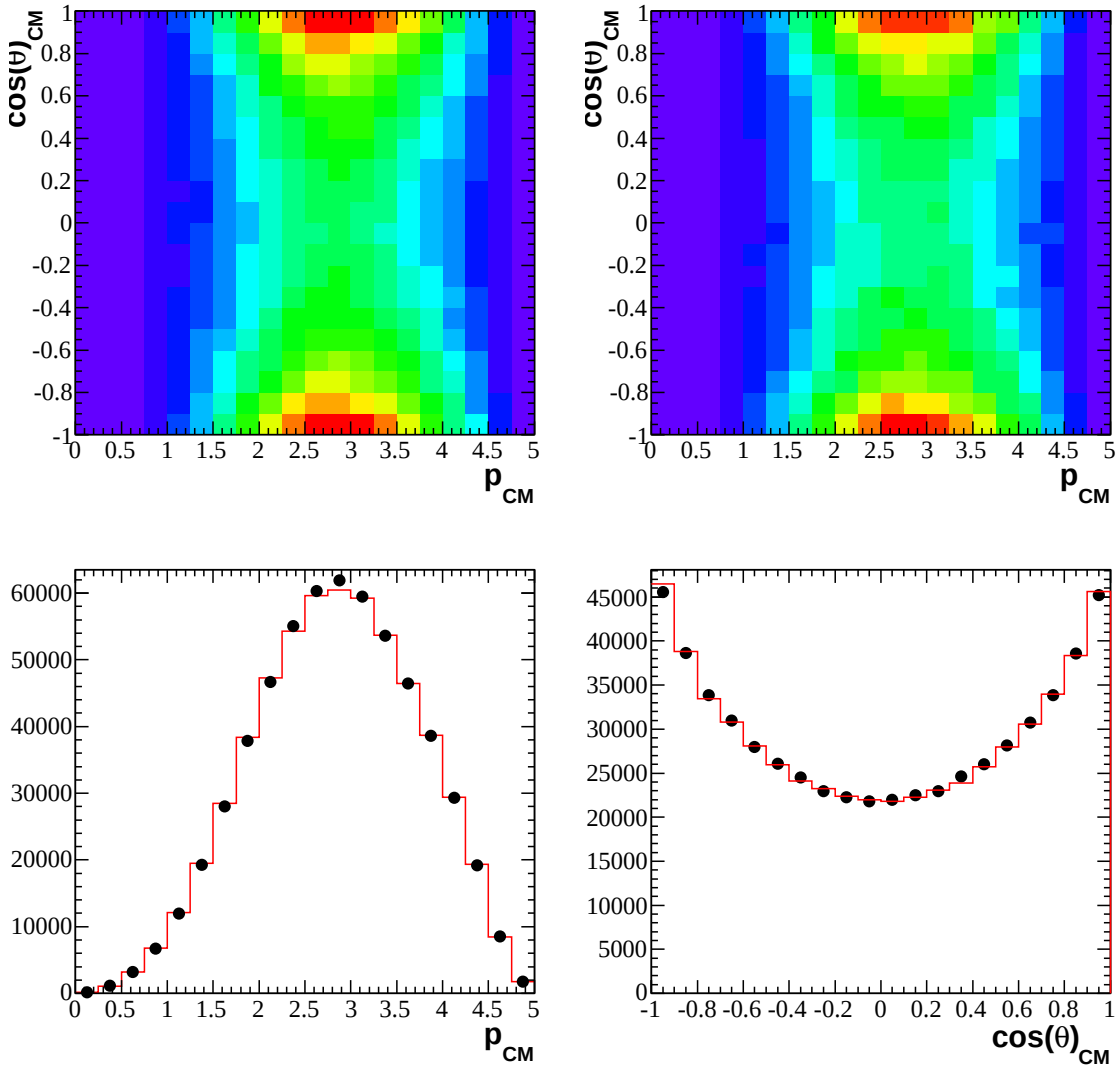

Figure 5.56: k Nearest-Neighbor model as a function of p_{CM} and $cos(\theta)_{CM}$. The BaBar MC is shown in the top left, top right are events generated from the kNN. The lower plots are the projections with the kNN model shown in red.

$$\alpha = \frac{\int_{SR} S(m(D))}{\int_{SR} S(m(D)) + \int_{SR} B(m(D))} \tag{5.6.2}$$

$$\beta = \frac{\int_{BR} S(m(D))}{\int_{BR} S(m(D)) + \int_{BR} B(m(D))} \tag{5.6.3}$$

$$\begin{pmatrix} P_{SR}(p_{CM}, \cos(\theta)_{CM}) \\ P_{BR}(p_{CM}, \cos(\theta)_{CM}) \end{pmatrix} = \begin{pmatrix} \alpha & (1-\alpha) \\ \beta & (1-\beta) \end{pmatrix} \begin{pmatrix} P_S(p_{CM}, \cos(\theta)_{CM}) \\ P_B(p_{CM}, \cos(\theta)_{CM}) \end{pmatrix} \quad (5.6.4)$$

We obtain the distribution of signal events according to equation 5.6.4 as a function of $\cos(\theta)_{CM}$ in equally populated bins of p_{CM}. The binning of the data in p_{CM} and $\cos(\theta)_{CM}$ are shown in Figure 5.57. The two dimensional P_S and P_B distributions and their projections are shown in Figure 5.58. The equally populated histograms are shown in Figure 5.59. The distribution of Monte Carlo events with respect to the binning in data is shown in Figure 5.60.

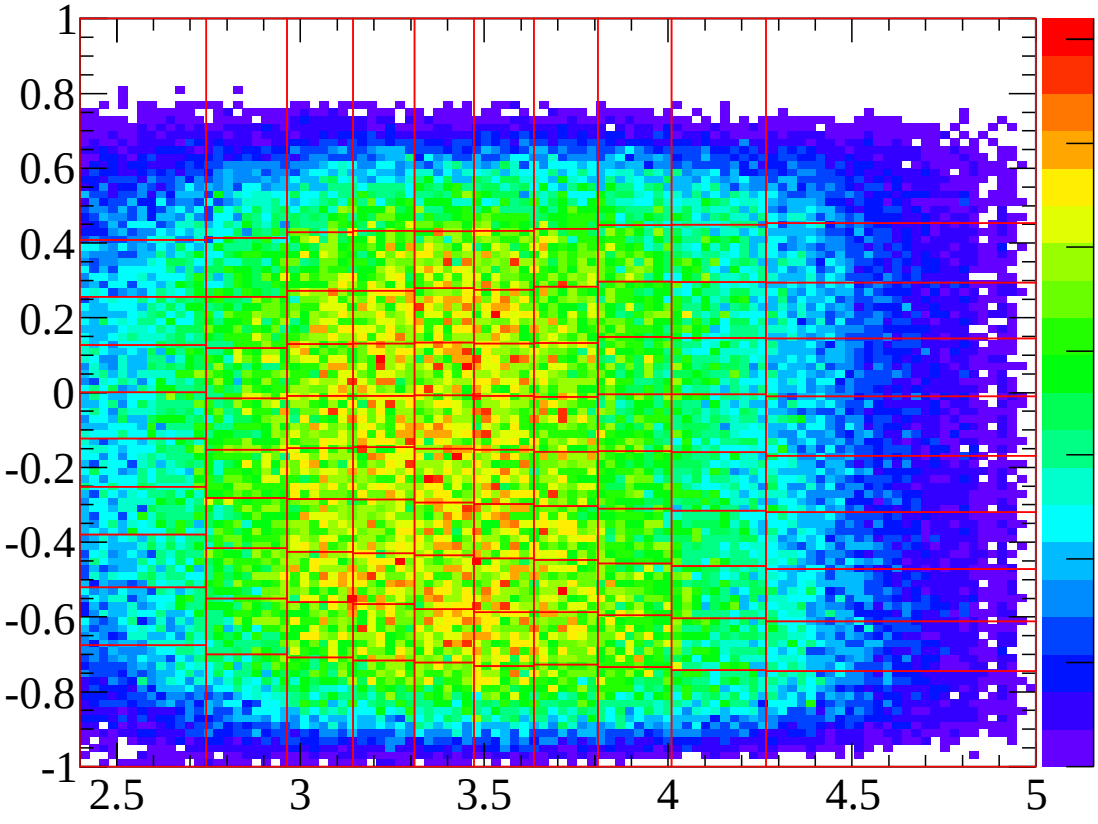

Figure 5.57: Binning of the distribution of production variables for events in the signal region. The same binning is used for the background events

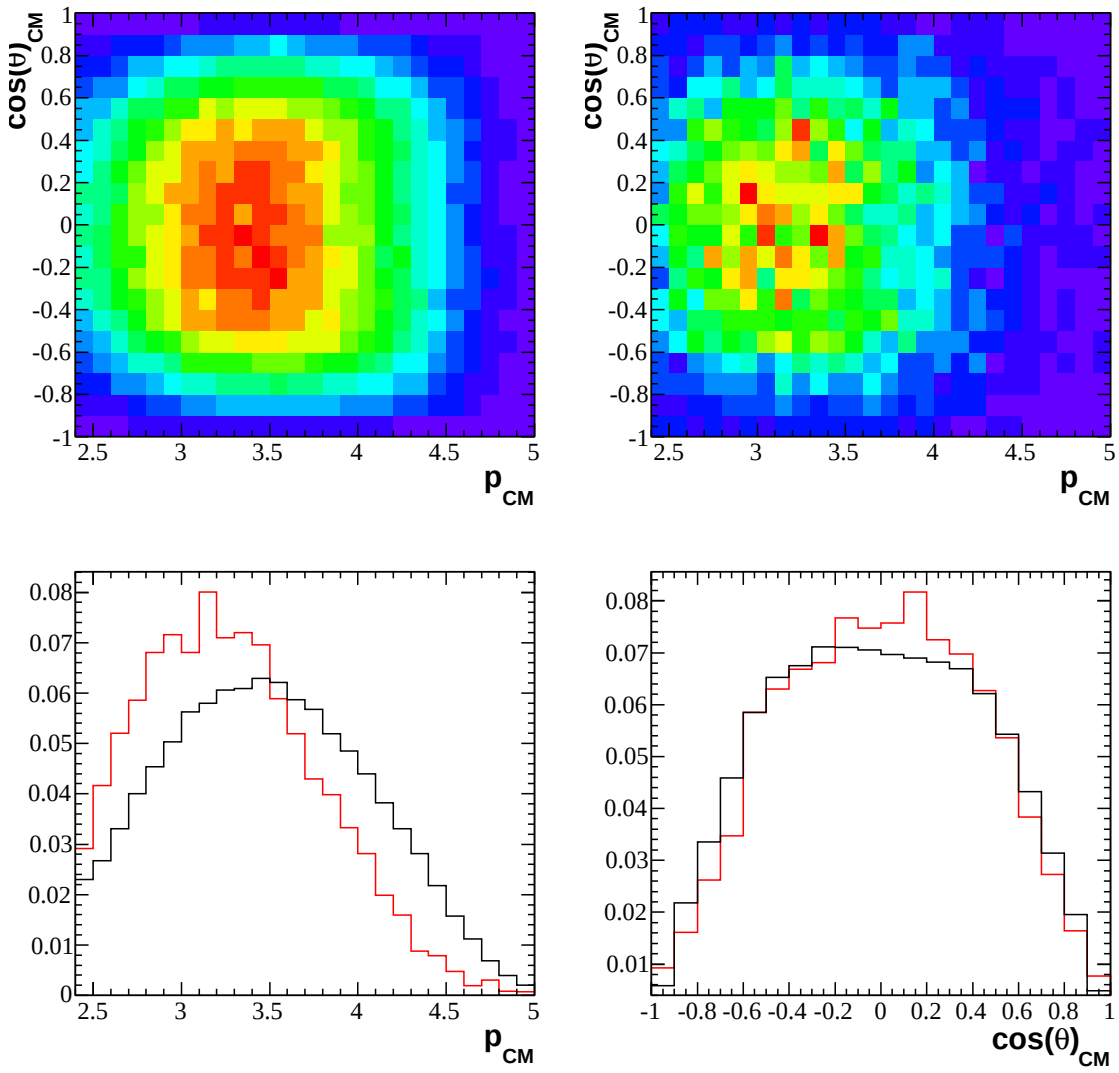

Figure 5.58: Two-dimensional histogram of P_S (top left) and P_B (top right). The projections are shown in the bottom plots, where the background is shown in red.

Now that we have the signal distributions in data, we can find the ratio of data and Monte Carlo, $P_R(p_{CM}, \cos(\theta)_{CM}$. The ratio is a correction that can be applied to the signal Monte Carlo when meauring the reconstruction efficiency. The ratio plots are shown in Figure 5.62. The ratios are obtained from the ratio of plots in data (Figure 5.59) and the Monte Carlo plots (Figure 5.60) scaled to the number of events in data.

5.6.3. Data Corrections to the Monte Carlo. We correct for tracking asymmetries and production modeling in the Monte Carlo, using data to Monte Carlo

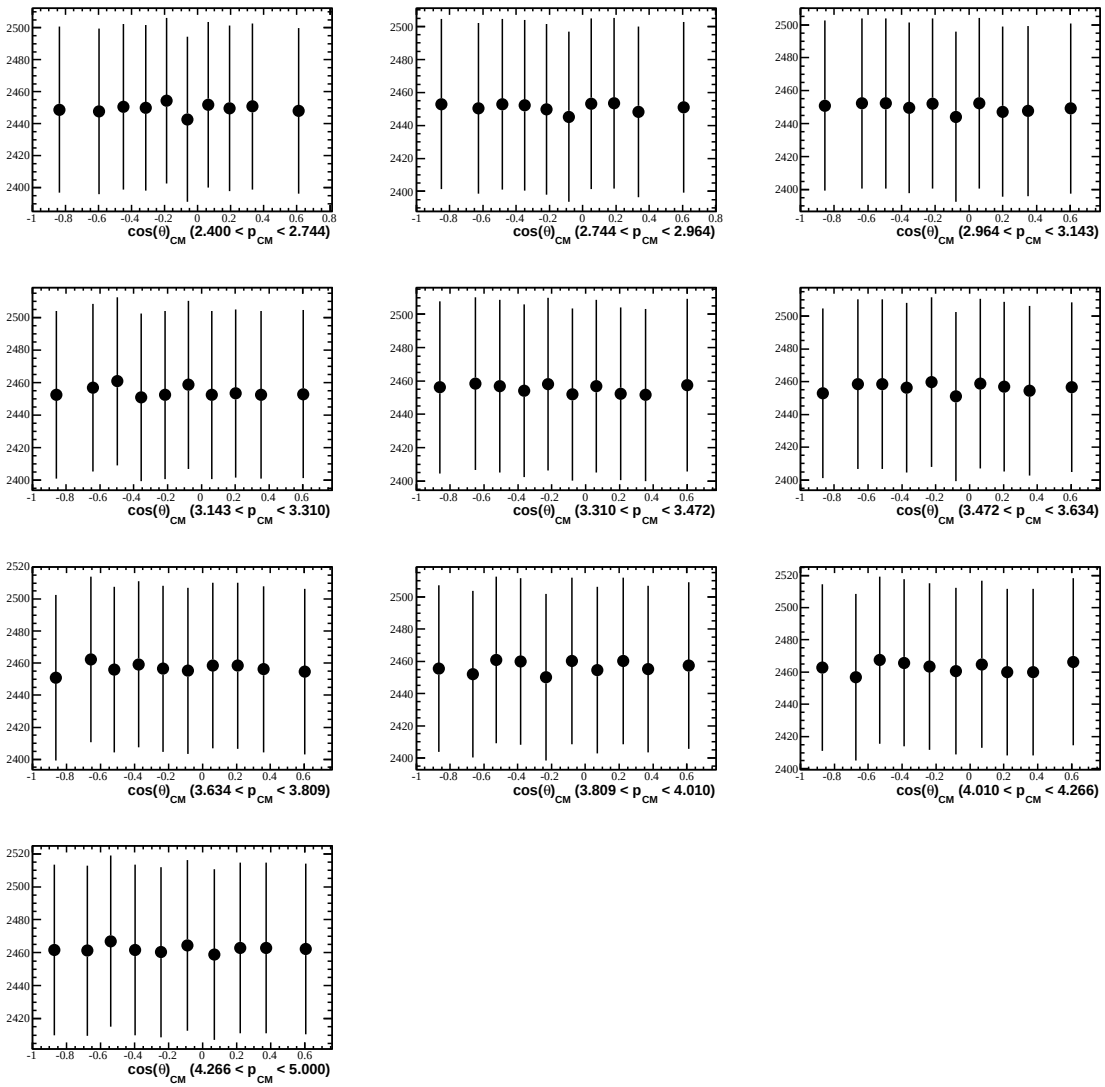

Figure 5.59: Equally populated histrograms as a function of $\cos(\theta)_{CM}$ in bins of p_{CM}.

ratios. The first correction applied is the tracking asymmetry correction, which includes the tracking efficiency and asymmetry measured from the decays of τ leptons.

The tracking ratio is taken as the following ratio of tracking efficiencies:

$$R_{Track} = \frac{[\epsilon^{\pm}_{K_1}(p_3(K_1))\epsilon^{\mp}_{K_2}(p_3(K_2))\epsilon^{\pm}_{\pi}(p_3(\pi))]_{Data}}{[\epsilon^{\pm}_{K_1}(p_3(K_1))\epsilon^{\mp}_{K_2}(p_3(K_2))\epsilon^{\pm}_{\pi}(p_3(\pi))]_{MC}} \tag{5.6.5}$$

The tracking efficiencies are obtained from the Tau31 study which is documented in BAD 2258 [**37**]. The production ratios $P_R(p_{CM},\ \cos(\theta)_{CM})$ are found in Figure 5.62.

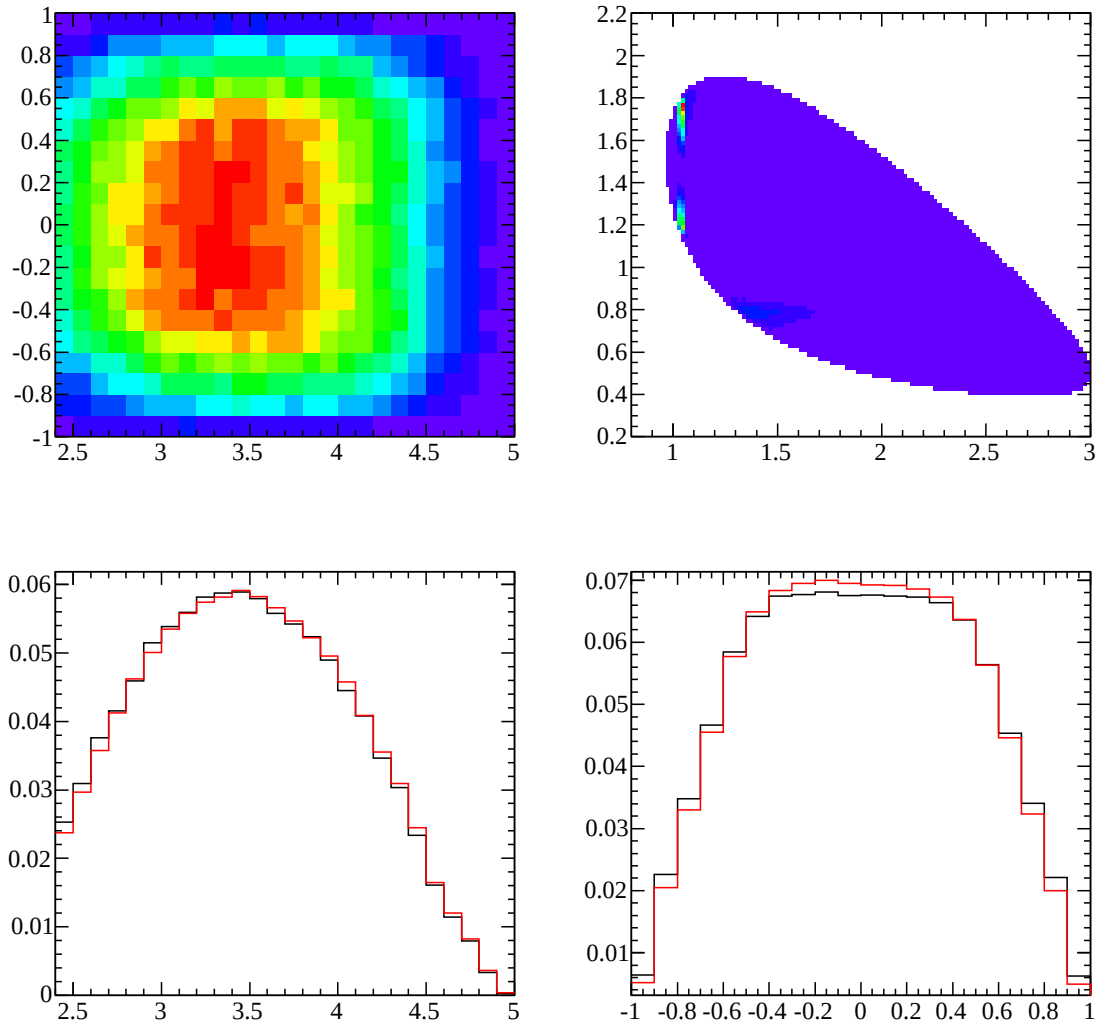

Figure 5.60: Production distributions in data and reconstructed signal Monte Carlo (re-weighted by the Isobar model). The top histograms show the Monte Carlo distrbutions. The projections of data (black histogram) and Monte Carlo (red histogram) are shown along the bottom.

The Dalitz plot efficienecy $\epsilon_{MC}(x,y)$ now becomes the following:

$$\epsilon_{MC} \rightarrow \epsilon'_{MC} = P_R(p_{CM}, \cos(\theta)_{CM}) R_{Track}(p_3(K_1^{\pm}), p_3(K_2^{\mp}), p_3(\pi_3^{\pm}) \epsilon_{MC} \qquad (5.6.6)$$

The Monte Carlo underestimates the tracking efficiency, which is evident in the plots which compares the following Dalitz plot efficiencies

•Monte Carlo efficiency

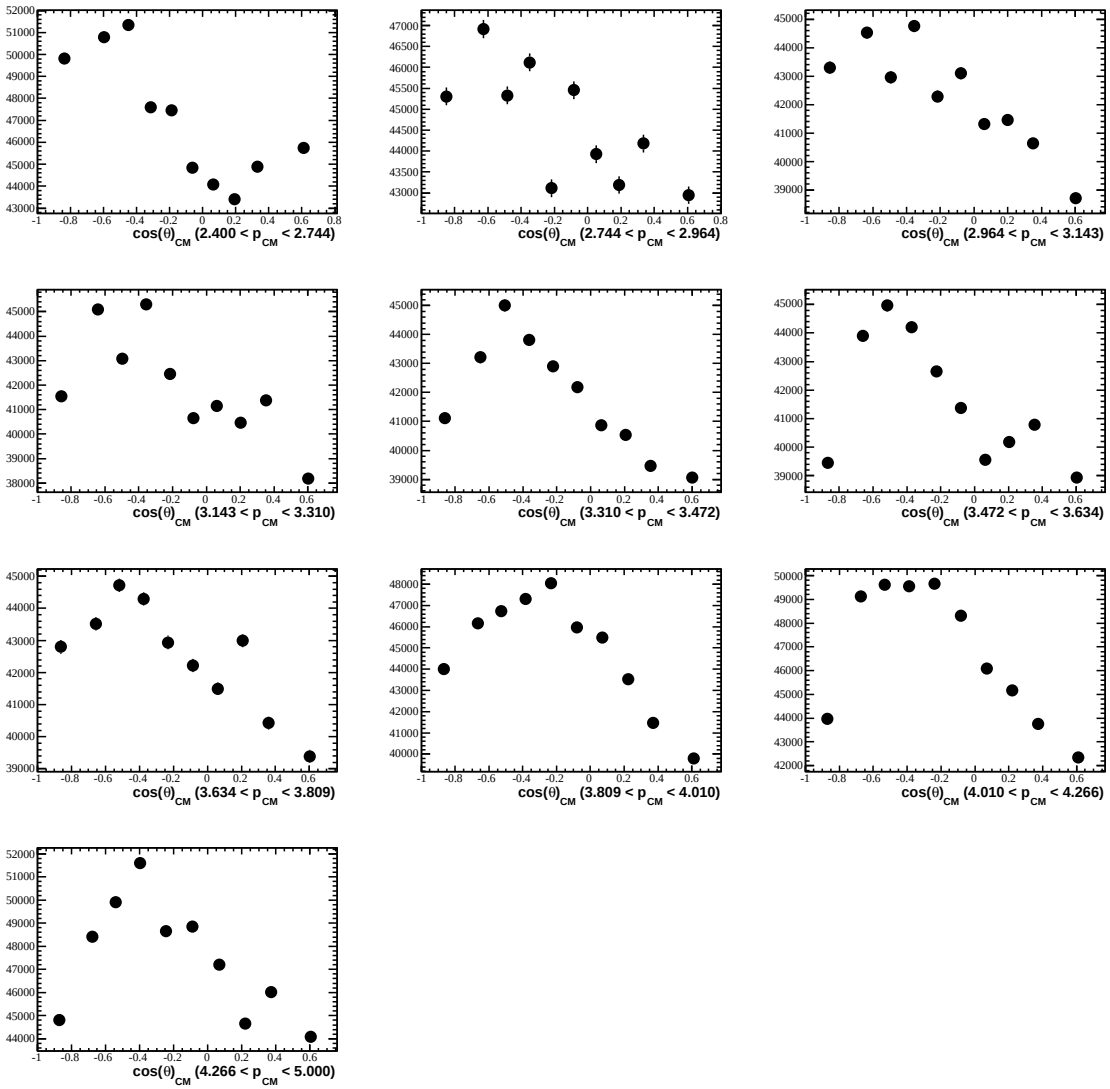

Figure 5.61: Monte Carlo histrograms as a function of $\cos(\theta)_{CM}$ in bins of p_{CM}. The binning is chosen from data.

- Monte Carlo efficiency corrected for tracking
- Monte Carlo efficiency corrected for tracking and production modeling

The comparison plots of these effiencies are shown in Figure 5.63 and Figure 5.64

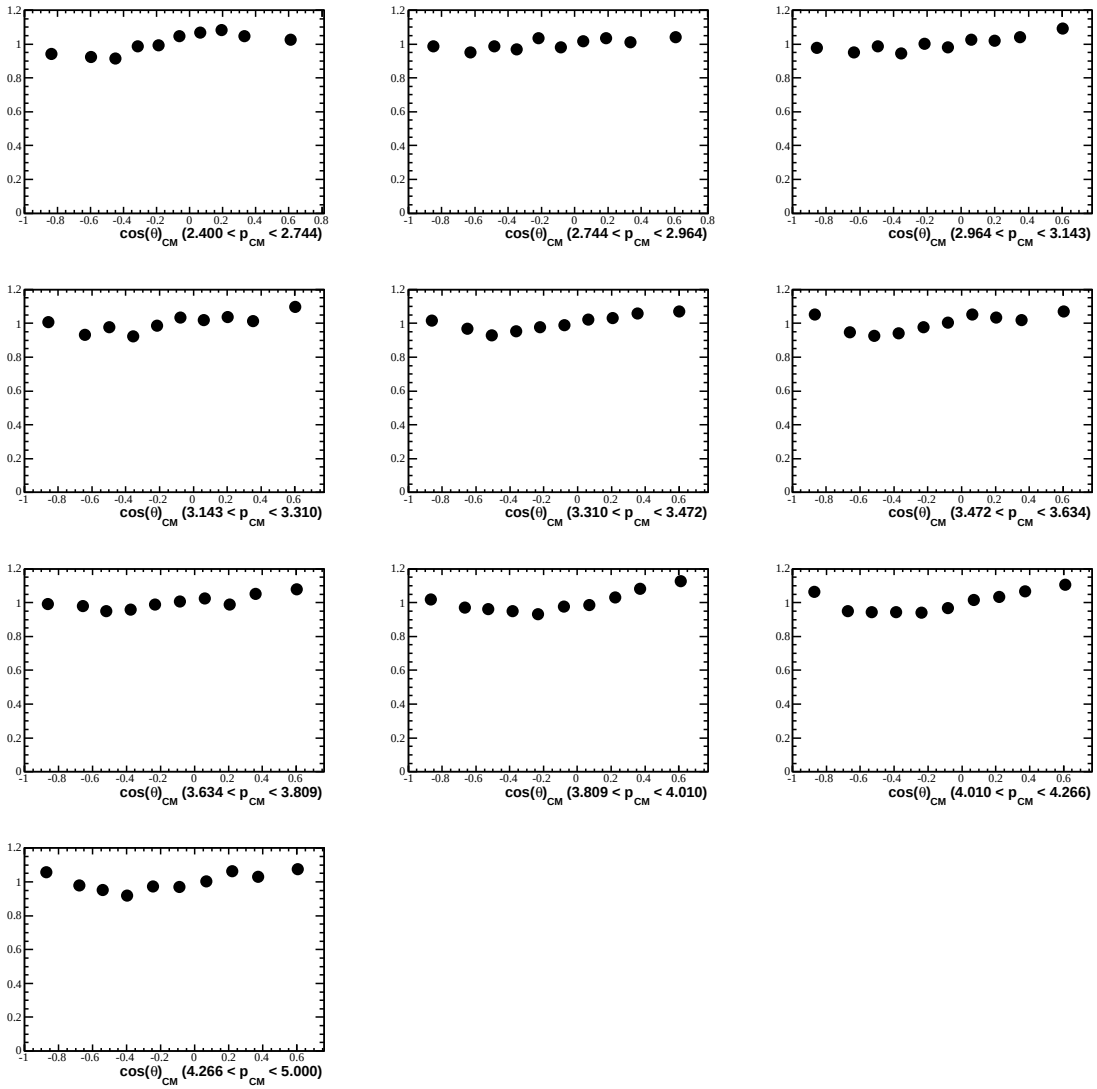

Figure 5.62: Data to Monte Carlo ratios as a function of the production variables (p_{CM},$\cos(\theta)_{CM}$).

5.6.4. Parameterization of the D^+ Decay Amplitude [11]. As discussed in the introduction, the amplitude of the decay of the D^+ is described as a coherent sum of a number of intermediate quasi-two-body amplitudes (resonance and bachelor particle) where the bachelor particle is one of three final-state particles while the resonance decays into the remaining pair

$$A = \sum_i c_i e^{i\phi_i} A_i \times Z \tag{5.6.7}$$

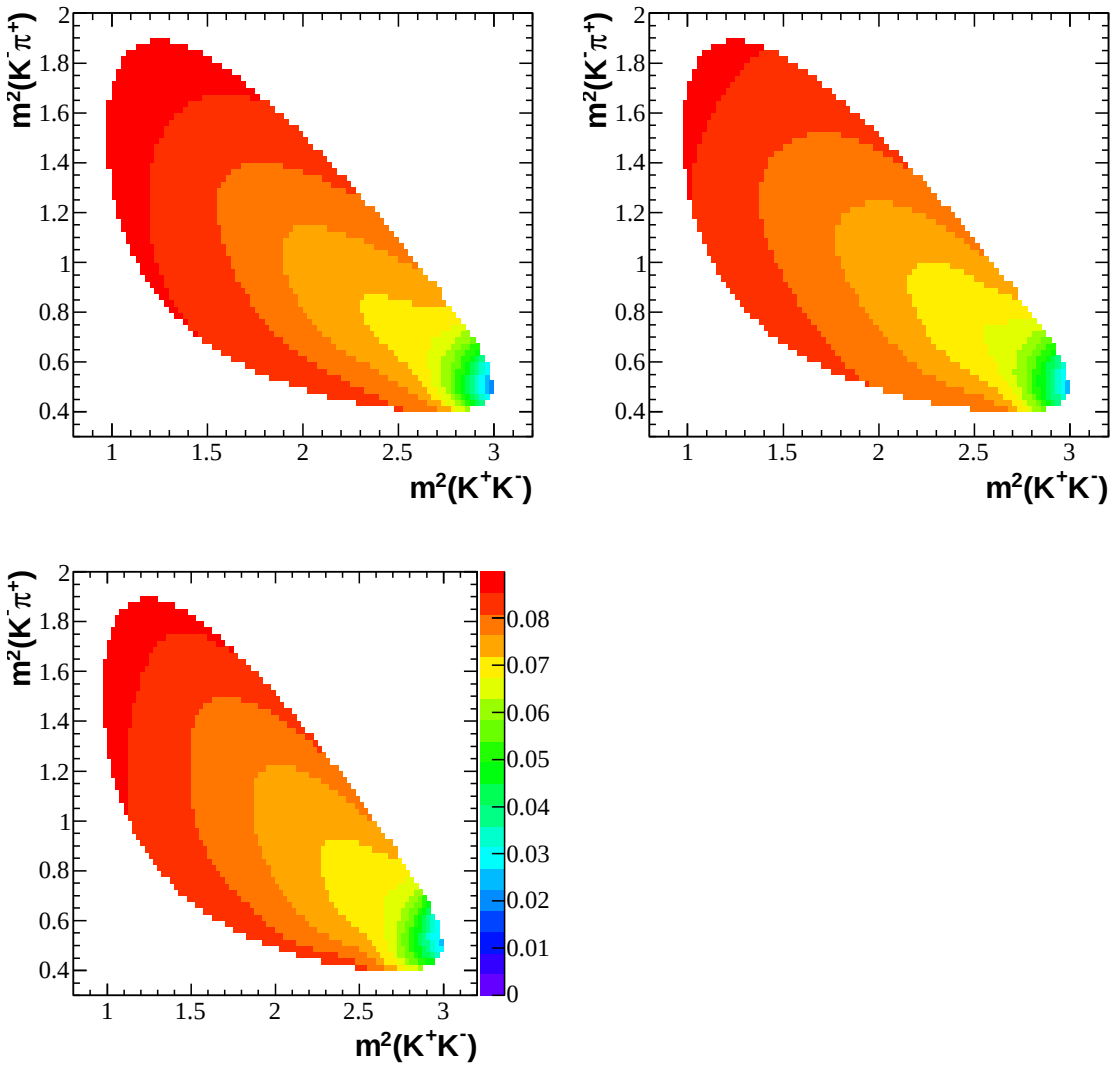

Figure 5.63: Dalitz plot Monte Carlo Efficiencies. The top left is the Monte Carlo efficiency. The top right is the Monte Carlo efficiency corrected for tracking efficiency and asymmetry from τ decays. The bottom plot is the Monte Carlo efficiency corrected for production modeling and tracking. The scale in the bottom plot corresponds to all the plots shown.

Z describes the angular distribution of the decay and A_i are complex amplitudes described as a product of centrifugal barrier factors and a dynamical function describing the intermediate resonance. In this section we describe in detail the kinematics of the Dalitz plot, the Zemach tensors which describe the angular dependence

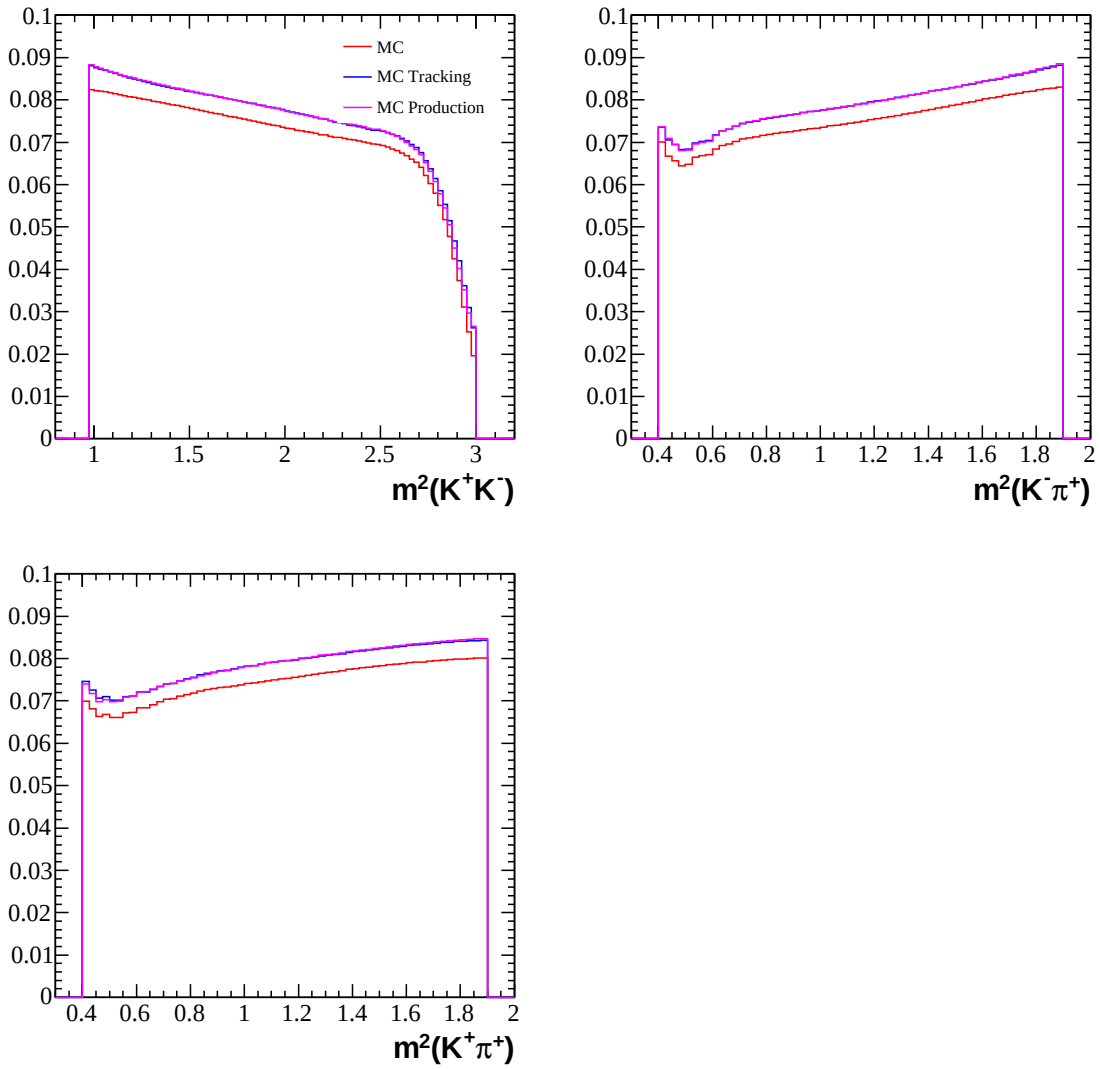

Figure 5.64: Monte Carlo efficiency projections. The production modeling does not affect the Dalitz plot efficiency significantly, however, the tracking correction increases the efficiency.

of the decay, the Blatt-Weisskopf form factors which describe the centrifugal barrier effects of decaying mesons, and various models to describe the dynamics of a resonance or scattering of final-state particles.

5.6.4.1. *Kinematics.* We define several kinematic quantities that are used throughout the discussion of the Dalitz plot decay amplitude. Consider the decay of the D^+, with an intermediate resonance R, such that $D^+ \to RC$ and $R \to AB$ as shown in Figure 5.65.

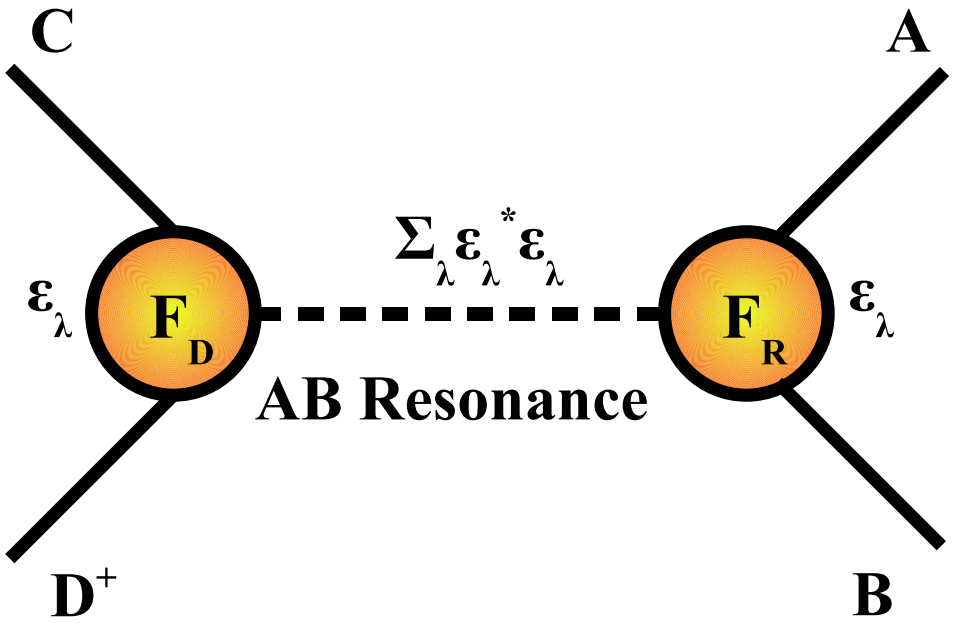

Figure 5.65: Diagram for the decay $D^+ \to CR(R \to AB)$. R is the resonance particle of spin 0, 1, or 2. F_D and F_R are the Blatt-Weisskopf barrier form factors for D^+ and R, respectively. Each vertex contains a spin factor ϵ_λ, and the decay amplitude depends on the spin-sum $\sum_\lambda \epsilon_\lambda^* \epsilon_\lambda$.

•s The invariant 2-body mass-squared m_{AB}^2.

•q The momentum of the child particle in the resonance rest frame.

$$q = \frac{\sqrt{(m_{AB}^2 - m_B^2 + m_A^2)^2 - 4m_{AB}^2 m_A^2}}{2m_{AB}} \tag{5.6.8}$$

•p The momemtum of the bachelor particle in the resonance rest frame.

$$p = \frac{\sqrt{(m_D^2 - m_C^2 + m_{AB}^2)^2 - 4m_{AB}^2 m_C^2}}{2m_{AB}} \tag{5.6.9}$$

•q_0 The momentum of the child in the resonance rest frame at the resonant mass, m_R.

$$q_0 = \frac{\sqrt{(m_R^2 - (m_A - m_B)^2)(m_R^2 - (m_A + m_B)^2)}}{2m_R} \tag{5.6.10}$$

•$\cos(\theta)_H$ The helicity angle, defined as

$$\frac{\vec{q}\cdot\vec{p}}{qp} \tag{5.6.11}$$

5.6.4.2. *Blatt-Weisskopf Penetration Factors.* In strong decays, the shape and partial width of any resonance into any decay channel is influenced by "centrifugal barrier effects". This arises due to the angular momentum of a resonance being limited by the momentum q. The dependence of the orbital angular momentum L with q is apparent if we consider the semiclassical impact parameter,

$$b = [L(L+1)]^{1/2}/q \tag{5.6.12}$$

and consider the effective meson potential with an effective radius R,

$$U_L(r) = V(r) + \frac{\hbar^2 L(L+1)}{2\mu r^2}, r > R \tag{5.6.13}$$

$$U_L(r) \sim -U_0, r < R \tag{5.6.14}$$

where V(r) is the nuclear potential, and the typical meson effective radius is 1.5 GeV^{-1}. The solutions of the non-relativistic Schrödinger equation are known as the Blatt-Weisskopf penetration factors $B_L(q)$ ([**12**],[**19**]) found in Table 5.16.

Angular Momentum	$B_L(q, q_0)$
0	1
1	$\frac{\sqrt{1+z_0^2}}{\sqrt{1+z^2}}$
2	$\frac{\sqrt{9+3z_0^2+z_0^4}}{\sqrt{9+3z^2+z^4}}$

Table 5.16: Blatt-Weisskopf Penetration Factors. $z = Rq$ and $z_0 = Rq_0$, where $R = 1.5$ GeV^{-1}.

5.6.4.3. *Angular Distribution.* The angular dependence of the decay products must be taken into account to describe the decay amplitude. The typical form of

the angular dependence, shown in Table 5.17, are known as Zemach tensors [**16**]. The derivation of the angular dependence begins with evaluating the spin-sum [**18**]:

$$Spin - Sum = \sum_{\lambda} \epsilon_{\lambda}^{\mu *} \epsilon_{\lambda}^{\nu}, \tag{5.6.15}$$

where ϵ_{λ} is a spin factor which depends on the type of decay, i.e. scalar, vector or tensor.

Angular Momentum	Z
0	1
1	$-2qp\cos(\theta)_H$
2	$4q^2p^2(\frac{3}{2}\cos^2(\theta)_H - \frac{1}{2})$

Table 5.17: Angular Dependence based on the helicity angle, q the momentum of the child in resonance rest frame, and p the momentum of the bachelor in the resonance rest frame.

5.6.4.4. *Dynamical Functions for Intermediate Resonances.* For a resonance $R \rightarrow AB$ with an invariant mass, $\sqrt{s}$, T_R is a Relativistic Breit-Wigner (RBW)[**12**]

$$T_R = \frac{F_r F_D}{m_0^2 - s - i m_0 \Gamma(q)} \tag{5.6.16}$$

where $\Gamma(q)$ is a function of $\sqrt{s}$, the momentum q, the spin of the resonance l, and the width of the resonance Γ_0. The expression is:

$$\Gamma(q) = \Gamma_0 (\frac{q}{q_0})^{(2l+1)} \frac{m_0}{\sqrt{s}} B_L^2. \tag{5.6.17}$$

Resonances near the $K\bar{K}$ thresholds, namely the $f_0(980)$ and $a_0(980)$ are described by a coupled-channel Breit-Wigner, known as a Flatté [**20**] distribution:

$$T_R = \frac{1}{m_0^2 - s - i m_0 (g_{\pi\pi}\rho_{\pi\pi} + g_{K\bar{K}}\rho_{K\bar{K}})} \tag{5.6.18}$$

where ρ is Lorentz invariant phase-space, $2q/\sqrt{s}$, and reduces to the following form

$$\rho_i = \sqrt{1 - \frac{4m_i^2}{s}}. \tag{5.6.19}$$

The coupling constants for the $a_0(980)$ are taken from the analysis of $\bar{p}p$ annihilation to the $K_L K^{\pm}\pi^{\mp}$ final state [**23**].

$$m(a_0(980)) = 0.982 \pm 0.003 GeV$$

$$g_1 = g_{\pi\eta} = 0.324 \pm 0.015 GeV^2/c^4$$

$$g_2^2/g_1^2 = 1.03 \pm 0.14$$

The $f_0(980)$ coupling constants are taken from BES measurement [**24**].

$$m_0 = 0.965 \pm 0.008 \pm 0.006 GeV/c^2$$

$$g_{\pi\pi}^2 = 0.165 \pm 0.010 \pm 0.015 GeV^2/c^4$$

$$g_{KK}^2/g_{\pi\pi}^2 = 4.21 \pm 0.25 \pm 0.21$$

5.6.4.5. *Isobar Model.* We consider, as an initial model, the Isobar Model which is described by the coherent sum of overlapping Breit-Wigner resonances in the $K^-\pi^+$ and K^+K^- systems and a non-resonant term, $c_0 e^{i\phi_0}$. As a model for the s-wave of the $K^-\pi^+$ system, we include the $\bar{K}^{*0}(1430)$ and a broad s-wave state referred to as the κ [**22**]. Several masses and widths are floated, namely for resonances which have poorly determined measurements.

5.6.4.6. *Elastic $K^-\pi^+$ Scattering.* As an alternative to the assumption that the S-wave in the $K^-\pi^+$ can be described by a combination of s-wave resonances and a non-resonant contribution, we consider a purely elastic amplitude [**25**] and take

	Fit Range (GeV/c^2)	m_R (GeV/c^2)	Γ_R (GeV/c^2)	a GeV/c $^{-1}$	b GeV/c $^{-1}$
LASS A	$0.825 < \sqrt{s} < 1.450$	1.435 ± 0.005	0.279 ± 0.006	1.95 ± 0.09	1.76 ± 0.36
LASS B	$0.825 < \sqrt{s} < 1.455$	1.415 ± 0.005	0.300 ± 0.006	2.07 ± 0.09	3.32 ± 0.34

Table 5.18: Parameters measured by the LASS collaboration from fit to S-wave amplitudes from $K^-\pi^+$ scattering

parameters measured from the LASS experiment. The details of the s-wave parameterization, comparisons from various experiments and analyses, and parameters used from the LASS have been summarized by William Dunwoodie [**27**]. However, the following form of the S-wave amplitude we take directly from reference [**25**] while using parameters documented in [**27**]. The Lorentz-invariant amplitude, which describes the decay rather than the scattering amplitude as measured in LASS is detailed here:

$$T_R(s) = (\frac{\sqrt{s}}{p}) \sin[\gamma(s) - \gamma_0] e^{i[\gamma(s)-\gamma_0]} \tag{5.6.20}$$

$$\gamma_s = \gamma_R + \gamma_B + \gamma_0 \tag{5.6.21}$$

$$\cot \gamma_B = \frac{1}{pa} + \frac{1}{2} bp \tag{5.6.22}$$

$$\cot \gamma_R = \frac{m_R^2 - s}{m_R \Gamma(r_R, s)} \tag{5.6.23}$$

$$\gamma_0 = 0 \tag{5.6.24}$$

The parameters for m_R, Γ_R, a, and b are shown in Table 5.18. An additional arbitrary phase, γ_0, is included and fixed to zero.

5.6.4.7. *Generalized $K^-\pi^+$ S-wave Model.* The previous section applies only to elastic scattering, and the final-state interactions which occur in the decay of the D^+ meson may not be purely elastic. Therefore, there may be a relative phase between the non-resonant component of the s-wave and the resonant component.

The formulalism has been described in detail and fitted to decays of $D^0 \to K_s\pi^+\pi^-$ decays from BaBar data [**28**].

$$T_R = Be^{i\phi_B}\frac{(\cos\phi_B + \cot\delta_B \sin\phi_B)\sqrt{s}}{q(s)\cot\delta_B - iq(s)} + Re^{i\phi_R}e^{i2(\delta_B+\phi_B)}\frac{m_R\Gamma_R m_R/q_0}{m_R^2 - s - im_R\Gamma(s)} \tag{5.6.25}$$

with

$$q(s)\cot\delta_B = \frac{1}{a} + \frac{rq(s)^2}{2} \tag{5.6.26}$$

and

$$e^{i2\delta_B} = \frac{q(s)\cot\delta_B + iq(s)}{q(s)\cot\delta_B - iq(s)} \tag{5.6.27}$$

This form reduces back to the elastic case when $B = R = 1$, $\phi_B = \phi_R = 0$.

5.6.4.8. *S-wave Model in ϕ(1020) mass region.* Recently, a model-independent partial wave analysis was performed on BaBar data for the decay $D_s \to K^+K^-\pi^+$ in the vicinity of the $\phi(1020)$ resonance [**31**]. The authors show that there is indeed a scalar contribution in the low K^+K^- mass region which interferes with the $\phi(1020)$. The scalar contribution is usually referred to as the $f_0(980)$, which is a resonance typically modeled with the Flatté distribution described previously. The lineshape of this resonance is not well-known. To determine the line-shape more precisely, the authors extract an effective parameterization of the $f_0(980)$ by fitting simultaneoulsy plots of the S-wave, P-wave, and the cosine S-P phase difference. They model the $f_0(980)$ with a RBW of the form

$$A_{f_0(980)} = \frac{1}{m_0^2 - m^2 - im_0\Gamma_0\rho_{K\bar{K}}} \tag{5.6.28}$$

They obtain a mass and width for the $f_0(980)$

$$m_0 = 0.922 \pm 0.003 GeV/c^2$$

$$\Gamma_0 = 0.26 \pm 0.08 GeV/c^2$$

We include here the moment distributions in the K^+K^- mass region for the $D_s \to K^+K^-\pi^+$ decay, the first moment in the decays of $D_s \to K^+K^-e^+\nu$ and $D^0 \to \bar{K}^0K^+K^-$.

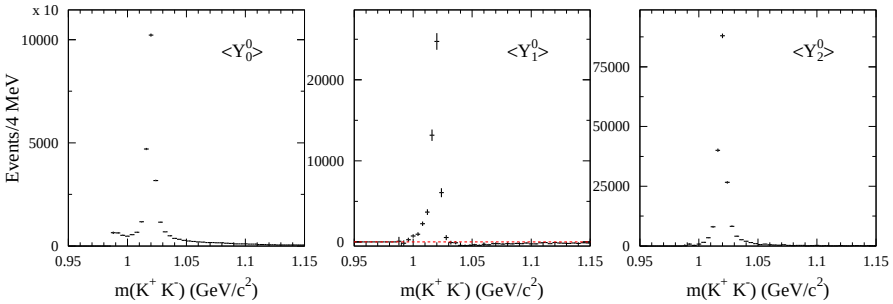

Figure 5.66: $D_s \to K^+K^-\pi^+$ $\langle Y^0_0 \rangle$, $\langle Y^0_1 \rangle$ and $\langle Y^0_2 \rangle$ moments with background subtracted and corrected for efficiency and phase space.

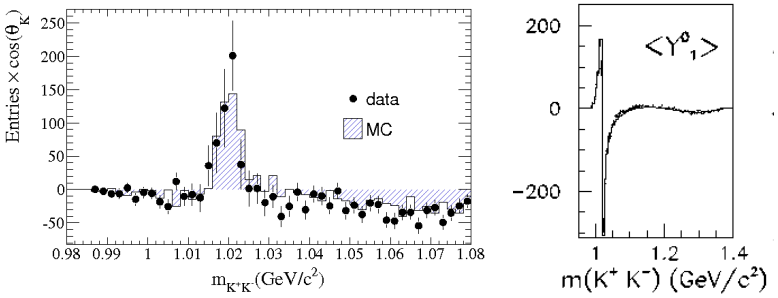

Figure 5.67: $\langle Y^0_1 \rangle$ moment of *a*) $D^+_s \to K^+K^-e^+\nu$ and *b*) $D^0 \to \bar{K}^0K^+K^-$ decays.

5.7. Charge Independent Dalitz Plot Fits

The model we use to describe the data is 3-dimensional and consists of a component to describe the decay of the D meson and the reconstructed mass of the D meson. We perform an unbinned maximum likelihood fit with the following three variables:

- The mass of the D meson
- $m^2(K^+K^-)$
- $m^2(K^-\pi^+)$

5.7.1. Fit Fractions. The fraction of each resonance (FF_i) is determined from the signal pdf, and is defined as the integral of a single amplitude divided by the integral of the full amplitude over the entire Dalitz plot.

$$FF_i = \frac{\iint |c_i \mathrm{M}_i|^2 dxdy}{\iint |\sum_j c_j \mathrm{M}_j|^2 dxdy} \tag{5.7.1}$$

In the case of the $K^-\pi^+$ S-wave, we only determine the fraction of the entire S-wave since this is not described by individual resonances.

5.7.2. Goodness of Fit. For the goodness-of-fit we have three measures of the χ^2

$$\chi^2 = \sum_{i=1}^{Nbins} \frac{(N_i^{obs} - N_i^{pred})^2}{N_i^{pred}}. \tag{5.7.2}$$

The best measure of goodness-of-fit, from a quantitative point-of-view, is measured in bins of equal population. The Dalitz plot density varies dramatically, especially in the region of the $\phi(1020)$, and therefore requires variable bin sizes in the two-dimensional Dalitz plot. The number of bins chosen to measure the χ^2 depends on the sample size n [**33**]

$$B = 2n^{2/5}. \tag{5.7.3}$$

•Carolitz adaptive binning which creates 289 equally populated bins. The χ^2 is found from the estimating the number of predicted events of the model with integration. The error in the χ^2 we take as the number of predicted events,

$$N_i^{pred} = \iint f\epsilon_{MC}(x_i, y_i)S(x_i, y_i)\mathrm{d}x\mathrm{d}y + (1-f)\iint B(x_i, y_i)\mathrm{d}x\mathrm{d}y \qquad (5.7.4)$$

where f is the fraction of signal events.

•2-dimensional χ^2 over the Dalitz plot from histograms of data and MC generated events from the model. We generate ten times the amount of events in data. The error in the χ^2 is taken as the number of predicted events divided by 10.

•1-dimensional χ^2 from projections of the data and the MC generated events in all three Dalitz plot variables, $m^2(K^+K^-)$, $m^2(K^-\pi^+)$, and $m^2(K^+\pi^+)$.

5.7.3. Background Pdf. The background probability distribution is composed of 5 components which describe the shape of the background within the $\phi(1020)$ mass region (section 5.2.6.3), the $\bar{K}^{*0}$ mass region (section 5.2.6.3) and the remaining region of the Dalitz plot (section 5.2.6.2). In regions of the $\phi(1020)$ and $\bar{K}^{*0}$, the parameters of the background model are determed previously from the fit to the sideband data, except that we now assume the PDG masses and widths for the Breit-Wigner. The kNN is trained with mass-constrained Dalitz plot variables from the sideband regions. In the fit of the signal and background, we float the fraction of each of the background components.

5.7.4. Likelihood Function. We perform an unbinned maximum likelihood fit to the constrained Dalitz plot variables, $m^2(K^+K^-)$ and $m^2(K^-\pi^+)$, minimizing $-2ln\mathcal{L}$, where $\mathcal{L}$ is the likelihood function describing the density over the Dalitz plot. The likelihood function contains a mass-dependent probability $p(m_i)$ which is multiplied by the parameter C. Depending on the background model, the likelihood function has additional parameters to vary different components of the background.

We minimize the following likelihood function to determine the nominal model of the Dalitz plot.

$$-2\ln\mathcal{L} = -2\sum_{i=1}^{N_{ob}} \ln\left(Cp(m_i)\frac{\epsilon_{MC}(x_i,y_i)S(x_i,y_i)}{\iint \epsilon_{MC}(x_i,y_i)S(x_i,y_i)\mathrm{d}x\mathrm{d}y} + (1-Cp(m_i))B(x_i,y_i)\right) \tag{5.7.5}$$

The reconstructed D^+ mass-dependent probability $p(m)$ is defined as

$$p(m_i) = \frac{S(m_i)}{S(m_i)+B(m_i)} \tag{5.7.6}$$

where $S(m)$ and $B(m)$ are determined from the mass fit described in section 5.4.2.

Penalty terms may also be added to the likelihood function when allowing the masses and widths of resonances to float in the fit. We form the χ^2 from the floated mass and width, m_R and Γ_R, and the PDG average value and error. No limits are imposed are the parameters in fit.

$$\chi^2_{penalty} = \frac{(m_R - m_R^{PDG})^2}{(\Delta m_R^{PDG})^2} + \frac{(\Gamma_R - \Gamma_R^{PDG})^2}{(\Delta\Gamma_R^{PDG})^2} \tag{5.7.7}$$

5.7.4.1. *kNN Background Density.*

$$B(x_i,y_i) = \frac{kNN(x_i,y_i)}{\iint kNN(x_i,y_i)dxdy} \tag{5.7.8}$$

5.7.4.2. *Alternative Background Density (TBD).*

$$\begin{aligned} B(x_i,y_i) =& f_1\frac{BW_\phi P_{02}}{\iint BW_\phi P_{02}dxdy} + f_2\frac{BG_\phi P_{02}}{\iint BG_\phi P_{02}dxdy} \\ &+ f_3\frac{BW_{\bar{K}^{*0}} P_{02}}{\iint BW_{\bar{K}^{*0}} P_{02}dxdy} + f_4\frac{BG_\phi P_{02}}{\iint BG_\phi P_{02}dxdy} + f_5\frac{kNN}{\iint kNNdxdy} \end{aligned} \tag{5.7.9}$$

where

$$f_5 = 1 - f_1 - f_2 - f_3 - f_4 \tag{5.7.10}$$

and

$$BW = \frac{1}{4m_{x,y}qp}|A_{BW}|^2 \frac{P_0^2 + bw_{11}P_1^2 + bw_{22}P_2^2 + bw_{01}P_0P_1 + bw_{02}P_0P_2 + bw_{21}P_2P_1 + bw_{\cos(\theta)}\cos(\theta)}{2(1 + bw_{11}/3 + bw_{22}/5)} \tag{5.7.11}$$

$$BG = \frac{1}{4m_{x,y}qp}\left[\frac{1}{\int dm} + a(m - m_{\phi,\bar{K}^{*0}})\right] \frac{P_0^2 + p_{11}P_1^2 + p_{22}P_2^2 + p_{01}P_0P_1 + p_{02}P_0P_2 + p_{21}P_2P_1 + p_{\cos(\theta)}\cos(\theta)}{2(1 + p_{11}/3 + p_{22}/5)}. \tag{5.7.12}$$

What needs to be noted here is that the Jacobian

$$|J| = \frac{1}{4m_{x,y}qp} \tag{5.7.13}$$

has been included in the background functions, since we are now in the space of m_x^2, m_y^2 rather than $m_{x,y}, \cos(\theta)_{x,y}$.

5.7.5. Fit Procedure. We take the mass dependent signal and background pdfs from the integrated mass fit. For the Dalitz plot model, we consider all resonances up to the D mass. The following 16 resonances are included in the fit: $\bar{K}^{*0}(892)$, $\bar{K}^{*0}(1430)$, $\phi(1020)$, $a_0(1450)$, $\phi(1680)$, $\bar{K}_0^{*2}(1430)$, $\bar{K}_0^{*1}(1410)$, $f_2(1270)$, $f_0(1370)$, $f_0(1500)$, $f_2(1525)$, κ, $f_0(980)$, $a_0(980)$, $f_0(1710)$, and a non-resonant term. The $f_0(980)$ and $a_0(980)$ are modeled with coupled-channel Breit-Wigner (Flatte) resonances, and other resonances are considered relativistic Breit-Wigners. We provide Table 5.19 of masses and widths used in the preliminary fit.

The fitting of the Dalitz plot is performed in two steps. The first fit we assume that the reconstruction efficiency over the Dalizt plot obtained from the Monte Carlo is correct. We train the artificial neural network based on the ratio of reconstructed events to what is generated. The second fit is performed with a corrected efficiency. The reconstructed Monte Carlo events are weighted by the product of two data to Monte Carlo ratios. The neural network is retrained for the second fit.

Resonance	Mass (MeV)	Width (MeV)
$\bar{K}^{*0}(892)$	895.94 ± 0.22	48.7 ± 0.8
$\bar{K}^{*0}(1430)$	1425 ± 50	270 ± 80
$\phi(1020)$	1019.455 ± 0.02	4.26 ± 0.04
$a_0(1450)$	1474 ± 19	265 ± 13
$\phi(1680)$	1680 ± 20	150 ± 50
$\bar{K}_0^{*2}(1430)$	1432.4 ± 1.3	109 ± 5
$\bar{K}_0^{*1}(1410)$	1414 ± 15	232 ± 21
$\bar{K}^{*0}(1680)$	1717 ± 27	322 ± 110
$f_2(1270)$	1275 ± 1.2	185 ± 2.9
$f_0(1370)$	1370 ± 300	350 ± 300
$f_0(1500)$	1505 ± 6	109 ± 7
$f_2(1525)$	1525 ± 5	73 ± 6
κ	672 ± 40	550 ± 34
$f_0(980)$	965 ± 10	70 ± 100
$a_0(980)$	984.7 ± 20	100 ± 50
$f_0(1710)$	1720 ± 6	135 ± 8
non-resonant	0	0

Table 5.19: Resonance masses and widths fixed in the preliminary fit to the charge independent Dalitz plot distribution

5.7.6. Fit Results for Various Models. In this section we describe several models that have been fit to the data, and we report the results of each fit. The various models are different with respect to the s-wave in the $K\pi$ system, which are described below. The s-wave in the KK system, typically referred to as the $f_0(980)$, is modeled with the effective parameterization decribed in section 5.6.4.8. The relativistic Breit-Wigner resonances included in each fit are listed in Table 5.20, indicating whether the mass and width is floated in the fit. For resonances with floated parameters, the PDG values and errors are used to constrain the parameters in the fit. The background model used in these fits is the 3-region background model described in section 5.2.6.3. The artificial neural network efficiency with both the tracking and production correction is included in these fits. The results of each fit are reported in Table 5.21, with the exception of the κ model which is in progress. The traditional "isobar" model provides the best description of the data, with the exception that the κ fit is in progress. The projections and moments of the isobar fit are included in this section.

Resonance	Mass,Width
$\bar{K}^{*0}(892)$	floated
$\phi(1020)$	floated
$a_0(1450)$	floated
$\phi(1680)$	fixed
$\bar{K}_0^{*2}(1430)$	fixed
$\bar{K}_0^{*1}(1410)$	fixed
$\bar{K}^{*0}(1680)$	floated
$f_2(1270)$	fixed
$f_0(1370)$	floated
$f_0(1500)$	fixed
$f_2(1525)$	fixed
$f_0(1710)$	fixed

Table 5.20: Resonance masses and widths fixed in the preliminary fit to the charge independent Dalitz plot distribution

Model 1 (Isobar Model):

•$\bar{K}^{*0}(1430)$ (mass and width floated)

•Non-resonant magnitude and phase

Model 2 (Resonance Model):

•$\bar{K}^{*0}(1430)$ (mass and width floated)

Model 3 (LASS Model A):

•LASS A parameters

•LASS resonance mass and width floated

Model 4 (LASS Model B):

•LASS B parameters

•LASS resonance mass and width floated

Model 5 (κ Model - TBD):

•Broad low $K\pi$-mass scalar (κ mass and width floated)

Model	Carolitz ($\chi^2/ndof$)	Likelihood
1	734.3 (3.00)	-266512
2		
3	1565.3 (6.29)	-264944
4	1924.03 (7.73)	-264902
5		

Table 5.21: Goodness of Fit values for various models used to describe the data. The traditional "isobar" model provides the best fit to the data, and the projections of the model and data are found in Figure 5.68

5.8. Charge-Dependent Dalitz Plot Fits and CP asymmetry

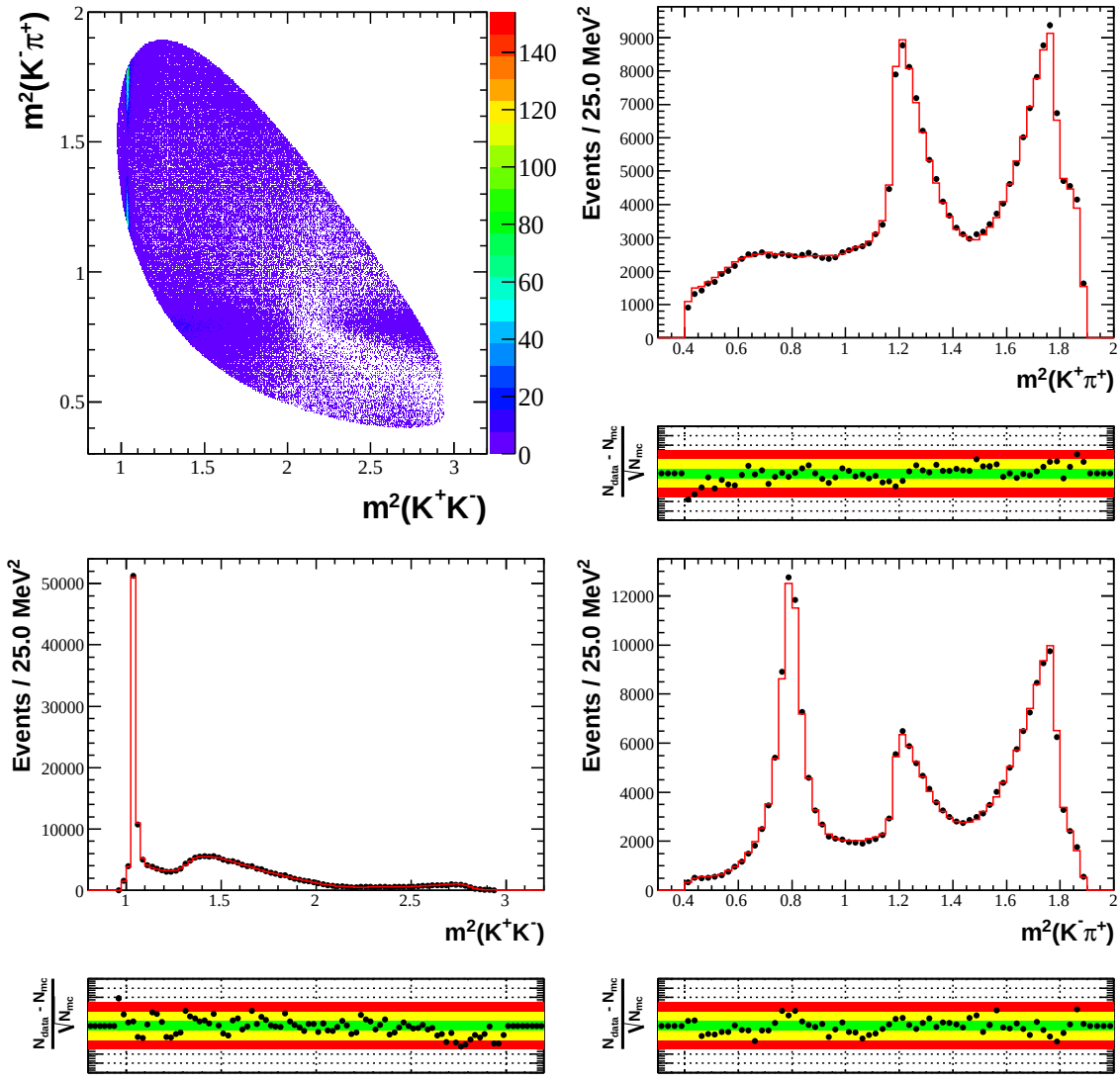

Figure 5.68: Dalitz plot fit projections for the current fit, corresponding to the last entry in Table 5.21. The Dalitz plot shown is the data, the projections of three dimensions are plotted with the normalized residual below each plot. The data are shown in black points, the model is the red histogram. The color bands of the residual plots correspond to 1σ, 3σ, and 5σ.

5.9. Systematics and Cross-Checks

Preliminary list of possible sources of systematic error that need to be investigated.

•Particle Identification of Kaons. Comparison of K^+ and K^- spectra from data for D^+ and D^- events.

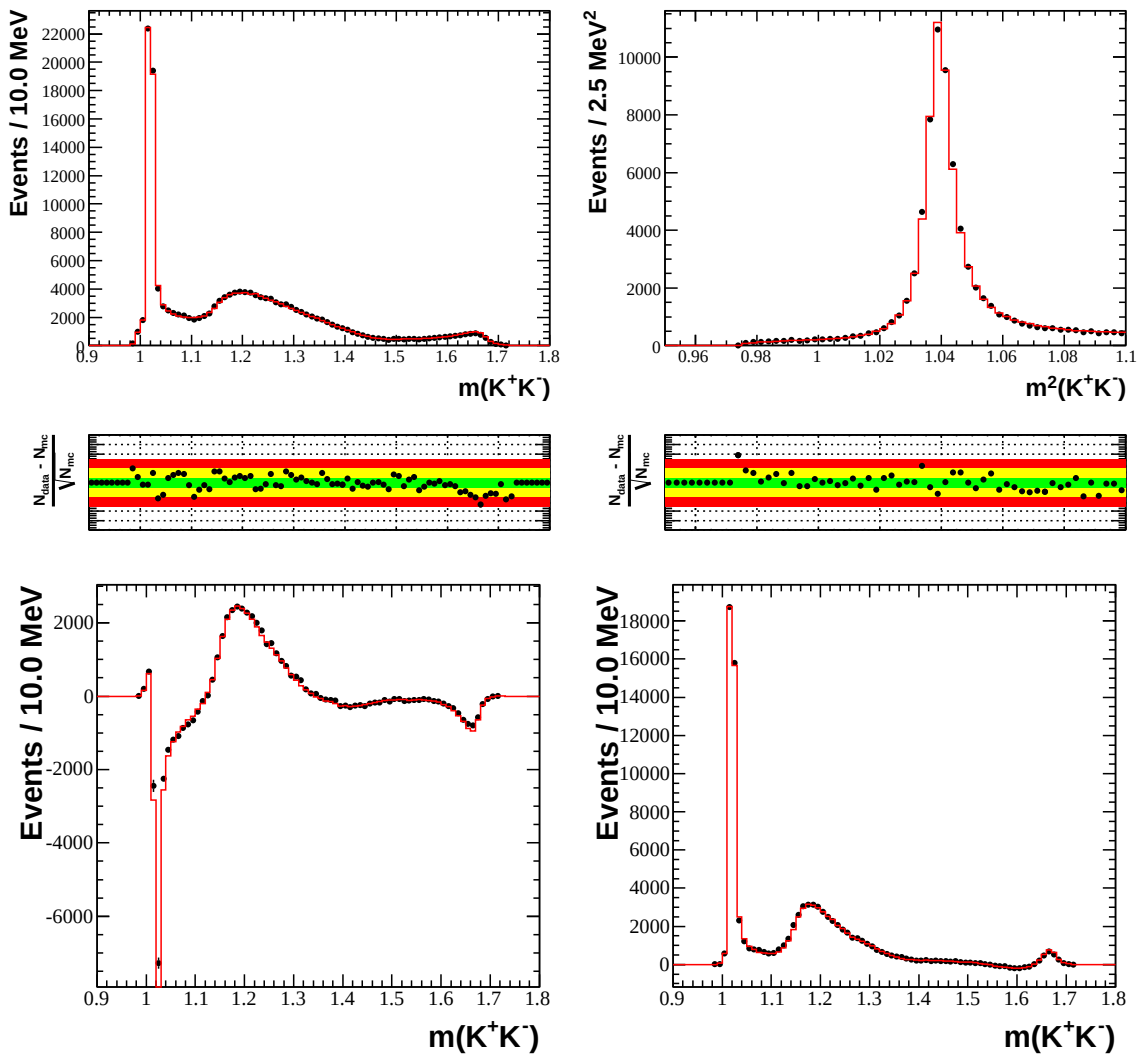

Figure 5.69: Dalitz plot fit K^+K^- moments and projection in the $\phi(1020)$ region for the current fit, corresponding to the last entry in Table 5.21. The data are shown in black points, the model is the red histogram. The color bands of the residual plots correspond to 1σ, 3σ, and 5σ.

•Monte Carlo Simulation. Tracking asymmetry and production distributions simluated in Monte Carlo are corrected from data.

•Choice of binning for the production correction.

•Background. Choice of binning in nominal model. Choice of a different model.

•Event selection. p_{CM} cut, vertexing cut, and Likelihood Ratio cut.

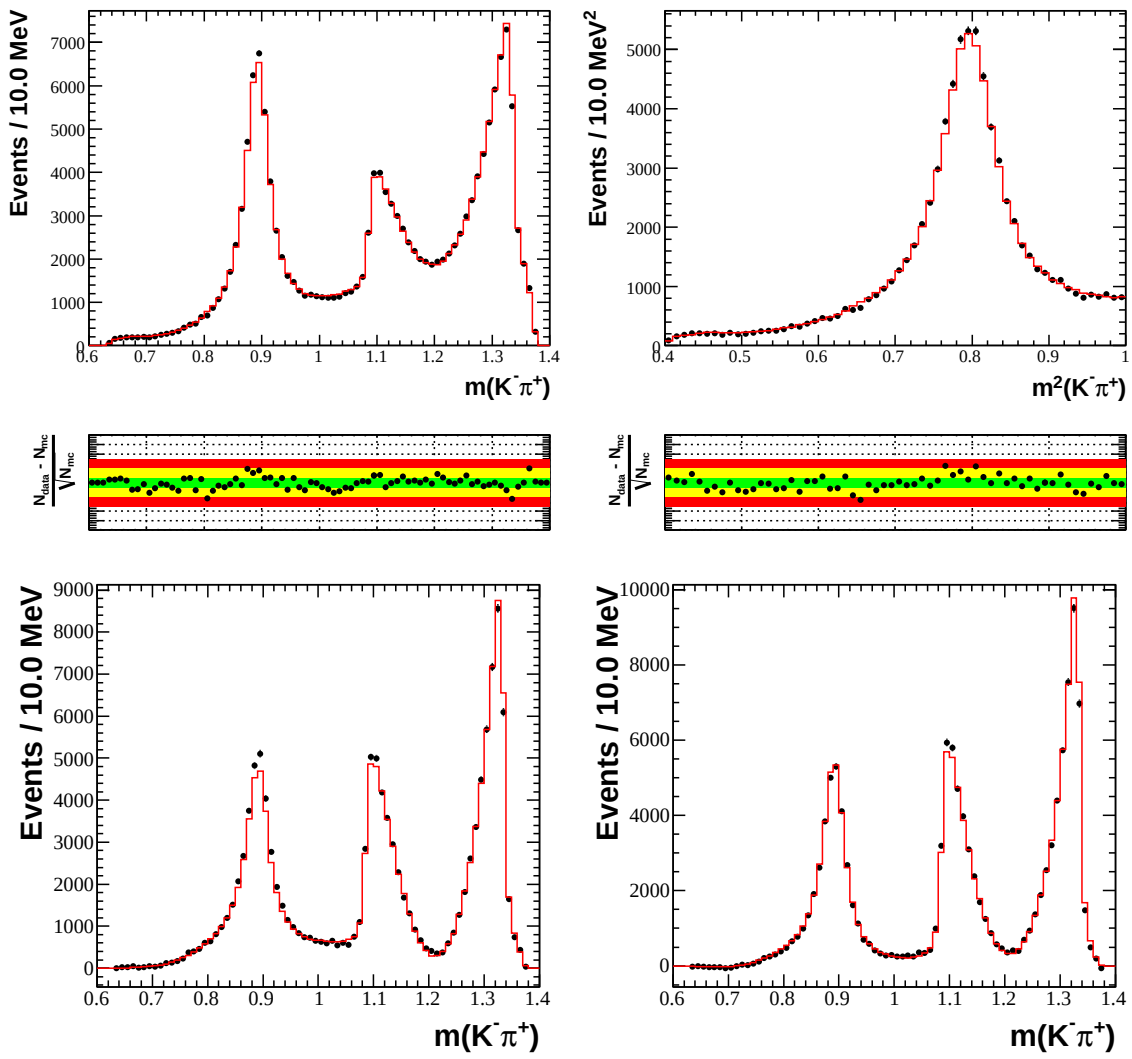

Figure 5.70: Dalitz plot fit $K^-\pi^+$ moments and projection in the $\bar{K}^{*0}(892)$ region for the current fit, corresponding to the last entry in Table 5.21. The data are shown in black points, the model is the red histogram. The color bands of the residual plots correspond to 1σ, 3σ, and 5σ.

5.9.1. Kaon Particle Identifition Asymmetry. Previous studies of systematic uncertainties due to kaon particle indentification [**38**] showed that asymmetries are small, around 0.3%. These asymmetries were measured from the decays $D^0 \to K^-\pi^+$ and $D^+ \to K^-\pi^+\pi^+$.

We compare the momentum spectra of kaons after background subtraction, using the same method that is described in section on production. We measure the asymmetry as a function of lab momentum

Yield (S)	Error (ΔS)	S/ΔS	Cut
223631.55	626.22	357.11	0.85
218928.38	567.89	385.51	0.86
214001.37	584.88	365.89	0.87
202338.58	518.47	390.26	0.89
195683.80	494.23	395.94	0.90
188372.31	501.97	375.27	0.91
180539.03	464.84	388.39	0.92
171594.15	435.76	393.78	0.93
160922.39	410.69	391.83	0.94
148586.71	389.21	381.77	0.95
133396.25	359.05	371.53	0.96
112781.13	318.66	353.93	0.97
85452.49	276.96	308.54	0.98
42705.90	187.07	228.28	0.99

Table 5.22: Signal yield and significance as a function of the likelihood ratio cut

$$A_{p_{lab}}(K^{\pm}) = \frac{N_{K^+}(p_{lab}) - N_{K^-}(p_{lab})}{N_{K^+}(p_{lab}) + N_{K^-}(p_{lab})} \tag{5.9.1}$$

The asymmetry is measured for the following:

•Asymmetry in first daughter track, $K^+(D^+)$,$K^-(D^-)$

•Asymmetry in second daughter track, $K^+(D^-)$,$K^-(D^+)$

•Asymmetry in first and second daughter tracks from D^+, $K^+(D^+)$,$K^-(D^+)$

•Asymmetry in first and second daughter tracks from D^-, $K^+(D^-)$,$K^-(D^-)$

The mean kaon momenta does not show any diffence in charge except at very high momenta, greater than 5 GeV/c. In this region, there are very few events. Any effect due to particle momenta would be dominant up to 3 GeV/c, and the K^+ and K^- do not exhibit differences in their spectra.

5.9.2. Likelihood Ratio Cut. We evaluate the signal yield and signal significance as a function of the likelihood ratio cut to determine the appropiate change in the cut to evaluate a systematic uncertainty.

5.9.3. CP Asymmetry measured as a function of $\cos(\theta)_{CM}$**.** We study various systematic effects on the CP asymmetry in data. The following systematic studies were performed on the data sample:

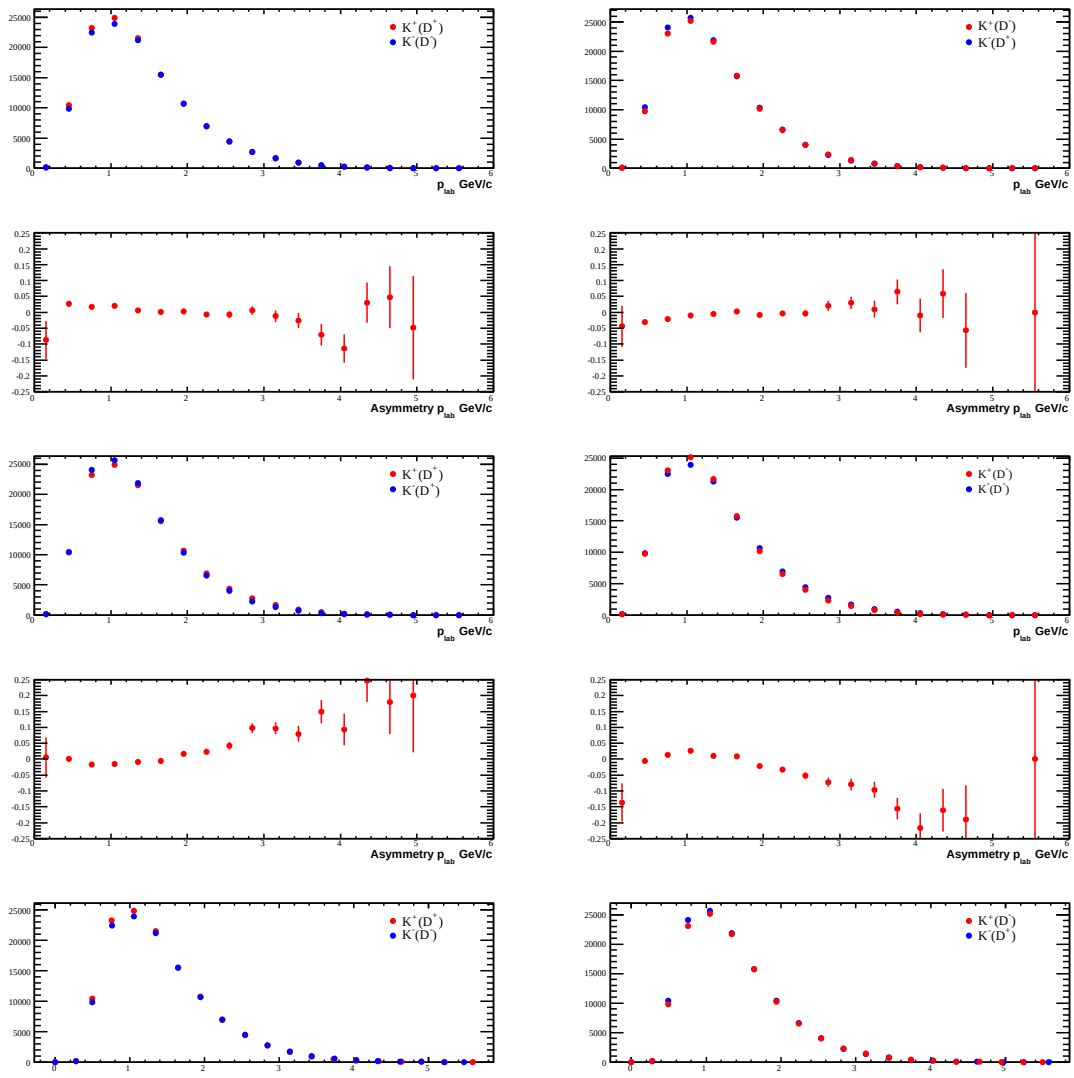

Figure 5.71: Kaon Particle Id asymmetry for KBDT Tight selector used in this analysis. The corresponding asymmetry plots lie below the comparison plot. The final row of plots represent the mean kaon momenta in each bin rather than the value at the bin center, as the 1st and 3rd row show.

•vary the likelihood ratio cut from 0.85 to 0.86;

•measure the asymmetry in a single bin for the forward region and backward region;

•measure the asymmetry using 6 bins in $\cos\theta_{CM}$

•remove the tracking correction from the efficiency;

•apply a different tracking correction;

•remove the production correction from the efficiency;

Average $\cos\theta$ Asymmetry	$\Delta A_{CP}[\%]$	$A_{FB}[\%]$
Average of $A_{CP}(\theta)$	0.0	-2.92 ± 0.33
Vary LH ratio	0.07	-2.96 ± 0.30
Single forward and backward bin	0.01	-2.12 ± 0.35
Change in binning	0.04	-2.76 ± 0.33
No tracking correction	0.03	-2.90 ± 0.33
No Production correction	0.0	-2.92 ± 0.33
$D^+ \to K_s\pi^+$ Tracking Correction	0.23	-2.82 ± 0.33
Efficiency Weighted Mass Fit	0.0	-2.38 ± 0.41

Table 5.23: Systematic uncertainties for the integrated CP asymmetry as a function of production angle and forward-backward asymmetries. We fit for the yields in the forward region and backward region as a function of production angle, averaging the asymmetries to obtain A_{CP}. The difference between the central value and average A_{CP} after testing for a systematic shift is reported here.

•fit to the efficiency-corrected yields in bins of the production angle.

To study the systematic effect due to tracking efficiency and asymmetry, we reevaluate the efficiency without applying a tracking correction and applying a different correction. As an alternative to measuring the tracking asymmetry from τ decays, we use the tracking asymmetry correction that is documented in the analysis of $D^+ \to K_s\pi^+$ [**?**]. We weight each D^- reconstructed event with the correction factor according to the pion lab momentum and polar angle $\cos\theta$. The tracking correction as a function of lab momentum and polar angle is shown in Figure 5.72.

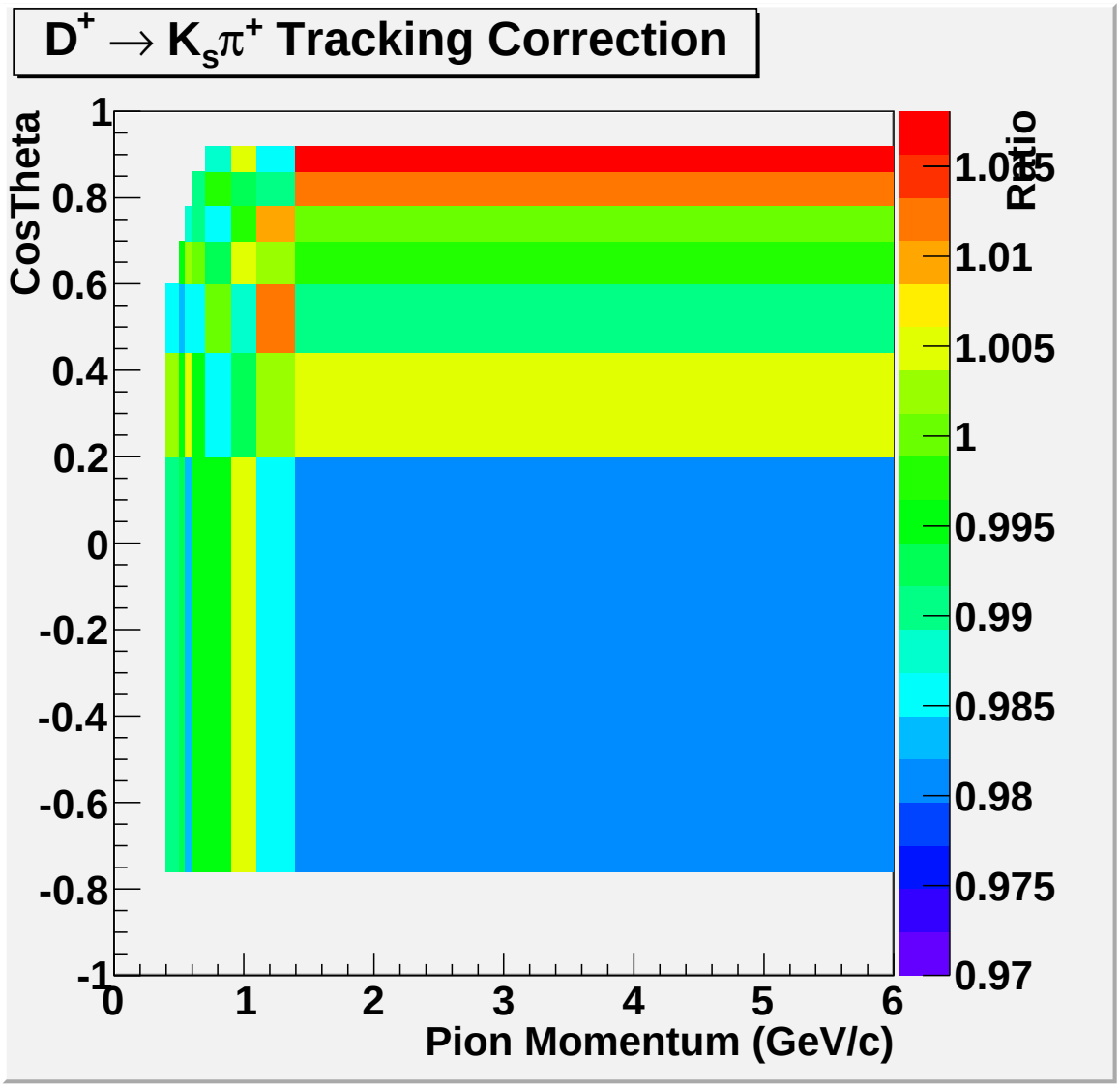

Figure 5.72: Tracking correction map from the $D^+ \to K_s\pi^+$ analysis. The correction is used to weight π^- reconstructed MC tracks when determining the efficiency. The difference between the two A_{CP} measurements is taken as a systematic uncertainty.

Chapter 6

Summary and Conclusions

The analysis of the singly-Cabibbo suppressed decay of $D^+ \to K^+K^-\pi^+$, using data collected from the BaBar experiment, is the most precise measurement of direct CP asymmetry in this channel to date. The integrated CP asymmetry measurement is competitive in both statistical uncertainty and systematic uncertainty when compared to other existing CP asymmetry measurements, which are tabulated in Table 6.1. The final, unblinded measurement of direct CP asymmetry is

$$A_{CP} = 0.30 \pm 0.31 \pm 0.24 \tag{6.0.2}$$

where the first error is statistical and the second error is the sytematic uncertainty.

The notable feature of this analysis is the consideration of detector-related tracking asymmetries, which represent the largest contribution to the systematic uncertainty. Two independent analyses based on extracting the detector tracking asymmetry from data are used to correct the Monte Carlo efficiency. The corrected efficiency is then incorporated into the CP asymmetry measurement. Previous measurements from other experiments, including the CLEO-c measurement, did not consider the impact of detector asymmetries on the measurement.

In addition, corrections to the Monte Carlo with respect to the production of charm mesons, is also an important ascpect of this work. The distributions of production variables in Monte Carlo are known to inaccurately describe these distributions in data.

Establishing the integrated CP asymmetry measurement is a milestone in this research, removing the assumption that the asymmetry is zero when fitting the

Analysis	$A_{CP}[\%]$
Standard Model Prediction	0.23
This analysis	$0.30 \pm 0.31 \pm 0.24$
BaBar Runs 1-2	$1.4 \pm 1.0 \pm 0.8$
E-791	-1.4 ± 2.9
CLEO-c	$-0.03 \pm 0.84 \pm 0.29$
$D^+ \to K_s\pi^+$	$-0.44 \pm 0.13 \pm 0.10$
$D^0 \to K^+K^-$	$0.00 \pm 0.34 \pm 0.13$
$D^0 \to \pi^+\pi^-$	$-0.24 \pm 0.52 \pm 0.22$
$D^0 \to K^+K^-\pi^0$	$1.00 \pm 1.67 \pm 0.25$
$D^0 \to \pi^+\pi^-\pi^0$	$-0.31 \pm 0.41 \pm 0.17$

Table 6.1: Summary of current integrated CP asymmetry measurements in Charm decays. The result in this analysis is blinded with a random number added to the central value.

Dalitz plot. Several models to describe the Dalitz plot with no CP asymmetry have been presented here, and an accurate description of the Dalitz plot decay of the $D^{\pm}$ meson is now within reach. Suprisingly, the traditional "Isobar" model provides the best description of the data. The data is also sensitive to masses and widths of the well-measured $\bar{K}^{*0}(892)$ and $\phi(1020)$ resonances and to several resonances whose parameters have not been measured accurately before.

This research compliments many analyses within the BaBar experiment, where direct and indirect CP asymmetry have been measured in several charm decays. Establishing the level of CP violation in charm decays is an integral part of flavor physics research which will provide physicists on future flavor physics experiments a guide of both where and how to measure these asymmetries in data with much higher sensitivity. Two such experiments are possibilities in the near future, BELLE-II and the proposed Super-B experiment to be conducted in Italy.

Bibliography

1. A. D. Sakharov, ZhETF Pis'ma **5**, No. 1, 32 (1967)

2. M. Kobayashi and T. Maskawa, Prog. Theor. Phys. **49**, 652 (1973)

3. L. Wolfenstein, Phys. Rev. Lett. **51** 1945 (1983)

4. I. I. Bigi, A. I. Sanda, *CP Violation*, Cambridge (2000)

5. S. Eidelman *et. al*, Physics Letters B **592**, 1 (2004).

6. F. Buccella, M. Lusignoli and A. Pugliese, Phys. Lett. B **379**, 249 (1996)

7. B. Aubert et al., [BABAR Collab.], "A search for CP violation and a measurement of the relative branching fraction in $D^+ \to K^+K^-\pi^+$ decays", Phys. Rev. **D**71 (2005) 091101, arXiv:hep-ex/**0501075**.

8. F. Yumiceva and M. Purohit, "A search for CP violation and a measurement of the relative branching fraction in $D^+ \to K^+K^-\pi^+$ decays", B. A. D. 503.

9. E. M. Aitala *et al.*, Phys Lett. **B403**, 377, (1997)

10. P. Rubin *et al.*, Phys. Rev. bf D78, 072003 (2008)

11. R. H. Dalitz, Phil. Mag. **44**, 1068 (1953).

12. J. Blatt and V. Weisskopf, *Theoretical Nuclear Physics*, John Wiley & Sons (1952).

13. D. Asner, "Charm Dalitz plot analysis formalism and results," arXiv:hep-ex/0410014

14. `http://babar-hn.slac.stanford.edu:5090/cgi-bin/internal/cvsweb.cgi/FilterTools/DcToKKPiPromptPath.tcl`

15. J. J. Sakurai, *Modern Quantum Mechanics*, Addison-Wesley (1994)

16. C. Zemach, Phys. Rev. B **133** 1201 (1964).

17. V. Filippini, A. Fontana, and A. Rotondi, Phys. Rev. D **51** 2247 (1995).

18. CLEO Collaboration, S. Kopp *et. al*, Phys. Rev. D **63**, 092001 (2001)

19. F. von Hippel and C. Quigg, Phys. Rev. D 5, 624 (1972)

20. S. M. Flatté Phys. Lett. **B63**, 224 (1976)

21. B. Aubert *et. al*, Nucl. Instrum. Methods **A479**, 1 (2002)

22. D. V. Bugg Phys. Lett **B572**, 1 (2003)

23. A. Abele *et al.*, Phys. Rev **D57**, 3860 (1998)

24. M. Ablikim *et al.*, Phys. Lett. **B607**, 243 (2005)

25. E. M. Aitala *et al*, W. M. Dunwoodie, "Model Independent Measurement of S-wave $K^-\pi^+$ systems using $D^+ \to K\pi\pi$ Decays from Fermilab E791," arXiv:hep-ex/0507099

26. K. Mishra, "Amplitude Analysis of $D^0 \to K^-K^+\pi^0$", B. A. D. 1502

27. W. Dunwoodie, private communication `http://www.slac.stanford.edu/~wmd/kpi\_swave/kpi\_swave\_fit.note`

28. R. Andreassen, *et. al*, "Measurement of $D^0 - \bar{D}^0$ mixing with a time dependent ampltiude analysis of $D^0 \to K^0_s\pi^+\pi^-$ and $D^0 \to K^0_sK^+K^-$", B. A. D. 1898.

29. S. Malvezzi, *I*ntersections of Particle and Nuclear Physics: 7th Conference Proceedings, **AIP Conf.Proc.549:569-574,2002**

30. M. Pappagallo, "Dalitz plot analyses of the decays $D^+_s \to K^+K^-\pi^+$, $D^+_s \to K^0_sK^0_s\pi^+$", and $D^+_s \to \pi^+\pi^-\pi^+$, B. A. D. 1463.

31. M. Pappagallo and A. Palano, "Dalitz plot analysis of $D^+_s \to K^+K^-\pi^+$", B. A. D. 2259.

32. Francis Halzen and Allen D. Martin, *Q*uarks & Leptons: An Introductory Course in Modern Particle Physics, John Wiley & Sons (1984).

33. B. Aslan and G. Zech, *Comparison of Different Goodness of Fit Tests*, arXiv::math/0207300v1, math.PR **31** (2002)

34. K. S. Cranmer, *Kernel Estimation in High-Energy Physics*, Comp. Phys. Comm. **136**, 198 (2001) [hep-ex/0011057c1]

35. `http://www.slac.stanford.edu/BFROOT/www/Physics/TrackEfficTaskForce/TauEff/R22d/TauEff.html`

36. I. Nugent, "Tau31 Tracking Efficiency Study for 2004", B.A.D. 931.

37. M.V. Purohit, R. M. White, "Techniques for the Measurement of Tracking Efficiency and Asymmetry", B. A. D. 2258.

38. M.V. Purohit, R. M. White, H. Liu, "Conservative Estimates of PID Systematics", B. A. D. 1465.

39. http://www.slac.stanford.edu/BFROOT/www/Physics/Tools/Pid/Hadrons/Description_of_the_LH_selectors.html

40. http://tmva.sourceforge.net/

41. http://root.cern.ch

42. http://root.cern.ch/root/html/TMultiLayerPerceptron.html

43. R. Andreassen, "A Likelihood selector for $D^+ \to K^-\pi^+\pi^+$", B. A. D. 1623.

Appendix A

Minuit Fit Results for Tau 31 sample

NO.	NAME	VALUE	ERROR
1	A_0	7.27808e-01	1.30456e-01
2	p0	5.93713e-03	8.72436e-03
3	tau	7.54981e-02	1.43502e-02
4	B_0	1.71287e-02	2.09114e-03
5	p1	7.81093e-01	3.71042e-02
6	tau_prime	8.80375e-01	2.00866e-01
7	asymmetry_0	8.21539e-03	1.41094e-02
8	asymmetry_1	-4.54376e-03	6.27107e-03
9	asymmetry_2	2.96776e-03	2.99234e-03
10	asymmetry_3	-1.31572e-02	1.13516e-02
11	plus_acceptanceloss	3.70700e-01	
12	plus_acceptancelosscat1	5.47188e-01	
13	plus_acceptancelosscat2	5.07692e-01	
14	plus_conversions	2.25882e-01	1.44893e-01
15	plus_bgd	9.95527e-02	3.01867e-01
16	plus_uds	5.45207e-01	fixed
17	plus_cc	4.90112e-01	fixed
18	plus_bb	3.13119e-01	fixed
19	minus_acceptanceloss	6.13923e-11	2.76052e-01
20	minus_acceptancelosscat1	5.88997e-01	1.84777e-02
21	minus_acceptancelosscat2	3.66294e-01	9.12865e-02
22	minus_conversions	2.41900e-01	1.50836e-01
23	minus_bgd	1.27923e-01	3.68920e-01

```
24  minus_uds    5.45207e-01     fixed
25  minus_cc     4.90112e-01     fixed
26  minus_bb     3.13119e-01     fixed
```

Appendix B

Likelihood Based Event Selection

In the case of charm events at e^+e^- B-factories, $b\bar{b}$ events can be removed with momentum and event shape cuts, however, contributions from *uds* and other non-signal charm events produce extreme levels of background.

A multivariate classifier, based on machine learning techniques, is used in this analysis to extract significant and pure signal samples of Singly-Cabibbo suppressed charm decays. In particular, the projective likelihood estimator, which consists of building a model out of probability density functions (PDFs) of various input variables for signal and background events, provides signal event classification with excellent stability. We base our likelihood technique on the software package TMVA [**40**].

The method of maximum likelihood requires that a model be built from PDFs that describe the input variables for signal and background. For any given event, the likelihood for being of signal type is obtained by multiplying all the signal probability densities of the input variables, and normalizing this by the sum of signal and background likelihoods. Correlations among input variables are ignored, which is valid if the input variables are not highly correlated (correlation scatter plots are shown in figures Figure B.4 and Figure B.5). If they were, the likelihood would require a multidimensional PDF.

The likelihood ratio R for a given event i is given by

$$R = \frac{L_s(i)}{L_S(i) + L_B(i)} \tag{B.0.3}$$

The likelihoods are defined as

$$L_{S(B)}(i) = \prod_{k=1}^{n_{var}} p_{S(B),k}(x_k(i)) \tag{B.0.4}$$

where $p_{S(B),k}$ is the signal (background) PDF for the kth input variable x_k. The PDFs are normalized

$$\int_{-\infty}^{+\infty} p_{S(B),k}(x_k)dx_k = 1, \forall k \tag{B.0.5}$$

The PDFs for signal and background discriminating variables are obtained as follows:

•Determine the signal and background regions of events in the mass plot. The signal and background regions are defined by σ_{Total} from the fit to the mass plot. Signal regions are taken to $\pm 2\sigma_{Total}$ from the mean μ. The background regions are taken from $\pm 6\sigma_{Total}$ to $\pm 10\sigma_{Total}$ from the mean μ. The background histograms are taken as is, but a sideband subtraction technique must be applied to the signal histograms. Therefore, the background histograms are scaled by a factor of 1/2 (the background area is twice as large as the signal area) and subtracted from the signal histogram. The result is a signal distribution for a given discriminating variable.

•The background-subtracted signal histograms and the background histograms are smoothed, using the ROOT [**41**] smoothing function "TH1::SmoothArray", which is an implementation of the algorithm 353QH twice.

•The parametric form of the PDFs are typically unknown, therefore the PDF shapes are empirically approximated from the smoothed histgrams by nonparametric functions, which are polynomial splines of second order. The spline functions are taken from TMVA [**40**].

Histograms of the discriminating variables are shown in figures Figure B.2 and Figure B.3. The figures also show the smoothed histogram and the resulting PDF for signal and background.

For a given event i, the probabality that the event is signal or background is computed based on the value of the discriminating varible. These probabilities are used in equation B.0.4 to compute the likelihood, and then the likelihood ratio is found from equation B.0.3. The distribution should peak at 1 for signal events and at 0 for background events (figure Figure B.6).

The likelihood PDFs are derived from two variables. The following discriminant variables are with respect to the parent D meson candidate.

•Signed decay distance in the transverse plane (D_{xy}), defined in equation B.0.6. The distributions of signal and background are shown in figure Figure B.2.

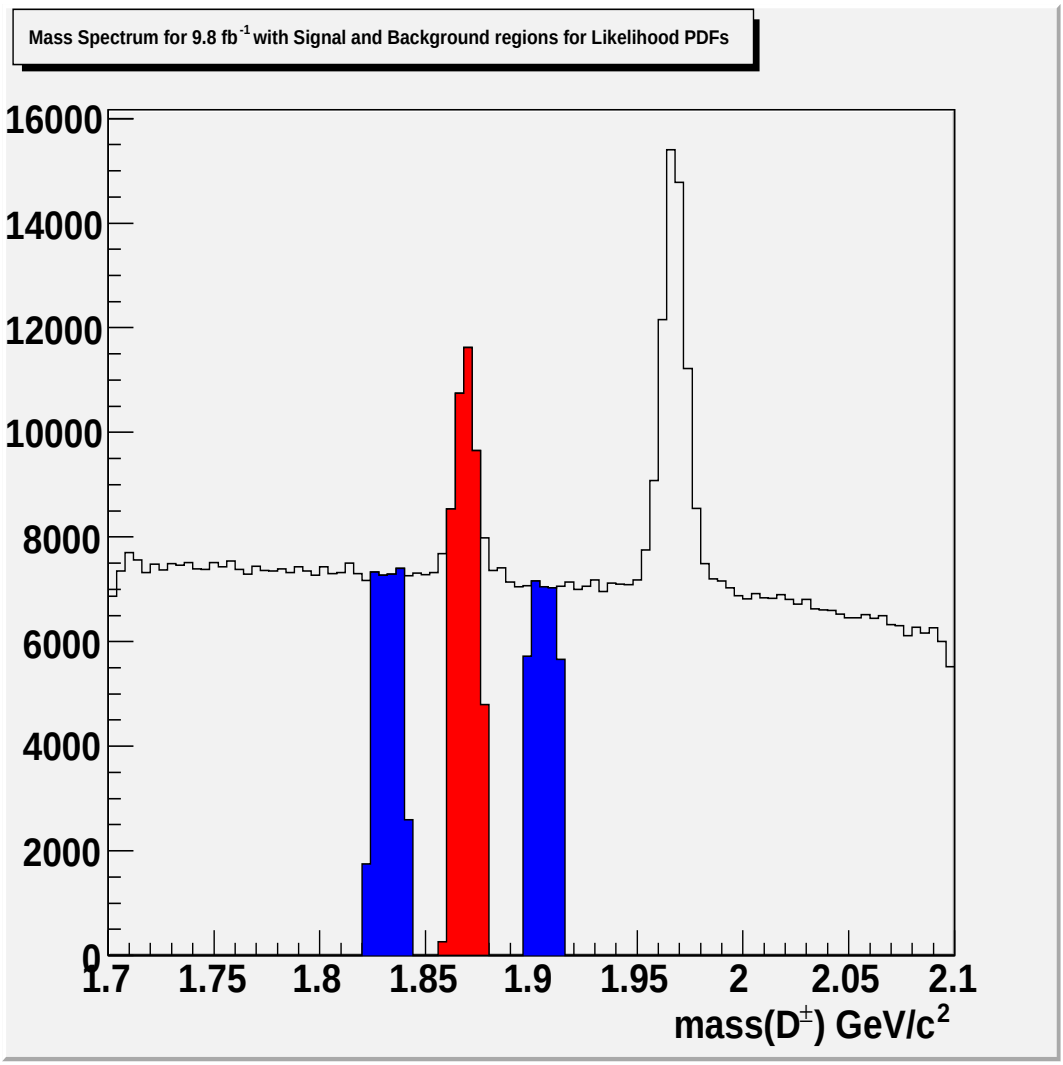

Figure B.1: Multivariate discriminant training regions for signal (red) and background (blue) events. Regions are determined from the σ_{Total} of the fit to this mass distribution. The signal region is $\pm 2\sigma_{Total}$ from the D mass and the background regions are $6\sigma_{Total}$ to $10\sigma_{Total}$ from the D mass in the lower and upper sideband regions.

$$D_{xy} = \frac{\vec{d}_{xy} \bullet \hat{p}_D}{\sigma_{d_{xy}}} \tag{B.0.6}$$

The signed decay distance is calculated as follows. Fit the D candidate with the requirement that it originate from the beam spot, so that the momentum vector of the D points from the beam spot to the decay vertex. Calculate the vector from the beam spot to the decay vertex in the x-y plane. Determine the sign of this vector by dotting it with the unit vector in the direction of the D momentum. Finally, determine the error in the

distance calculation. The signed, scaled decay "distance" is the signed distance in units of error (see reference [**43**]).

•Center-of-mass momentum (p^*). The distributions of signal and background are shown in figure Figure B.3.

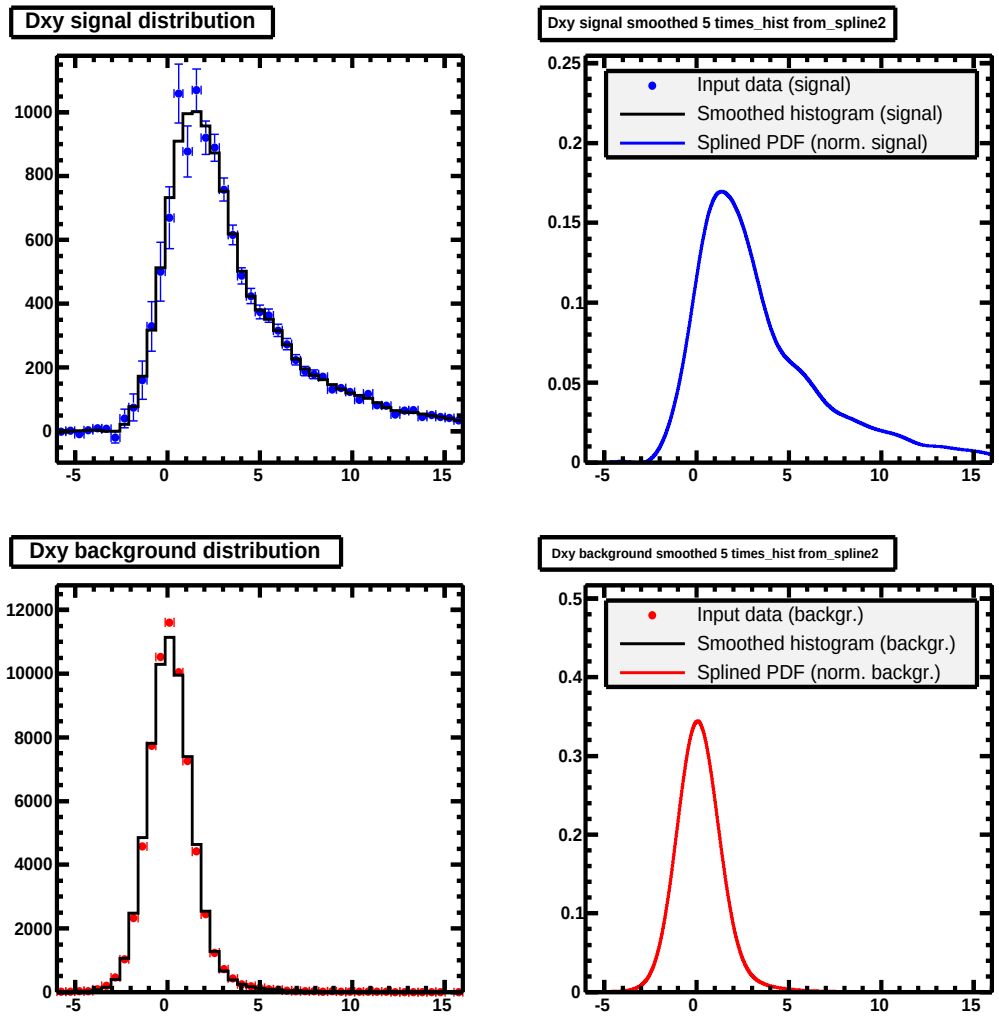

Figure B.2: Probability distribution function of the decay distance measured in the transverse plane D_{xy} (right)

The likelihood classifier provides a tool to remove multiple candidates per event. Before measuring the overall performance of the classifier, the candidate with the largest R per event is kept and the remaining candidates are rejected. Table Table B.6 summarizes the number of candidates per event and the fraction of those events in the data. 11% of events have zero candidates after the initial Q value cut and m(KK) cut, leaving 72% of events

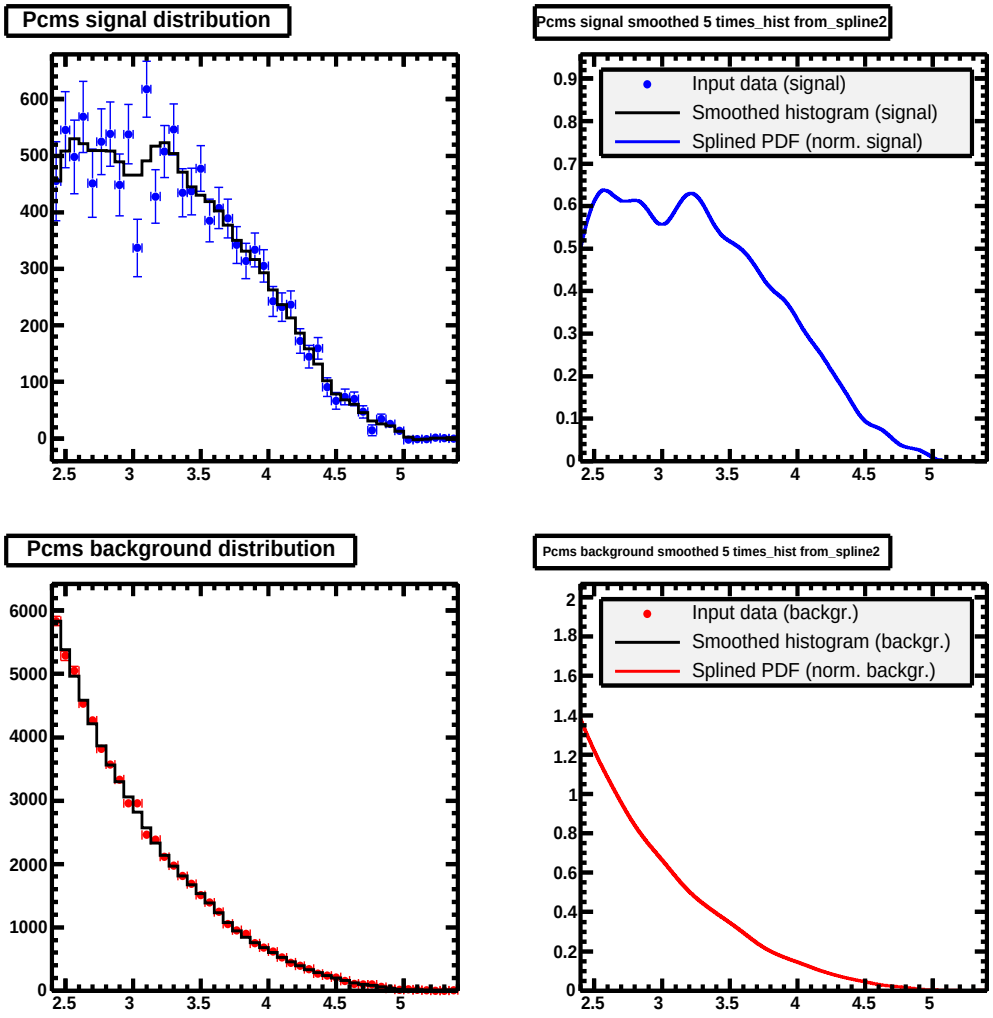

Figure B.3: Probability distribution functions of the center-of-mass momentum p*.

with exactly one candidate. Events that have more than one candidate typically have poorly measured D candidates and are rejected later by the tight cut on R.

CandidatesEvent	Fraction of Events (%)
0	11.4
1	71.7
2	13.1
3 or more	3.4

Table B.6: Breakdown of the number of candidates per event and the fraction of those events in the data set. Most of the events have exactly one candidate.

Using ten independent samples of 10 fb^{-1}, a measure of the fractional error on the significance is found. The training of the estimator is performed on one of the ten samples,

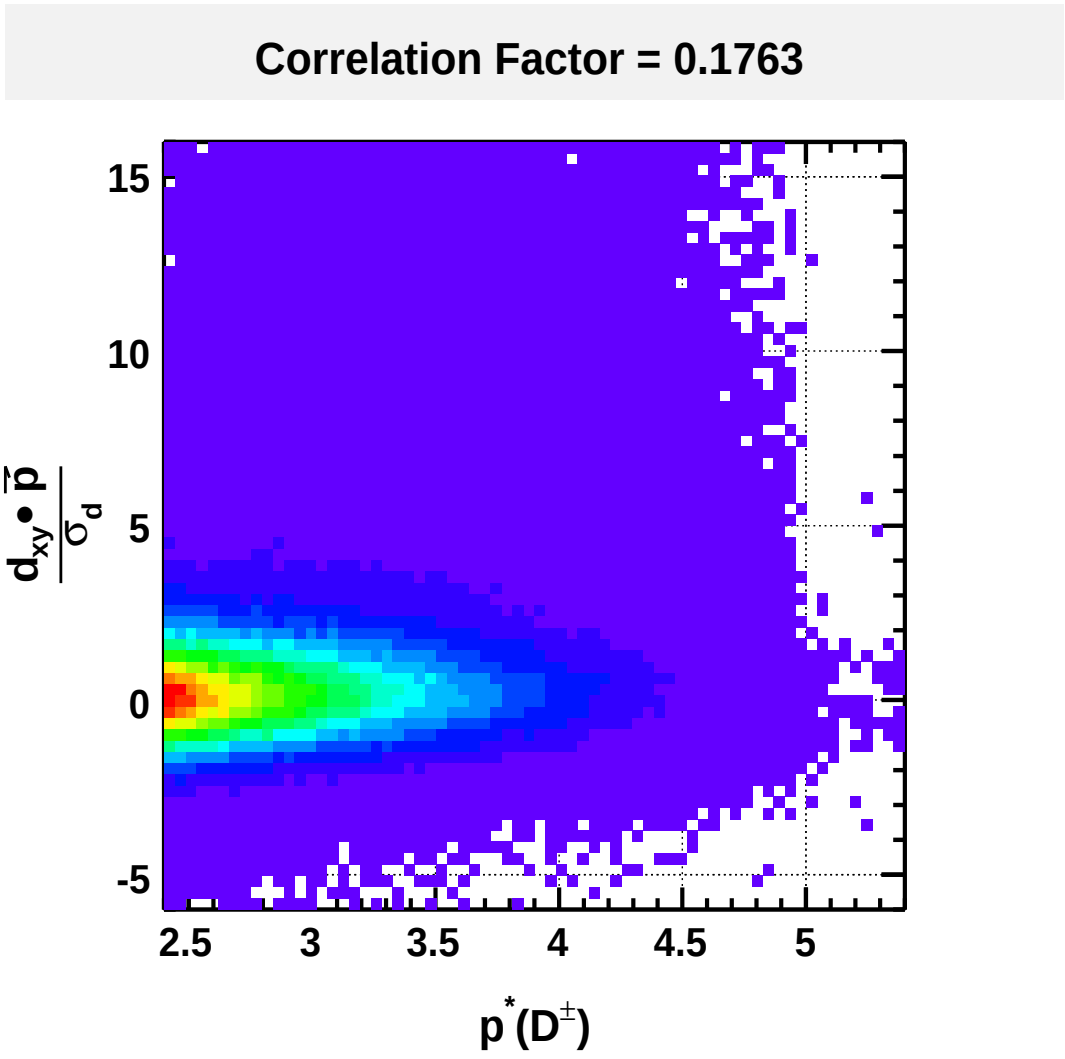

Figure B.4: Correlation scatter plots for signal + background discriminating variables. The correlation factor for the signal pdfs of p* and D_{xy} is 17%. Since the pdfs are taken directly from data, we cannot produce a scatter plot of the pdfs for signal due to the background subtraction that needs to be applied to obtain the signal pdfs.

and the resulting PDFs are used to test the remaining nine samples. The RMS deviation calculated from independent samples leads to a measurement of the fractional error. The RMS for a given likelihood ratio i is given by

$$\sigma_{S_i} = \sqrt{\frac{(S_i - \bar{S}_i)^2}{n}} \tag{B.0.7}$$

where n is the number of samples, in this case nine. Therefore, the error on S is given by

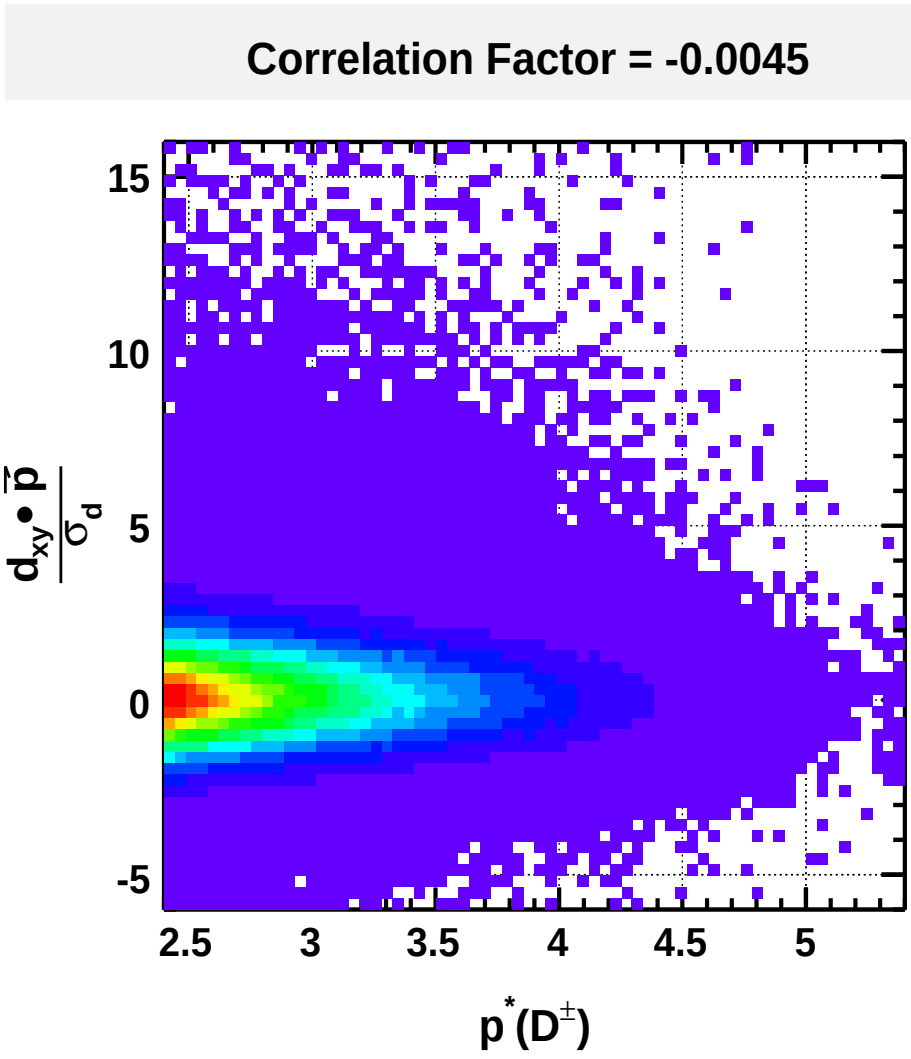

Figure B.5: Correlation scatter plots for background discriminating variables. The correlation factor for the background pdfs is nearly zero.

$$\Delta S_i = \frac{\sigma_{S_i}}{\sqrt{n}} \tag{B.0.8}$$

and the fractional error

$$\frac{\Delta s_i}{s_i} \tag{B.0.9}$$

The fractional error as a function of the cut R, shown in figure Figure B.7, has a mean of 0.45%.

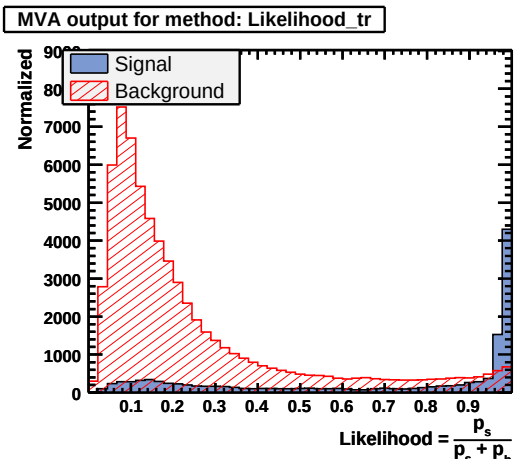

Figure B.6: Signal and background distributions of the likelihood ratio R. Signal events are expected to peak at one, while the background events are expected to peak around zero.

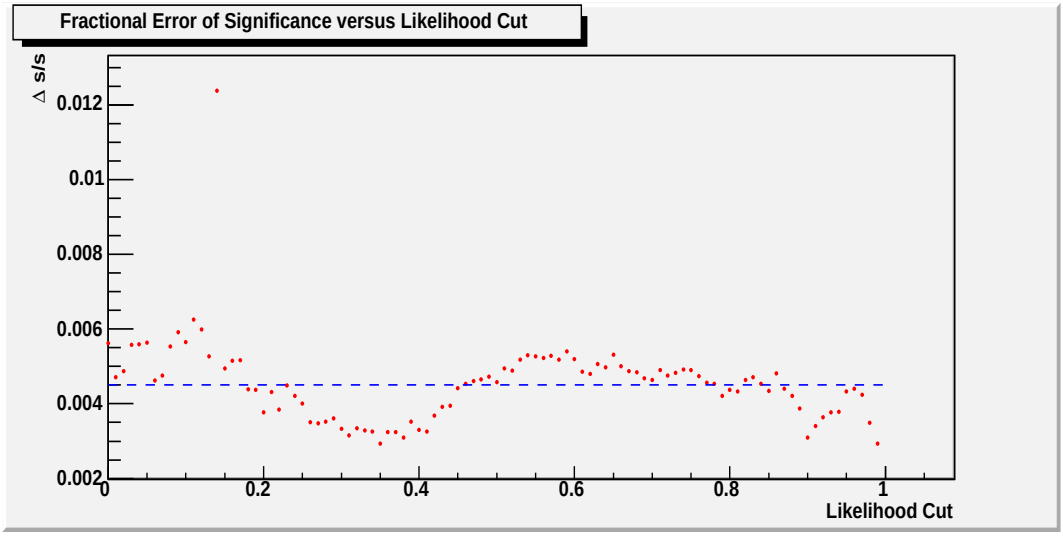

Figure B.7: The fractional error, $\frac{\Delta s_i}{s_i}$, as a function of $R(i)$ has a mean (blue-dashed) of 0.45%

Appendix C

uds Monte Carlo Backgrounds

	N	N/Nb	Decay	K^+	K^-	π^+
	1461					
35	228	0.16	$K^* \to K\pi$	N/A	$K^-(K^{*0})$	$\pi^+(K^{*0})$
36	8	0.01	$K^*Ln \to K^-\pi$	N/A	$K^-(K^{*0})$	$\pi^+(K^{*0})$
37	1	0.00	$K^* \to K\pi$	$\pi^+(K^{*0})$	$K^-(K^{*0})$	N/A
38	4	0.00	$K^* \to K\pi$	$K^+(K^{*0})$	N/A	$\pi^-(K^{*0})$
40	166	0.11	$K^* \to K\pi$	N/A	$K^-(K^{*0})$	π_r^+
43	170	0.12	$\Phi \to K^+K^-$	K^+	K^-	N/A
44	71	0.05	$\Phi \to K^+K^-$	N/A	$K^-(\Phi)$	$K^+(\Phi)$
45	12	0.01	$\Phi \to K^+K^-$	K_r^+	$K^-(\Phi)$	N/A
46	21	0.01	$\Phi \to K^+K^-$	$K^+(\Phi)$	K_r^-	N/A
47	223	0.15	$K\bar{K}$ Resonance	K^+	K^-	N/A
48	6	0.00	$\Delta^{++} \to p\pi^+$	$p^+(\Delta^{++})$	N/A	$\pi^+ i(\Delta^{++})$
49	5	0.00	$\gamma \to e^+e^-$			
50	148	0.10	$K^{*+} \to K^+\pi^0$			
52	1	0.00	$\rho^0 \to \pi^+\pi^-$			
53	13	0.01	$\rho^+ \to \pi^+\pi^0$			$\pi^+(\rho^+)$
54	30	0.02	$\rho^0 \to \pi^+\pi^-$			$\pi^+(\rho^+)$
55	354	0.24	Other			

Table C.0: Breakdown of uds MC background events for D^+ in the lower mass sideband region.

	N	N/Nb	Decay	K^+	K^-	π^+
	1336					
35	248	0.19	$K^* \to K\pi$	N/A	$K^-(K^{*0})$	$\pi^+(K^{*0})$
36	8	0.01	$K^*Ln \to K^-\pi$	N/A	$K^-(K^{*0})$	$\pi^+(K^{*0})$
37	5	0.00	$K^* \to K\pi$	$\pi^+(K^{*0})$	$K^-(K^{*0})$	N/A
38	8	0.01	$K^* \to K\pi$	$K^+(K^{*0})$	N/A	$\pi^-(K^{*0})$
40	139	0.10	$K^* \to K\pi$	N/A	$K^-(K^{*0})$	π_r^+
43	155	0.12	$\Phi \to K^+K^-$	K^+	K^-	N/A
44	62	0.05	$\Phi \to K^+K^-$	N/A	$K^-(\Phi)$	$K^+(\Phi)$
45	8	0.01	$\Phi \to K^+K^-$	K_r^+	$K^-(\Phi)$	N/A
46	18	0.01	$\Phi \to K^+K^-$	$K^+(\Phi)$	K_r^-	N/A
47	211	0.16	$K\bar{K}$ Resonance	K^+	K^-	N/A
48	6	0.00	$\Delta^{++} \to p\pi^+$	$p^+(\Delta^{++})$	N/A	$\pi^+ i(\Delta^{++})$
49	1	0.00	$\gamma \to e^+e^-$			
50	148	0.11	$K^{*+} \to K^+\pi^0$			
52	3	0.00	$\rho^0 \to \pi^+\pi^-$			
53	9	0.01	$\rho^+ \to \pi^+\pi^0$			$\pi^+(\rho^+)$
54	22	0.02	$\rho^0 \to \pi^+\pi^-$			$\pi^+(\rho^+)$
55	285	0.21	Other			

Table C.0: Breakdown of uds MC background events for D^- in the lower mass sideband region.

	N	N/Nb	Decay	K^+	K^-	π^+
	1267					
35	203	0.16	$K^* \to K\pi$	N/A	$K^-(K^{*0})$	$\pi^+(K^{*0})$
36	14	0.01	$K^*Ln \to K^-\pi$	N/A	$K^-(K^{*0})$	$\pi^+(K^{*0})$
37	1	0.00	$K^* \to K\pi$	$\pi^+(K^{*0})$	$K^-(K^{*0})$	N/A
38	3	0.00	$K^* \to K\pi$	$K^+(K^{*0})$	N/A	$\pi^-(K^{*0})$
40	118	0.09	$K^* \to K\pi$	N/A	$K^-(K^{*0})$	π_r^+
43	150	0.12	$\Phi \to K^+K^-$	K^+	K^-	N/A
44	50	0.04	$\Phi \to K^+K^-$	N/A	$K^-(\Phi)$	$K^+(\Phi)$
45	7	0.01	$\Phi \to K^+K^-$	K_r^+	$K^-(\Phi)$	N/A
46	14	0.01	$\Phi \to K^+K^-$	$K^+(\Phi)$	K_r^-	N/A
47	191	0.15	$K\bar{K}$ Resonance	K^+	K^-	N/A
48	4	0.00	$\Delta^{++} \to p\pi^+$	$p^+(\Delta^{++})$	N/A	$\pi^+ i(\Delta^{++})$
49	3	0.00	$\gamma \to e^+e^-$			
50	144	0.11	$K^{*+} \to K^+\pi^0$			
52	3	0.00	$\rho^0 \to \pi^+\pi^-$			
53	19	0.01	$\rho^+ \to \pi^+\pi^0$			$\pi^+(\rho^+)$
54	28	0.02	$\rho^0 \to \pi^+\pi^-$			$\pi^+(\rho^+)$
55	315	0.25	Other			

Table C.0: Breakdown of uds MC background events for D^+ in the upper mass sideband region.

	N	N/Nb	Decay	K^+	K^-	π^+
	1258					
35	180	0.14	$K^* \to K\pi$	N/A	$K^-(K^{*0})$	$\pi^+(K^{*0})$
36	11	0.01	$K^*Ln \to K^-\pi$	N/A	$K^-(K^{*0})$	$\pi^+(K^{*0})$
37	5	0.00	$K^* \to K\pi$	$\pi^+(K^{*0})$	$K^-(K^{*0})$	N/A
38	3	0.00	$K^* \to K\pi$	$K^+(K^{*0})$	N/A	$\pi^-(K^{*0})$
40	145	0.12	$K^* \to K\pi$	N/A	$K^-(K^{*0})$	π_r^+
43	131	0.10	$\Phi \to K^+K^-$	K^+	K^-	N/A
44	50	0.04	$\Phi \to K^+K^-$	N/A	$K^-(\Phi)$	$K^+(\Phi)$
45	8	0.01	$\Phi \to K^+K^-$	K_r^+	$K^-(\Phi)$	N/A
46	20	0.02	$\Phi \to K^+K^-$	$K^+(\Phi)$	K_r^-	N/A
47	211	0.17	$K\bar{K}$ Resonance	K^+	K^-	N/A
48	14	0.01	$\Delta^{++} \to p\pi^+$	$p^+(\Delta^{++})$	N/A	$\pi^+ i(\Delta^{++})$
49	1	0.00	$\gamma \to e^+e^-$			
50	132	0.10	$K^{*+} \to K^+\pi^0$			
52	3	0.00	$\rho^0 \to \pi^+\pi^-$			
53	17	0.01	$\rho^+ \to \pi^+\pi^0$			$\pi^+(\rho^+)$
54	21	0.02	$\rho^0 \to \pi^+\pi^-$			$\pi^+(\rho^+)$
55	306	0.24	Other			

Table C.0: Breakdown of uds MC background events for D^- in the upper mass sideband region.

Appendix D

ccbar Monte Carlo Backgrounds

	N	N/Nb	Decay	K^+	K^-	π^+
	6397					
1	203	0.03	$D^+ \to K^+K^-\pi^+$	$K^+(D^+)$	$K^-(D^+)$	π_r^+
2	45	0.01	$D^+ \to K^+K^-\pi^+$	$K^+(D^+)$	$K^-(D^+)$	not π^+
3	489	0.08	$D^+ \to K^+\pi^-\pi^+$	K_r^+	$K^-(D^+)$	$\pi^+(D^+)$
4	3	0.00	$D^+ \to K^+K^-\pi^+$	$K^+(D^+)$	K_r^-	$\pi^+(D^+$
5	2	0.00	$D^+ \to K^+\pi^-\pi^+$	$K^+(D^+)$	$\pi^-(D^+)$	$\pi^+(D^+)$
7	206	0.03	$D^+ \to K^+K^-\pi^+$	$\pi^+(D^+)$	$K^-(D^+)$	$\pi^+(D^+)$
8	6	0.00	$D^+ \to K^-\pi^+e^+(\mu^+)\nu_{e,\mu}$	$e^+(\mu^+)(D^+)$	π_r^+	$K^-(D^+)$
10	11	0.00	$D^+ \to K^-\pi^+e^+(\mu^+)\nu_{e,\mu}$	$\pi^+(D^+)$	$K^-(D^+)$	$e^+(\mu^+)(D^+)$
11	176	0.03	$D^+ \to K^+K^{*0}$	K^+	$K^-(K^{*0})$	π_r^+
12	113	0.02	$D_s^+ \to K^+K^-\pi^+$	K^+	K^-	π^+
13	3	0.00	$D_s^+ \to K^+K^-\pi^+$	π^+	K^-	K^+
14	107	0.02	$D_s^+ \to K^+K^-K^+$	K^+	K^-	K^+
15	34	0.01	$D_s^+ \to K^+K^{*0}$	K^+	K_r^-	$\pi^+(K^{*0})$
16	161	0.03	$D_s^+ \to K^+K^{*0}$	K^+	$K^-(K^{*0})$	π_r^+
17	61	0.01	$D_s^+ \to K^+K^-\pi^+$	K^+	K^-	π_r^+
18	47	0.01	$D_s^+ \to K^+K^-\pi^+$	K^+	K^-	π^+
19	85	0.01	$D_s^+ \to K^+K^-\pi^+$			
20	1	0.00	$D^* \to D^0 \to K\pi(K)$	$\pi^+, K^+(D^0$	$K^-(D^0$	$\pi^+(D^{*+})$
21	191	0.03	$D^0 \to K^+K^-$	K^+	K^-	N/A
22	25	0.00	$D^0 \to K^+K^-$	N/A	K^-	K^+
23	233	0.04	$D^0 \to K^-\pi^+\pi^0$	K_r^+	K^-	π^+
24	152	0.02	$D^0 \to K^-\pi^+$	K_r^+	K^-	π^+
25	11	0.00	$D^0 \to Ke(\mu)\nu$	K^+	$e^-(\mu^-)$	N/A
26	309	0.05	$D^0 \to Ke(\mu)\nu$	N/A	K^-	$e^+(\mu^+)$
27	36	0.01	$D^0 \to K^-\pi^+$	π^+	K^-	N/A
28	2	0.00	$D^0 \to K^-\pi^+$	N/A	π^-	K^+
29	48	0.01	$D^0 \to K^{*0}\pi^+\pi^-$	K_r^+	$K^-(K^*)$	π^+
31	88	0.01	D^0 Decay			
32	6	0.00	$\Lambda_c \to pK^-\pi^+$	p	K^-	π^+
33	2	0.00	$\Lambda_c Decay$			
34	286	0.04	$K^* \to K\pi$ (Charm)	N/A	$K^-(K^{*0})$	$\pi^+(K^{*0})$
35	86	0.01	$K^* \to K\pi$	N/A	$K^-(K^{*0})$	$\pi^+(K^{*0})$
36	5	0.00	$K^*Ln \to K^-\pi$	N/A	$K^-(K^{*0})$	$\pi^+(K^{*0})$
37	121	0.02	$K^* \to K\pi$	$\pi^+(K^{*0})$	$K^-(K^{*0})$	N/A
38	30	0.00	$K^* \to K\pi$	$K^+(K^{*0})$	N/A	$\pi^-(K^{*0})$
40	105	0.02	$K^* \to K\pi$	N/A	$K^-(K^{*0})$	π_r^+
41	163	0.03	$K^* \to K\pi$	N/A	$K^-(K^{*0})$	π_r^+
42	492	0.08	$\Phi \to K^+K^-$(Charm)	K^+	K^-	N/A
43	33	0.01	$\Phi \to K^+K^-$	K^+	K^-	N/A
44	88	0.01	$\Phi \to K^+K^-$	N/A	$K^-(\Phi)$	$K^+(\Phi)$
45	28	0.00	$\Phi \to K^+K^-$	K_r^+	$K^-(\Phi)$	N/A
46	136	0.02	$\Phi \to K^+K^-$	$K^+(\Phi)$	K_r^-	N/A
47	53	0.01	$K\bar{K}$ Resonance	K^+	K^-	N/A
48	3	0.00	$\Delta^{++} \to p\pi^+$	$p^+(\Delta^{++})$	N/A	$\pi^+ i(\Delta^{++})$
49	4	0.00	$\gamma \to e^+e^-$			
50	522	0.08	$K^{*+} \to K^+\pi^0$			
51	1	0.00	τ Decay			
52	85	0.01	$\rho^0 \to \pi^+\pi^-$			
53	181	0.03	$\rho^+ \to \pi^+\pi^0$			$\pi^+(\rho^+)$
54	308	0.05	$\rho^0 \to \pi^+\pi^-$			$\pi^+(\rho^+)$
55	811	0.13	Other			

Table D.0: Breakdown of background events for ccbar MC for D^- events in the lower mass sideband region.

	N	N/Nb	Decay	K^+	K^-	π^+
	6268					
1	202	0.03	$D^+ \to K^+K^-\pi^+$	$K^+(D^+)$	$K^-(D^+)$	π_r^+
2	53	0.01	$D^+ \to K^+K^-\pi^+$	$K^+(D^+)$	$K^-(D^+)$	not π^+
3	442	0.07	$D^+ \to K^+\pi^-\pi^+$	K_r^+	$K^-(D^+)$	$\pi^+(D^+)$
4	3	0.00	$D^+ \to K^+K^-\pi^+$	$K^+(D^+)$	K_r^-	$\pi^+(D^+$
5	2	0.00	$D^+ \to K^+\pi^-\pi^+$	$K^+(D^+)$	$\pi^-(D^+)$	$\pi^+(D^+)$
7	179	0.03	$D^+ \to K^+K^-\pi^+$	$\pi^+(D^+)$	$K^-(D^+)$	$\pi^+(D^+)$
8	14	0.00	$D^+ \to K^-\pi^+e^+(\mu^+)\nu_{e,\mu}$	$e^+(\mu^+)(D^+)$	π_r^+	$K^-(D^+)$
10	9	0.00	$D^+ \to K^-\pi^+e^+(\mu^+)\nu_{e,\mu}$	$\pi^+(D^+)$	$K^-(D^+)$	$e^+(\mu^+)(D^+)$
11	171	0.03	$D^+ \to K^+K^{*0}$	K^+	$K^-(K^{*0})$	π_r^+
12	128	0.02	$D_s^+ \to K^+K^-\pi^+$	K^+	K^-	π^+
13	2	0.00	$D_s^+ \to K^+K^-\pi^+$	π^+	K^-	K^+
14	79	0.01	$D_s^+ \to K^+K^-K^+$	K^+	K^-	K^+
15	36	0.01	$D_s^+ \to K^+K^{*0}$	K^+	K_r^-	$\pi^+(K^{*0})$
16	164	0.03	$D_s^+ \to K^+K^{*0}$	K^+	$K^-(K^{*0})$	π_r^+
17	63	0.01	$D_s^+ \to K^+K^-\pi^+$	K^+	K^-	π_r^+
18	41	0.01	$D_s^+ \to K^+K^-\pi^+$	K^+	K^-	π^+
19	81	0.01	$D_s^+ \to K^+K^-\pi^+$			
20	4	0.00	$D^* \to D^0 \to K\pi(K)$	$\pi^+, K^+(D^0$	$K^-(D^0$	$\pi^+(D^{*+})$
21	158	0.03	$D^0 \to K^+K^-$	K^+	K^-	N/A
22	19	0.00	$D^0 \to K^+K^-$	N/A	K^-	K^+
23	268	0.04	$D^0 \to K^-\pi^+\pi^0$	K_r^+	K^-	π^+
24	150	0.02	$D^0 \to K^-\pi^+$	K_r^+	K^-	π^+
25	5	0.00	$D^0 \to Ke(\mu)\nu$	K^+	$e^-(\mu^-)$	N/A
26	276	0.04	$D^0 \to Ke(\mu)\nu$	N/A	K^-	$e^+(\mu^+)$
27	36	0.01	$D^0 \to K^-\pi^+$	π^+	K^-	N/A
29	49	0.01	$D^0 \to K^{*0}\pi^+\pi^-$	K_r^+	$K^-(K^*)$	π^+
31	102	0.02	D^0 Decay			
32	2	0.00	$\Lambda_c \to pK^-\pi^+$	p	K^-	π^+
33	3	0.00	$\Lambda_c Decay$			
34	289	0.05	$K^* \to K\pi$ (Charm)	N/A	$K^-(K^{*0})$	$\pi^+(K^{*0})$
35	72	0.01	$K^* \to K\pi$	N/A	$K^-(K^{*0})$	$\pi^+(K^{*0})$
36	7	0.00	$K^*Ln \to K^-\pi$	N/A	$K^-(K^{*0})$	$\pi^+(K^{*0})$
37	118	0.02	$K^* \to K\pi$	$\pi^+(K^{*0})$	$K^-(K^{*0})$	N/A
38	33	0.01	$K^* \to K\pi$	$K^+(K^{*0})$	N/A	$\pi^-(K^{*0})$
40	106	0.02	$K^* \to K\pi$	N/A	$K^-(K^{*0})$	π_r^+
41	116	0.02	$K^* \to K\pi$	N/A	$K^-(K^{*0})$	π_r^+
42	498	0.08	$\Phi \to K^+K^-$(Charm)	K^+	K^-	N/A
43	21	0.00	$\Phi \to K^+K^-$	K^+	K^-	N/A
44	73	0.01	$\Phi \to K^+K^-$	N/A	$K^-(\Phi)$	$K^+(\Phi)$
45	24	0.00	$\Phi \to K^+K^-$	K_r^+	$K^-(\Phi)$	N/A
46	139	0.02	$\Phi \to K^+K^-$	$K^+(\Phi)$	K_r^-	N/A
47	43	0.01	$K\bar{K}$ Resonance	K^+	K^-	N/A
48	6	0.00	$\Delta^{++} \to p\pi^+$	$p^+(\Delta^{++})$	N/A	$\pi^+ i(\Delta^{++})$
49	5	0.00	$\gamma \to e^+e^-$			
50	553	0.09	$K^{*+} \to K^+\pi^0$			
51	1	0.00	τ Decay			
52	101	0.02	$\rho^0 \to \pi^+\pi^-$			
53	183	0.03	$\rho^+ \to \pi^+\pi^0$			$\pi^+(\rho^+)$
54	367	0.06	$\rho^0 \to \pi^+\pi^-$			$\pi^+(\rho^+)$
55	772	0.12	Other			

Table D.0: Breakdown of background events of ccbar MC for D^+ events in the lower mass sideband region.

	N	N/Nb	Decay	K^+	K^-	π^+
	5786					
1	187	0.03	$D^+ \to K^+K^-\pi^+$	$K^+(D^+)$	$K^-(D^+)$	π_r^+
2	21	0.00	$D^+ \to K^+K^-\pi^+$	$K^+(D^+)$	$K^-(D^+)$	not π^+
3	453	0.08	$D^+ \to K^+\pi^-\pi^+$	K_r^+	$K^-(D^+)$	$\pi^+(D^+)$
4	2	0.00	$D^+ \to K^+K^-\pi^+$	$K^+(D^+)$	K_r^-	$\pi^+(D^+$
5	8	0.00	$D^+ \to K^+\pi^-\pi^+$	$K^+(D^+)$	$\pi^-(D^+)$	$\pi^+(D^+)$
7	170	0.03	$D^+ \to K^+K^-\pi^+$	$\pi^+(D^+)$	$K^-(D^+)$	$\pi^+(D^+)$
8	9	0.00	$D^+ \to K^-\pi^+e^+(\mu^+)\nu_{e,\mu}$	$e^+(\mu^+)(D^+)$	π_r^+	$K^-(D^+)$
10	9	0.00	$D^+ \to K^-\pi^+e^+(\mu^+)\nu_{e,\mu}$	$\pi^+(D^+)$	$K^-(D^+)$	$e^+(\mu^+)(D^+)$
11	172	0.03	$D^+ \to K^+K^{*0}$	K^+	$K^-(K^{*0})$	π_r^+
12	271	0.05	$D_s^+ \to K^+K^-\pi^+$	K^+	K^-	π^+
13	8	0.00	$D_s^+ \to K^+K^-\pi^+$	π^+	K^-	K^+
15	80	0.01	$D_s^+ \to K^+K^{*0}$	K^+	K_r^-	$\pi^+(K^{*0})$
16	305	0.05	$D_s^+ \to K^+K^{*0}$	K^+	$K^-(K^{*0})$	π_r^+
17	66	0.01	$D_s^+ \to K^+K^-\pi^+$	K^+	K^-	π_r^+
18	39	0.01	$D_s^+ \to K^+K^-\pi^+$	K^+	K^-	π^+
19	111	0.02	$D_s^+ \to K^+K^-\pi^+$			
20	2	0.00	$D^* \to D^0 \to K\pi(K)$	$\pi^+, K^+(D^0$	$K^-(D^0$	$\pi^+(D^{*+})$
21	139	0.02	$D^0 \to K^+K^-$	K^+	K^-	N/A
22	15	0.00	$D^0 \to K^+K^-$	N/A	K^-	K^+
23	216	0.04	$D^0 \to K^-\pi^+\pi^0$	K_r^+	K^-	π^+
24	152	0.03	$D^0 \to K^-\pi^+$	K_r^+	K^-	π^+
25	12	0.00	$D^0 \to Ke(\mu)\nu$	K^+	$e^-(\mu^-)$	N/A
26	373	0.06	$D^0 \to Ke(\mu)\nu$	N/A	K^-	$e^+(\mu^+)$
27	54	0.01	$D^0 \to K^-\pi^+$	π^+	K^-	N/A
28	2	0.00	$D^0 \to K^-\pi^+$	N/A	π^-	K^+
29	44	0.01	$D^0 \to K^{*0}\pi^+\pi^-$	K_r^+	$K^-(K^*)$	π^+
31	90	0.02	D^0 Decay			
32	9	0.00	$\Lambda_c \to pK^-\pi^+$	p	K^-	π^+
33	1	0.00	$\Lambda_c Decay$			
34	183	0.03	$K^* \to K\pi$ (Charm)	N/A	$K^-(K^{*0})$	$\pi^+(K^{*0})$
35	73	0.01	$K^* \to K\pi$	N/A	$K^-(K^{*0})$	$\pi^+(K^{*0})$
36	4	0.00	$K^*Ln \to K^-\pi$	N/A	$K^-(K^{*0})$	$\pi^+(K^{*0})$
37	77	0.01	$K^* \to K\pi$	$\pi^+(K^{*0})$	$K^-(K^{*0})$	N/A
38	20	0.00	$K^* \to K\pi$	$K^+(K^{*0})$	N/A	$\pi^-(K^{*0})$
40	80	0.01	$K^* \to K\pi$	N/A	$K^-(K^{*0})$	π_r^+
41	111	0.02	$K^* \to K\pi$	N/A	$K^-(K^{*0})$	π_r^+
42	213	0.04	$\Phi \to K^+K^-$(Charm)	K^+	K^-	N/A
43	22	0.00	$\Phi \to K^+K^-$	K^+	K^-	N/A
44	64	0.01	$\Phi \to K^+K^-$	N/A	$K^-(\Phi)$	$K^+(\Phi)$
45	16	0.00	$\Phi \to K^+K^-$	K_r^+	$K^-(\Phi)$	N/A
46	179	0.03	$\Phi \to K^+K^-$	$K^+(\Phi)$	K_r^-	N/A
47	59	0.01	$K\bar{K}$ Resonance	K^+	K^-	N/A
48	11	0.00	$\Delta^{++} \to p\pi^+$	$p^+(\Delta^{++})$	N/A	$\pi^+ i(\Delta^{++})$
49	3	0.00	$\gamma \to e^+e^-$			
50	476	0.08	$K^{*+} \to K^+\pi^0$			
51	4	0.00	τ Decay			
52	49	0.01	$\rho^0 \to \pi^+\pi^-$			
53	165	0.03	$\rho^+ \to \pi^+\pi^0$			$\pi^+(\rho^+)$
54	296	0.05	$\rho^0 \to \pi^+\pi^-$			$\pi^+(\rho^+)$
55	661	0.11	Other			

Table D.0: Breakdown of background events for ccbar MC events for D^+ events in the upper mass sideband region.

	N	N/Nb	Decay	K^+	K^-	π^+
	5929					
1	180	0.03	$D^+ \to K^+K^-\pi^+$	$K^+(D^+)$	$K^-(D^+)$	π_r^+
2	24	0.00	$D^+ \to K^+K^-\pi^+$	$K^+(D^+)$	$K^-(D^+)$	not π^+
3	461	0.08	$D^+ \to K^+\pi^-\pi^+$	K_r^+	$K^-(D^+)$	$\pi^+(D^+)$
4	2	0.00	$D^+ \to K^+K^-\pi^+$	$K^+(D^+)$	K_r^-	$\pi^+(D^+$
5	8	0.00	$D^+ \to K^+\pi^-\pi^+$	$K^+(D^+)$	$\pi^-(D^+)$	$\pi^+(D^+)$
7	169	0.03	$D^+ \to K^+K^-\pi^+$	$\pi^+(D^+)$	$K^-(D^+)$	$\pi^+(D^+)$
8	12	0.00	$D^+ \to K^-\pi^+e^+(\mu^+)\nu_{e,\mu}$	$e^+(\mu^+)(D^+)$	π_r^+	$K^-(D^+)$
10	8	0.00	$D^+ \to K^-\pi^+e^+(\mu^+)\nu_{e,\mu}$	$\pi^+(D^+)$	$K^-(D^+)$	$e^+(\mu^+)(D^+)$
11	187	0.03	$D^+ \to K^+K^{*0}$	K^+	$K^-(K^{*0})$	π_r^+
12	275	0.05	$D_s^+ \to K^+K^-\pi^+$	K^+	K^-	π^+
13	7	0.00	$D_s^+ \to K^+K^-\pi^+$	π^+	K^-	K^+
14	1	0.00	$D_s^+ \to K^+K^-K^+$	K^+	K^-	K^+
15	95	0.02	$D_s^+ \to K^+K^{*0}$	K^+	K_r^-	$\pi^+(K^{*0})$
16	341	0.06	$D_s^+ \to K^+K^{*0}$	K^+	$K^-(K^{*0})$	π_r^+
17	66	0.01	$D_s^+ \to K^+K^-\pi^+$	K^+	K^-	π_r^+
18	48	0.01	$D_s^+ \to K^+K^-\pi^+$	K^+	K^-	π^+
19	99	0.02	$D_s^+ \to K^+K^-\pi^+$			
21	135	0.02	$D^0 \to K^+K^-$	K^+	K^-	N/A
22	18	0.00	$D^0 \to K^+K^-$	N/A	K^-	K^+
23	250	0.04	$D^0 \to K^-\pi^+\pi^0$	K_r^+	K^-	π^+
24	145	0.02	$D^0 \to K^-\pi^+$	K_r^+	K^-	π^+
25	16	0.00	$D^0 \to Ke(\mu)\nu$	K^+	$e^-(\mu^-)$	N/A
26	367	0.06	$D^0 \to Ke(\mu)\nu$	N/A	K^-	$e^+(\mu^+)$
27	46	0.01	$D^0 \to K^-\pi^+$	π^+	K^-	N/A
28	2	0.00	$D^0 \to K^-\pi^+$	N/A	π^-	K^+
29	41	0.01	$D^0 \to K^{*0}\pi^+\pi^-$	K_r^+	$K^-(K^*)$	π^+
31	77	0.01	D^0 Decay			
32	8	0.00	$\Lambda_c \to pK^-\pi^+$	p	K^-	π^+
33	1	0.00	$\Lambda_c Decay$			
34	192	0.03	$K^* \to K\pi$ (Charm)	N/A	$K^-(K^{*0})$	$\pi^+(K^{*0})$
35	65	0.01	$K^* \to K\pi$	N/A	$K^-(K^{*0})$	$\pi^+(K^{*0})$
36	15	0.00	$K^*Ln \to K^-\pi$	N/A	$K^-(K^{*0})$	$\pi^+(K^{*0})$
37	84	0.01	$K^* \to K\pi$	$\pi^+(K^{*0})$	$K^-(K^{*0})$	N/A
38	13	0.00	$K^* \to K\pi$	$K^+(K^{*0})$	N/A	$\pi^-(K^{*0})$
40	102	0.02	$K^* \to K\pi$	N/A	$K^-(K^{*0})$	π_r^+
41	116	0.02	$K^* \to K\pi$	N/A	$K^-(K^{*0})$	π_r^+
42	236	0.04	$\Phi \to K^+K^-$(Charm)	K^+	K^-	N/A
43	23	0.00	$\Phi \to K^+K^-$	K^+	K^-	N/A
44	58	0.01	$\Phi \to K^+K^-$	N/A	$K^-(\Phi)$	$K^+(\Phi)$
45	28	0.00	$\Phi \to K^+K^-$	K_r^+	$K^-(\Phi)$	N/A
46	151	0.03	$\Phi \to K^+K^-$	$K^+(\Phi)$	K_r^-	N/A
47	56	0.01	$K\bar{K}$ Resonance	K^+	K^-	N/A
48	1	0.00	$\Delta^{++} \to p\pi^+$	$p^+(\Delta^{++})$	N/A	$\pi^+ i(\Delta^{++})$
49	5	0.00	$\gamma \to e^+e^-$			
50	492	0.08	$K^{*+} \to K^+\pi^0$			
51	1	0.00	τ Decay			
52	50	0.01	$\rho^0 \to \pi^+\pi^-$			
53	159	0.03	$\rho^+ \to \pi^+\pi^0$			$\pi^+(\rho^+)$
54	325	0.05	$\rho^0 \to \pi^+\pi^-$			$\pi^+(\rho^+)$
55	668	0.11	Other			

Table D.0: Breakdown of background events for ccbar MC for D^- events in the upper mass sideband region.

Appendix E

B^+B^- Monte Carlo Backgrounds

	N	N/Nb	Decay	K^+	K^-	π^+
	449					
1	1	0.00	$D^+ \to K^+K^-\pi^+$	$K^+(D^+)$	$K^-(D^+)$	π_r^+
2	1	0.00	$D^+ \to K^+K^-\pi^+$	$K^+(D^+)$	$K^-(D^+)$	not π^+
3	13	0.03	$D^+ \to K^+\pi^-\pi^+$	K_r^+	$K^-(D^+)$	$\pi^+(D^+)$
7	1	0.00	$D^+ \to K^+K^-\pi^+$	$\pi^+(D^+)$	$K^-(D^+)$	$\pi^+(D^+)$
11	1	0.00	$D^+ \to K^+K^{*0}$	K^+	$K^-(K^{*0})$	π_r^+
15	2	0.00	$D_s^+ \to K^+K^{*0}$	K^+	K_r^-	$\pi^+(K^{*0})$
16	6	0.01	$D_s^+ \to K^+K^{*0}$	K^+	$K^-(K^{*0})$	π_r^+
19	1	0.00	$D_s^+ \to K^+K^-\pi^+$			
21	18	0.04	$D^0 \to K^+K^-$	K^+	K^-	N/A
22	2	0.00	$D^0 \to K^+K^-$	N/A	K^-	K^+
23	57	0.13	$D^0 \to K^-\pi^+\pi^0$	K_r^+	K^-	π^+
24	20	0.04	$D^0 \to K^-\pi^+$	K_r^+	K^-	π^+
26	30	0.07	$D^0 \to Ke(\mu)\nu$	N/A	K^-	$e^+(\mu^+)$
27	1	0.00	$D^0 \to K^-\pi^+$	π^+	K^-	N/A
29	4	0.01	$D^0 \to K^{*0}\pi^+\pi^-$	K_r^+	$K^-(K^*)$	π^+
31	5	0.01	D^0 Decay			
34	10	0.02	$K^* \to K\pi$ (Charm)	N/A	$K^-(K^{*0})$	$\pi^+(K^{*0})$
36	1	0.00	$K^*Ln \to K^-\pi$	N/A	$K^-(K^{*0})$	$\pi^+(K^{*0})$
37	1	0.00	$K^* \to K\pi$	$\pi^+(K^{*0})$	$K^-(K^{*0})$	N/A
41	16	0.04	$K^* \to K\pi$	N/A	$K^-(K^{*0})$	π_r^+
42	41	0.09	$\Phi \to K^+K^-$(Charm)	K^+	K^-	N/A
43	2	0.00	$\Phi \to K^+K^-$	K^+	K^-	N/A
44	5	0.01	$\Phi \to K^+K^-$	N/A	$K^-(\Phi)$	$K^+(\Phi)$
46	4	0.01	$\Phi \to K^+K^-$	$K^+(\Phi)$	K_r^-	N/A
47	7	0.02	$K\bar{K}$ Resonance	K^+	K^-	N/A
50	33	0.07	$K^{*+} \to K^+\pi^0$			
51	5	0.01	τ Decay			
53	20	0.04	$\rho^+ \to \pi^+\pi^0$			$\pi^+(\rho^+)$
54	23	0.05	$\rho^0 \to \pi^+\pi^-$			$\pi^+(\rho^+)$
55	118	0.26	Other			

Table E.0: Breakdown of background events of bpbm MC for D^+ events in the lower mass sideband region.

	N	N/Nb	Decay	K^+	K^-	π^+
	442					
1	1	0.00	$D^+ \to K^+K^-\pi^+$	$K^+(D^+)$	$K^-(D^+)$	π_r^+
2	1	0.00	$D^+ \to K^+K^-\pi^+$	$K^+(D^+)$	$K^-(D^+)$	not π^+
3	23	0.05	$D^+ \to K^+\pi^-\pi^+$	K_r^+	$K^-(D^+)$	$\pi^+(D^+)$
7	1	0.00	$D^+ \to K^+K^-\pi^+$	$\pi^+(D^+)$	$K^-(D^+)$	$\pi^+(D^+)$
11	1	0.00	$D^+ \to K^+K^{*0}$	K^+	$K^-(K^{*0})$	π_r^+
16	6	0.01	$D_s^+ \to K^+K^{*0}$	K^+	$K^-(K^{*0})$	π_r^+
17	2	0.00	$D_s^+ \to K^+K^-\pi^+$	K^+	K^-	π_r^+
19	2	0.00	$D_s^+ \to K^+K^-\pi^+$			
21	17	0.04	$D^0 \to K^+K^-$	K^+	K^-	N/A
22	3	0.01	$D^0 \to K^+K^-$	N/A	K^-	K^+
23	32	0.07	$D^0 \to K^-\pi^+\pi^0$	K_r^+	K^-	π^+
24	19	0.04	$D^0 \to K^-\pi^+$	K_r^+	K^-	π^+
26	30	0.07	$D^0 \to Ke(\mu)\nu$	N/A	K^-	$e^+(\mu^+)$
29	3	0.01	$D^0 \to K^{*0}\pi^+\pi^-$	K_r^+	$K^-(K^*)$	π^+
31	7	0.02	D^0 Decay			
34	11	0.02	$K^* \to K\pi$ (Charm)	N/A	$K^-(K^{*0})$	$\pi^+(K^{*0})$
37	1	0.00	$K^* \to K\pi$	$\pi^+(K^{*0})$	$K^-(K^{*0})$	N/A
41	6	0.01	$K^* \to K\pi$	N/A	$K^-(K^{*0})$	π_r^+
42	43	0.10	$\Phi \to K^+K^-$(Charm)	K^+	K^-	N/A
43	4	0.01	$\Phi \to K^+K^-$	K^+	K^-	N/A
44	4	0.01	$\Phi \to K^+K^-$	N/A	$K^-(\Phi)$	$K^+(\Phi)$
45	4	0.01	$\Phi \to K^+K^-$	K_r^+	$K^-(\Phi)$	N/A
46	3	0.01	$\Phi \to K^+K^-$	$K^+(\Phi)$	K_r^-	N/A
47	7	0.02	$K\bar{K}$ Resonance	K^+	K^-	N/A
50	43	0.10	$K^{*+} \to K^+\pi^0$			
51	2	0.00	τ Decay			
53	19	0.04	$\rho^+ \to \pi^+\pi^0$			$\pi^+(\rho^+)$
54	31	0.07	$\rho^0 \to \pi^+\pi^-$			$\pi^+(\rho^+)$
55	116	0.26	Other			

Table E.0: Breakdown of background events for bpbm MC for D^- events in the lower mass sideband region.

	N	N/Nb	Decay	K^+	K^-	π^+
	467					
1	2	0.00	$D^+ \to K^+K^-\pi^+$	$K^+(D^+)$	$K^-(D^+)$	π_r^+
2	2	0.00	$D^+ \to K^+K^-\pi^+$	$K^+(D^+)$	$K^-(D^+)$	not π^+
3	12	0.03	$D^+ \to K^+\pi^-\pi^+$	K_r^+	$K^-(D^+)$	$\pi^+(D^+)$
7	1	0.00	$D^+ \to K^+K^-\pi^+$	$\pi^+(D^+)$	$K^-(D^+)$	$\pi^+(D^+)$
15	2	0.00	$D_s^+ \to K^+K^{*0}$	K^+	K_r^-	$\pi^+(K^{*0})$
16	2	0.00	$D_s^+ \to K^+K^{*0}$	K^+	$K^-(K^{*0})$	π_r^+
17	1	0.00	$D_s^+ \to K^+K^-\pi^+$	K^+	K^-	π_r^+
18	2	0.00	$D_s^+ \to K^+K^-\pi^+$	K^+	K^-	π^+
19	2	0.00	$D_s^+ \to K^+K^-\pi^+$			
21	12	0.03	$D^0 \to K^+K^-$	K^+	K^-	N/A
22	2	0.00	$D^0 \to K^+K^-$	N/A	K^-	K^+
23	37	0.08	$D^0 \to K^-\pi^+\pi^0$	K_r^+	K^-	π^+
24	20	0.04	$D^0 \to K^-\pi^+$	K_r^+	K^-	π^+
26	34	0.07	$D^0 \to Ke(\mu)\nu$	N/A	K^-	$e^+(\mu^+)$
27	3	0.01	$D^0 \to K^-\pi^+$	π^+	K^-	N/A
29	3	0.01	$D^0 \to K^{*0}\pi^+\pi^-$	K_r^+	$K^-(K^*)$	π^+
31	4	0.01	D^0 Decay			
34	15	0.03	$K^* \to K\pi$ (Charm)	N/A	$K^-(K^{*0})$	$\pi^+(K^{*0})$
35	2	0.00	$K^* \to K\pi$	N/A	$K^-(K^{*0})$	$\pi^+(K^{*0})$
41	14	0.03	$K^* \to K\pi$	N/A	$K^-(K^{*0})$	π_r^+
42	36	0.08	$\Phi \to K^+K^-$(Charm)	K^+	K^-	N/A
43	3	0.01	$\Phi \to K^+K^-$	K^+	K^-	N/A
44	4	0.01	$\Phi \to K^+K^-$	N/A	$K^-(\Phi)$	$K^+(\Phi)$
45	2	0.00	$\Phi \to K^+K^-$	K_r^+	$K^-(\Phi)$	N/A
46	7	0.01	$\Phi \to K^+K^-$	$K^+(\Phi)$	K_r^-	N/A
47	11	0.02	$K\bar{K}$ Resonance	K^+	K^-	N/A
50	44	0.09	$K^{*+} \to K^+\pi^0$			
51	4	0.01	τ Decay			
53	29	0.06	$\rho^+ \to \pi^+\pi^0$			$\pi^+(\rho^+)$
54	40	0.09	$\rho^0 \to \pi^+\pi^-$			$\pi^+(\rho^+)$
55	115	0.25	Other			

Table E.0: Breakdown of background events for bpbm MC for D^- events in the upper mass sideband region.

	N	N/Nb	Decay	K^+	K^-	π^+
	455					
1	1	0.00	$D^+ \to K^+K^-\pi^+$	$K^+(D^+)$	$K^-(D^+)$	π_r^+
3	11	0.02	$D^+ \to K^+\pi^-\pi^+$	K_r^+	$K^-(D^+)$	$\pi^+(D^+)$
7	5	0.01	$D^+ \to K^+K^-\pi^+$	$\pi^+(D^+)$	$K^-(D^+)$	$\pi^+(D^+)$
15	1	0.00	$D_s^+ \to K^+K^{*0}$	K^+	K_r^-	$\pi^+(K^{*0})$
16	5	0.01	$D_s^+ \to K^+K^{*0}$	K^+	$K^-(K^{*0})$	π_r^+
17	1	0.00	$D_s^+ \to K^+K^-\pi^+$	K^+	K^-	π_r^+
19	1	0.00	$D_s^+ \to K^+K^-\pi^+$			
21	18	0.04	$D^0 \to K^+K^-$	K^+	K^-	N/A
22	2	0.00	$D^0 \to K^+K^-$	N/A	K^-	K^+
23	47	0.10	$D^0 \to K^-\pi^+\pi^0$	K_r^+	K^-	π^+
24	24	0.05	$D^0 \to K^-\pi^+$	K_r^+	K^-	π^+
26	38	0.08	$D^0 \to Ke(\mu)\nu$	N/A	K^-	$e^+(\mu^+)$
27	1	0.00	$D^0 \to K^-\pi^+$	π^+	K^-	N/A
29	4	0.01	$D^0 \to K^{*0}\pi^+\pi^-$	K_r^+	$K^-(K^*)$	π^+
31	7	0.02	D^0 Decay			
34	15	0.03	$K^* \to K\pi$ (Charm)	N/A	$K^-(K^{*0})$	$\pi^+(K^{*0})$
35	4	0.01	$K^* \to K\pi$	N/A	$K^-(K^{*0})$	$\pi^+(K^{*0})$
41	18	0.04	$K^* \to K\pi$	N/A	$K^-(K^{*0})$	π_r^+
42	32	0.07	$\Phi \to K^+K^-$(Charm)	K^+	K^-	N/A
43	3	0.01	$\Phi \to K^+K^-$	K^+	K^-	N/A
44	5	0.01	$\Phi \to K^+K^-$	N/A	$K^-(\Phi)$	$K^+(\Phi)$
45	2	0.00	$\Phi \to K^+K^-$	K_r^+	$K^-(\Phi)$	N/A
47	7	0.02	$K\bar{K}$ Resonance	K^+	K^-	N/A
50	27	0.06	$K^{*+} \to K^+\pi^0$			
51	2	0.00	τ Decay			
53	17	0.04	$\rho^+ \to \pi^+\pi^0$			$\pi^+(\rho^+)$
54	35	0.08	$\rho^0 \to \pi^+\pi^-$			$\pi^+(\rho^+)$
55	122	0.27	Other			

Table E.0: Breakdown of background events for bpbm MC for D^+ events in the upper mass sideband region.

Appendix F

$B^0\bar{B}^0$ Monte Carlo Backgrounds

	N	N/Nb	Decay	K^+	K^-	π^+
	468					
1	12	0.03	$D^+ \to K^+K^-\pi^+$	$K^+(D^+)$	$K^-(D^+)$	π_r^+
2	7	0.01	$D^+ \to K^+K^-\pi^+$	$K^+(D^+)$	$K^-(D^+)$	not π^+
3	133	0.28	$D^+ \to K^+\pi^-\pi^+$	K_r^+	$K^-(D^+)$	$\pi^+(D^+)$
7	36	0.08	$D^+ \to K^+K^-\pi^+$	$\pi^+(D^+)$	$K^-(D^+)$	$\pi^+(D^+)$
11	12	0.03	$D^+ \to K^+K^{*0}$	K^+	$K^-(K^{*0})$	π_r^+
16	6	0.01	$D_s^+ \to K^+K^{*0}$	K^+	$K^-(K^{*0})$	π_r^+
19	1	0.00	$D_s^+ \to K^+K^-\pi^+$			
21	3	0.01	$D^0 \to K^+K^-$	K^+	K^-	N/A
22	2	0.00	$D^0 \to K^+K^-$	N/A	K^-	K^+
23	8	0.02	$D^0 \to K^-\pi^+\pi^0$	K_r^+	K^-	π^+
24	3	0.01	$D^0 \to K^-\pi^+$	K_r^+	K^-	π^+
26	4	0.01	$D^0 \to Ke(\mu)\nu$	N/A	K^-	$e^+(\mu^+)$
29	2	0.00	$D^0 \to K^{*0}\pi^+\pi^-$	K_r^+	$K^-(K^*)$	π^+
31	1	0.00	D^0 Decay			
34	15	0.03	$K^* \to K\pi$ (Charm)	N/A	$K^-(K^{*0})$	$\pi^+(K^{*0})$
35	5	0.01	$K^* \to K\pi$	N/A	$K^-(K^{*0})$	$\pi^+(K^{*0})$
37	1	0.00	$K^* \to K\pi$	$\pi^+(K^{*0})$	$K^-(K^{*0})$	N/A
41	9	0.02	$K^* \to K\pi$	N/A	$K^-(K^{*0})$	π_r^+
42	56	0.12	$\Phi \to K^+K^-$(Charm)	K^+	K^-	N/A
43	3	0.01	$\Phi \to K^+K^-$	K^+	K^-	N/A
44	2	0.00	$\Phi \to K^+K^-$	N/A	$K^-(\Phi)$	$K^+(\Phi)$
45	2	0.00	$\Phi \to K^+K^-$	K_r^+	$K^-(\Phi)$	N/A
46	4	0.01	$\Phi \to K^+K^-$	$K^+(\Phi)$	K_r^-	N/A
47	9	0.02	$K\bar{K}$ Resonance	K^+	K^-	N/A
50	30	0.06	$K^{*+} \to K^+\pi^0$			
51	3	0.01	τ Decay			
53	9	0.02	$\rho^+ \to \pi^+\pi^0$			$\pi^+(\rho^+)$
54	4	0.01	$\rho^0 \to \pi^+\pi^-$			$\pi^+(\rho^+)$
55	86	0.18	Other			

Table F.0: Breakdown of background events for b0b0bar MC events for D^+ events in the lower mass sideband region.

	N	N/Nb	Decay	K^+	K^-	π^+
	511					
1	10	0.02	$D^+ \to K^+K^-\pi^+$	$K^+(D^+)$	$K^-(D^+)$	π_r^+
2	3	0.01	$D^+ \to K^+K^-\pi^+$	$K^+(D^+)$	$K^-(D^+)$	not π^+
3	130	0.25	$D^+ \to K^+\pi^-\pi^+$	K_r^+	$K^-(D^+)$	$\pi^+(D^+)$
7	40	0.08	$D^+ \to K^+K^-\pi^+$	$\pi^+(D^+)$	$K^-(D^+)$	$\pi^+(D^+)$
11	14	0.03	$D^+ \to K^+K^{*0}$	K^+	$K^-(K^{*0})$	π_r^+
16	7	0.01	$D_s^+ \to K^+K^{*0}$	K^+	$K^-(K^{*0})$	π_r^+
17	3	0.01	$D_s^+ \to K^+K^-\pi^+$	K^+	K^-	π_r^+
19	1	0.00	$D_s^+ \to K^+K^-\pi^+$			
21	8	0.02	$D^0 \to K^+K^-$	K^+	K^-	N/A
22	1	0.00	$D^0 \to K^+K^-$	N/A	K^-	K^+
23	2	0.00	$D^0 \to K^-\pi^+\pi^0$	K_r^+	K^-	π^+
24	1	0.00	$D^0 \to K^-\pi^+$	K_r^+	K^-	π^+
26	8	0.02	$D^0 \to Ke(\mu)\nu$	N/A	K^-	$e^+(\mu^+)$
27	1	0.00	$D^0 \to K^-\pi^+$	π^+	K^-	N/A
31	1	0.00	D^0 Decay			
34	14	0.03	$K^* \to K\pi$ (Charm)	N/A	$K^-(K^{*0})$	$\pi^+(K^{*0})$
35	10	0.02	$K^* \to K\pi$	N/A	$K^-(K^{*0})$	$\pi^+(K^{*0})$
41	16	0.03	$K^* \to K\pi$	N/A	$K^-(K^{*0})$	π_r^+
42	72	0.14	$\Phi \to K^+K^-$(Charm)	K^+	K^-	N/A
43	1	0.00	$\Phi \to K^+K^-$	K^+	K^-	N/A
44	2	0.00	$\Phi \to K^+K^-$	N/A	$K^-(\Phi)$	$K^+(\Phi)$
45	6	0.01	$\Phi \to K^+K^-$	K_r^+	$K^-(\Phi)$	N/A
46	3	0.01	$\Phi \to K^+K^-$	$K^+(\Phi)$	K_r^-	N/A
47	13	0.03	$K\bar{K}$ Resonance	K^+	K^-	N/A
50	40	0.08	$K^{*+} \to K^+\pi^0$			
53	12	0.02	$\rho^+ \to \pi^+\pi^0$			$\pi^+(\rho^+)$
54	7	0.01	$\rho^0 \to \pi^+\pi^-$			$\pi^+(\rho^+)$
55	85	0.17	Other			

Table F.0: Breakdown of background events for b0b0bar MC for D^- in the lower mass sideband region

	N	N/Nb	Decay	K^+	K^-	π^+
	452					
1	15	0.03	$D^+ \to K^+K^-\pi^+$	$K^+(D^+)$	$K^-(D^+)$	π_r^+
2	13	0.03	$D^+ \to K^+K^-\pi^+$	$K^+(D^+)$	$K^-(D^+)$	not π^+
3	129	0.29	$D^+ \to K^+\pi^-\pi^+$	K_r^+	$K^-(D^+)$	$\pi^+(D^+)$
7	40	0.09	$D^+ \to K^+K^-\pi^+$	$\pi^+(D^+)$	$K^-(D^+)$	$\pi^+(D^+)$
11	12	0.03	$D^+ \to K^+K^{*0}$	K^+	$K^-(K^{*0})$	π_r^+
16	5	0.01	$D_s^+ \to K^+K^{*0}$	K^+	$K^-(K^{*0})$	π_r^+
17	2	0.00	$D_s^+ \to K^+K^-\pi^+$	K^+	K^-	π_r^+
18	2	0.00	$D_s^+ \to K^+K^-\pi^+$	K^+	K^-	π^+
21	4	0.01	$D^0 \to K^+K^-$	K^+	K^-	N/A
23	6	0.01	$D^0 \to K^-\pi^+\pi^0$	K_r^+	K^-	π^+
24	4	0.01	$D^0 \to K^-\pi^+$	K_r^+	K^-	π^+
26	1	0.00	$D^0 \to Ke(\mu)\nu$	N/A	K^-	$e^+(\mu^+)$
27	1	0.00	$D^0 \to K^-\pi^+$	π^+	K^-	N/A
34	13	0.03	$K^* \to K\pi$ (Charm)	N/A	$K^-(K^{*0})$	$\pi^+(K^{*0})$
35	6	0.01	$K^* \to K\pi$	N/A	$K^-(K^{*0})$	$\pi^+(K^{*0})$
36	1	0.00	$K^*Ln \to K^-\pi$	N/A	$K^-(K^{*0})$	$\pi^+(K^{*0})$
41	6	0.01	$K^* \to K\pi$	N/A	$K^-(K^{*0})$	π_r^+
42	50	0.11	$\Phi \to K^+K^-$(Charm)	K^+	K^-	N/A
44	2	0.00	$\Phi \to K^+K^-$	N/A	$K^-(\Phi)$	$K^+(\Phi)$
45	6	0.01	$\Phi \to K^+K^-$	K_r^+	$K^-(\Phi)$	N/A
46	3	0.01	$\Phi \to K^+K^-$	$K^+(\Phi)$	K_r^-	N/A
47	10	0.02	$K\bar{K}$ Resonance	K^+	K^-	N/A
50	25	0.06	$K^{*+} \to K^+\pi^0$			
53	8	0.02	$\rho^+ \to \pi^+\pi^0$			$\pi^+(\rho^+)$
54	4	0.01	$\rho^0 \to \pi^+\pi^-$			$\pi^+(\rho^+)$
55	84	0.19	Other			

Table F.0: Breakdown of background events for b0b0bar MC for $D-$ events in the upper mass sideband region.

	N	N/Nb	Decay	K^+	K^-	π^+
	428					
1	13	0.03	$D^+ \to K^+K^-\pi^+$	$K^+(D^+)$	$K^-(D^+)$	π_r^+
2	7	0.02	$D^+ \to K^+K^-\pi^+$	$K^+(D^+)$	$K^-(D^+)$	not π^+
3	109	0.25	$D^+ \to K^+\pi^-\pi^+$	K_r^+	$K^-(D^+)$	$\pi^+(D^+)$
7	32	0.07	$D^+ \to K^+K^-\pi^+$	$\pi^+(D^+)$	$K^-(D^+)$	$\pi^+(D^+)$
11	11	0.03	$D^+ \to K^+K^{*0}$	K^+	$K^-(K^{*0})$	π_r^+
16	7	0.02	$D_s^+ \to K^+K^{*0}$	K^+	$K^-(K^{*0})$	π_r^+
17	1	0.00	$D_s^+ \to K^+K^-\pi^+$	K^+	K^-	π_r^+
19	1	0.00	$D_s^+ \to K^+K^-\pi^+$			
21	6	0.01	$D^0 \to K^+K^-$	K^+	K^-	N/A
23	10	0.02	$D^0 \to K^-\pi^+\pi^0$	K_r^+	K^-	π^+
24	4	0.01	$D^0 \to K^-\pi^+$	K_r^+	K^-	π^+
26	9	0.02	$D^0 \to Ke(\mu)\nu$	N/A	K^-	$e^+(\mu^+)$
34	15	0.04	$K^* \to K\pi$ (Charm)	N/A	$K^-(K^{*0})$	$\pi^+(K^{*0})$
35	8	0.02	$K^* \to K\pi$	N/A	$K^-(K^{*0})$	$\pi^+(K^{*0})$
41	10	0.02	$K^* \to K\pi$	N/A	$K^-(K^{*0})$	π_r^+
42	38	0.09	$\Phi \to K^+K^-$(Charm)	K^+	K^-	N/A
43	2	0.00	$\Phi \to K^+K^-$	K^+	K^-	N/A
44	2	0.00	$\Phi \to K^+K^-$	N/A	$K^-(\Phi)$	$K^+(\Phi)$
45	2	0.00	$\Phi \to K^+K^-$	K_r^+	$K^-(\Phi)$	N/A
46	1	0.00	$\Phi \to K^+K^-$	$K^+(\Phi)$	K_r^-	N/A
47	10	0.02	$K\bar{K}$ Resonance	K^+	K^-	N/A
50	21	0.05	$K^{*+} \to K^+\pi^0$			
52	1	0.00	$\rho^0 \to \pi^+\pi^-$			
53	11	0.03	$\rho^+ \to \pi^+\pi^0$			$\pi^+(\rho^+)$
54	10	0.02	$\rho^0 \to \pi^+\pi^-$			$\pi^+(\rho^+)$
55	87	0.20	Other			

Table F.0: Breakdown of background events for b0b0bar MC for D^+ events in the upper mass sideband region.

Appendix G

Background slices of $m^2(K^+K^-)$ and $m^2(K^-\pi^+)$

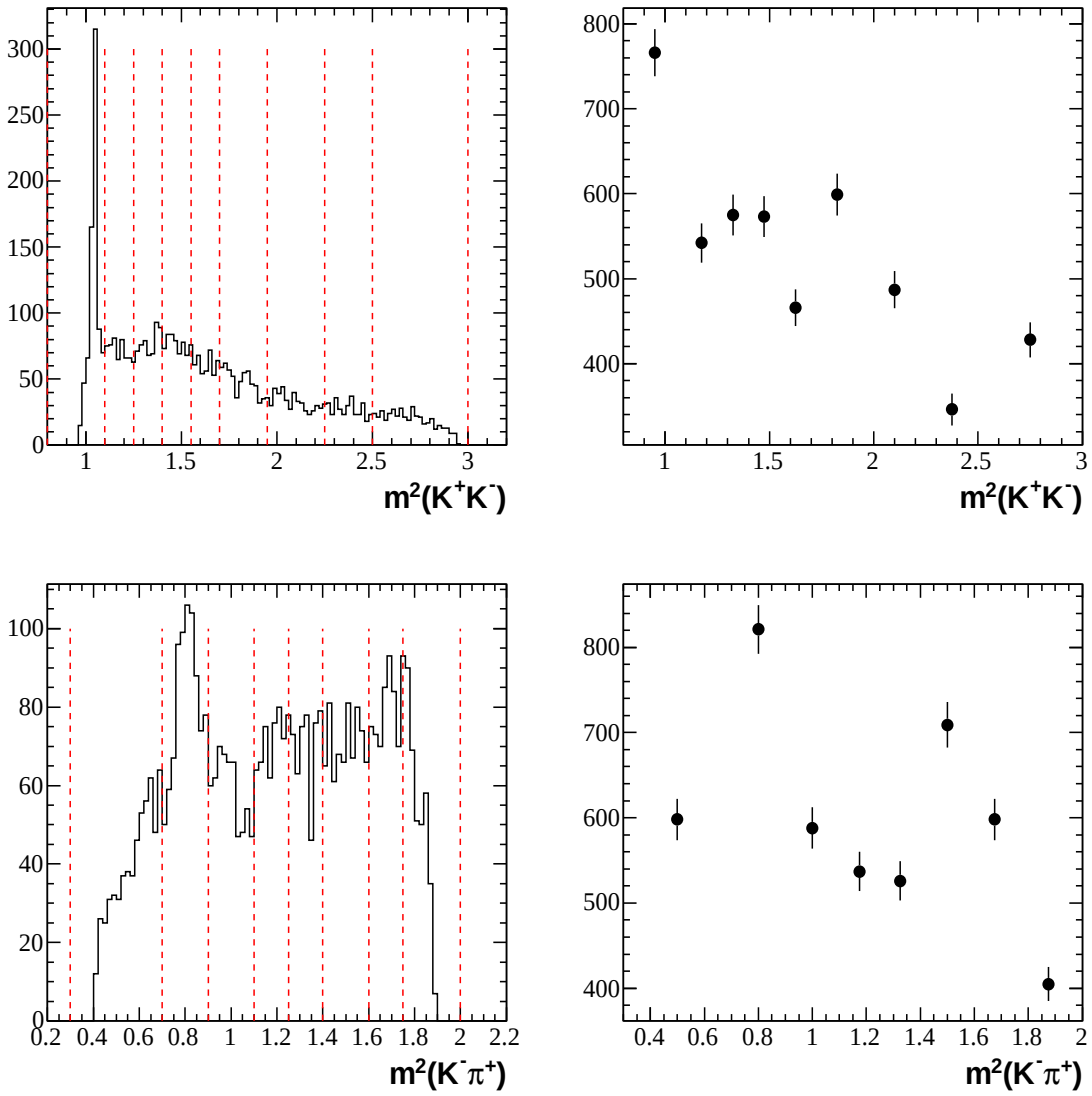

Figure G.1: D^+ low mass sideband region binning scheme for slices of Dalitz plot variables.

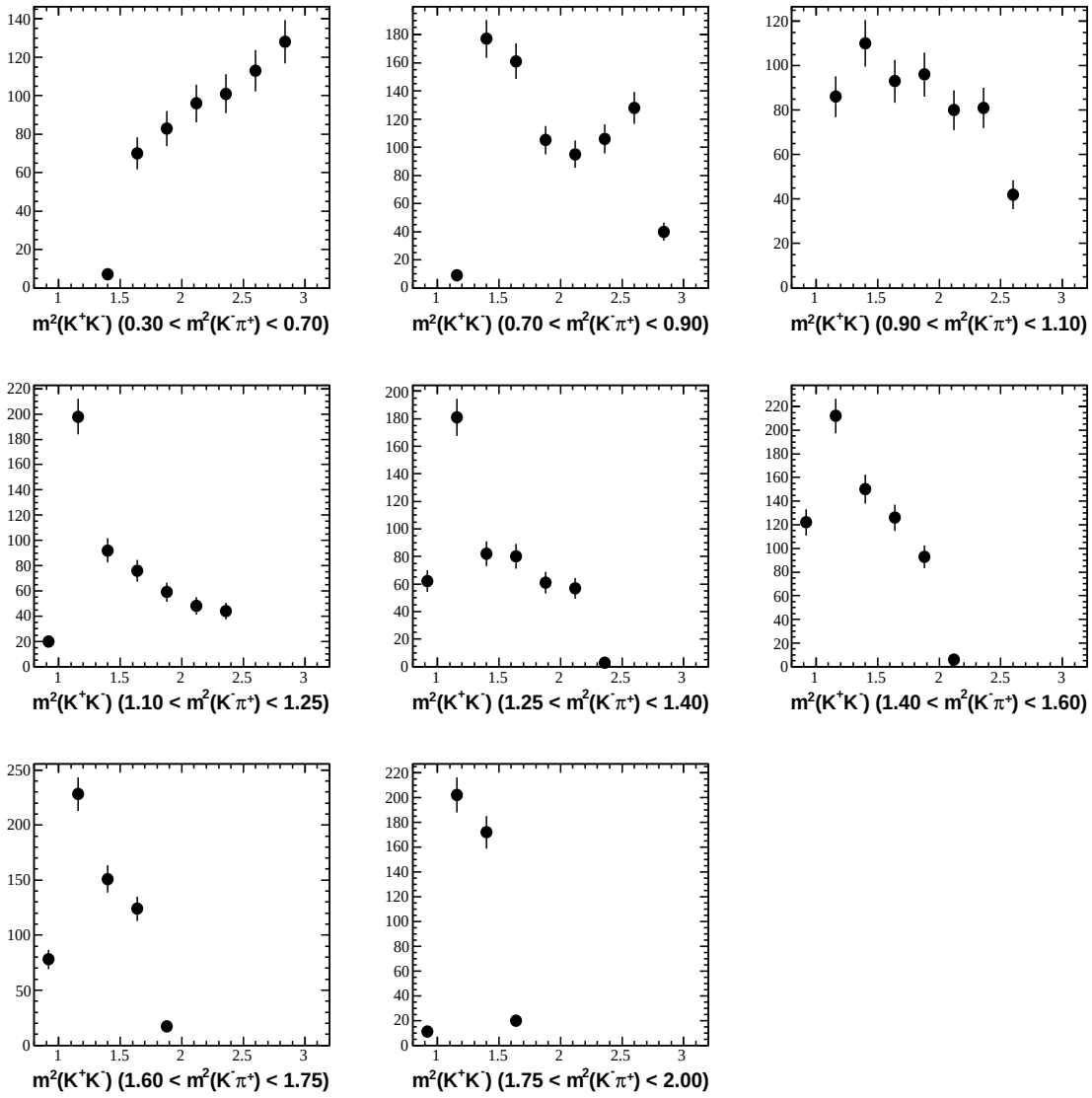

Figure G.2: D^+ low mass sideband region plots for $m^2(K^+K^-)$ in slices of $m^2(K^-\pi^+)$

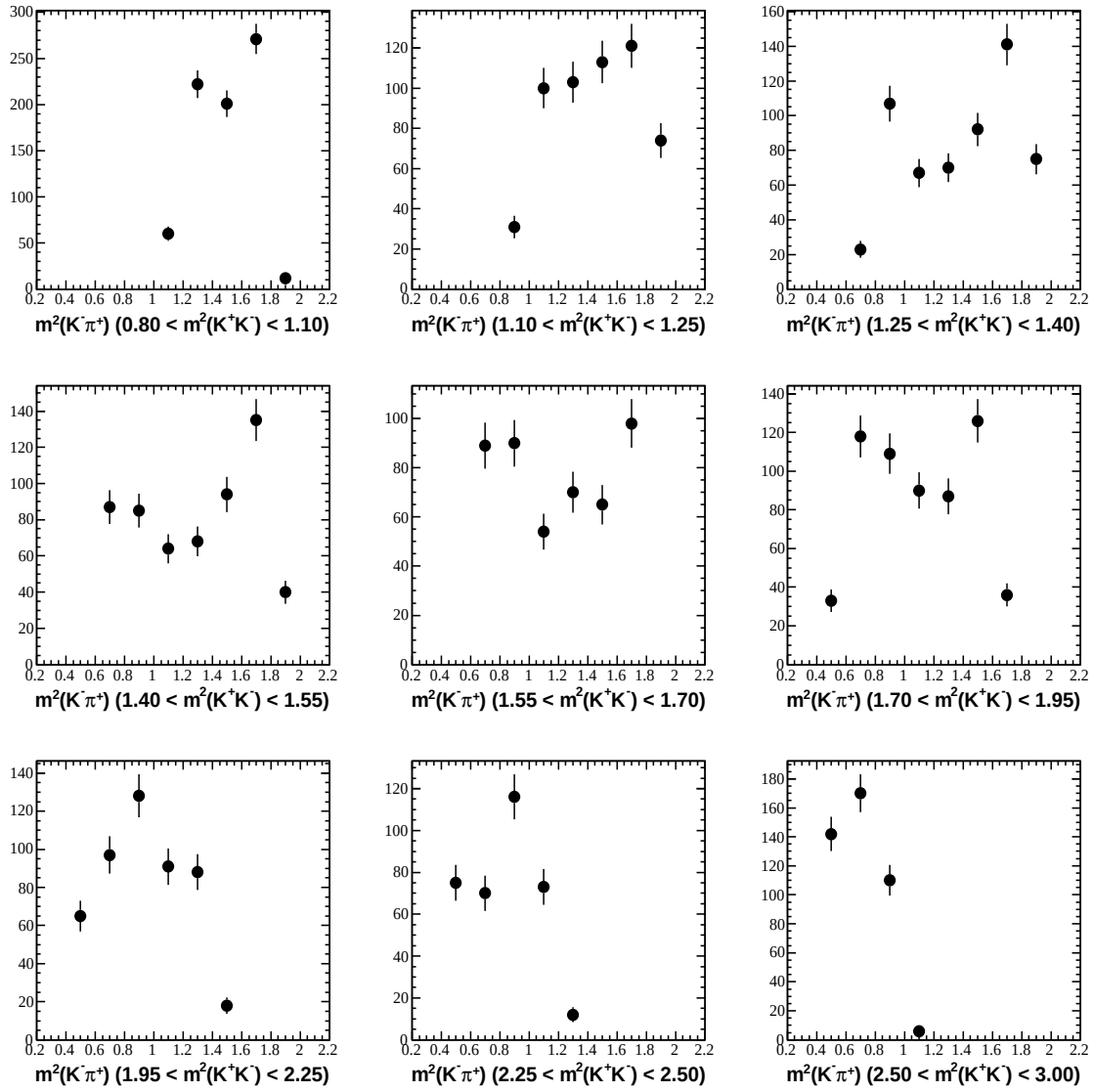

Figure G.3: D^+ low mass sideband region plots for $m^2(K^-\pi^+)$ in slices of $m^2(K^+K^-)$

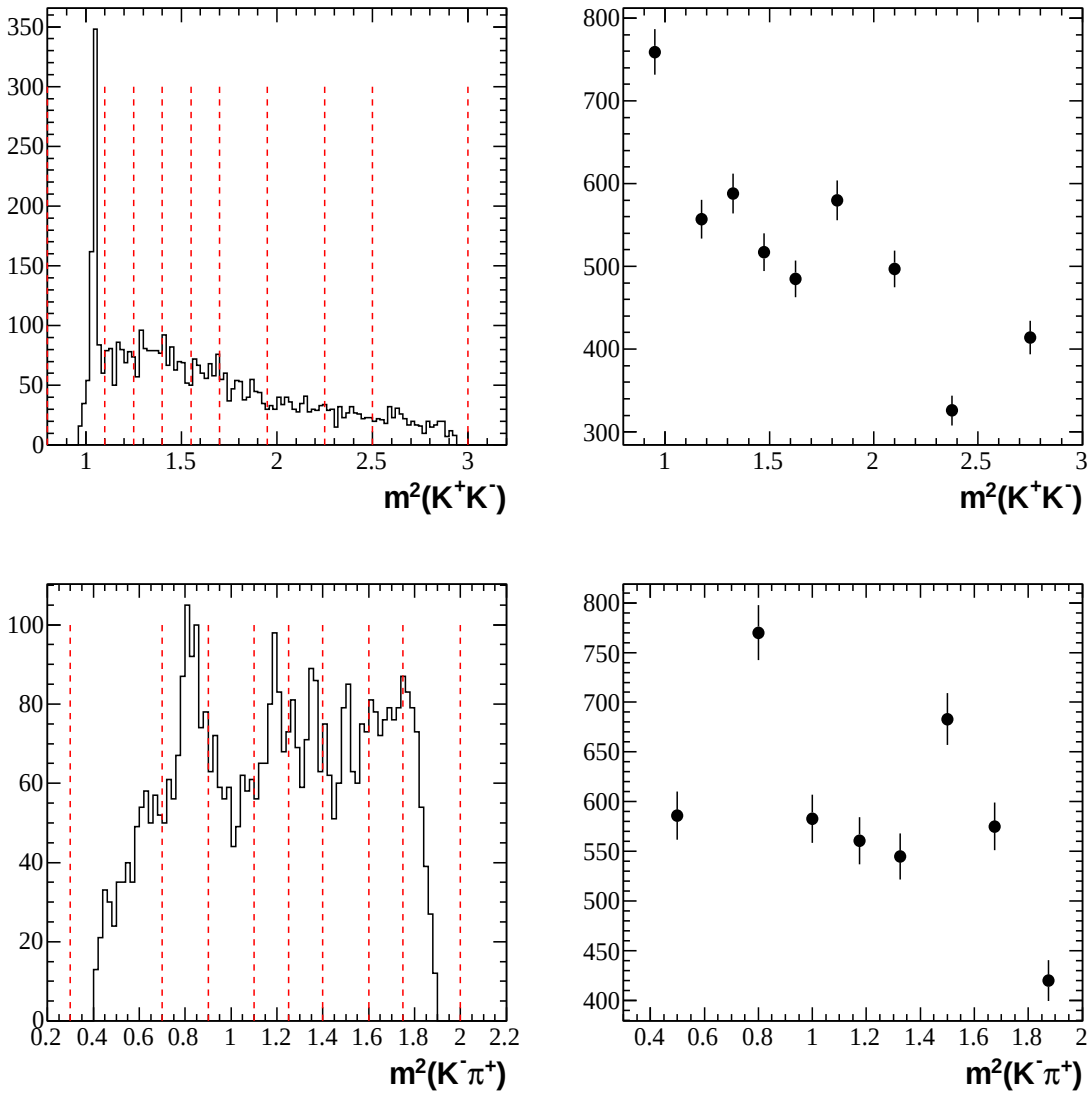

Figure G.4: D^- low mass sideband region binning scheme for slices of Dalitz plot variables.

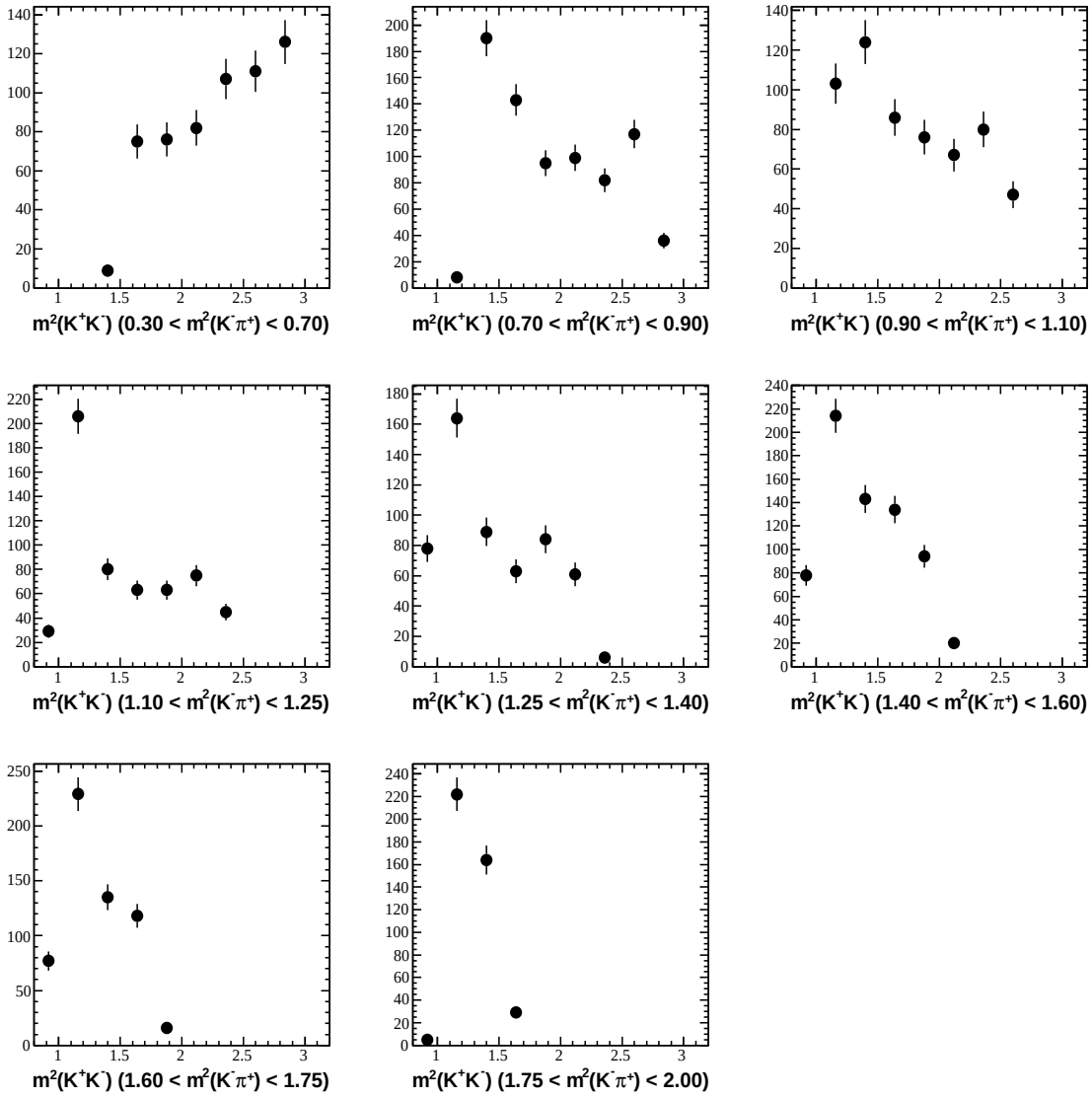

Figure G.5: D^- low mass sideband region plots for $m^2(K^+K^-)$ in slices of $m^2(K^-\pi^+)$

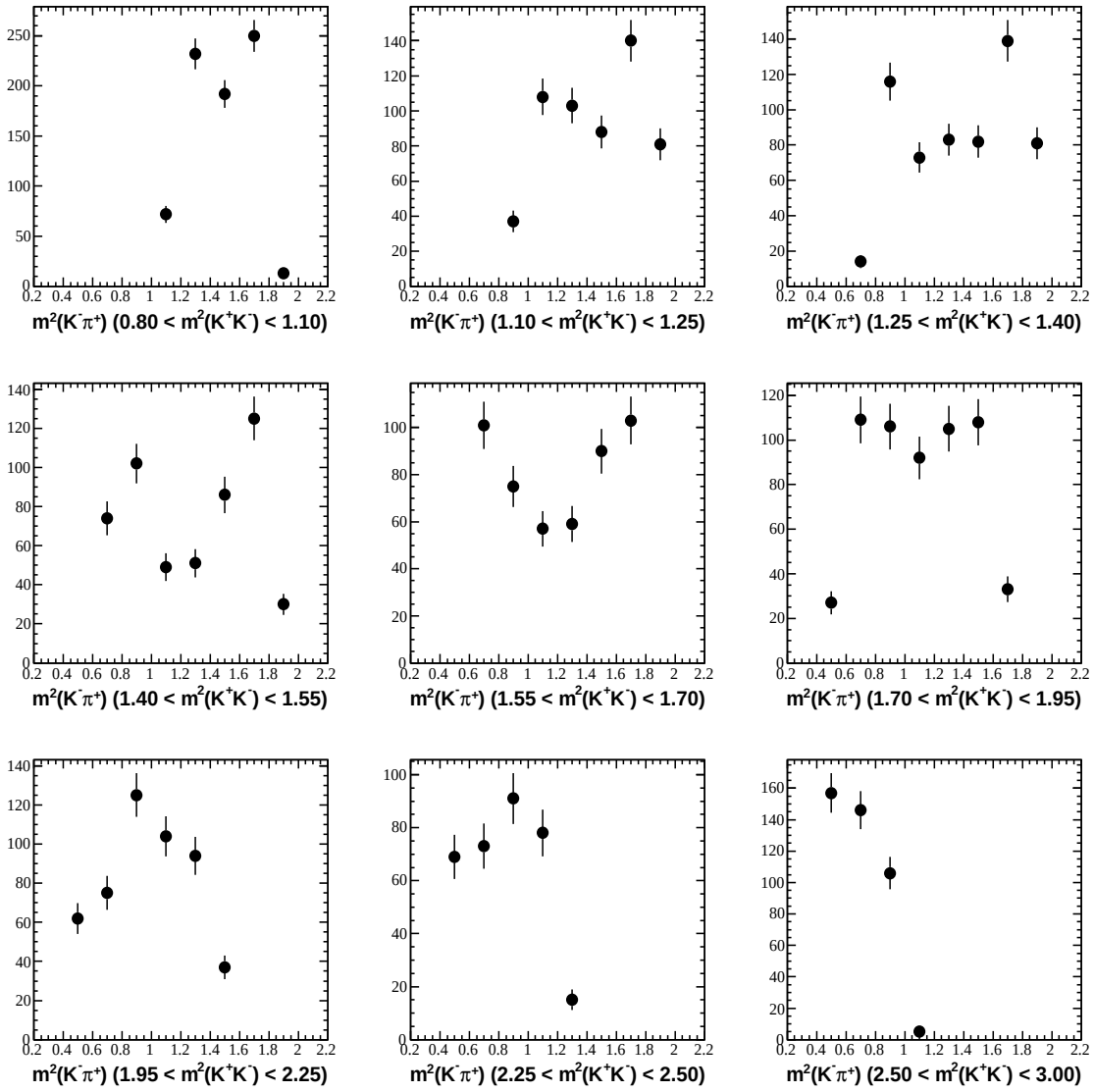

Figure G.6: D^- low mass sideband region plots for $m^2(K^-\pi^+)$ in slices of $m^2(K^+K^-)$

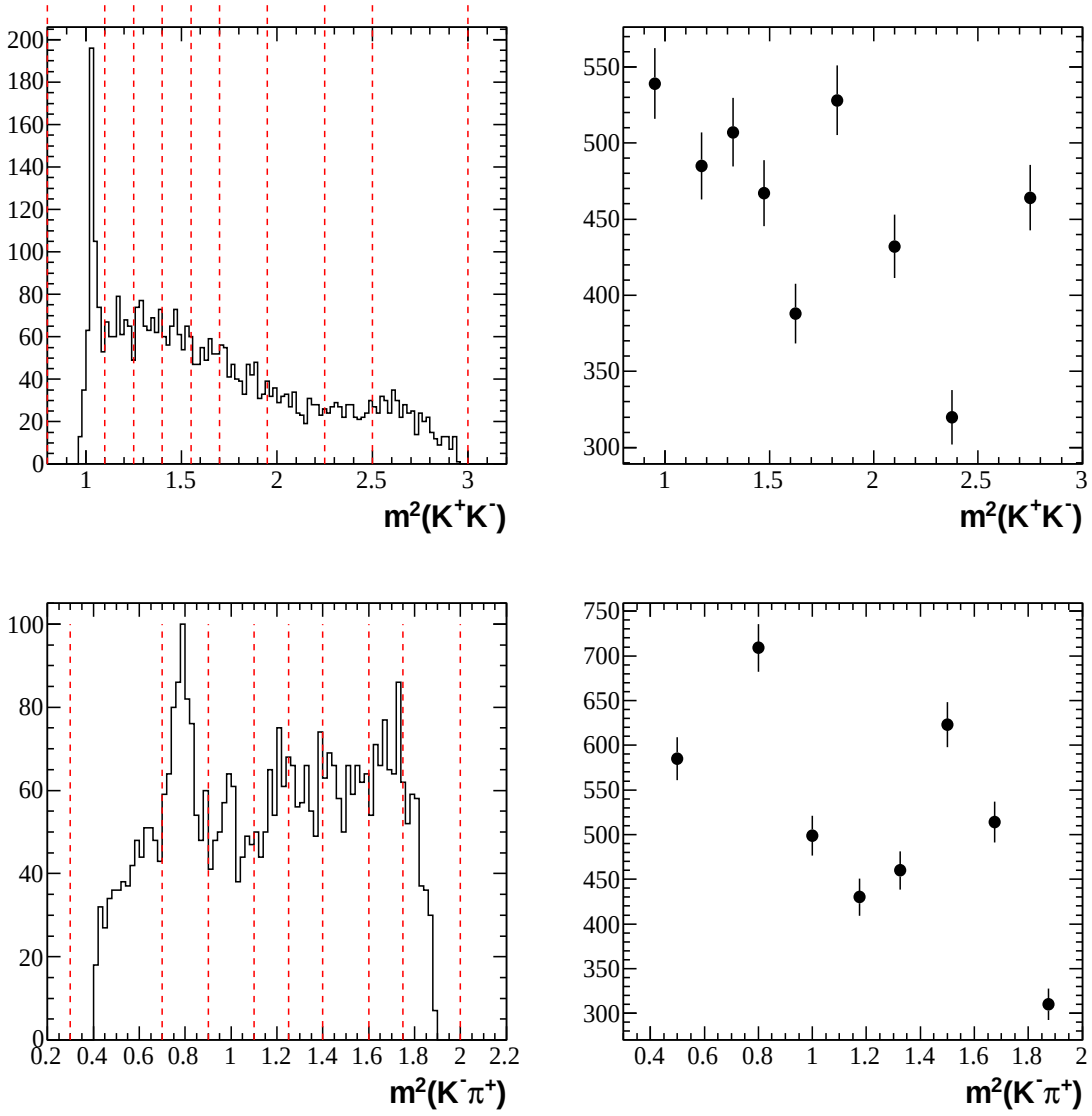

Figure G.7: D^+ high mass sideband region binning scheme for slices of Dalitz plot variables.

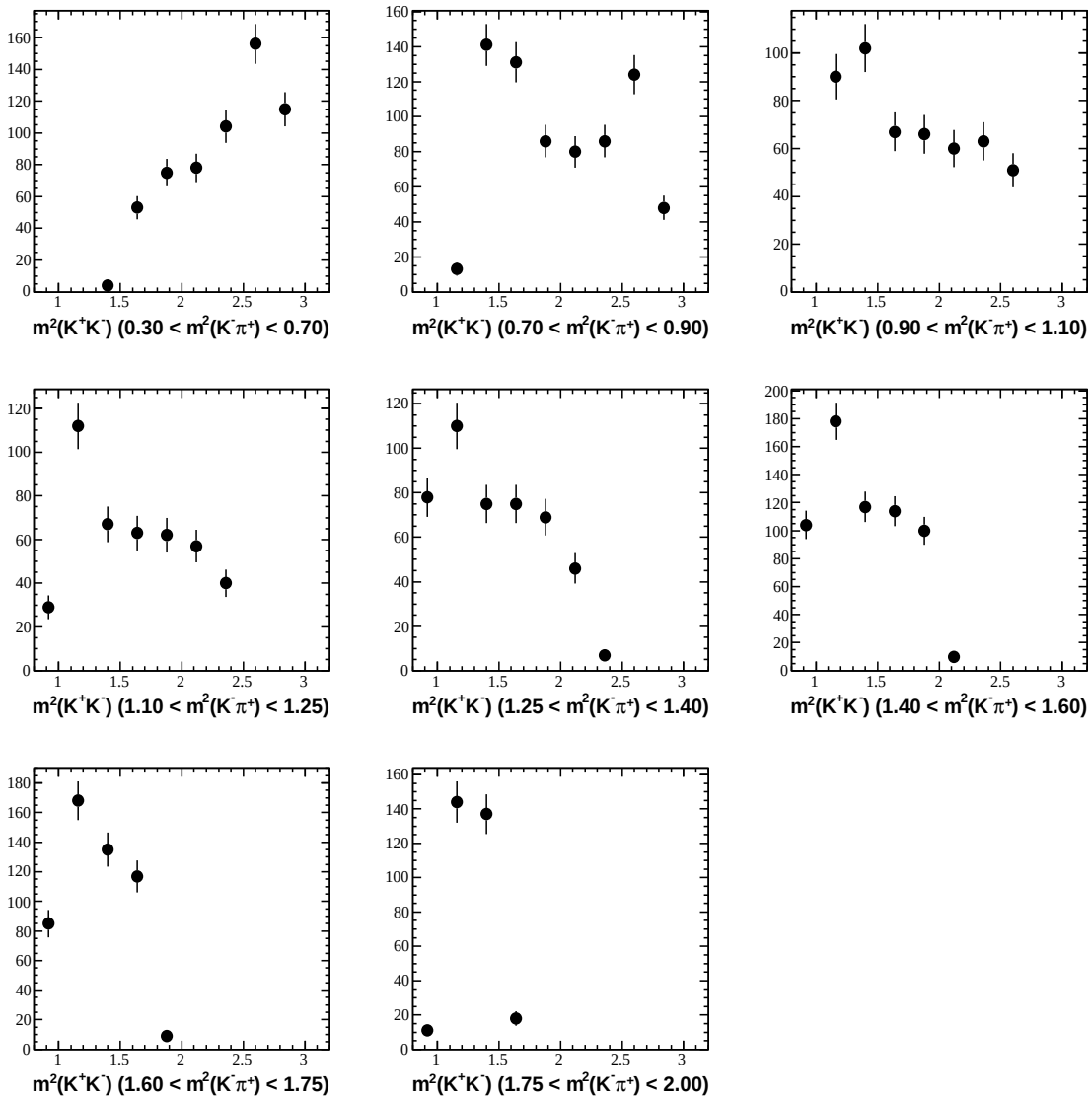

Figure G.8: D^+ high mass sideband region plots for $m^2(K^+K^-)$ in slices of $m^2(K^-\pi^+)$

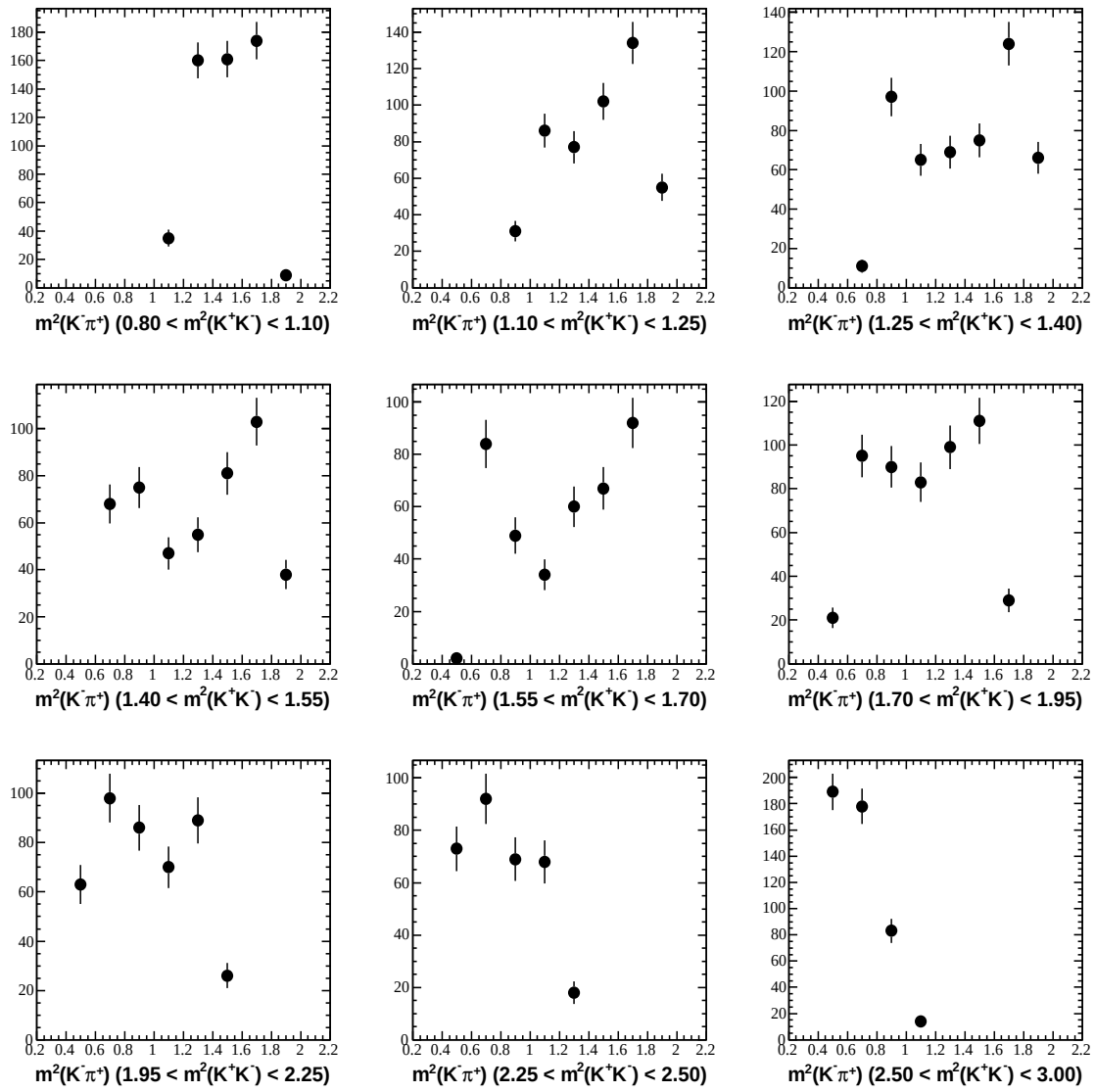

Figure G.9: D^+ high mass sideband region plots for $m^2(K^-\pi^+)$ in slices of $m^2(K^+K^-)$

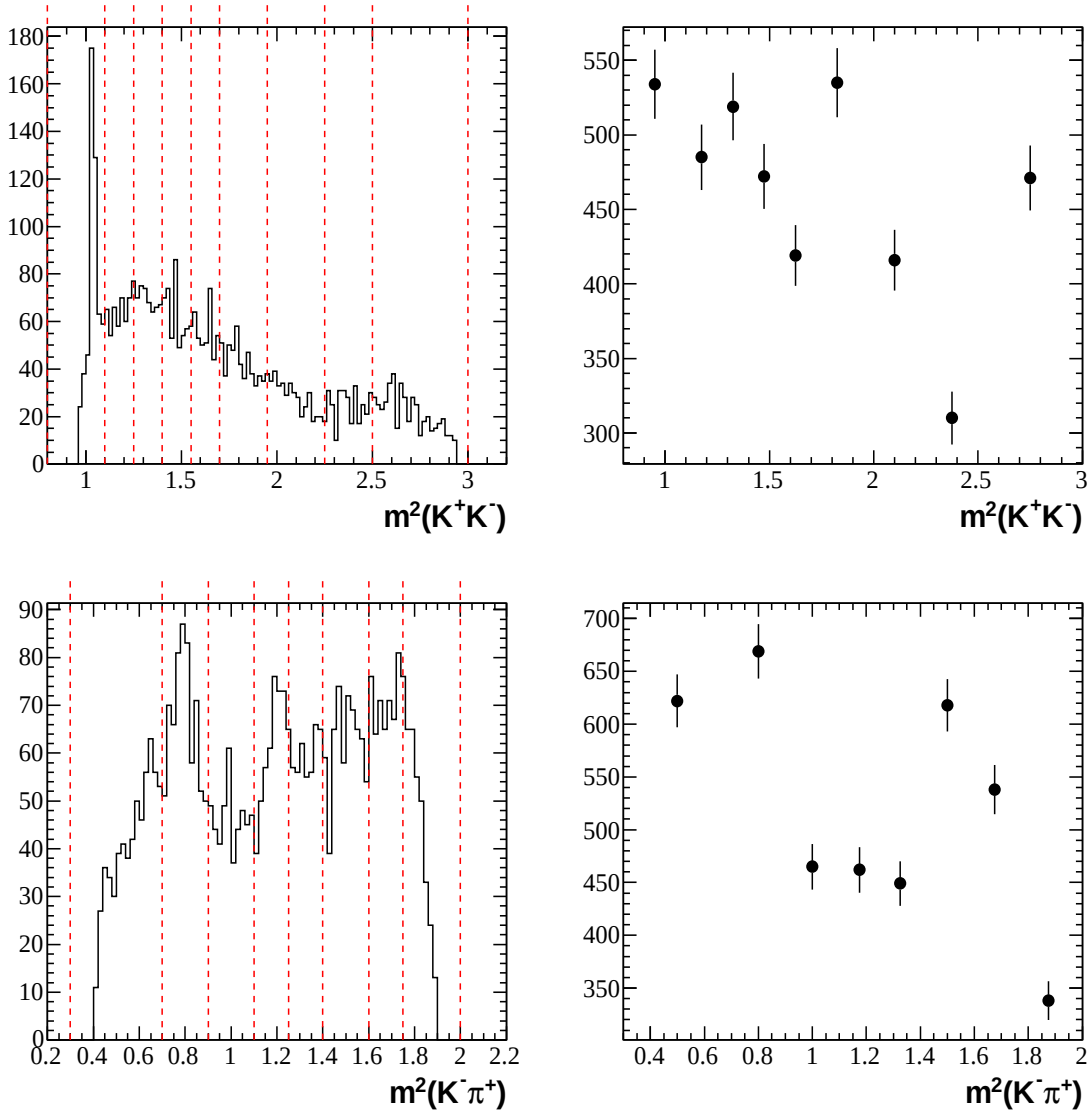

Figure G.10: D^- high mass sideband region binning scheme for slices of Dalitz plot variables.

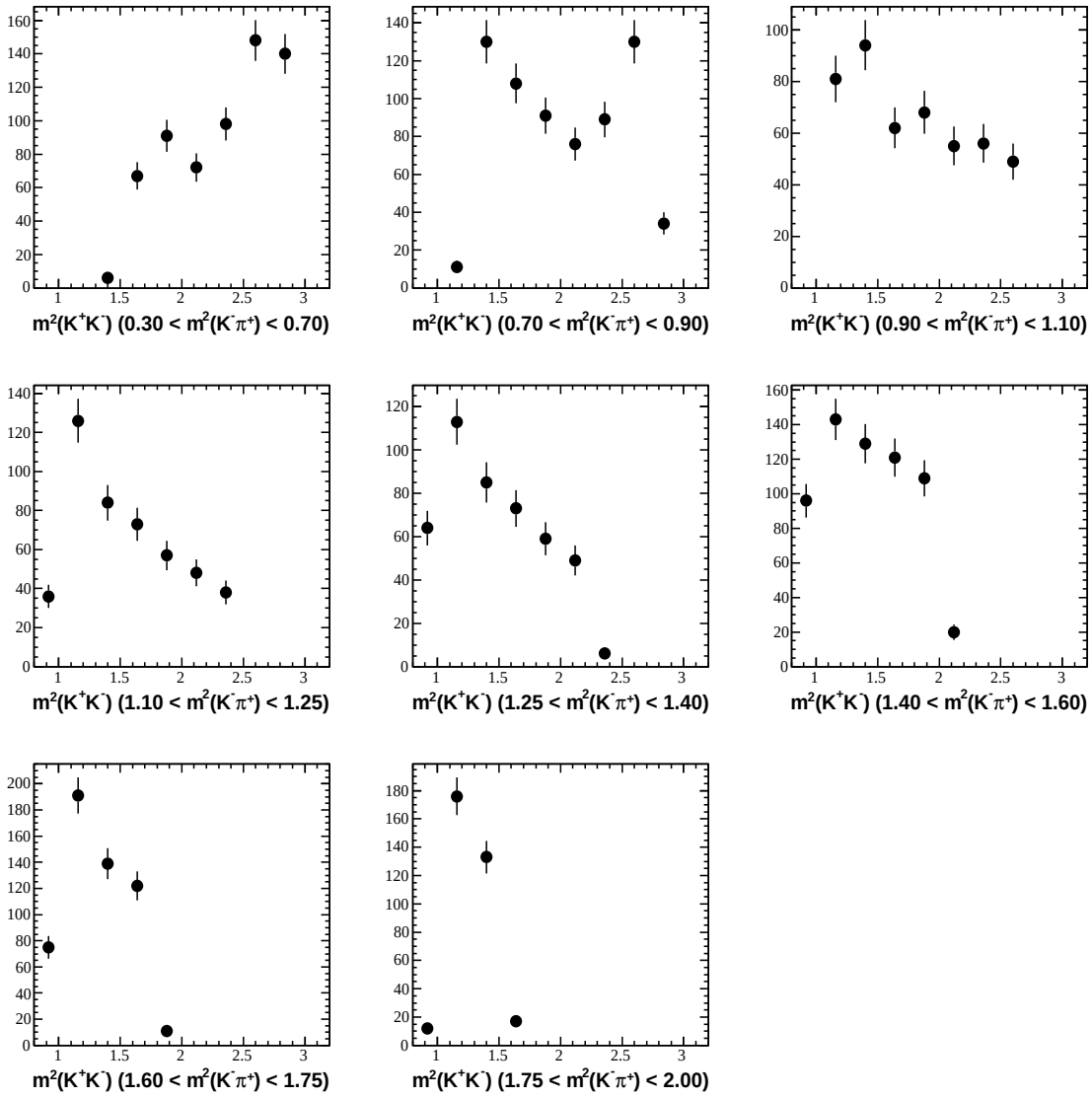

Figure G.11: D^- high mass sideband region plots for $m^2(K^+K^-)$ in slices of $m^2(K^-\pi^+)$

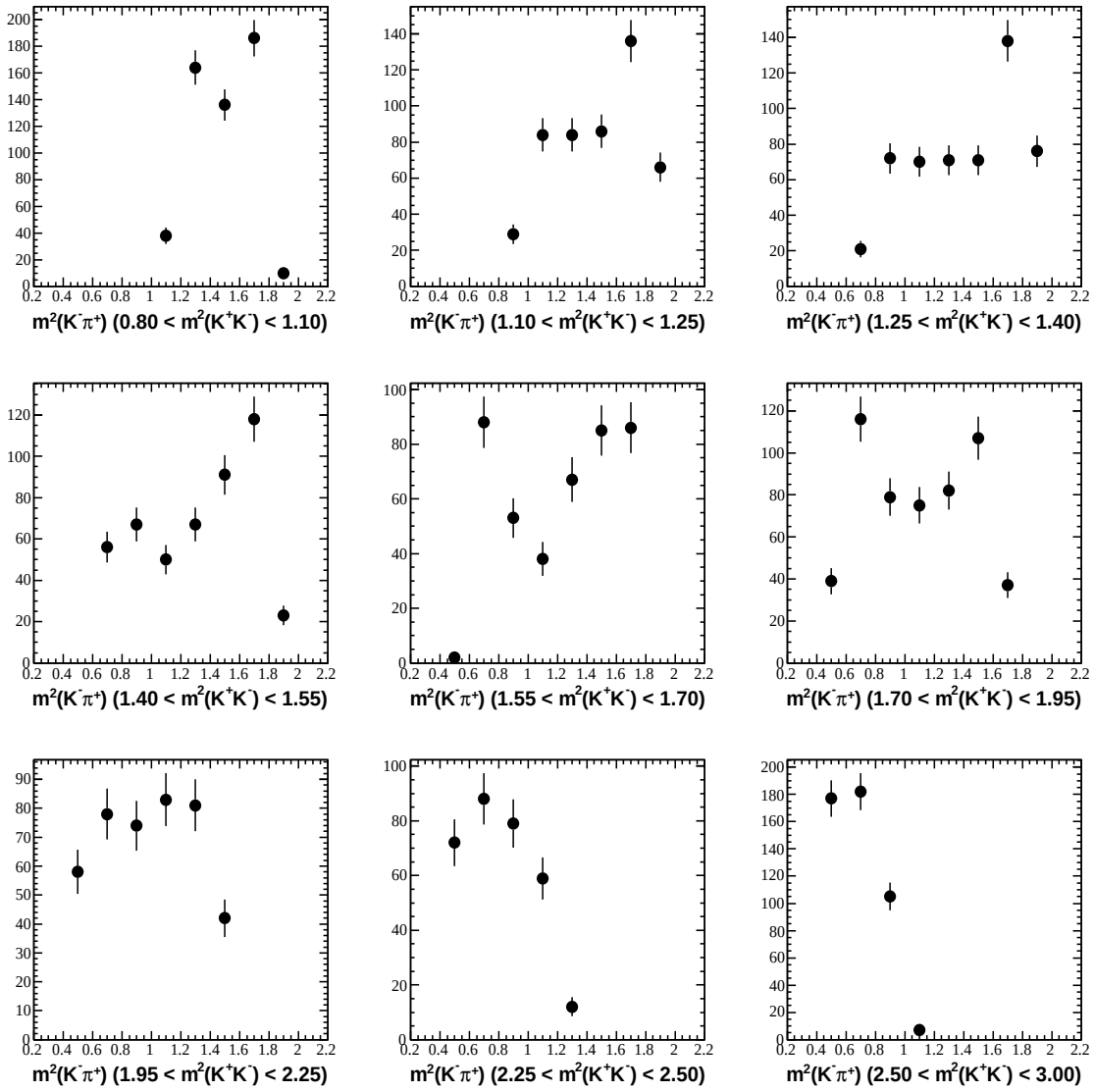

Figure G.12: D^- high mass sideband region plots for $m^2(K^-\pi^+)$ in slices of $m^2(K^+K^-)$

Appendix H

Background slices of Square Dalitz plot Variables

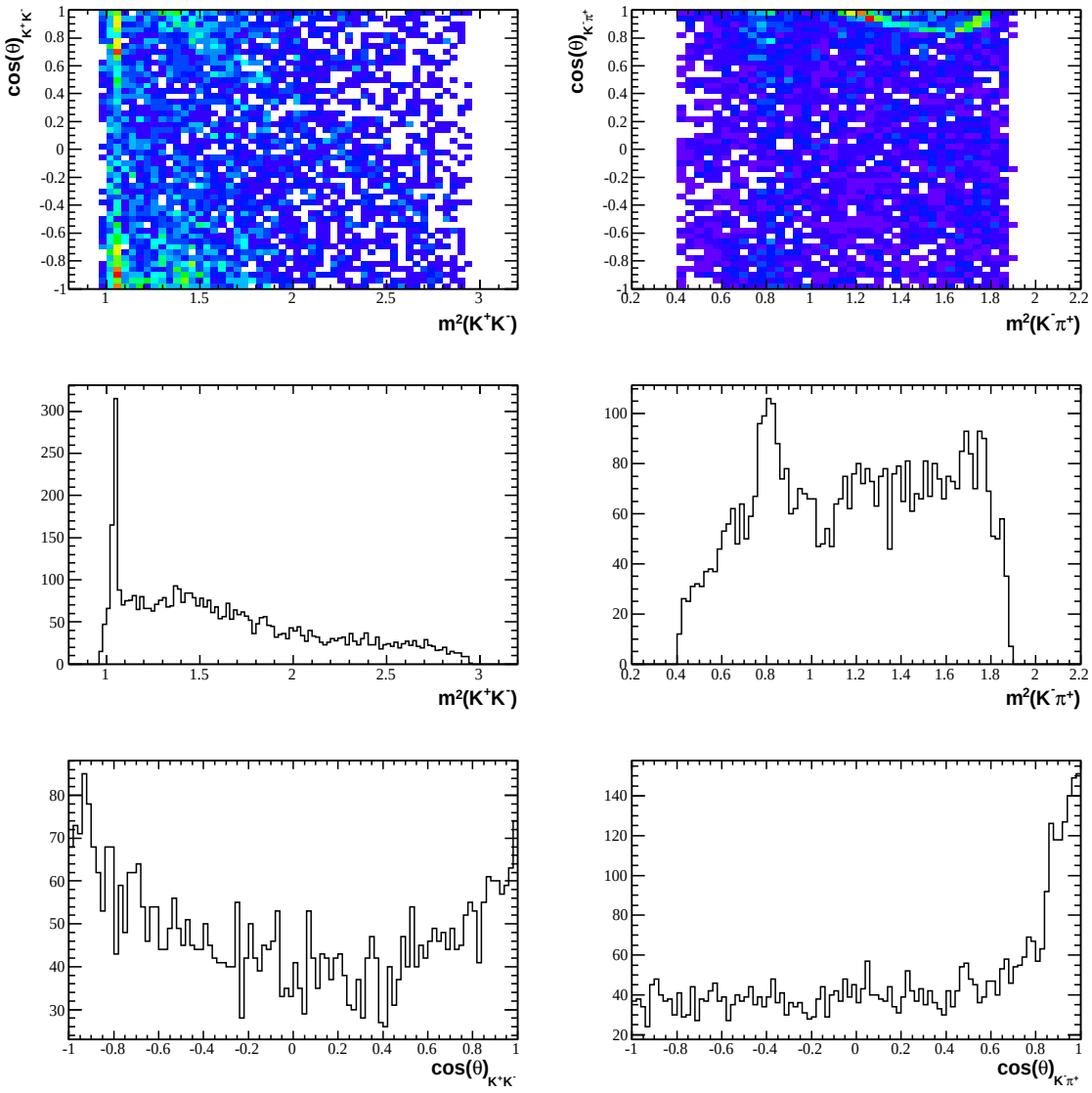

Figure H.1: D^+ low mass sideband region Square Dalitz plot and projections

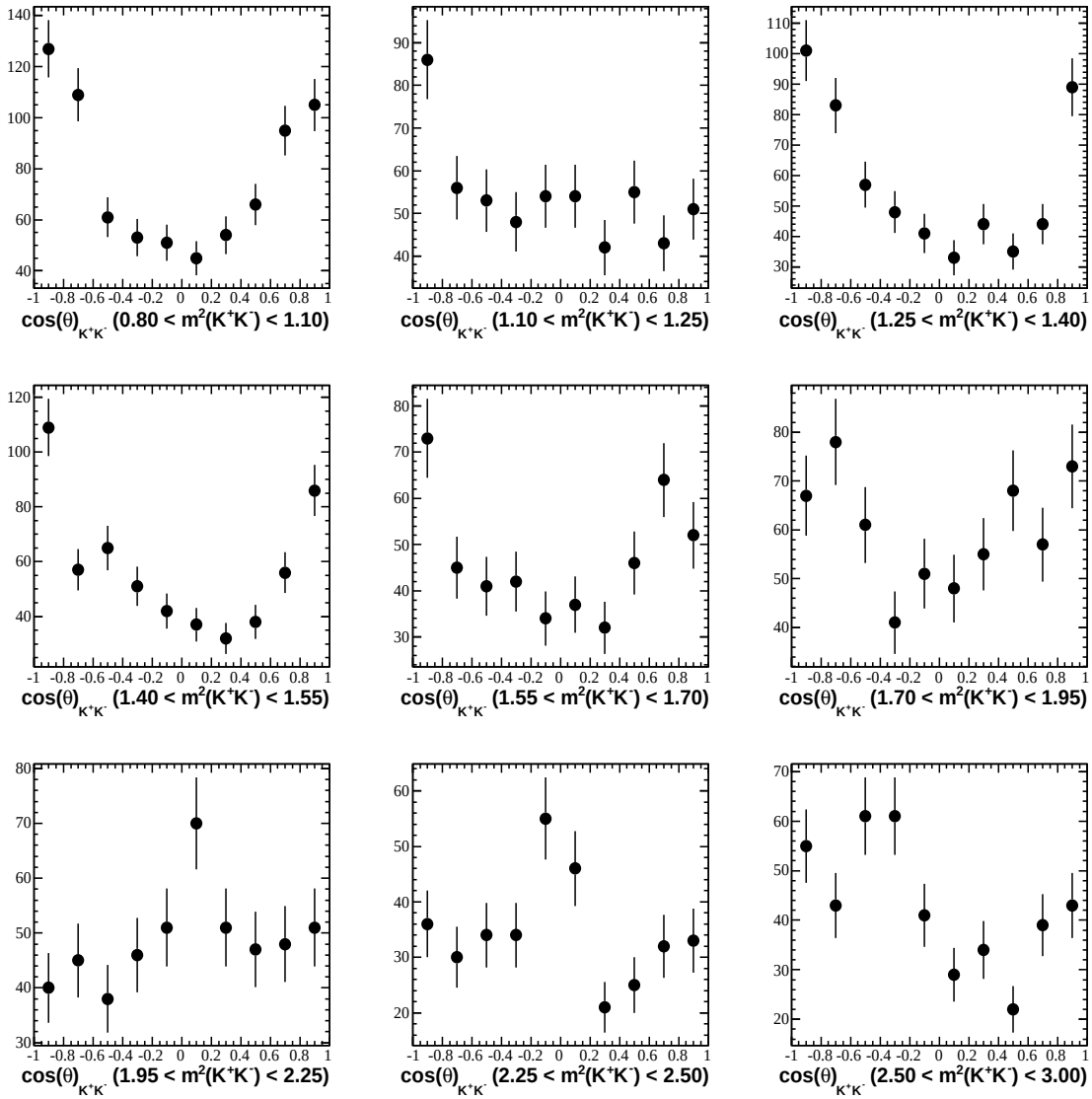

Figure H.2: D^+ low mass sideband region K^+K^- helicity angle in slices of $m^2(K^+K^-)$

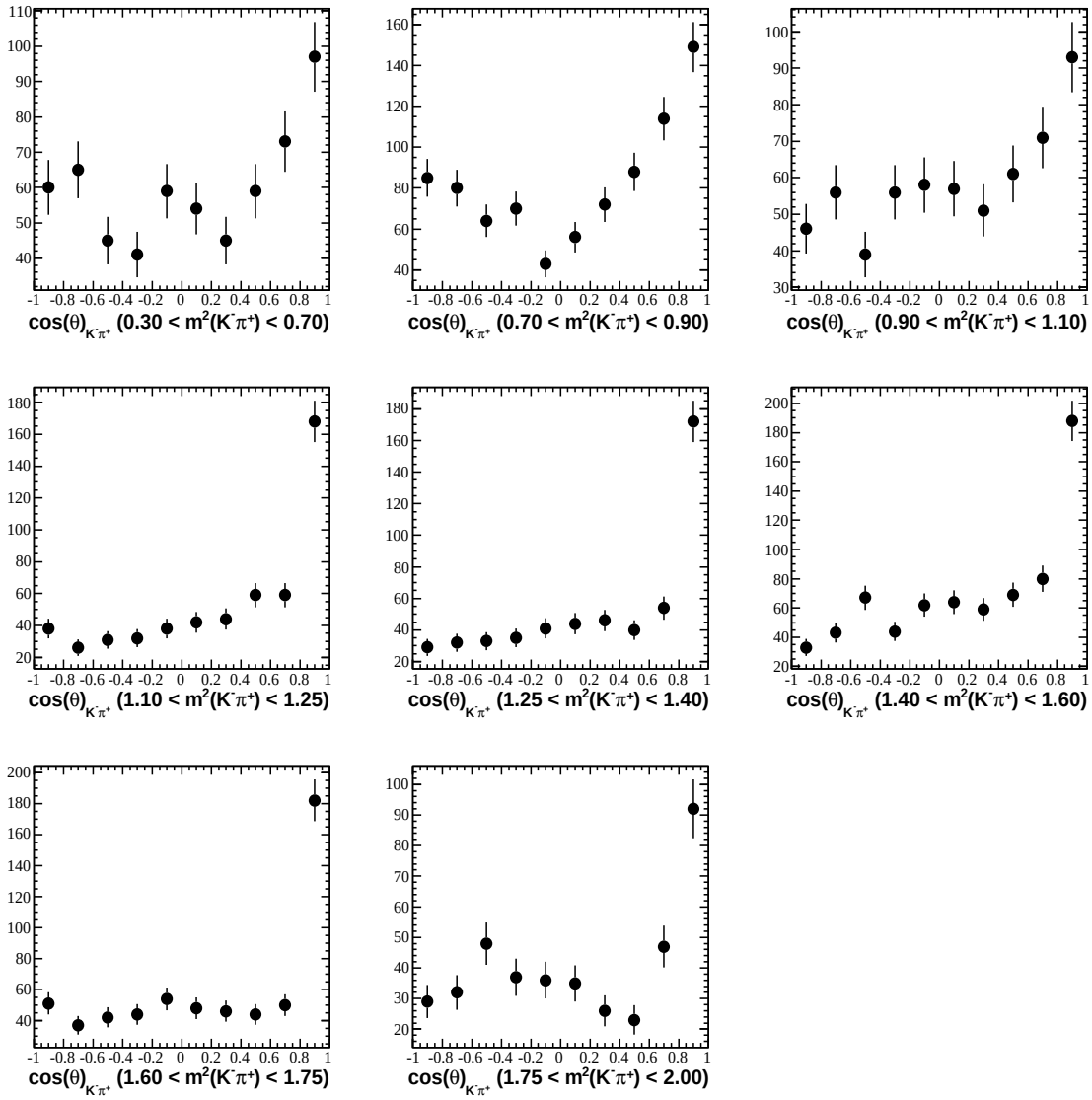

Figure H.3: D^+ low mass sideband region $K^-\pi^+$ helicity angle in slices of $m^2(K^-\pi^+)$

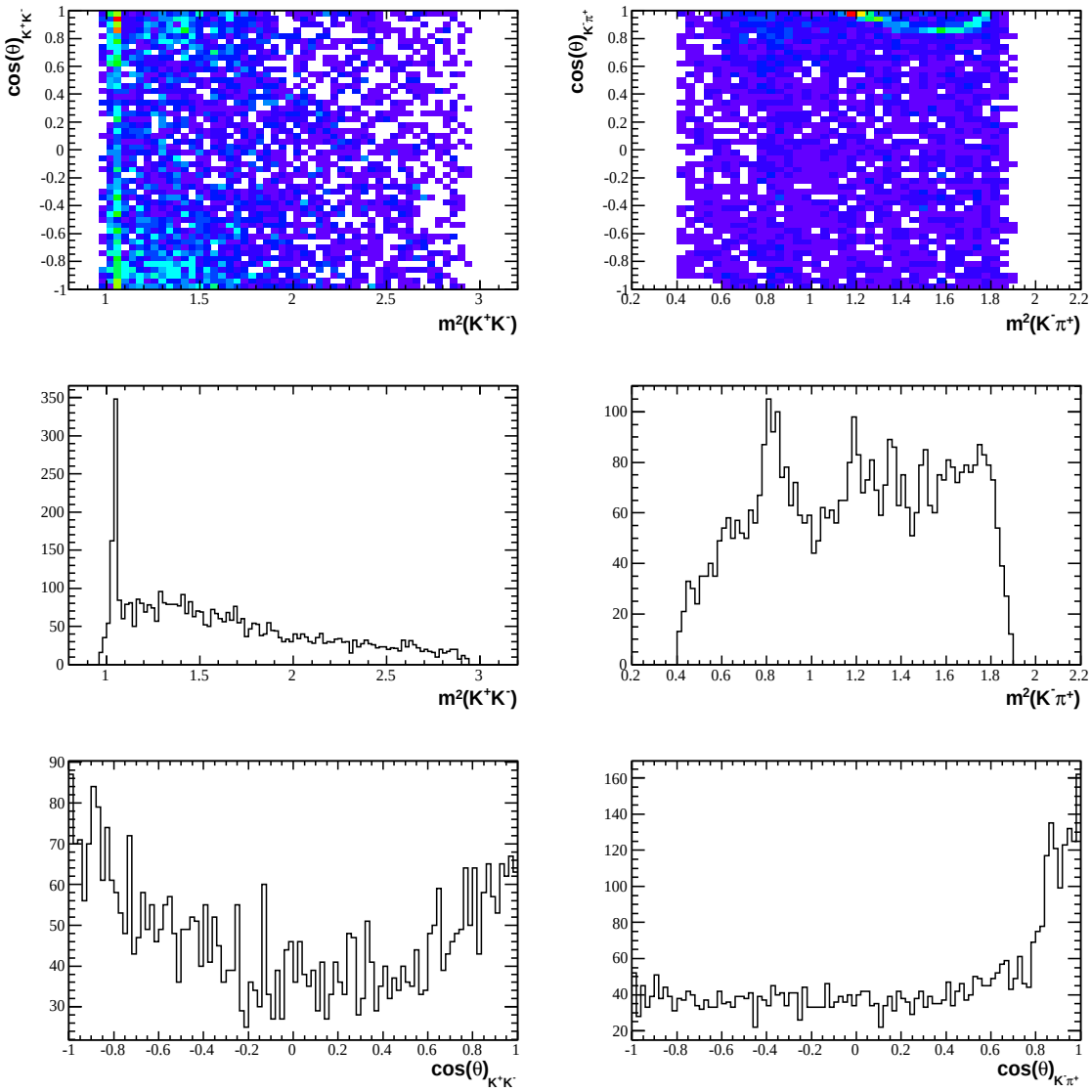

Figure H.4: D^- low mass sideband region Square Dalitz plot and projections

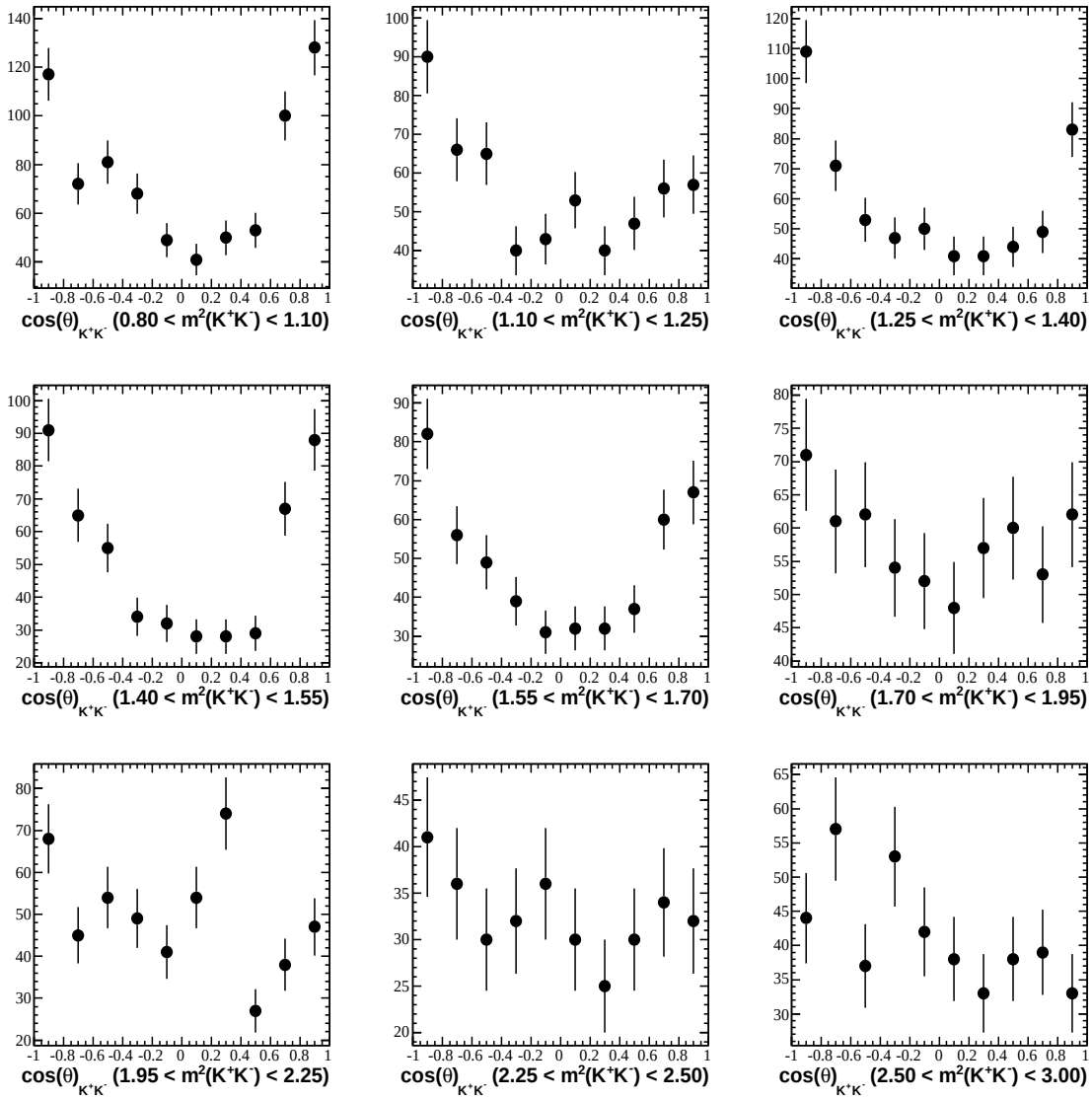

Figure H.5: D^- low mass sideband region K^+K^- helicity angle in slices of $m^2(K^+K^-)$

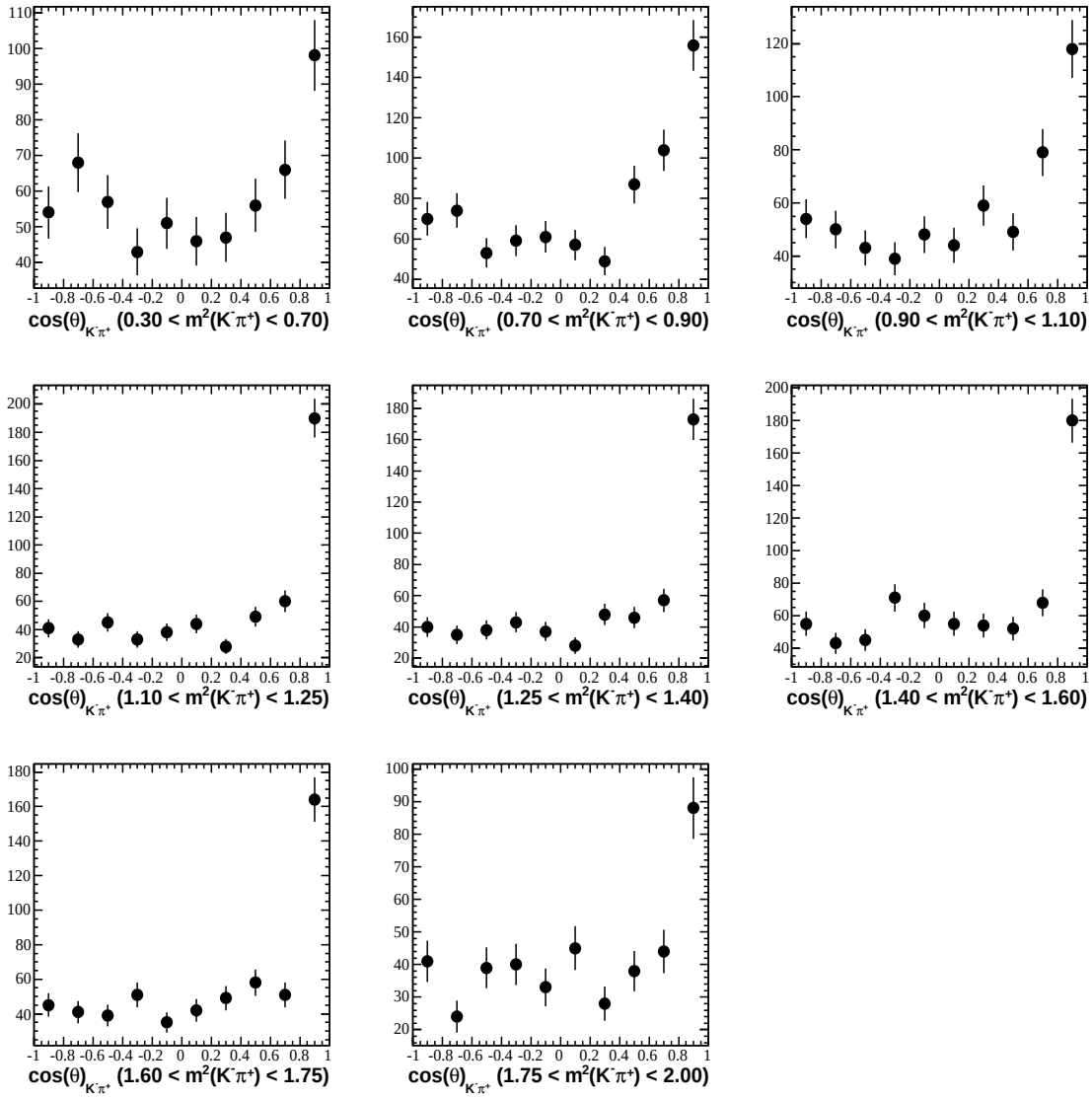

Figure H.6: D^- low mass sideband region $K^-\pi^+$ helicity angle in slices of $m^2(K^-\pi^+)$

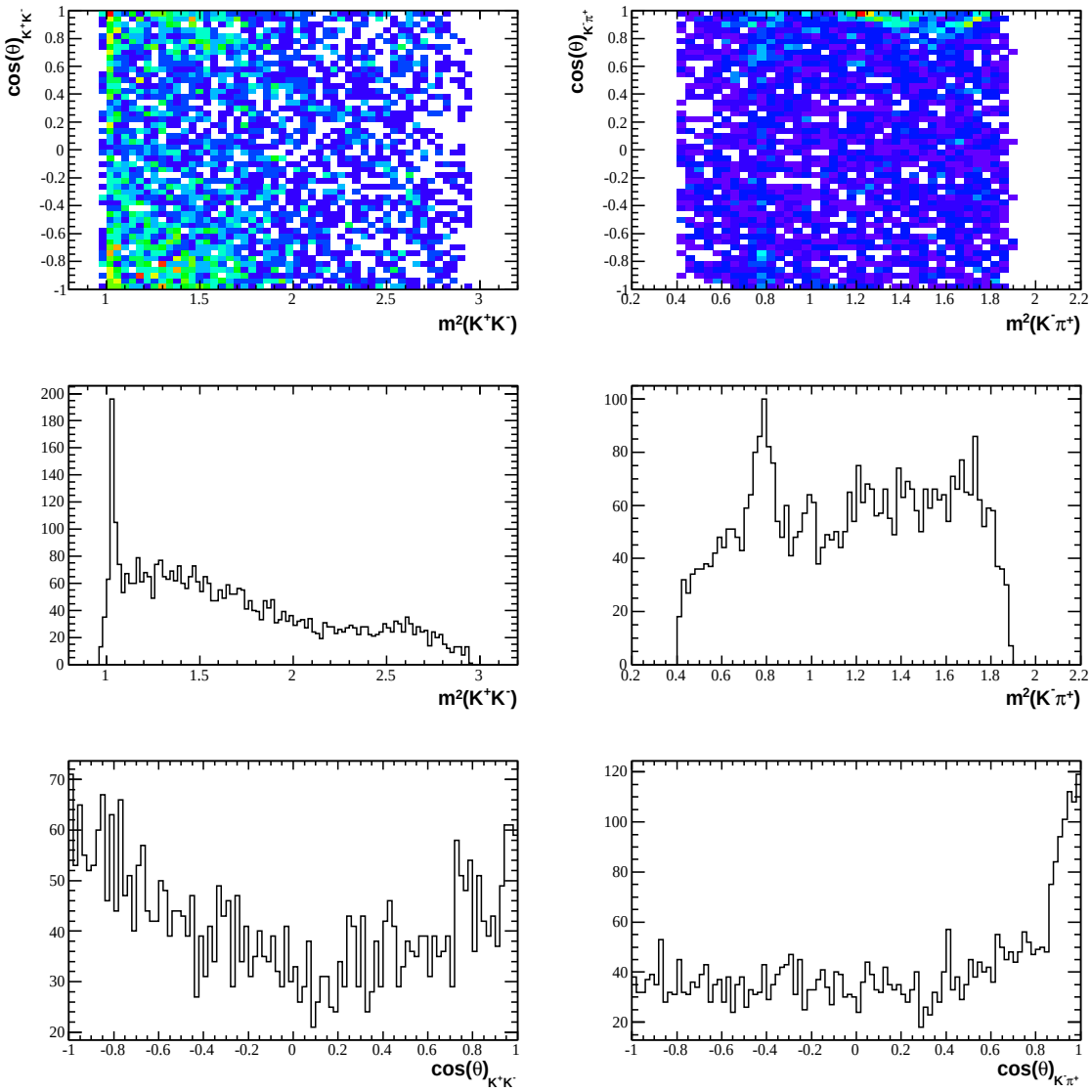

Figure H.7: D^+ high mass sideband region Square Dalitz plot and projections

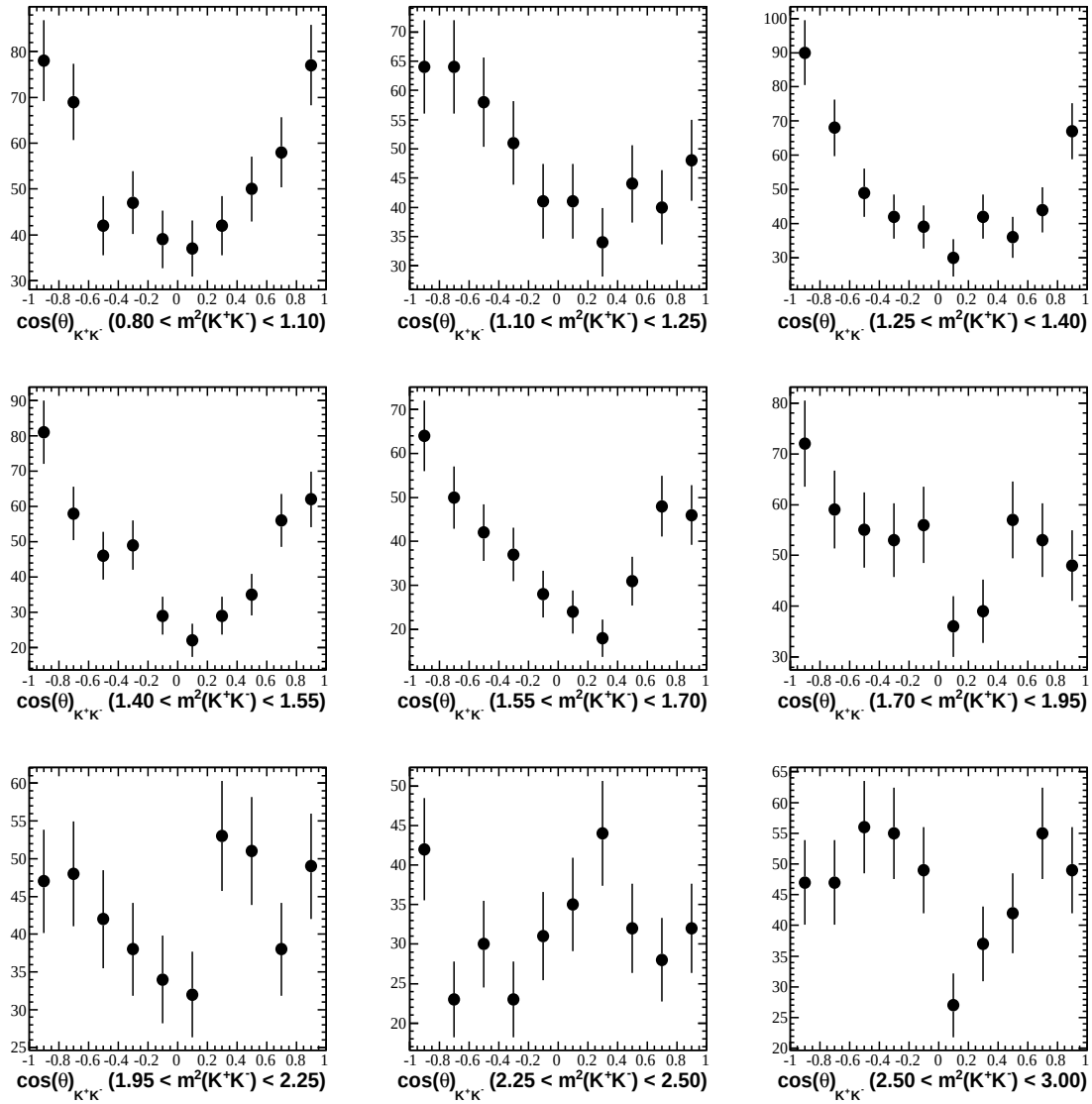

Figure H.8: D^+ high mass sideband region K^+K^- helicity angle in slices of $m^2(K^+K^-)$

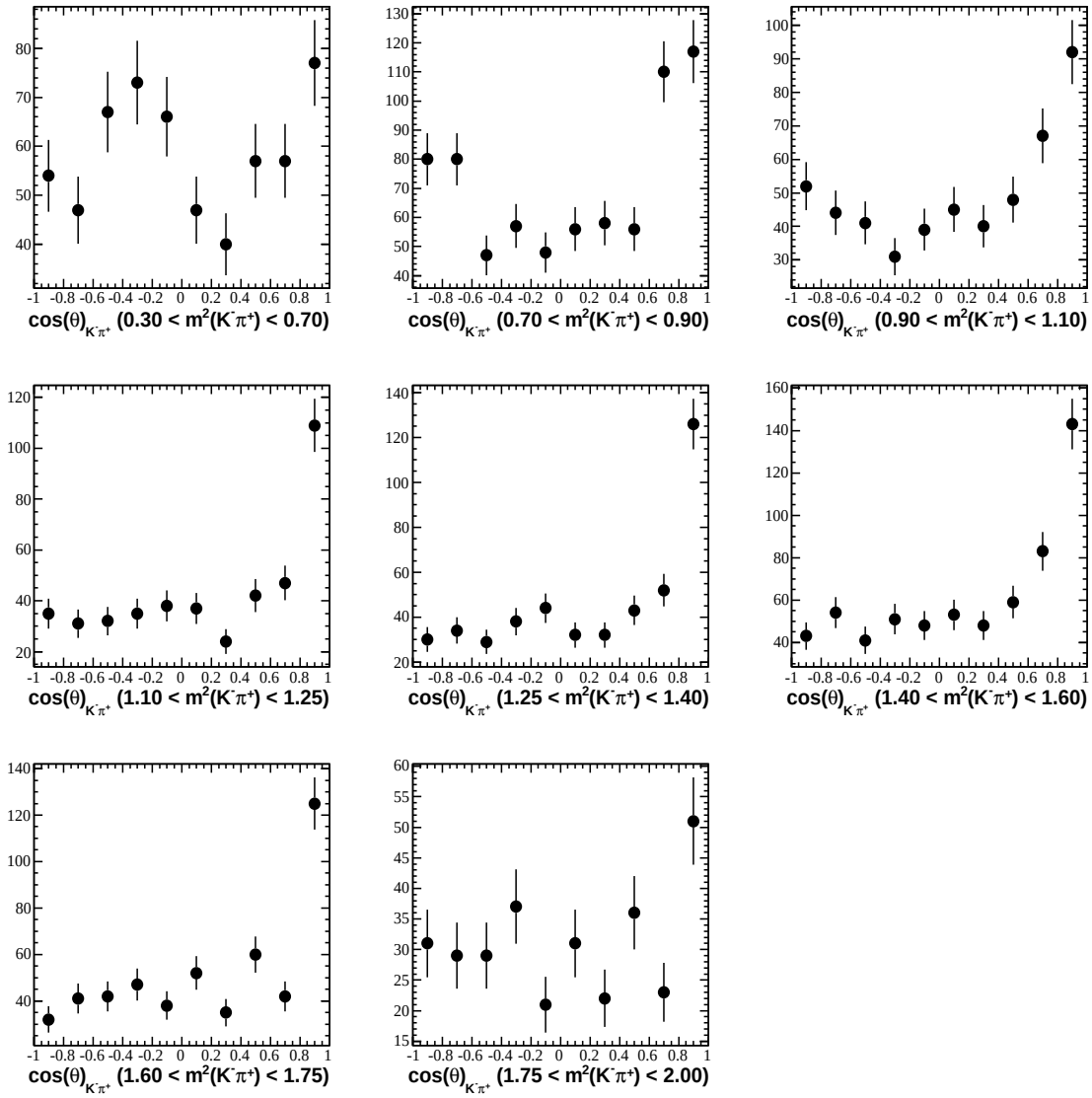

Figure H.9: D^+ high mass sideband region $K^-\pi^+$ helicity angle in slices of $m^2(K^-\pi^+)$

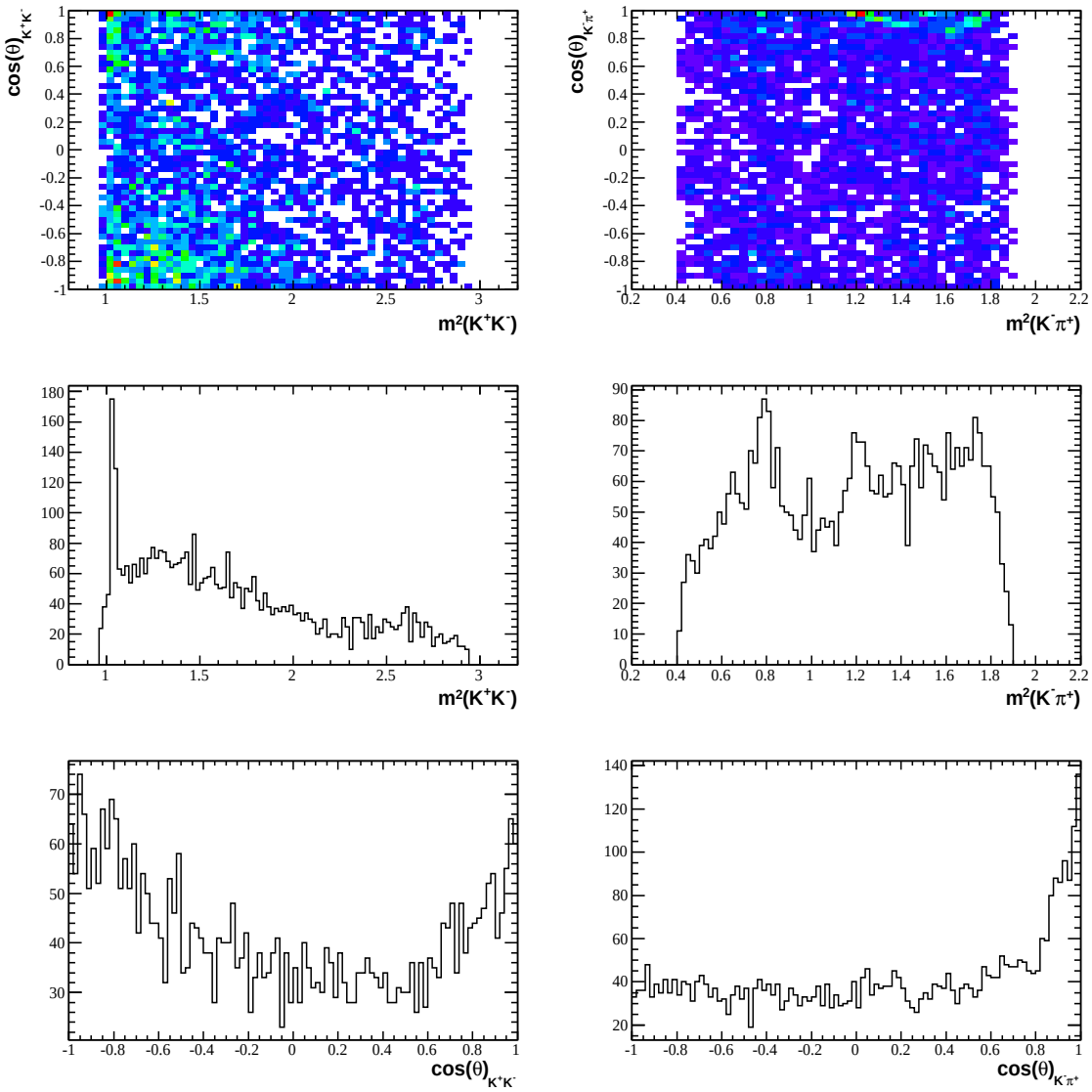

Figure H.10: D^- high mass sideband region Square Dalitz plot and projections

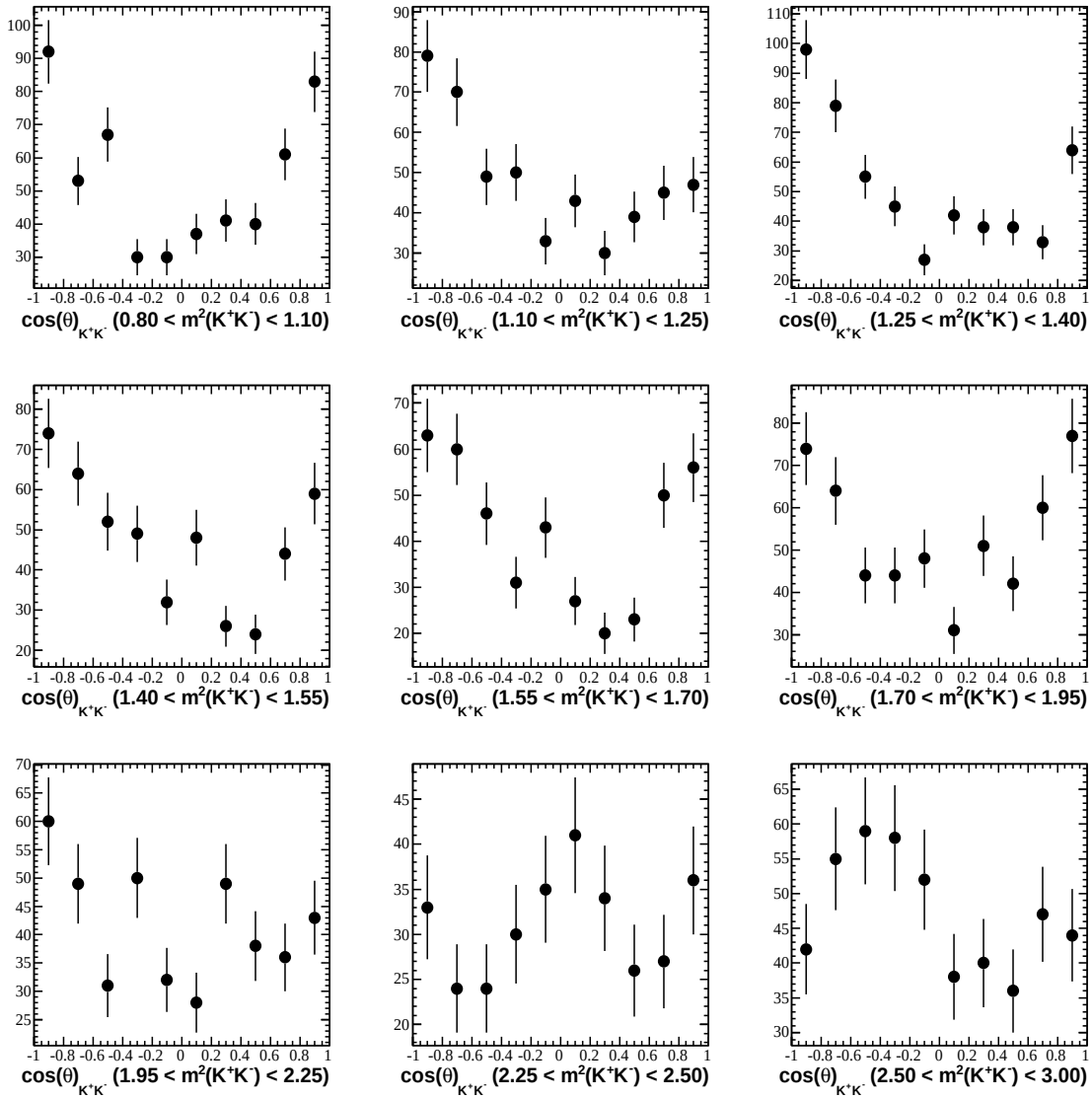

Figure H.11: D^- high mass sideband region K^+K^- helicity angle in slices of $m^2(K^+K^-)$

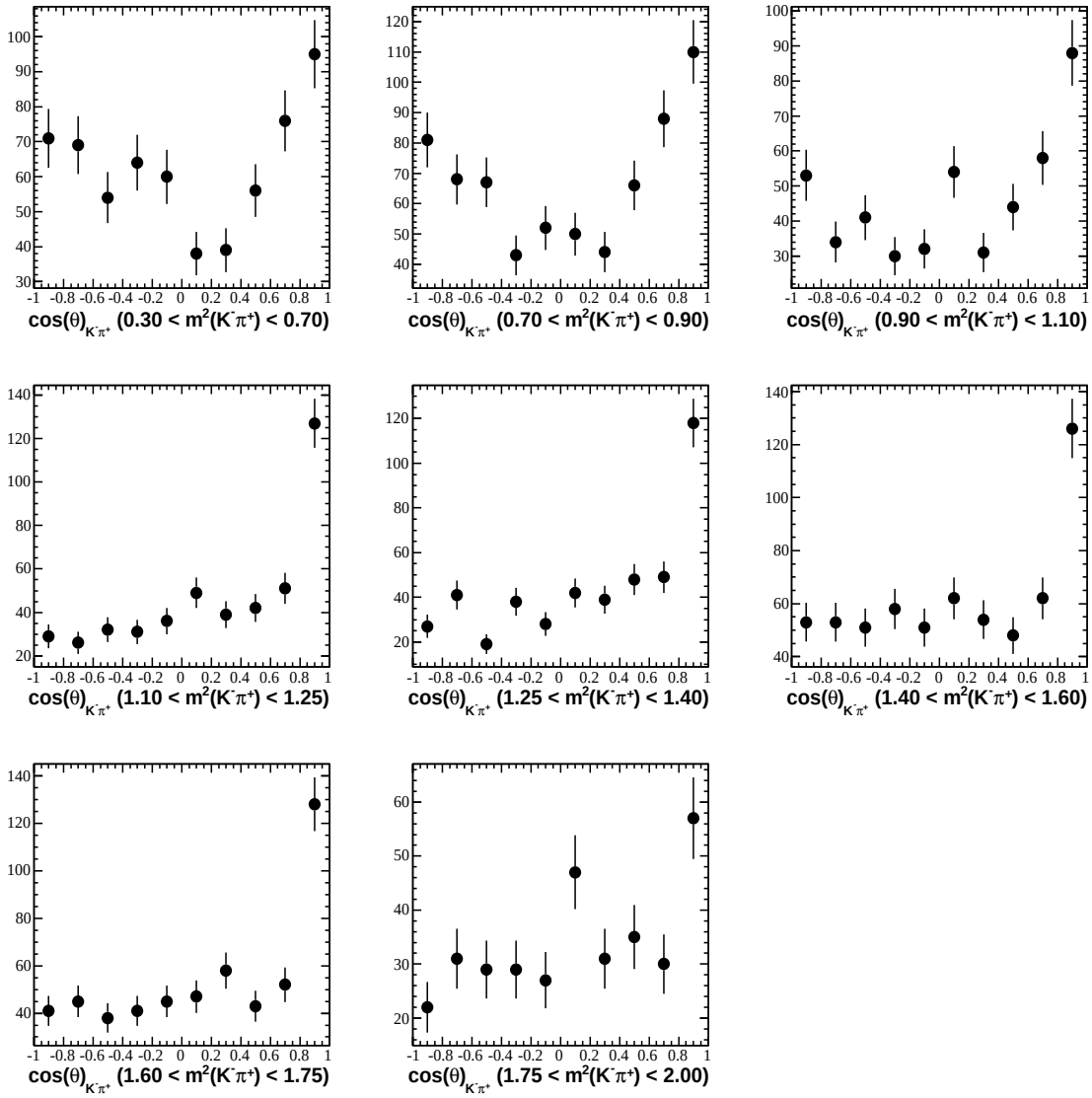

Figure H.12: D^- high mass sideband region $K^-\pi^+$ helicity angle in slices of $m^2(K^-\pi^+)$

Appendix I

Monte Carlo Background Pdfs

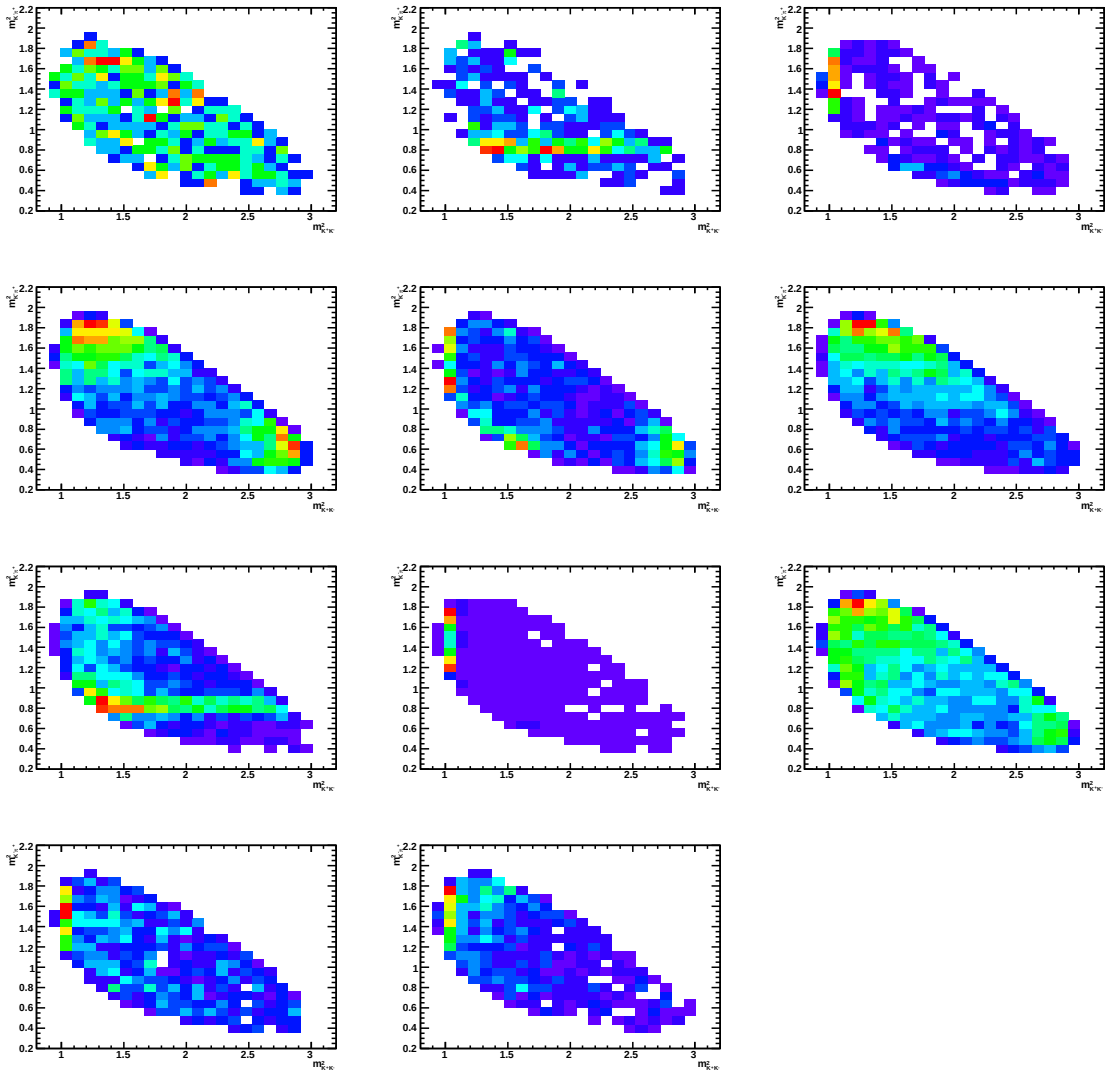

Figure I.1: Low mass sideband distributions for D^+ from uds, $c\bar{c}$, and $b\bar{b}$ MC.

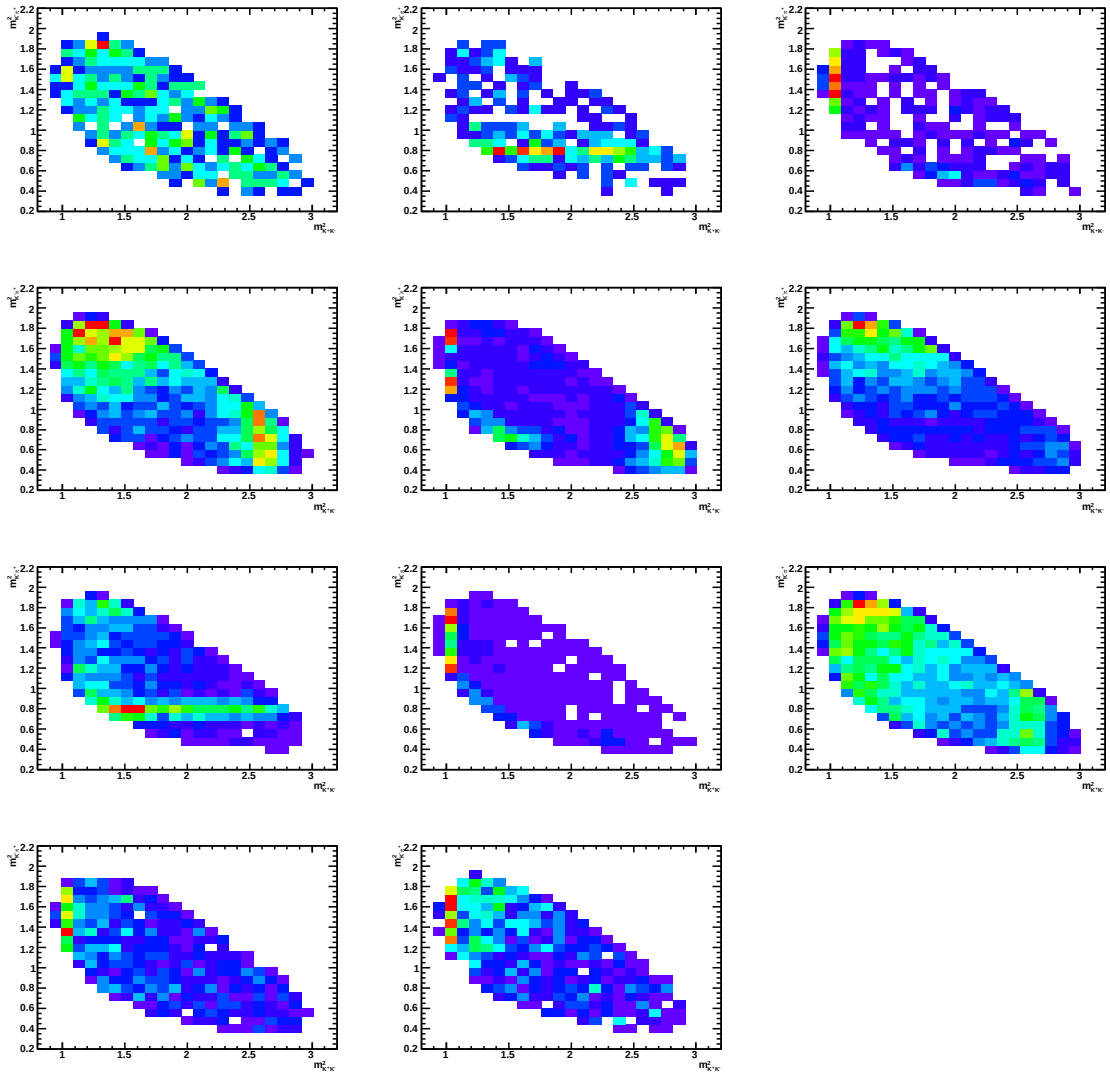

Figure I.2: High mass sideband distributions for D^+ from uds, $c\bar{c}$, and $b\bar{b}$ MC.

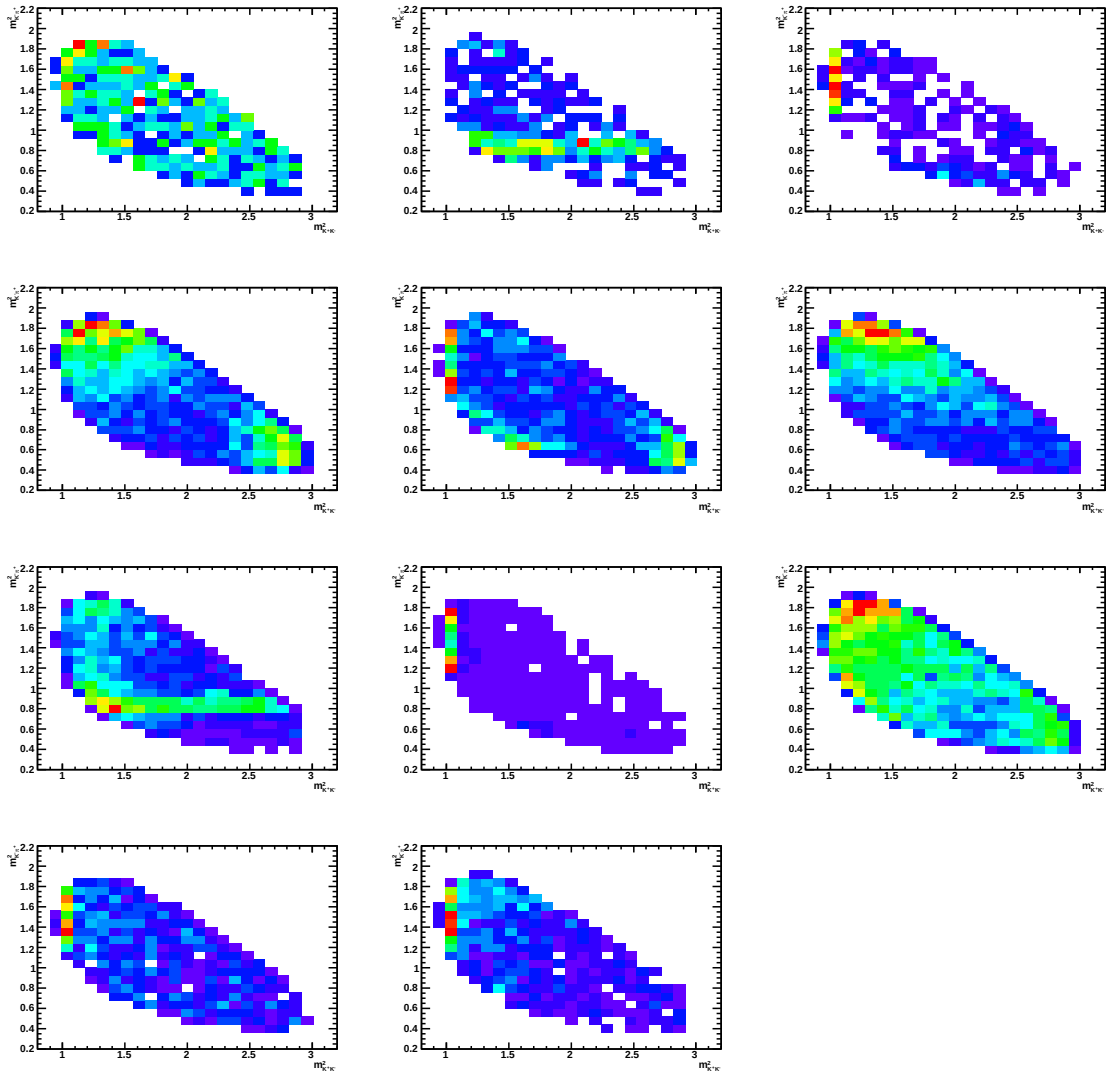

Figure I.3: Low mass sideband distributions for D^- from uds, $c\bar{c}$, and $b\bar{b}$ MC.

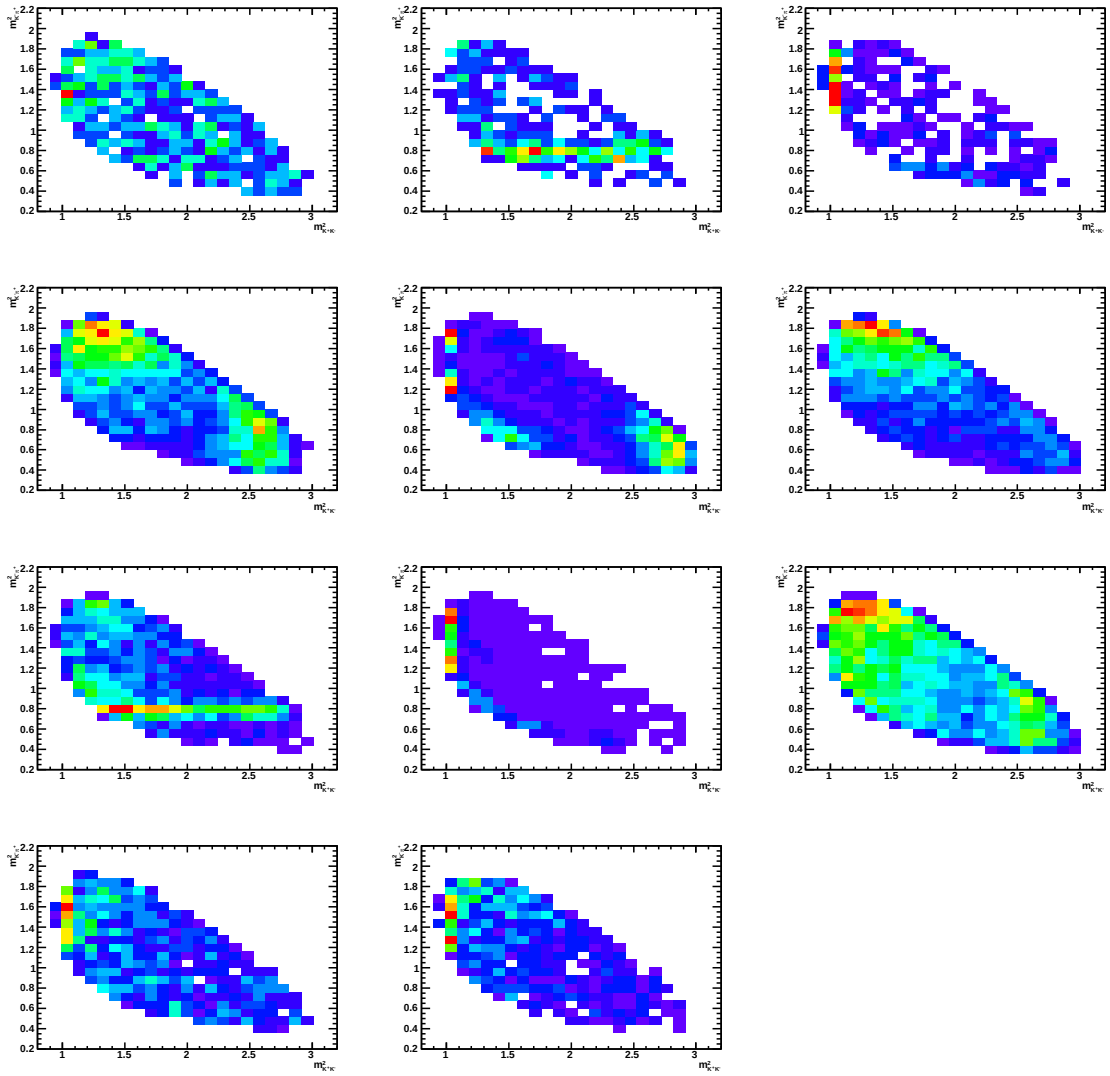

Figure I.4: High mass sideband distributions for D^- from uds, $c\bar{c}$, and $b\bar{b}$ MC.

Appendix J

MINUIT Fit Results for Integrated Mass Fit

NO.	NAME	VALUE	ERROR
1	NGaus1	7.94657e+04	6.38215e+03
2	NGaus2	1.41195e+05	6.48617e+03
3	NRad	3.22637e+03	3.43341e+02
4	Mean	1.86970e+00	1.17808e-05
5	Sigma	6.38494e-03	1.17389e-04
6	GauRatio	6.32122e-01	5.78273e-03
7	PolyHeight	8.67262e+04	4.86502e+02
8	Slope	-4.13447e-02	6.94614e-03
9	Quad	0.00000e+00	constant
10	Cube	0.00000e+00	constant

NO.	NAME	VALUE	ERROR
1	NSignal	2.23881e+05	5.86252e+02
2	GausFraction	6.28353e-01	4.30828e-02
3	RadFraction	1.44316e-02	2.77732e-03
4	Mean	1.86970e+00	1.34527e-05
5	Sigma	6.37496e-03	1.97515e-04
6	GauRatio	6.32532e-01	1.05709e-02
7	PolyHeight	8.67333e+04	5.30318e+02
8	Slope	-4.13299e-02	8.79571e-03
9	Quad	0.00000e+00	constant
10	Cube	0.00000e+00	constant

Appendix K

MINUIT Fit Results for Square Dalitz plot Fits of ϕ and $\bar{K}^{*0}$

K.1. $\phi(1020)$ Background Fit Results

NO.	NAME	VALUE	ERROR
1	N	1.29121e+03	5.45347e+01
2	mass	1.01946e+00	1.94627e-05
3	Gamma	4.26251e-03	3.98380e-05
4	P11	1.08036e+00	4.01117e-01
5	P22	-5.58669e-03	3.72069e-01
6	P01	1.43289e-01	9.42705e-02
7	P02	8.17260e-01	9.70063e-02
8	P21	-5.18170e-02	2.76934e-01
9	PcosH	6.82893e-02	9.42705e-02
10	Nbg	4.89758e+02	5.01530e+01
11	bgSlope	2.36925e+03	6.74319e+02
12	bgP11	7.07148e-01	2.84395e-01
13	bgP22	5.91817e-01	9.10204e-01
14	bgP01	-7.07839e-01	8.25889e-01
15	bgP02	2.87482e-01	2.63192e-01
16	bgP21	-6.78455e-02	6.34893e-01
17	bgPcosH	0.00000e+00	1.41421e+00

K.2. $\bar{K}^{*0}(892)$ Background Fit Results

NO.	NAME	VALUE	ERROR
1	N	1.35870e+03	8.58198e+01

```
 2  mass         8.95936e-01   2.16261e-04
 3  Gamma        4.88148e-02   7.85438e-04
 4  P11          7.43240e-01   1.01901e-01
 5  P22          9.41479e-02   1.10915e-01
 6  P01          2.22209e-01   1.25641e-01
 7  P02          3.54901e-01   3.88916e-02
 8  P21          1.73242e-01   8.70966e-02
 9  PcosH        1.42918e-01   2.24769e-01
10  Nbg          3.29330e+03   9.14721e+01
11  bgSlope      1.06382e+01   1.69368e+00
```